Swansea University
Prifysgol Abertawe

Development of Microneedles for diagnostic and Therapeutics

Sarah McIntyre

Swansea University

Submitted to Swansea University in fulfillment of the requirements for the Degree of
Doctor of Philosophy

December 2023

Declarations

This work has not previously been accepted in substance for any degree and is not being concurrently submitted in candidature for any degree.

Signed

Date...............05/12/23...

This thesis is the result of my own investigations, except where otherwise stated. Other sources are acknowledged by footnotes giving explicit references. A bibliography is appended.

Signed

Date...............05/12/23...

I hereby give consent for my thesis, if accepted, to be available for electronic sharing after expiry of a bar on access approved by the Swansea University.

Signed

Date...............05/12/23...

The University's ethical procedures have been followed and, where appropriate, that ethical approval has been granted.

Signed

Date...............05/12/23...

Acknowledgements

I wish to thank the following:

My supervisors Prof Owen Guy and Dr Sanjiv Sharma for their help and guidance throughout my project.

My funding body KESS II for their funding opportunists, training programmes and support.

Innoture Ltd and Ryan Bamsey for technologies, support and continued collaborations.

Ionut Ichim for sharing his fabrication expertise and helping when I came across issues in the labs.

The technical lab support team especially Gareth Blayney and Ryan Bigham who helped as much as they could by fix equipment quickly and supporting any experiments I wanted to do.

My colleagues who became fast friends for all the fun we had and keeping my spirits up when things were difficult.

Steve Edwards for letting me borrow some of his silver electrodes and sharing his electrochemistry knowledge.

and finally,

My family and boyfriend for all of their love and support throughout especially to my mum who has helped me check and correct my thesis and read through all of it several times.

Abstract

This work examines the fabrication and use of polymer microneedles made using an adapted screen printing method and UV curable polymer in both diagnostic and therapeutic applications. Starting with smaller round ended microneedles used only for cosmetics, this work looks at optimising the microneedle shape using this printing fabrication method and penetration efficiency and how the microneedles can be adapted for diagnostics such as cholesterol or chloride and delivery of drugs such as pravastatin. The polymer microneedles were prepared by a highly flexible microlithographic 3D printing (ML3DP) process. This process was a type of stencil printing. The process is adaptable using stencils with different aperture sizes, aperture shapes, the number of sequential depositions and the type of UV curable polymer chosen because it is possible to fabricated in an additive manner. Unlike other fabrication methods, it can easily be scaled up for high volume manufacturing and can be readily adapted to produce microneedles of different shape and size. This reduces the cost of the microneedles compared to those fabricated by etching or small scale printing.

The microneedle fabrication process previously used to make rounded tip cylindrical shaped microneedles, was optimised to make sharper microneedles for optimum penetration more suited to drug delivery and diagnostic applications. The optimised microneedles fabricated by ML3DP produced a conical shaped base with a stencil of apertures 400µm in diameter. Evenly spaced print gaps were used to fabricate these microneedles. A tipping stencil of 150µm diameter was used after fabrication of the base and the optimised microneedles reliably produced tips with the average diameter of 8µm. This fabrication method yielded microneedles with on average a penetration efficacy 82.42%. Histology and methylene blue staining were used to illustrate the penetration. These results confirm that the sharpness of the tip is critical in the success of penetration, height and width of the microneedles are also important factors for penetration efficiency. Some polymer microneedles were left uncoated and some metallised using various metals. Compression testing was used to determine suitability of both metal coated and uncoated polymer microneedles to withstand penetration forces.

For use as diagnostic electrodes the ML3DP microneedles were metallised. Chloride and cholesterol detection were looked at as there are not any current microneedle devices that can detect these analytes. Chloride levels can determine dehydration or cystic fibrosis and cholesterol levels can be an indicator for heart disease. For chloride detection the microneedles were metallised with silver and for detection of glucose or cholesterol the microneedles were metallised with platinum.

Silver bar electrodes and silver microneedles successfully determined the concentration of chloride solutions in the required range between 2.5 and 40mM and gave a linear

relationship.

Platinum microneedle devices were functionalised for diagnostic application by immobilising glucose oxidase or cholesterol oxidase on the surface and were successful in detecting a range of concentrations of glucose or cholesterol. The linear detection region was between 2.5 and 20mM for glucose and between 1.25 and 15mM for cholesterol which is in line with the concentrations of glucose or cholesterol found in the human body.

These ML3DP polymer microneedles were shown to be capable of delivering drugs, such as small molecule drug like calcein and large molecule drugs such as pravastatin through a 'poke and patch' method. A Franz cell method was utilised to measure drug diffused through porcine skin into a PBS solution within the cell. These tests showed the polymer microneedles facilitated some delivery through the skin albeit not as good as hypodermic needles and silicon microneedles.

Microneedles have the potential to be an important part of point of care devices within diagnostics and drug delivery. These polymer microneedles have shown the possible use of microneedles in diagnostic devices for determining chloride for the diagnostics of dehydration or cystic fibrosis and cholesterol for the monitoring of conditions such as heart disease. These polymer microneedles have also highlighted the use as a drug delivery alternative for drugs such as pravastatin for the treatment of high cholesterol.

Contents

List of Figures

List of Tables

Glossary

Abbreviations

ChEt	Cholesterol Esterase
ChOx	Cholesterol Oxidase
Cu-BTC	Copper benzene-1,3,5-tricarboxylate
CV	Cyclic voltammetry
CF	Cystic fibrosis
DC	Direct Current
DI	Deionised water
Fc	Ferricenium
FAD	Flavin adenine dinucleotide
FCA	Ferrocenecarboxylic acid
FDA	US Food and Drug Administration
FDM	Fused deposition modelling
GOx	Glucose oxidase
HDL	High density lipoprotein
HPLC	High performance liquid chromatography
ISE	Ion selective electrode
ISF	Interstitial fluid
LDL	Low density lipoprotein
LED	Light emitting diode
MA	Maleic Acid
ML3DP	Microlithographic 3D printing
MN	Microneedle
MRI	Magnetic resonance imaging
MWCNT	Multi walled carbon nanotubes
NAD	Nicotinamide adenine dinucleotide
NADH	Nicotinamide adenine dinucleotide hydride

NADP	Nicotinamide adenine dinucleotide phosphate
OCT	Optical coherence tomography
PBS	Phosphate buffered saline
PD	1,10-phenanthroline-5-6-dione
PDA	Photo diode array
PDMS	Polydimethylsiloxane
PEG	Poly (ethylene glycol)
PETG	Polyethylene terephthalate glycol
PET	Positron emission tomography
PLGA	Poly (lactic-co-glycolic acid)
PLA	Polylactic Acid
PMMA	Poly (methyl methacrylate)
PMVE	Poly (methyl vinyl ether)
PTFE	Polytetrafluoroethylene
PVA	Polyvinyl alcohol
PVD	Physical Vapour Deposition
PVP	Polyvinylpyrrolidone
SAM	Self-assembled monolayers
SC	*Stratum corneum*
SEM	Scanning electron microscopy
SLA	stereolithography
SU-8	Epoxy based negative photoresist
TFA	Trifluoroacetic acid
UV	Ultraviolet

Symbols

A	Cross-sectional area
a	Chemical activity
c	Distance from axis
C*	Bulk ion concentration
D	Diffusion coefficient
E^0	Standard Potential
E	Potential
E	Young's modulus
E	Enzyme
F	Faraday's constant
$F_{Bending}$	Bending Force
$F_{Buckling}$	Buckling Force
$F_{Compressive}$	Compressive Force
K_M	Michaelis constant
K_{sp}	Solubility product
I	Moment of Inertia
J	Current density
J	Flux rate
L	Length
P	Product
P_{Pierce}	Pierce pressure
m	mass
n	ion charge
R	Universal gas constant
δ_Y	Yield strength
S	Substrate
S_c	Substrate concentration
T	Total number of MN
t	Current pulse time
t	time
T	Temperature in Kelvin
ΔV	Potential difference
V_{max}	Max velocity
v	Velocity

Units

Å	angstroms
kÅ	kiloangstroms
A	amps
mA	milliamp
nm	nanometres
μm	micrometres
mm	millimetres
cm	centimetres
m	metres
°C	degrees Celcius
g	grams
mg	milligrams
μg	micrograms
kg	kilograms
μl	microlitres
ml	millilitres
SCCM	Standard cubic centimeters per minute
μM	micromolar
mM	millimolar
M	molar
mN	milli newtons
kN	kilo newtons
N	newtons
GPa	giga pascals
s	seconds
min	minutes
hr	hours
mV	millivolts
V	volts
W	watts

1 Introduction

1.1 Literature Introduction

Diagnostics are an essential part of medicine today using many different methods. These include medical imaging such as X-rays, Magnetic resonance imaging (MRI), positron emission tomography (PET) and ultrasonography. These methods usually show anatomy and a comparison can be made to the normal range of anatomy in humans [1, 2].

There are many invasive forms of diagnostics such as blood tests, or endoscopy. Endoscopy is an optical method of diagnostics which involves the insertion of a viewing tube called an endoscope through a bodily opening with a view to directly observing cavities inside the body or inside organs. The larynx, lungs, gastrointestinal tract, bladder and uterus can all be viewed by passing an endoscope through the nose, mouth, anus, urethra and vagina respectively. There are some circumstances where an incision needs to be created to pass the endoscope into a cavity, these incisions are used to view places such as the joints, abdominal cavity and lungs [1].

Other diagnostics are performed using analysis from tissues such as cell biopsies or bodily fluids such as serum, plasma, saliva, urine, tear and spinal fluid. These fluids are relatively easily accessible with minimal or no discomfort to a patient. These fluids contain many different types of biomarkers ranging from proteins to lipids. Raman spectroscopy is one technique which is used to analyse lipids and offers high chemical specificity and information on molecular structure without needing staining or labelling. Raman spectroscopy can provide real-time molecular information and high resolution imaging of samples. However it is not a point of care diagnostic which is an important part of making diagnostics accessible [3, 4].

For rapid detection of analytes in a patient setting, point of care testing is essential. It can also facilitate better management, diagnosis and monitoring of diseases. A biosensor is the most important part of the point of care device as it provides the bioanalytical analysis of the device. Biosensors can be electrochemical or optical and include technologies such as microfluidics, device automation, signal readout and lab-on-a-chip which are just some advancements on point of care devices [5]. One of the most well known

point of care devices are continuous glucose monitors. These have gained a huge amount of popularity within the diabetic community where the patient can self-administer the test. There are many different variations of these devices including Dexcom and Libre [6] and they all monitor glucose variability using a sensor that in inserted through the skin and left in the body usually on the back of an arm. These devices have been shown to reduce admissions to hospital compared to people who only utilised self monitoring of blood glucose [6].

Another area of diagnostic and drug delivery research is access to the body through or on the skin. The skin is the largest organ in the human body. Not only is it our barrier to the outside world therefore allowing bodily functions to happen within a contained and controlled environment, it is the main interface our bodies have with outer stimuli. The skin controls the passage of substances through it, in and out of the body with different mechanisms, however the most prominent barrier is the top *stratum corneum* layer. This layer is around 10 -20µm thick and is made up of corneocyte skin cells made from previous keratocytes from the epidermis layer beneath which contributes to skin hydrophobicity. The epidermis is a layer of living nucleated cells which is about 50-100µm thick and is where the main cycle of keratinocytes takes place. The cells in the epidermis are surrounded by interstitial fluid (ISF) as is the dermis below. The dermis is the main layer of the skin which is usually up to 1mm thick. It is comprised of mainly collagen, elastin, fibroblasts and contains hair follicles, capillaries, nerve endings, lymphatic vessels, sebaceous glands and sweat glands. These cells are surrounded by ISF. The hypodermis is the bottom most layer of the skin which is comprised of mostly subcutaneous fat. This layer is absent from thin skin areas of the body such as eyelids and contains bigger blood and lymphatic vessels. There is a flow of substances between the layers of the skin cells, the capillaries and the outside. Controlling this passage can be utilised for diagnostics or drug delivery. Microneedles (MNs) are one such method of bypassing the *stratum corneum* barrier for diagnostics and drug delivery [7, 8].

The concept of MNs has been around since the late 1970s where Gerstel and Martin envisioned it as a way to conquer the issue of pain in drug administration [9]. It was not until the late 1990s however that micro fabrication had advanced sufficiently to make MN manufacture possible [10]. The first microneedles were fabricated in 1998 with a deep reactive ion etching process on silicon wafers, the same technology used to make circuits. The MNs were fabricated using masking and etching techniques. It started with chromium dots on the wafers to determine the size of the eventual microneedles and then controlled plasma etching very deep valleys into the silicon which forms the MNs.

These MNs were used to investigate the transdermal drug delivery of small molecule drugs such as calcein and demonstrated passive transport of the drug through the skin [11, 12, 10, 13].

MNs have been developed to overcome the challenges faced by the more traditional methods such as injections, vaccines, urine testing, blood tests by hypodermic needle and suction blistering. MNs are minimally invasive due to only penetrating the epidermis [14] and sometimes the superficial dermis. Figure 1.1 shows a schematic of MNs inserted into the skin. Due to the MN length, patients do not experience pain as they would with a hypodermic needle as there are no pain receptors found in the epidermis and, in the superficial dermis the tips of the MNs are so narrow that they miss the nerve endings where the MN penetrates [14]. MNs of heights 180 μm and 280 μm, as seen in the study by Haq et al.[15], were reported to be pain free with only the feeling of pressure on the skin. For a MN array to be effective, it needs a design which is optimal for penetration, pain-free, effective for either diagnostics or drug delivery and biocompatible.
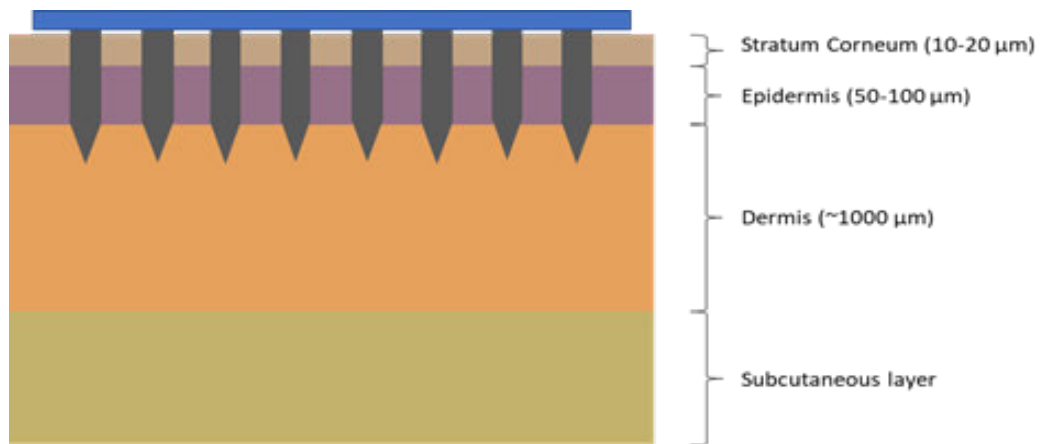
Figure 1.1: Schematic of MNs inserted into skin - cross section

Work within this thesis has been conducted in collaboration with Innoture Ltd as a sponsor. They had been using microneedles as an aid for cosmetic products in the context of cosmetic patches. A key part of their planned development going forward was to alter and optimise their current microneedle cosmetic patches to expand into drug delivery and diagnostics with commercially viable drug delivery or diagnostic microneedle patches. This step required more evidence based research to branch out into and therefore was a focus of the thesis going forward. The microneedles made for their

cosmetic patches using a 3D printing method prior to the start of this work were more cylindrical and small enough that they are not considered a medical device. The 3D printing method used is a very flexible, cost effective method that can be adapted to make polymer MNs of many different heights, shapes and degrees of sharpness. This method of microneedle fabrication will be investigated later in this thesis.

1.2 Microneedles for diagnostic applications

ISF is a biological fluid found in the epidermis and dermis layers of the skin which can be used to monitor biomarkers and diagnose disease. There have been studies comparing the biomarkers and other proteins found in ISF to serum and plasma. These studies show that the profile of ISF when compared to serum and plasma is very similar suggesting that ISF could be used in lieu of blood sampling. The proteomic profile between ISF, serum and plasma is 93% similar and the major differences are the quantity of the proteins in samples of the biological fluids. Extracting ISF from the skin is the major hurdle when testing and traditionally it is achieved through a technique called suction blistering. This can be a painful procedure but does provide access to biomarkers that are not within the serum or plasma. The technique involves applying negative pressure to the skin for up to 2 hours at temperatures up to at 40°C which separates the dermis and epidermis allowing dermal ISF to be drawn up by this suction into a blister which is then collected via a needle. The skin can be damaged and injuries can take weeks to heal. It is time consuming and there are also only small volumes available for collection which can limit which diagnostic techniques are used therefore the better alternative is to use microneedles to either extract ISF or detect biomarkers in vivo. The amounts which are able to be collected are in the µl range. In addition, there are biomarkers in ISF that are not present in serum or plasma including many inflammatory markers or local markers such as those attributed to some skin conditions [16, 17, 18, 19, 20].

1.2.1 Microneedle Materials

Materials used for microneedle fabrication are largely dependent on the fabrication methods available. Initially silicon, metals and glass were used, as the fabrication technology could process these materials. As micro fabrication technology progressed more MNs were made of polymers, sugars or ceramics using other fabrication techniques. Silicon is a crystalline structured material that was the first material used for microneedles using an ion etching technique and it has many desirable properties for MN fabrication. There is a flexibility in the way it can be processed to make many different shapes, allowing MN shape to be fine-tuned and controlled as the manufacturing methods are very precise and can be produced in batches. Silicon has high mechanical strength which makes it ideal for piercing the skin successfully to allow drug delivery. Despite this silicon is brittle and there is a slight biocompatibility issue should frag-

ments of silicon stay in the skin after insertion. Dry or wet etching is a common way of fabricating silicon MNs in addition to cutting or dicing. Silicon has disadvantages in that the fabrication cost is high, complex, often time consuming and also wasteful as it is a subtractive process [21, 22]. Silicon MNs can be made hollow or porous through other etching methods to allow for ways to store drugs or ISF and the dosing or load can be influenced by the structure of these MNs [23, 24].

Metals like stainless steel and titanium are common metals used in medical devices and implants due to knowledge about their biocompatibility and other material and mechanical properties. The majority of metal microneedles are produced using metals such as aluminium, titanium, stainless steel, palladium, nickel and palladium-cobalt alloys [25, 26, 22]. These materials are not only biocompatible, but they possess high elastic moduli (up to 180GPa) and unlike other materials these metals have a high fracture toughness also. This would make them a better option to silicon as a material for MN fabrication[12, 27]. Metal, like silicon, is used to create solid, hollow and porous MNs through various fabrication techniques including photochemical etching and laser cutting[26, 28]. They have also been made from assembling small hypodermic needles (e.g. 30 gauge) which were adjusted to form smaller MN heights of between 300 and 900 µm [29].

Ceramics are materials that form mainly ionic bonds between non-metallic and metallic elements. MNs have been made from ceramics due to their high mechanical strength and their stability in high temperatures in comparison to polymers. Alumina and Silicon nitride are examples of biologically compatible ceramics which have been used to fabricate MNs. Ceramic MNs have the potential to aid drug delivery as they are porous enough for drugs to be loaded into them and then released and they are usually fabricated using micro moulding or two photon polymerisation-micro moulding techniques. Micro moulding involves using a master mould which is filled with a slurry of the ceramic. The sample is then dried and sintered to obtain the MNs. Two photon polymerisation micro moulding is a sol gel process that creates a matrix between the organic and inorganic compounds [30, 31, 32].

A large variety of polymers can be utilised to fabricate MNs. The key advantages of using polymers are that they are lower cost than other materials, they have high biocompatibility, they can be biodegradable, and they offer reasonable strength and toughness and low toxicity. Other materials like metals and silicon have higher mechanical strength than polymers, but polymers can offer higher toughness than glass or ceramics. The manufacture of polymer MNs is generally low cost and quicker than alternative materials like silicon and can be additive rather than subtractive. There are many fabrication

6

techniques including injection moulding, laser micro machining, micro moulding, casting, drawing lithography and hot embossing. Each method can produce MNs or varying shapes and sizes including solid, hollow and porous [33, 34, 35]. As seen in the table below there is a large range of polymers used for fabricating microneedles. The type of polymer used varies depending on its application. Polymers used for making the main MN structure need to have high mechanical strength, toughness and biocompatibility for example polycarbonate [36, 37]. Polymers which are to be used for dissolvable MNs need to be biodegradable at the correct rate for the drug release time frame desired of which polyvinylpyrrolidone (PVP) is a common example [38]. Polymers are also often used as coatings on solid MNs in the form of hydrogels to be loaded with a drug and for controlled drug delivery release. These polymers need to be swellable to allow for release of the drug when inserted into the skin. Examples of hydrogels used for microneedles are Poly (methyl vinyl ether)/ maleic acid (PMVE/MA) and poly (ethylene glycol) (PEG). There is the possibility of bespoke polymers designed for specific MN applications [39]. Polysaccharides such as cellulose and sodium alginate are used as dissolvable MNs along with sugars such as Maltose [34, 40]. There are many composites of polymers trialled to combine the required properties for desired applications. Examples are composites of PEG and PMVE/MA hydrogels and alginate and maltose polysaccharides, among polymer and non-polymer composites.

1.2.2 Materials and Techniques used for microneedle biosensing

MNs must penetrate the skin efficiently in all applications. In the case of biosensing MNs it is to reliably access the ISF. Solid microneedles are used in biosensing as well as delivery. These MNs are used as the functionalised electrode in situ. The solid MNs for biosensing are made with materials like silicon, metal or polymers which have high mechanical strength and toughness. These materials allow the MNs to keep their shape well enough that they penetrate the skin efficiently [22, 41]. They can be used to sample ISF but are inefficient as they are prone to interference in results because of extended collection times. Solid MNs are usually coated in a metal or made of electrically conductive materials in order to work as in situ electrodes. The coatings on these MN usually contain enzymes and other biomolecules to act as selective biosensors or as the means to hold drug to be delivered. Coatings of materials like metals can be used to improve the mechanical and/or electrical properties of the MNs. Examples include coating in gold or platinum to improve mechanical strength, electrical conductivity and bio-compatibility [42, 43].

MNs made from non-electrically conductive materials like polymers or ceramics can be utilised as sampling techniques for out of body testing. These microneedle systems are usually either porous, hollow or swellable. Swellable microneedles are able to absorb the ISF, they are usually solid needles coated with Hydrogels such as alginate or PEG and are utilised to sample the ISF. The hydrogel coated MNs swell on contact with water which is the main constituent of ISF but during insertion they are sharp and hard enough to penetrate skin efficiently [34, 44]. One of the earliest instances of using MNs to sample ISF was for continuous glucose monitoring. These MNs were hollow and made from silicon and integrated to an external electrochemical biosensor. Capillary and evaporation forces drove the flow through the hollow MNs into the glucose biosensor [45].

Table 1.1: Types of polymer materials for solid, dissolvable and swellable microneedles

MN Type	Polymer Type	Polymer	Fabrication Methods	Tensile Strength	Solubility in Water	Moisture Content	Volume Increase	Ref.
Solid	Thermoplastic	Polycarbonate	Injection moulding	55-77 MPa	Not soluble	<0.03%		[36, 37, 46]
		polylactic acid (PLA)	3D printing and wet etching	59 MPa	Not soluble	As low as possible		[47, 48]
		poly methyl methacrylate (PMMA)	Solvent casting moulding	75 MPa	Not soluble	<1.1%		[49, 50, 51]
		Polypropylene (PP)	Laser ablated mould and injection moulding	25-33 MPa	Not soluble	<0.2%		[52, 53, 54]
	Photocurable	Dymax	Photocuring	17 MPa	Not soluble	very low		[55]
Dissolvable	Polyvinylpyrrolidone (PVP)	PVP	Moulding	1.4 MPa	Soluble	7.21-10.53%		[38, 56]
	Polysaccharides	Cellulose	Laser writing and moulding	6.7-2.52 MPa	Soluble	Up to 20%		[34, 57, 58, 59]
		Sodium alginate	Moulding	1-3.92 MPa	Soluble	33-97%		[34, 60, 61, 62]
	Sugars / carbohydrates	Maltose	Melting		Soluble			[34, 40, 63]
Swellable	Hydrogels	PEG	photo-polymerisation	Up to 2 MPa	Soluble		18.88%	[39, 64, 65]
		PMVE/MA	Micro-moulding		Soluble	38-52%	40%	[39, 66, 67]

1.2.3 MN Image Characterisation

MNs can be characterised by imaging using various techniques. These can be used to identify structural characteristics and changes in response to stimuli. The most common way of imaging microneedles is through scanning electron microscopy (SEM) as this allows views of the shape and surface features of the MNs. An SEM is a type of electron microscope that uses a focused electron beam which interacts with a sample to produce signals to be converted into an image. Images can be taken from different angles and there is no light reflection as can occur in an optical microscope image. The magnification ability is also large from 20x to 30000x times over an area between 5µm and 1cm with a spatial resolution of $50 - 100$ nm depending on the specification of the machine [68]. Examples of MNs imaged by SEM seen below in figure 1.2 [69, 70]

(a)   (b)

(c)   (d)
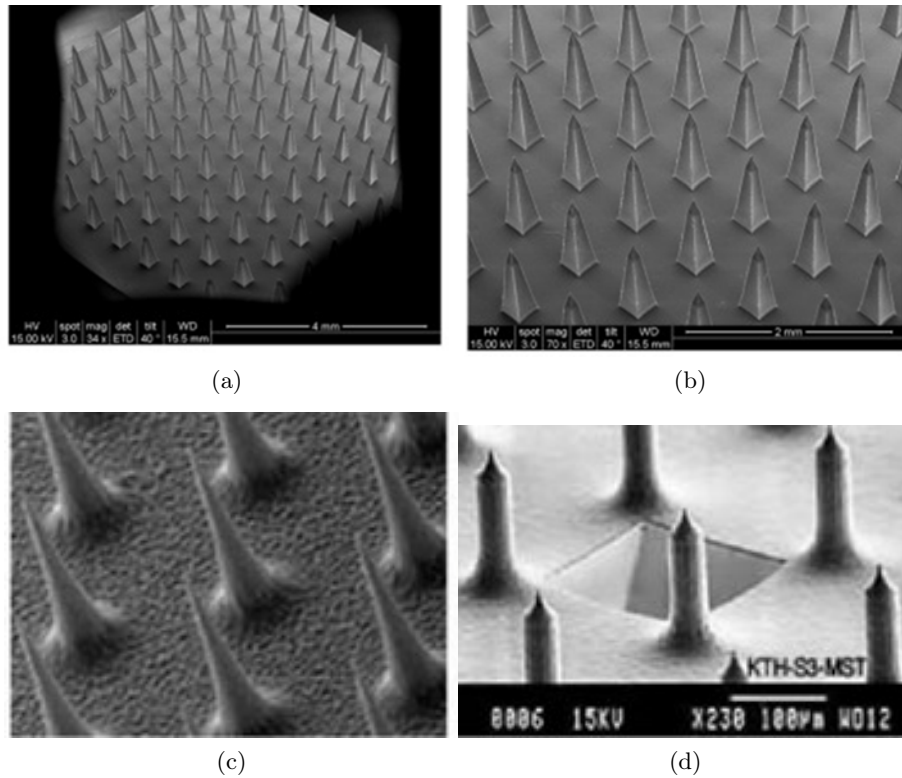
Figure 1.2: a) and b) SEM images of polymer MNs , c) and d) SEM images of silicon MN

Characterisation methods to determine penetration efficiency include optical coherence tomography (OCT) and histology. MN treated skin (animal or human) can be

stained simply by dyes such as methylene blue to confirm MN penetration. These dyes will stain only the viable epidermis and not the *stratum corneum* so that the micropores created by the MNs can be identified. There is no identification of the efficiency of the penetration from this test, just that penetration of the *stratum corneum* has occurred. Some measurement of the micropore is possible by measuring the diameter of the dye spots, this however has its limitations as movement of the dye in a lateral direction can cause over estimation of size. False positive can also happen if the dye pools in an indentation of the *stratum corneum* [71, 72].

Figure 1.3 shows an example of methylene blue stained MN pores [72].
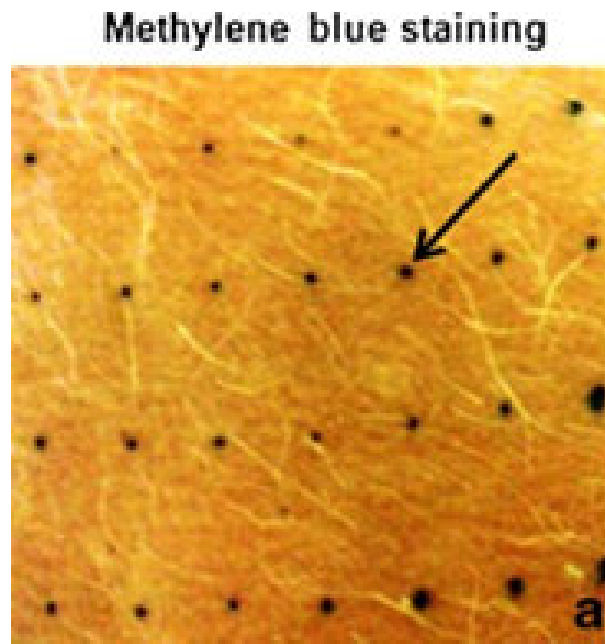
Figure 1.3: Methylene blue staining of MN pores into skin

Histology and skin staining are an improvement on the visible staining tests, it does however take a long time to do in comparison to other techniques. In this case the MN treated skin is taken from the bulk and flash frozen with liquid nitrogen. This piece is then sliced in a cryostat to obtain slices of around 6-12µm thick. Usually the slices are then stained with eosin and hematoxylin to make the microchannels visible [73, 74]. This technique is quite destructive as there is a lot of mechanical manipulation and the potential for pores to deform or change shape before staining leading to mismeasurements of micropore diameter. Histology can be used to determine the depth of insertion by the MNs. Figure 1.4 shows an example of a stained section with micropores showing

[72].

Histological sectioning
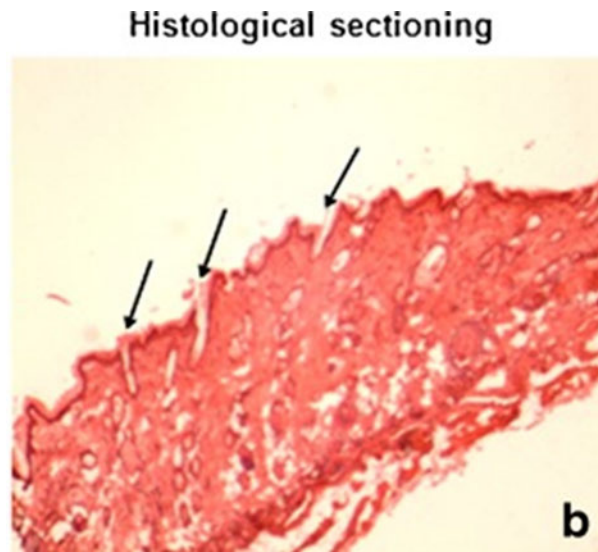
Figure 1.4: Stained histological section showing micropores caused by MNs

Confocal microscopes are also useful for imaging ex-vivo and in-vivo MNs. It involves treating skin samples with a fluorescent solution after MN insertion and then imagining the fluorescent probes which have migrated down the pores. This allows for depth measurement of the micropores in a non-invasive way without having the long staining and sectioning process for histology. The main issue with this method is that depth of image is a maximum of 250µm below the skin surface. This depth is shorter than the length of many microneedles [22, 40, 71].

OCT is the best option for imaging the insertion and penetration depth of MNs. It can be done in real time and does not require mechanical manipulation of or excision of the skin samples. It can 3D image in-vivo with no need for removal of tissue or pre-treatment down to a depth of about 3mm. The technique is similar to a traditional ultrasound as it uses an echo technique using reflections of light to generate images of the structure [22, 75, 76].

Figure 1.5 shows an example of an OCT section after MN insertion [75].
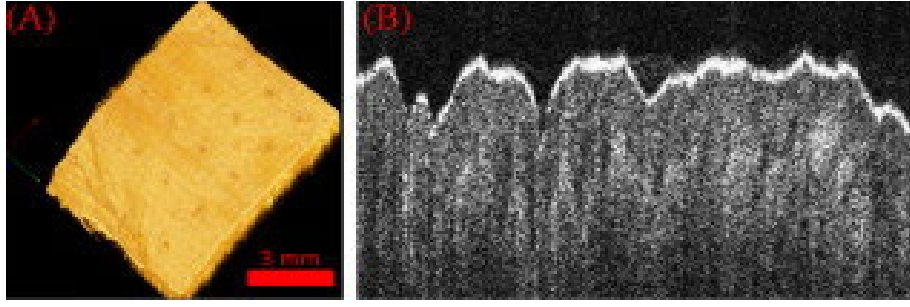
Figure 1.5: Section of OCT image showing micropores after MN insertion

1.2.4 Mechanical Characterisation

Mechanical characterisation of MNs needs to be carried out, including the different modes of failure, to assess the safety of the MN arrays. A wide variety of stresses are exerted on MNs especially during insertion and removal. Stresses induce buckling and bending of the MNs and fracture of the base plates. The first fracture tests were done on single microneedles described by Zahn et al. They used a force gauge to gradually increase vertical forces from 0-20g on the MN tips until it fractures [77].

Axial tests are used on MNs and involve applying a force which is perpendicular to the base plate. Usually a mechanical force transducer is used to perform this type of test. The transducer will record force and displacement as the MNs are pushed against a defined hard surface. Fractures can be observed in the data through a sudden decrease in the force illustrated on the force displacement curve recorded [78, 22].

During insertion of MNs there is the potential for transverse forces to occur. These can be tested with a force testing transducer like the axial tests. MNs are fixed with the base plate parallel to the force applied and a specific point on the side of a MN is subject to the force until it breaks. This is recorded as a sudden decrease in a force displacement graph similar to the axial force tests. The transverse force can be applied to a row of MNs instead of a single MN and then the force per MN is calculated by dividing by the number in the row. It can be difficult to accurately align the MNs in these tests to the same point of the MN in each case leading to some inaccuracies in measurements even with the use of a microscope or microscope camera as an aid [22, 78, 14].

Insertion forces are an important parameter to calculate as when combined with the fracture force data, a safety consideration can be decided. This safety consideration will look at if the MNs will shatter or deform with adverse effects on the skin or body. Skin tissue samples are required to make insertion force measurements and the majority of

studies use histology and microscopy to evaluate the MNs ability to pierce the skin. In order to calculate insertion forces, force displacement measurements are required using a mechanical force station with the skin tissue samples. Tests like these have been carried out on MNs varying in diameter, yielding results which vary between 10mN and 4.75 N per MN depending on the size and shape of the MN and the tip sharpness. [73, 14, 79]. For MNs to be safe, the fracture forces need to be significantly higher than the force of insertion. Applicators are used to control the force and placement of insertion [80].

There are different mechanisms of deformation which MNs can experience. The mechanics of the MNs can be best described by the following equations.

The maximum compressive force that the MN can withstand:

$$F_{Compressive} = \delta_Y A \tag{1.1}$$

Where δ_Y is the yield strength and A is cross-sectional area of the needle tip.

The buckling force is given by:

$$F_{Buckling} = \pi^2 \frac{EI}{L^2} \tag{1.2}$$

Where E is Young's modulus, I is the moment of inertia of the cylindrical section and L is the length of MN.

After the skin is punctured the resistive force is governed by:

$$F_{Resistance} = P_{Pierce} A \tag{1.3}$$

Where P_{Pierce} is the pressure required to puncture the skin.

The Bending force the needle can resist is given by:

$$F_{Bending} = \frac{\delta_Y I}{cL} \tag{1.4}$$

Where δ_Y is the yield strength, c is the distance from axis to outer edge of the MN, I is moment of inertia of the cylindrical section and L is the length of MN [81].

Table 1.2: Mechanical properties of microneedles of different materials and fabrication methods

MN	Failure forces	Failure mode	Insertion forces	Safety margins	Insertion depth (% of total height)	Insertion depth μm	Ref
PVP dissolving micromoulded	1N per MN	Bending, Height reduction	0.15N for Sclera tissue- 0.41N cornea tissue		75		[38]
Gantrez co-polymer micromoulded		Compression when tested on metal block, Height reduction	10N	Compression occurred on pressure with aluminium block only	83	500	[82]
Silicon Photolithography	500g	Compression, Height reduction	50g	Insertion for is 10% of failure force			[83]
Micromoulding, using SU8, PLGA	0.5N for a single MN	Height reduction		Multiple polymers			

1.2.5 Electrochemical Characterisation

MN biosensors must be conductive in order to function as intended. They can be characterised electrochemically like other sensors to determine quality and reproducibility and identify impurities. The electrical conductivity of the microneedle sensors can be measured using an four point IV probe to measure resistance. This is important to test the surface of the array of MNs to ensure uniformity between different MN sensors. The electrode surface can be studied using cyclic voltammetry (CV). CV allows the identification of regions of the redox system and the properties of the electroactive species in the solution. This set up is achieved with a 3-electrode system where the relative potential from a reference point is scanned at the working electrode and characterises the electrode material for the application. Most commonly the ferro/ferricyanide redox system is used to give an indication of the electroactive surface area of the MN electrode. The technique enables rapid identification of redox couples [84].

1.2.6 Current and Potential Uses for Microneedles for Biosensing Applications

1.2.6.1 Currently researched uses for microneedles for biosensing applications

Microneedle biosensors are a relatively new technology. Many different applications have been utilised with microneedle biosensors, they range from measuring or monitoring the levels of drugs in the skin to pH sensing and biomarker sensing. They are not widely used by patients and are largely in the research stage [85]. The most prevalent application is the sensing of glucose and lactate, this is because of the large industry related to diabetes and sports science[86, 87, 88]. Microneedle biosensors have also been used to detect alcohol [89], nerve agents (e.g. methyl paraoxon) [90] (120), β-lactam antibiotics[91], urea[92], K+ and Na+ ions, nitrogen oxide[93, 88], therapeutic drugs[93], and skin burns[94]. The needles on the biosensor can be hollow or solid and can sense by extracting ISF or sensing whilst in the skin.

Glucose is the most commonly detected analyte using MN biosensors. The detection of glucose is used to monitor the condition of patients with diabetes to help them better manage. The enzyme glucose oxidase is immobilised on the sensor surface to detect glucose through the presence of H_2O_2 generated by the reaction of the analyte with the glucose oxidase enzyme [88]. Glucose dehydrogenase is also used as an enzyme for detection of glucose. It is a useful enzyme as it does not require oxygen for its enzymatic reaction and has a rapid electron transfer rate however it is relatively expensive in

comparison to glucose oxidase and less stable. There are many different glucose MN sensors, made from all sorts of materials from silicon to polymers. Some of these are 1st generation glucose sensors utilising the reaction of H_2O_2 for the sensing data and others are 2nd generation glucose sensors which utilise redox mediators such as vinylferrocene or ferrocenemonocarboxylic acid. The linear ranges of these sensors vary greatly also, from a short linear range up to 0.6mM to a wider linear ranges of 0-20mM. These sensors show a lot of promise for minimally invasive continuous glucose monitoring [95, 96, 97]. One study has shown the possibility of a self-powered glucose sensor and reports using this concept with metallised MNs to obtain a linear range of up to 80mM [98]. Jina et al in 2014 conducted a clinical study with diabetic patients and a working in vivo MN prototype. The sensor was tested continuously over 72 hours and showed results consistent with blood glucose measurements from a commercial finger stick device [99].

Glutamate is another analyte which has been detected by a MN sensor. It is a neurotransmitter present in the synapses in the central nervous system. The levels of glutamate are an indicator of the health of a patient's central nervous system. There have been clinical studies which show a correlation between glutamate levels in the ISF and the levels in cerebrospinal fluid which would indicate MN to be a viable much less invasive testing alternative [100].

Lactate is also a very common analyte detected using biosensors as it can diagnose muscle fatigue and sepsis. It is the natural bi-product of anaerobic respiration in the glucose metabolism. Blood lactate levels are typically 1mM to 2mM at rest or during moderate exercise, they increase as anaerobic respiration occurs. Lactate cannot be fully processed in the muscles so it builds up in the muscles and then the bloodstream [101, 102]. Lactate can also be used as an aid in sepsis diagnosis. Critically ill patients who are suffering shock or hypo-perfusion have lactate levels above 2mM and those with a level above 4mM indicates the need for resuscitation and ICU admission. Elevated lactate levels can be associated with increased mortality [101]. For electrochemical sensing of lactate the two enzymes used are lactate oxidase and lactate dehydrogenase. The lactate oxidase catalyses the reaction of lactate to pyruvate which in the presence of oxygen forms hydrogen peroxide. This is chemically active and can be oxidised and reduced to give the peaks proportional to the lactate concentration. Using lactate oxidase however requires a high potential which can lead to interference by other electro-oxidisable species. Lactate dehydrogenase has high catalytic activity for the conversion of lactate to pyruvate and Nicotinamide adenine dinucleotide phosphate (NADP). Lactate dehydrogenase works in the presence of a co enzyme either Nicotinamide adenine dinucleotide (NAD) or NADP which act as mediators. The Nicotinamide

adenine dinucleotide hydride (NADH) is oxidised and it is this oxidation current which is proportional to the lactate concentration [103, 104]. Gold and platinum are the most common materials for electrodes as they have their own electrochemical characteristics that lean towards oxidation of hydrogen peroxide [105]. Other microneedle sensors use carbon and hydrogels on their surfaces. Lactate MNs sensors are also often combined with glucose sensors [106, 107].

1.2.6.2 Potential uses for microneedles for biosensing applications

Currently hydration can be tested using blood tests or wearable sweat tests [108]. MN tests would offer minimally invasive alternative to blood tests and a more accurate alternative to sweat tests which are prone to contamination. Urine tests are also used and can cost between 30 and a couple of hundred dollars for portable refractometers. Lab refractometers can cost as much as $4000 [109].

For cystic fibrosis currently heel prick tests are performed on babies and if this is positive, a sweat test is used to confirm [110]. When diagnosing cystic fibrosis (CF) A result of 29 or less mM chloride means CF is unlikely, between 30 and 59mM CF is possible and further testing is needed and greater than 60mM CF is very likely. Most current biosensors for cystic fibrosis utilise the sweat as the analyte fluid and are often wearable. A high salt level in the sweat would be considered over 60mM chloride to indicate cystic fibrosis. It does however need to be backed up by lab testing [111].

There are many methods of chloride measurement by electrochemical sensors to detect chloride ions. One example uses silver nanoparticles conjugated with a thiol linked oligonucleotides and immobilised on a gold electrode. If a specific potential is applied to the gold electrode in the presence of the chloride ions the silver is oxidised and AgCl is formed. Using cyclic voltammetry to detect the oxidation of the silver nanoparticles to form a Ag/AgCl layer, a strong oxidation peak is only seen when the silver nanoparticles are in the presence of Cl- ions [112].

Dong et al developed a sensor using a carbon fibre microelectrode with single walled carbon nanotubes and gold nano leaves. The high surface area of these three dimensional nanostructures increase the specificity of the sensor. This electrochemical sensor utilised differential pulse voltammetry to observe an anodic peak that indicated the presence of Cl- ions [113].

The majority of chloride sensors utilise an Ag/AgCl electrode as it is highly selective to chloride ions. Flexible chloride sensors have been fabricated, one example senses chloride ions without the use of a reference electrode. The sensor substrate is made

of polytetrafluoroethylene (PTFE) and is loaded with multi walled carbon nanotubes which Ag nanoparticles were then attached onto. This sensor was further enhanced by incorporating a hydrophilic copper benzene-1,3,5-tricarboxylate (Cu-BTC) to increase the adsorption of the chloride ions and the measured chloride ions response was defined by the resistance change when measured [114].

Screen printed electrode sensors have also been developed, an example of these sensors has carbon paste working and counter electrodes with a Ag/AgCl reference electrode. The sensor works by measuring the Nernstian shift of the voltammetric peak potential of ferrocenemethanol in the presence of chloride ions and made use of a pseudo-reference electrode within the system [115].

There are sensors which use chronopotentiometry and an Ag/AgCl working electrode with another identical Ag/AgCl pseudo-reference electrode. The difference potential is then used to measure the concentration of chloride ions. This two Ag/AgCl electrode method has been used to measure chloride in concrete and later will be described in Chapter 6 where it has been adapted to measure chloride with a MN array sensor .

Cholesterol is a type of lipid called a sterol, found in the body. It is an important analyte to to investigate as it is an indicator of risk for many different diseases such as cardiovascular disease. A healthy level of cholesterol in the body is below 5mM total cholesterol, below 4mM Non-HDL cholesterol, below 3mM LDL cholesterol and above 1mM HDL cholesterol for men and above 1.2mM HDL cholesterol for women [116].

The mechanisms for cholesterol electrochemical biosensors are mainly focused on the enzymatic reaction of cholesterol oxidase with cholesterol. Usually the sensors monitor the consumption of oxygen or the production of hydrogen peroxide as a result of the enzymatic reaction also known as electrocatalysis of hydrogen peroxide [117, 118]. Cholesterol can be determined in a similar way to glucose using either a first, second or third generation sensor.

The first-generation of sensors monitor the hydrogen peroxide produced as a result of an enzyme catalysed reaction. These are based on an enzyme substrate or product's electro activity [119]. Cholesterol Esterase (ChEt) can be used to break down cholesterol esters into free cholesterol through the following reaction so they are available to react with cholesterol oxidase as shown in Equation 1.5 [120].

$$Cholesterol ester + H_2O \rightarrow Cholesterol + fatty acid \tag{1.5}$$

Cholesterol oxidase (ChOx) catalyses the reaction of free cholesterol to cholestenone (Cholest-4-en-3-one). The cofactor Flavin adenine dinucleotide (FAD) in ChOx is re-

duced which then reacts with dissolved oxygen (O_2) and produces hydrogen peroxide (H_2O_2). The H_2O_2 is then measured by the sensor by oxidising it back to dissolved oxygen and water. It is then the oxidation and reduction of the hydrogen peroxide which is monitored. The equations and mechanism as shown in Equations 1.6, 1.7 and below in Figure 1.6 [121, 122].

$$Cholesterol + O_2 \rightarrow Cholest - 4 - en - 3 - one + H_2O_2 \qquad (1.6)$$

$$H_2O_2 \rightarrow O_2 + 2H^+ + 2e^- \qquad (1.7)$$
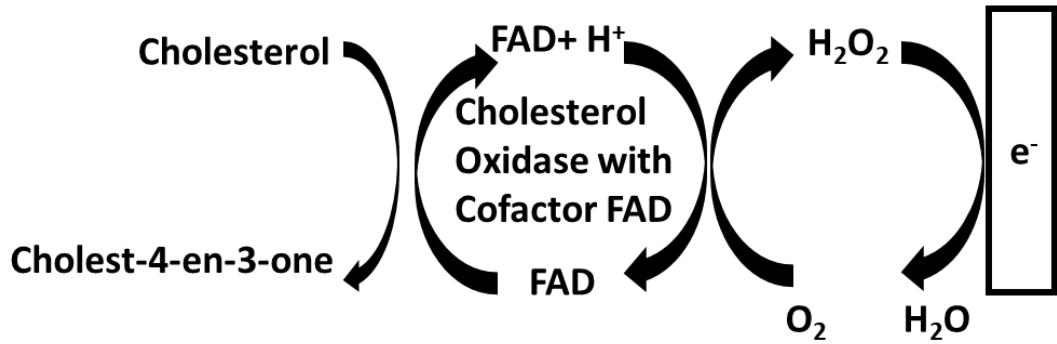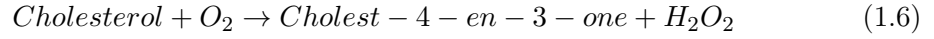
Figure 1.6: Schematic of the mechanism of a first-generation Cholesterol sensor

Normally a high anodic potential of +0.6V - +0.7V is required to carry out electro-oxidation of hydrogen peroxide, however this high anodic potential is susceptible to interference from oxidisable molecules commonly found in bio-samples such as ascorbic acid, uric acid and acetaminophen [118, 123, 124]. The effectiveness of the cholesterol oxidase biosensors is dependent on the success of the enzyme immobilisation onto the sensor. There are two main mechanisms for enzyme immobilisation onto the sensor which are direct adsorption and entrapment. Changes in pH, temperature and ionic strength can cause protein desorption of the enzyme which are weaknesses of the direct absorption mechanism [125]. Polymer films have been utilised as aids for entrapment and therefore immobilisation of the enzyme onto the surface. Examples of polymer membranes/films which have been utilised are polyvinyl alcohol(PVA), epoxy, polypyrrole, polyaniline, polyvinylsulfonate, polyacetate, polythiophene and polyindole. Many of which are conductive and can improve sensitivity and stability or act as charge control membranes [118, 126].

Second generation sensors aim to avoid interference of other electro-oxidative species by enlisting a redox mediator. Using a mediator allows the hydrogen peroxide reduction current to be measured at lower potentials such as +0.2V or +0.1V [124, 127]. Examples of mediators to be used in 2nd generation sensors are potassium ferrocyanide, Prussian blue, ferricenium ion, hydroxymethyl ferrocene and 1,10-phenanthroline-5-6-dione (PD) [117]. Prussian blue is well know to exhibit high activity and selectivity through catalytic reduction of hydrogen peroxide. It has been shown to have a catalytic rate constant of 3 x103 M-1 s-1 which is similar to the constant for peroxidase, this has given Prussian blue the name of 'artificial enzyme peroxidase' [124, 128, 129]. Using ferricenium ion (Fc+) as an example mediator the following equations 1.8, 1.9, 1.10 describe the electron transfer to the electrode [126].

The mechanism of second generation electrode is shown in Figure 1.7.

$$Cholesterol + ChOx_{ox} \rightarrow Cholest - 4 - en - 3 - one + ChOx_{red} \qquad (1.8)$$

$$ChOx_{red} + 2Fc^+ \rightarrow ChOx_{ox} + 2Fc \qquad (1.9)$$

$$2Fc \rightarrow 2Fc^+ + 2e^- \qquad (1.10)$$
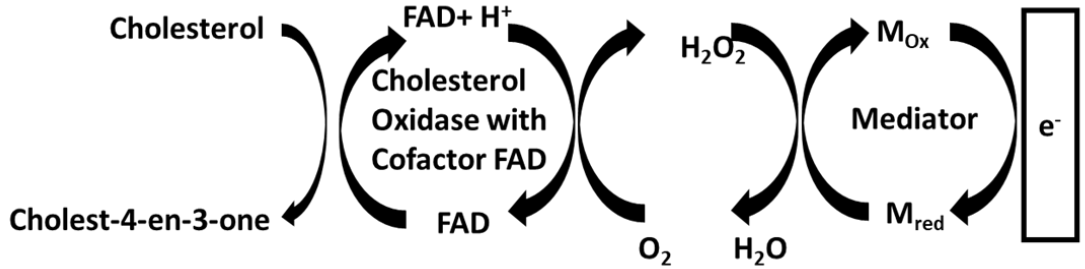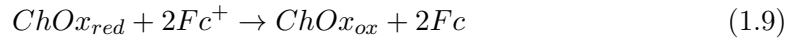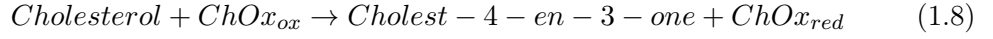
Figure 1.7: Schematic of the mechanism of a second-generation Cholesterol sensor using a mediator.

Some mediators such as Prussian blue can lose their catalytic effect by rapid desorption from the electrode surface which can limit the lifetime of the biosensors. When required in microneedle or other transdermal sensors, mediators such as ferrocene have the potential to present a toxicity issue. Leaching of the mediator causes a problem due to the small size of the molecules and therefore diffusion into the body [127, 130]. While mediators in second generation sensors do decrease interference in comparison to first generation sensors due to the lower potential used. When in the presence of interfering redox enzymes they can transfer electrons between other reactions as well as

the transfer between ChOx and electrode.

Third generation sensors are direct electron transfer sensors. These biosensors facilitate electron transfer between the electrode and the active centre of the redox enzyme. The redox enzyme acts as an electrocatalyst allowing the electron transfer directly without mediator or hydrogen peroxide thereby reducing the potential required. The transfer of electrons happens only between the electrode and enzyme as depicted in Figure 1.8 below.
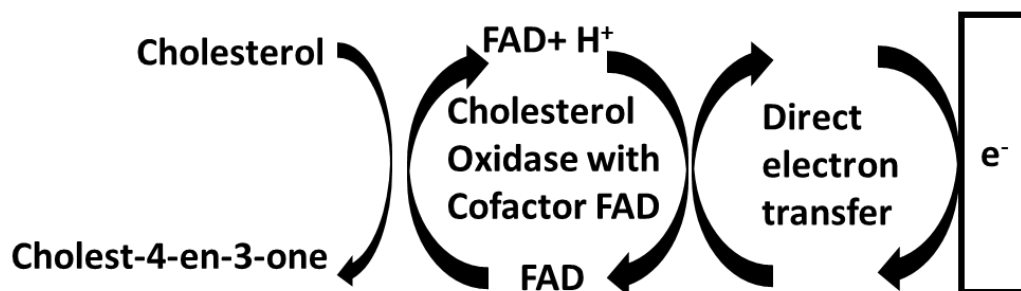
Figure 1.8: Schematic of a third-generation direct electron transfer mechanism

There is little to no interference with the direct electron transfer biosensors as they can operate in a potential range that is much closer to the enzyme's redox potential. This is achieved by the close integration of the electrode surface and the enzyme molecule. Third generation sensors can be difficult to optimise due to the requirement of a short distance between enzyme active centre and the electrode. The contact to the electrode surface can promote an electron tunnelling mechanism which forms part of the Marcus' theory for electron transfer kinetics. Not only does the distance between the redox centre need to be as close as possible, the reorganizational energy of the redox species and the potential difference needs to be optimal [119].

Usually the enzyme active site is deep within its protein structure and therefore the distance for direct electron transfer is long due to the protein shell shielding. This has lead to designing sensors which reduce the distance of this site from the electrode. Nanomaterials such as multi walled carbon nanotubes (MWCNTs) have been utilised for direct electron transfer cholesterol biosensors [125]. Other materials such as reduced graphene oxide, graphene, modified polyaniline, polyvinylpyrrolidone and gold nanoparticle modified MWCNTs in nafion matrix have been shown to increase the electrocatalytic activity giving potentials which match closely to the FAD redox active centre in the ChOx [117]. The studies by Zhang et al and Pakapongpan et al have

shown that these sensors can work at a potential of -0.4 and -0.484 V respectively, close to redox active centre potential [125, 131].

Methods including chemical modification of the surface can improve the reliability of immobilising the ChOx in the optimal orientation for direct electron transfer through the formation of self-assembled monolayers (SAM). These layers can stabilise and control the orientation to some extent. Cholesterol biosensors have been made with SAM modified surfaces using thioglycolic acid [132].

Cholesterol amperometric biosensors can also have increased direct electron transfer scope when coupling with other enzymes that possess a high direct electron transfer ability. An example would be to couple ChOx with peroxidase. The peroxidase which exhibits a high affinity for direct electron transfer acts as an electrocatalyst for hydrogen peroxide reduction. Third generation sensors are also limited by their electron transfer kinetics which are generally slower than the mediated second generation sensors [119, 125, 133].

The most appropriate method using a microneedle based sensor platform will be investigated in [134].

Multiple analyte devices are being researched such as this MN based biosensor by Gao J et al which simultaneously detects glucose, uric acid and cholesterol using flexible MNs and a multichannel portable electrochemical analyser. It works with a linear range of 1-12 mM for cholesterol [135].

1.3 Microneedles for drug delivery applications

Topical drug delivery is a popular method of delivery for drugs. It is however limited by the permeability of the *stratum corneum*. Only molecules with a weight of 500 Daltons or less can pass through the *stratum corneum* therefore a bypass mechanism is necessary to improve the efficacy of drug delivery across the skin barrier [12]. Topical creams and transdermal patches do not offer sufficient therapeutic action across the skin and hypodermic needles, though they offer up to 100% delivery of a drug, are invasive and painful due to penetrating deep in the dermis where there are nerve endings. MNs offer the desirable characteristics of both a transdermal patch and a hypodermic needle. MN can achieve efficient drug delivery without causing pain as they break the *stratum corneum* to allow passage of the drug but are minimally invasive so do not penetrate deep enough to stimulate nerves in the skin. Percentage of loaded drug delivered by MNs is as high as 100% whereas hypodermic offers 90-100% with pain and topical creams and transdermal patches only offer 10-20% of the total drug delivered [10].

1.3.1 Microneedle drug delivery techniques

Solid MNs can be used for drug delivery. They are primarily designed to break through the *stratum corneum* of the skin to create micropores. Through these pores the skin ISF can be accessed for drug delivery. The poke and patch method uses solid MNs to create these micropores and then apply a topical drug to the skin which then passes through. Coatings can be applied to functionalise the MNs and facilitate drug delivery more directly [32, 136]. The coatings or the entire solid MN can be swellable. Swellable MNs work by swelling once they pierce the skin absorbing the ISF and either releasing a drug into microcirculation or they collect the ISF for analysis. Hydrogels are a common type of material used on swellable MNs. Hydrogels are cross-linked polymers, the lower the number of cross-linking chains the more swellable the polymer. This can be used as a control for drug release. The main disadvantage of swellable MNs is the reduced mechanical strength which hinders the efficiency of the MN penetration [137, 138].

Dissolvable MNs are used in drug delivery, usually they are made with a sugar or biodegradable polymer. When inserted into the skin the biodegradable tips of the MNs dissolve and can release drugs which have been encapsulated in the polymer or carbohydrate matrix [138]. Polyvinylpyrrolidone (PVP), sucralose and cellulose are often used as materials for dissolvable MNs. This allows drug release over time which can be controlled based on the nature of the matrix of the MNs therefore drug release time can vary between minutes and days [139].

Porous MNs are solid needles which have pores that can be used to store a drug for delivery. The size of the pores can vary from the nano range to the micro range in size. Different sized pores have different delivery applications including vaccine encapsulation and drug encapsulation. The pores can be fabricated in a multitude of ways including the dissolving of small bubbles and etching. Porous MNs offer an increased volume for loaded drug to be stored however the pores can reduce the mechanical strength of the MN arrays [140, 141, 142].

1.3.2 Applications of Microneedles for drug delivery

MNs can be used to deliver many types of different substances, these can be categorised into biotherapeutics, vaccines and cosmetics. They are extremely useful for delivering macromolecules which would otherwise be too large to pass the *stratum corneum* barrier. They offer localised delivery and bypass the gastrointestinal system therefore lower systemic doses are required. One of the most widely studied biotherapeutic drug to be delivered by MNs is insulin due to the prevalence of diabetes and the importance of

regular insulin injections. Dissolving insulin loaded MNs have been shown to enable effective delivery of insulin to reduce the blood glucose level in a diabetic rat animal model [143, 144].

Other drugs which have been through clinical trials with MN delivery are the parathyroid hormone by the company Zosano Pharma who are developing a transdermal patch with titanium MNs coated in the drug with a hand-held applicator. The only other method of delivering this drug is by injection thus using MNs reduces the pain for the patient. They found that all the patch doses increased the spine bone mineral density of the patients [145]. The administration of local anaesthetics including lidocaine have been trialled on both solid and hollow MNs. Lidocaine delivery through hollow MNs has been tested versus delivery via a 26 gauge hypodermic needle. The pain levels between the two methods were compared at various time intervals after injection/application. The MNs were found to be significantly less painful on the different areas of the body. These results demonstrated that the MNs were just as effective at delivering the local anaesthesia [146]. Solid MNs have been shown to facilitate the delivery of a topical anaesthesia cream which reduces the time period needed to give a reduction in pain and showed a greater penetration depth of the local anaesthesia [147].

MN vaccine delivery is a large area of research amongst the literature. There are many advantages to administering a vaccine using MNs such as higher compliance among patients because of the reduced pain and a more targeted vaccine due to the immune cells found in the skin. There have been human trials for administering the influenza vaccine using a MN system. One such trial found that a lower dose of the vaccine administered gave a similar result to the ordinary dose delivered intramuscularly. The MN patches were the preferred method of delivery for the patients even with some irritation at administration site. They also had the advantage of being self-administered which would reduce staffing costs if widely accepted [148].

1.3.3 Microneedles in commercial drug delivery

There are some commercially available MN systems for drug delivery. Some of these include the LiteClear® which uses solid silicon MNs as a pre-treatment to skin before applying a topical cream with the active ingredients in it. It is sold in China as a treatment for Acne and in the rest of the world as a cosmetic blemish treatment product [149]. Soluvia® [150] is sold prefilled with influenza vaccine brands IDflu®, Intanza® and Fluzone Intradermal [151]. It consists of a 1.5mm long, single hollow MN which is attached to a syringe. Raphas® beauty patch is an array of dissolvable MNs designed to

deliver drugs or cosmetics transdermally [152]. MicronJet$^{®}$ is a device which consists of 4 hollow silicon MNs attached to a plastic adapter suitable for use with standard syringes [153, 21]. Another MN system for the delivery of vaccines is VaxiPatch which delivers the influenza vaccine also using a stainless steel MN array. In the delivery of vaccines the tissue trauma from MN insertion can be used as an adjuvant to improve immune response to a vaccine [154].

Many MN patches can be inserted just using a thumb pressure however for a more reliable and accurate insertion of the MN an applicator is used. There are many on the market at the moment, all of which have different types of mechanisms including impact applicators with retainers, spring applicators, pressing applicators, plungers with coiled compression springs, examples can be found in Table 1.3 [155, 156, 157].

Table 1.3: Description of MN applicators from different companies

Company	Description of MN Applicator	Year
Valeritas Inc.	The applicator includes a slidable disposable applicator plate, and a compression spring. The plate is moveable between a retracted position and a deployed position. It has an engaging surface suitable for pressing up against a microneedle patch and pressing it against a skin surface.	2016
Alza Corporation	An impact applicator which applies micro-protrusion membranes to the skin's surface with a retainer.	2005
	An impact spring applicator with a spring between the cap and piston of the applicator.	2006
Corium international Ltd.	MNs placed under the button of the device which then presses the needles into the skin upon application.	2008
3M Innovative Properties Company	A plunger device using a compressed coil to drive the plunger and a device using a leaf spring design.	2005
	Elastic band applicator. Placed around the arm and pulled to then recoil and cause the MN penetration.	2008
	Non-skin contacting, propels the needles across the distance between applicator and skin which the device determines.	2008
	Flexible sheet applicator. When force is applied the sheet undergoes stepwise motion and creates micropores on the skin surface.	2008
NanoBioSciences LLC	Handheld device with a planar application side and an actuation unit on the opposite side. The MNs were released when activating a button.	2007,2010
BD & Company	Pen type MN applicator with a liquid drug filled cartridge and plunger driven mechanism.	2009
uPRAX Microsolutions	A digitally controlled applicator containing an electromagnetic actuator (solenoid) which includes a 23 gauge plunger that a 2 gauge microneedle mount is attached. This moves in a vertical direction.	2018

27

1.3.4 Microneedles in commercial cosmetics

MNs are used in the cosmetics industry much like they are for drug delivery. The application of cosmetic MNs is mainly divided into two application categories. One is the use of just the needles to promote the healing of skin and the other is patch delivery of cosmetic products through the micropores that the MNs create in the skin resulting in more penetration and permeation [158]. See Table 1.4 for list of commercially available products.

1.3.4.1 Dermarolling

MNs can be used to stimulate skin repair and are often used as a treatment for scars (including acne scars), stretch marks and wrinkles. This concept is fairly recent with the first description of using dermal needling for scars in 1995, however the collagen induction therapy using dermarollers was introduced in 2006.

Standard dermarollers have around 200 MNs of 100µm in diameter and 500-1500µm in length. The MNs are usually made with etching techniques on silicon or stainless steel. The standard dermarolling procedure is carried out in a clinic usually, however there are home based rollers which have shorter MNs [159]. Most commonly dermarollers are used to improve acne scars. Acne scars are a huge cause of low self-esteem and other psychological issues and there have been limited ways of improving the appearance of the scars after experiencing acne. Some of these methods like dermabrasion are harsh and can affect daily activities near the treatment times whereas the gentler treatments do not produce results which are as efficient. This is where microneedling with a dermaroller is useful. The dermarolling process is generally well tolerated by patients and it produces a good result of scar reduction although it does not completely remove scarring[160].

There are many at home dermarollers, often termed as micro dermarollers, which can be used to increase the effectiveness of skincare products. Some of these products are sold alongside clinic skincare and others are for general use with normal serums and moisturisers. Some dermarollers come with multiple heads which carry different length microneedles for different uses, including brands like Swiss Clinic, ZGTS and the original Dermaroller [161, 162, 163]. There are many other brands that offer this at varying different price points. The most common length for the dermaroller MNs is between 200 and 500 µm although there are many brands which offer up to 2.5mm MNs such as The Body Dermaroller by Skin Radiance[164]. The commercially available MN systems called Dermapen® and Dermastamp™ work in a similar way to the dermaroller but on a flat substrate. The Dermastamp is inserted in a vertical motion to create the

micropores in the skin and The Dermapen also oscillates the MNs at different frequencies and uses a motor to avoid the variance of insertion force between users [165]. Skin Pen was the first FDA approved microneedling device and has been subject to clinical trials. The device creates micro injuries which stimulate wound healing mechanisms such as thickening of the skin with proteins for example collagen and with little to no inflammation. The device has been tested in animal studies and human trials and is used to help with scarring specifically from acne [166, 167, 168].

1.3.4.2 Cosmetic MN patches

Cosmetics can be delivered to the skin in a similar way to drug delivery patches by creating micropores in the skin so that the cosmetics can bypass the *stratum corneum* and penetrate deeper into the epidermis. A popular way to deliver product into the skin is through dissolvable patches which have the cosmetic ingredients encapsulated in dissolvable MNs, for example the brand Zitsticka offer 'Microdart' patches filled with ingredients such as niacinamide and salicylic acid to reduce and treat spots specifically the ones deeper under the skin [169]. The substrate is a hydrocolloid with the microdarts embedded onto it. Traditional spot stickers are just a hydrocolloid patch. The hydrocolloid can draw the moisture out of a spot but only affects surface spots and with the aid of the dissolvable microdarts the Zitstika delivers hyaluronic acid, niacinamide, salicylic acid and oligopeptide. Hyaluronic acid is for moisture retention, salicylic acid and niacinamide are used for acne and oligopeptide-76 is an antimicrobial. The microdarts deliver these ingredients directly into the spot under the skin where they dissolve. Another product is called MicroHyala and is also covered in dissolvable MNs which contain hyaluronic acid to treat wrinkles [170]. See Table 1.4 for examples.

Table 1.4: List of commercially available microneedle products and their application

Product name	Vaccines	Cosmetics	Drugs
LiteClear®		X	X
Soluvia®	X		
Raphas®		X	X
MicronJet®			X
Swiss Clinic dermaroller		X	
ZGTS dermaroller		X	
Original dermaroller		X	
Microdart		X	
MicroHyala		X	
Derma pen		X	
Derma stamp		X	
Vaxipatch	X		
Skin pen		X	

1.4 Conclusions and future trends

The progress of microneedles as drug delivery systems is far ahead of their use as in-situ biosensors with many commercially available MN drug or cosmetic delivery devices currently available. Although there is a lot of high quality research being undertaken in MN biosensing, there is currently no commercially available point of care MN systems due to most being in research or clinical trial stage and that microneedles need to be commercially produced at large enough scale to be cost effective. This is where polymer MNs and microneedles fabricated using easily adaptable and cost effective methods can overcome these barriers. The polymer screen printing method covered in this thesis has huge potential in this area as it is already used for larger scale factory fabrication of cosmetic MNs. It is expected in the near future for there to be point of care devices available as there have been human clinical trials using MN sensor systems that look promising for future development. More research is being done to fabricate multi analyte devices and devices which can simultaneously detect and deliver therapeutics, known as theranostics.

The outline of this work looks at the current status of research into microneedles, diagnostics and therapeutics. It covers fabrication and optimisation of the pre-existing process for fabrication of printed polymer microneedles, their characterisation and functionalisation for the application of biosensing and therapeutic delivery.

2 Experimental Methodology

This chapter describes the equipment and method set up for the experiments in the following chapters 3-6. This covers the methods to fabricate microneedles by modified stencil printing, metallising microneedles to give conductive microneedles suitable for biosensing, functionalising microneedles with either enzymes or silver chloride and characterising the microneedles ability to penetrate skin and be used for determining analytes such as chloride and cholesterol and delivery of drugs.

2.1 MN fabrication

2.1.1 MN fabrication - DEK Screen Printing Machine

A process called Microlithographic 3D printing (ML3DP), which is a modified stencil printing method was used for polymer fabrication of microneedles or other microstructures using a modified DEK Horizon 01 screen printing machine (ASMPT SMP Solutions, Germany) seen in Figure 2.2, typically used for surface mount technology in electronics. This process differs from the standard process which is widely used but not in this area in that the height of the stencil is varied with respect to the substrate to allow a gradual build up of layers and has been patented by Innoture Medical Technologies Ltd. In this process a board with the substrate attached is placed on a conveyor belt, which moves underneath a steel stencil of the 2D design. The design in the stencil can be of varying size, pattern or shape. For microneedles there is a pattern of small holes that have been cut into the steel. A UV curable viscous polymer is pushed through the stencil using squeegees onto the PETG polymer substrate below. The substrate then passes through to a ultraviolet (UV) lamp to cure the polymer. The polymer used in microneedle fabrication was Dymax 1180-M gel. An LED lamp (Dymax ECE 5000 flood lamp and LED curing system) seen in Figure 2.5, and a flood lamp (Lumen Dynamics Omnicure AC 8225) were used for polymer curing during this work. The board thickness including substrate, print gap, front and back squeegee pressure and separation speed can be set to adjust the shape and height of the layer printed. This

process is then repeated adjusting the parameters as required until the desired height
is reached as illustrated below in Figure 2.1.
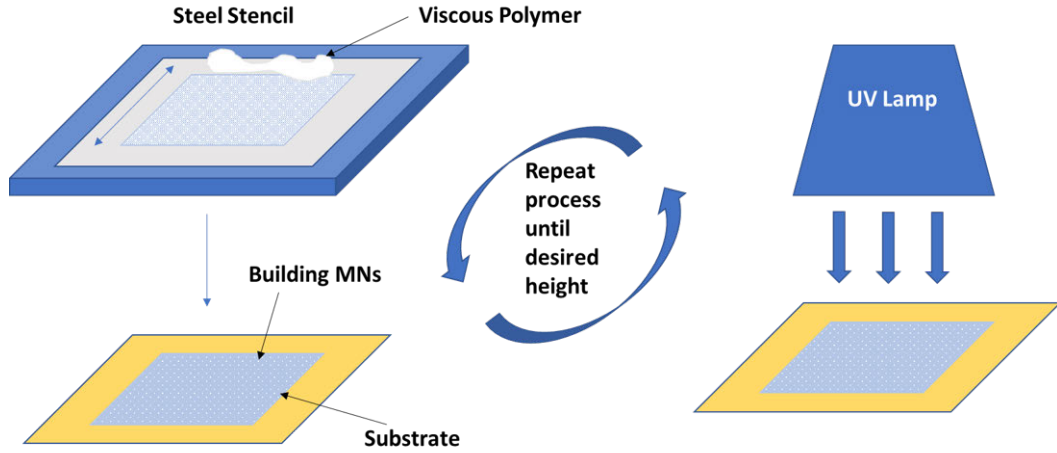
Figure 2.1: Microlithographic 3D Printing process illustration

During the set up of the DEK machine, there are alignment checks between the stencil
placed in the rail as seen in Figure 2.4b and the small board carrying the substrate seen
in Figure 2.3. The check is done using an onboard camera that matches the fiducials
between the stencil and the small board as seen in Figure 2.4a. This alignment is to
ensure a successful build. The MNs are produced in arrays of 2 x 2 cm and a total of 25
arrays in the centre of one stencil (Figure 2.4b) this matches the area of the small board
(Figure 2.3) where the substrate is secured. The printing is in layers that are controlled
by the print gap (the distance between the stencil and the small board/substrate).
With so many MN arrays on one stencil and protocols consisting of as little as 7-9
passes, around 3 sheets of MN arrays can be fabricated in an hour. This is with manual
movement of the boards between after curing with UV (Figure 2.5) and the start of the
next pass. Full automisation and a conveyor system would speed up this considerably.
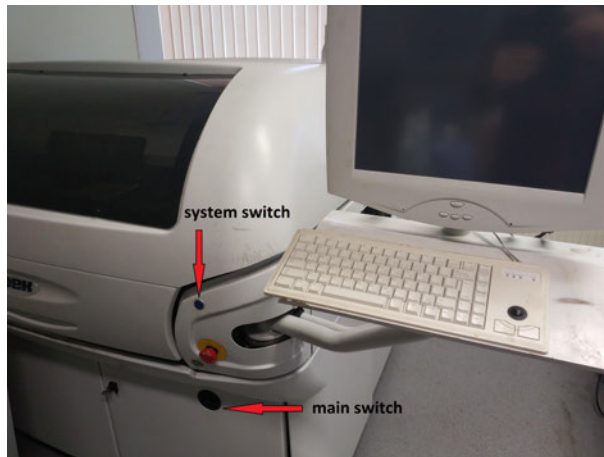
Figure 2.2: DEK machine system set up and power controls
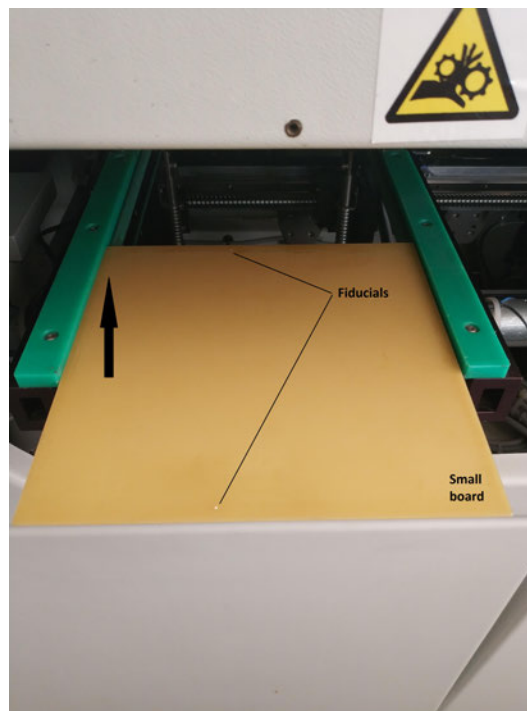
Figure 2.3: Small board with fiducials for alignment
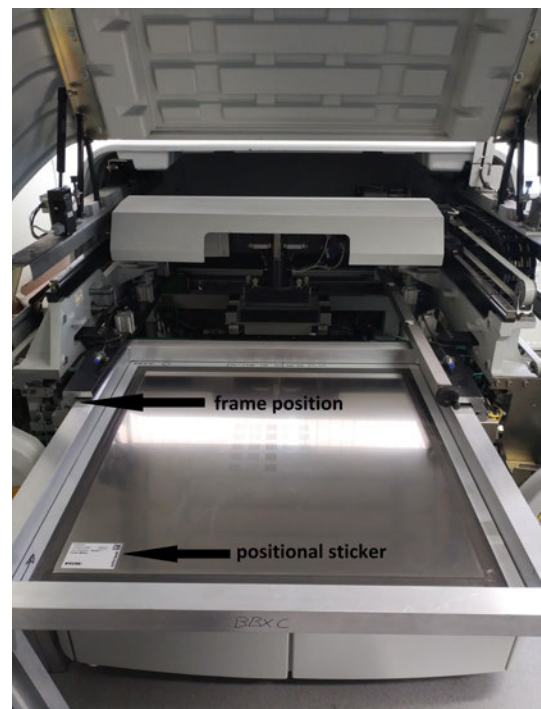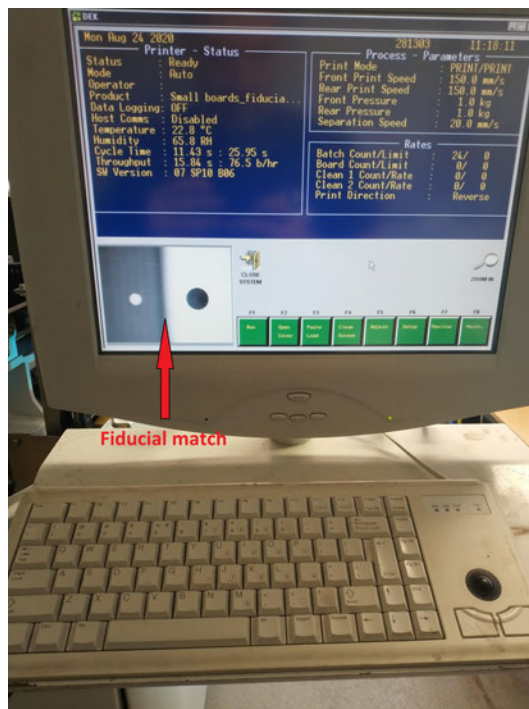
(a) Initial parameter set up and fiducial check   (b) DEK stencil placement and alignment control

Figure 2.4: Fiducial alignment of the stencil and board within the DEK system
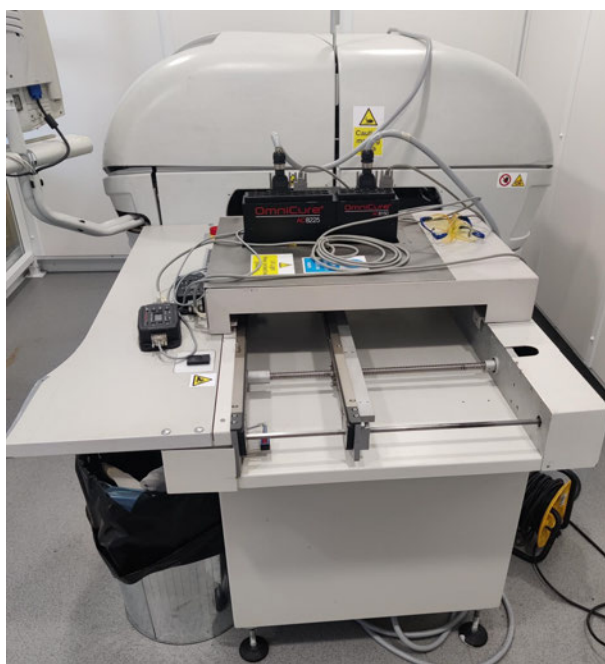
Figure 2.5: DEK LED UV lamp conveyor belt section

2.2 MN based Device Fabrication

2.2.1 Physical Vapour Deposition

In order for polymer MNs to be suitable for use in biosensing they need to be conductive. Coating the polymer MNs in metal achieves appropriate conductivity. A Kurt J. Lesker Company® PRO Line physical vapour deposition (PVD) 75 Thin Film Deposition System Platform within a cleanroom was used to coat devices with the required metals. The process works by vapourising a solid material target in a vacuum, which is then deposited on the part or substrate. The process includes 4 steps, evaporation, transportation, reaction and deposition. The evaporation occurs as the result of the material being bombarded by a high energy source to knock the atoms from the target surface. The atoms transport from the target to the substrate, and may react with the gas inside the chamber, often oxygen, or nitrogen. Diagram seen below. Figure 2.6 A DC source was used to deposit Titanium as a seed layer on the polymer substrate and the precious and functional metals, silver and platinum were then deposited on top of this layer. Argon was used as the gas to avoid a reaction of the target during the

transport phase. The power and argon gas was altered to give a fast enough deposition rate as shown in Table 2.1. The set up of the PVD machine can be seen in fig 2.6 [171]

Table 2.1: Physical Vapour Deposition settings for deposition of titanium, silver and platinum

Material	Layer	Argon (SCCM)	Power(W)	Deposition Rate	Thickness (kÅ)
Ti	Seed	60	100	1	20
Pt	Functional	30	10	1.2	250
Ti	Seed	60	100	1	20
Ag	Functional	30	30	1.6	250
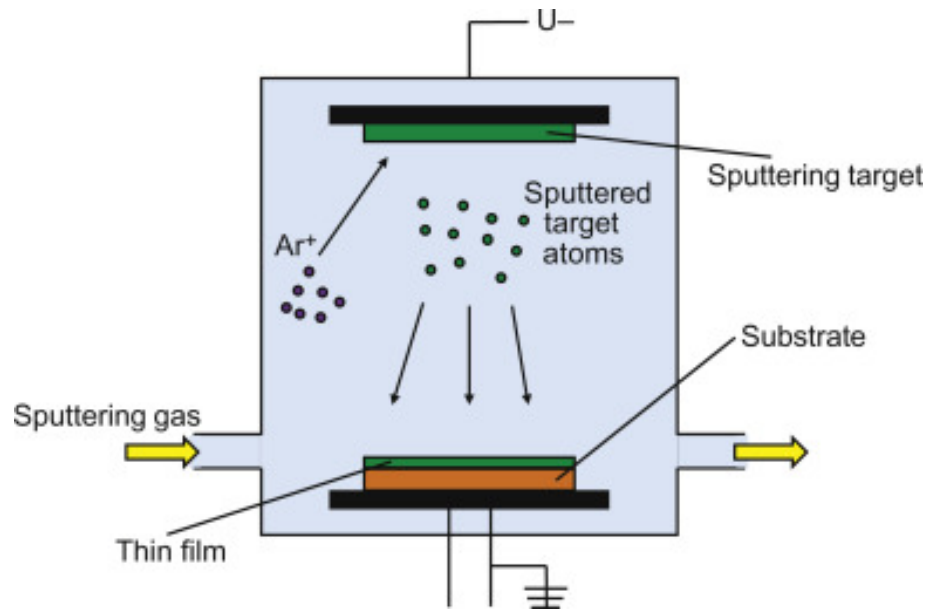
Figure 2.6: Diagram of the process of Physical Vapour Deposition

2.2.2 Wire Bonding of Microneedle Devices

To fabricate the biosensing devices a connection to the MN electrodes was required, this was achieved through wire bonding. First two holes were drilled on the side of each electrode using a Dremel with a 1mm drill bit attached. Silver paint was placed between the holes on the front and back of the electrodes and inside the holes. This is left to dry. 30 gauge wrapping wire was cut into 10cm lengths, stripped at either end and wrapped through the holes on each electrode. This was then sealed and covered with Bondic, a UV curable polymer to insulate the connection. A picture of a wire

bonded electrode can be seen in Figure 2.7 and a schematic seen in Figure below. This process could in future be automated.
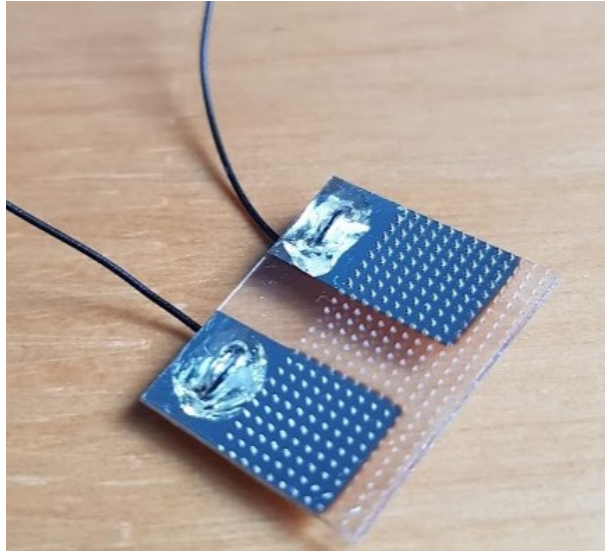
Figure 2.7: Wire bonded PVD coated platinum MN electrode pair
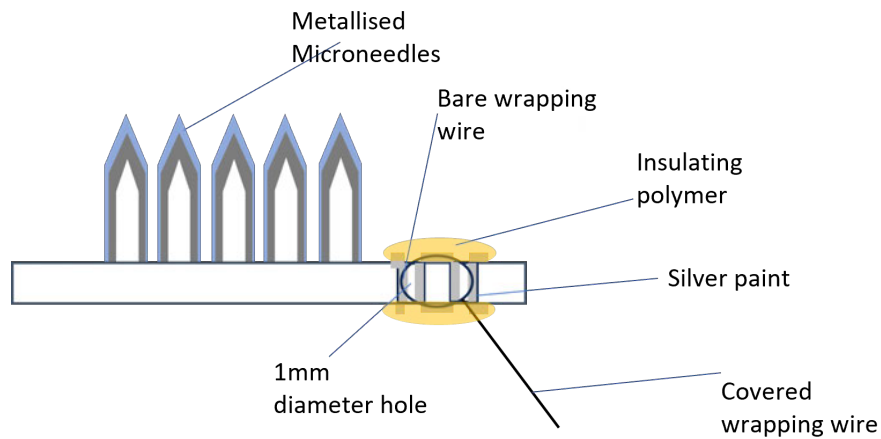
Figure 2.8: Schematic of wire bonded metallised microneedles

2.2.3 Silver Plating of Microneedle Devices

Although PVD could successfully apply a thin layer of metal to the MNs, an electroplating step was also evaluated to produce thicker metallic layers of silver with enhanced conductivity. The wire bonded and metallised MNs were connected to the negative

terminal of a Keithley power supply, a solid silver wire anode of 0.8mm diameter was connected to the positive terminal and submerged in silver plating solution purchased from Thermo fisher scientific including 6% potassium cyanide (CAS 151-50-8), 4% silver cyanide (CAS 506-64-9) and 3% potassium carbonate (CAS 584-08-7). The solution was a cyanide based solution and therefore the process was conducted in a fume cupboard. The set up was on a magnetic stirring platform with a magnetic stirrer in the solution. Set up seen in Figure 2.9. The Keithley power supply was initially set at 0V and then switched to apply 1V, it was was applied for 15, 30 and 45 s to produce devices with different thicknesses of silver plating. The electrodes were rinsed with deionised (DI) water after coating and left to dry.
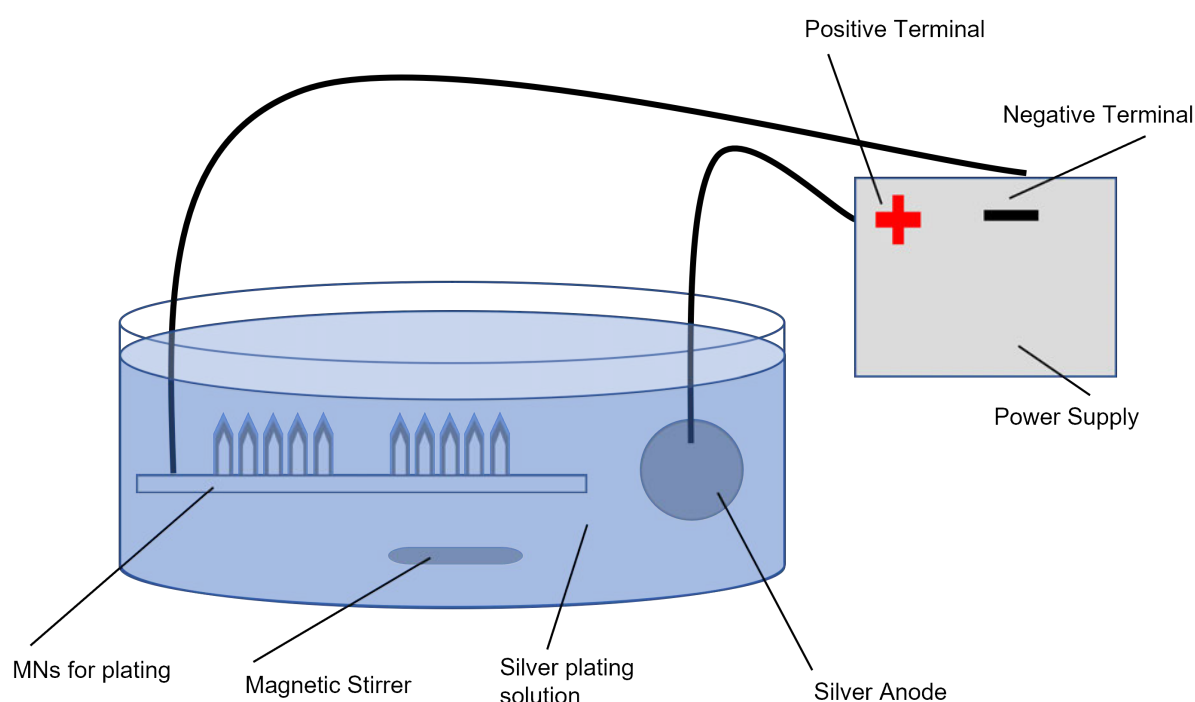
Figure 2.9: Systematic diagram of silver electroplating set up for MN electrodes.

2.2.4 Imaging of Microneedles

2.2.4.1 Scanning electro microscopy

Imaging the microneedles is an important step to characterise the size and shape and confirm that the fabrication method is producing MNs to specification. Prior to imaging, non-metalised samples were sputter coated with 15nm of Chromium in a Quorum

Technologies Q150TE Coater to reduce the chance of a charging effect in the Scanning Electron Microscope chamber (SEM). The MN imaging was taken using a Hitatchi S-4800 ultra high resolution SEM. This machine can magnify the image of a sample up to 1000x its actual size with a high resolution of 1nm. This system forms a beam of high energy electrons using a cold emission electron source which is directed at the surface of the sample. The detection of the back scatter is what then forms the image of the sample surface. The system can be seen in Figure 2.10 [172] below.
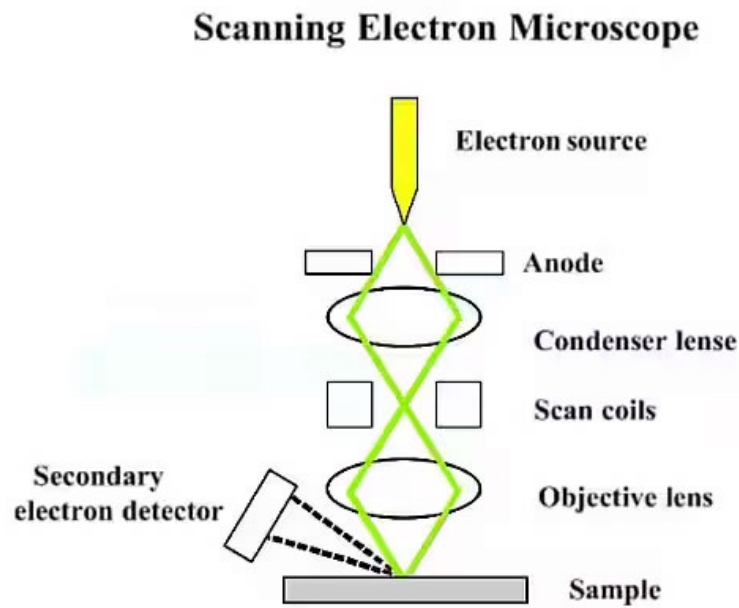
Figure 2.10: Schematic diagram of SEM imaging

2.2.4.2 Optical Microscopy

A Keyence VHX-950F series optical microscope was used to optically analyse non-metalised samples and histological slides of stained porcine skin samples. The Keyence microscope has more features than a standard optical microscope such as the function to take angled images up to 90 degrees and 5000x magnification. The user is also able to analyse the image data with the corresponding computer application to use functions for editing, annotation, 3D imaging and image colourisation.

2.2.5 Skin preparation

Porcine skin was used for drug delivery and force testing experiments. The skin was non scolded piglet skin sourced from Wetlabs Ltd where the pig was prepared and shipped the morning of delivery on ice. After delivery and defrosting, the preparation was completed using a standard scalpel blade to trim off any excess muscle or fat from the underside of the skin. The skin was then shaved using a pet shaver on its closest setting to provide better access for the MNs. The full thickness skin was cut into smaller pieces and some were stored wrapped in foil at -20°C for later use in histological and penetration analysis. Experiments requiring the use of Franz Cells warranted a thickness of skin 100-1000µm. To achieve this skin thickness an electric Pagett® dermatome was used due to its ability to adjust the thickness of skin shaved. After being cut these pieces were also wrapped in foil and stored at 20°C. Even skin stored wrapped in foil at -20°C if kept too long would dry out and become unusable for experiments. Before use skin was inspected as the damage can be seen visually by a skin colour and texture change.

2.2.6 Mechanical testing of microneedle arrays

Axial compression testing was completed using a Tinus Olsen force testing machine using a 1kN load cell Figure 2.11. The MNs were placed on the base plate under the load cell. The speed of the test was set to 1mm per minute programmed with different forces. The force started at 0N before contact with the tip of the MN and was increased as the displacement increased. If breakage occurs then this will be evident as a decreasing change in force on the force displacement graph. SEM images were taken to observe any displacement, bend or fracture.

Figure 2.11: Tinus Olsen force testing machine set up for mechanical testing of microneedles

Insertion force tests were also carried out where the MNs were attached to the top plate of the force testing machine and porcine skin pinned to the base plate. The MNs were then lowered at a rate of 1mm/min and the corresponding force displacement recorded.

2.2.7 Histological and penetration analysis

Analysis of MN penetration was completed using both methylene blue staining and cross sectional histological analysis.

Methylene blue was dropped onto the area of the porcine skin where the MNs have been removed after application. It is left there for 5 minutes before removing the excess by wiping it off the top of the skin with a wipe sprayed with isopropyl alcohol. Any blue staining in the holes indicates penetration of the *stratum corneum* of the skin.

Histological analysis was conducted using a cryostat to section porcine skin in order

to view the cross section showing microchannels made by the MNs. After applying MNs to the porcine skin sections they were placed in a -20°C freezer to freeze for 24hrs. To section the skin sample, it was placed perpendicular to the mounting piece and secured using Bright Instruments Cryo-m-bed embedding medium. This was placed back in the freezing section of the cryostat to keep the skin section in place. The cryostat was maintained at -30°C . After the stage mount was inserted into the cryostat the stage was moved close enough to the skin sample to begin sectioning. By rotating the handle the cryostat blade sliced off 30µm sections of the skin sample which were then mounted onto glass slides.

Haematoxylin and Eosin staining was used on the skin cross sections to highlight the channels made by the MNs in the skin. The samples were washed to remove OCT medium, then stained in haematoxylin, washed, dipped in acid alcohol 1%, then washed, counter stained in Eosin and then washed again.

The process was as follows in Table 2.2.

Table 2.2: Haematoxylin and Eosin staining procedure

Task	Time
Remove embedding medium by washing in DI water	2 min
Stain the samples in Haematoxylin	1 min
Wash samples in DI water	5 s
Wash in 1% acid alcohol	1 s
Wash samples in DI water	5 s
For bluing wash in Scott's tap water	1 min
Counter stain samples in 0.5% Eosin Y	1 s
Wash samples in DI water	5 s

They were then left to dry before imaging using an optical microscope.

2.2.8 Preparation of silver chloride electrodes for detection of chloride

An Autolab running Nova 2.1.4 software was used to carry out all electrochemical measurements. The Nova software was used to run and interpret the readings. To test the method before using MNs for the electrodes, two silver bar electrodes were used. These had a diameter of 6mm giving a surface area of $28.274mm^2$. They were coated with AgCl by applying 0.5mA to a two electrode system as set out in Figure 2.12a for 90 seconds. A solution of 100mM KCl made using potassium chloride (Sigma Aldrich CAS 7447-40-7) was used as the coating solution. During electrochemical measurement, the solution was not stirred. This application of current resulted in a layer of AgCl on the

surface that appears as a dulled silver. The same method is applied for converting the surface of the MN electrodes however an applied current of 0.5mA is used for MNs with a surface area of around 54mm^2 and the time shortened to 45 seconds to account for the thinner layer of silver in comparison to the abundance of silver in the bar electrodes. The following Autolab conditions in Table 2.3 were used.

Table 2.3: Autolab conditions for coating silver electrodes in AgCl

Autolab conditions	
Mode	Galvanostatic
Current range	10mA
Applied Current	0.5mA
Interval time	1 s
Duration for bar electrodes	90 s
Duration for MN electrodes	45 s
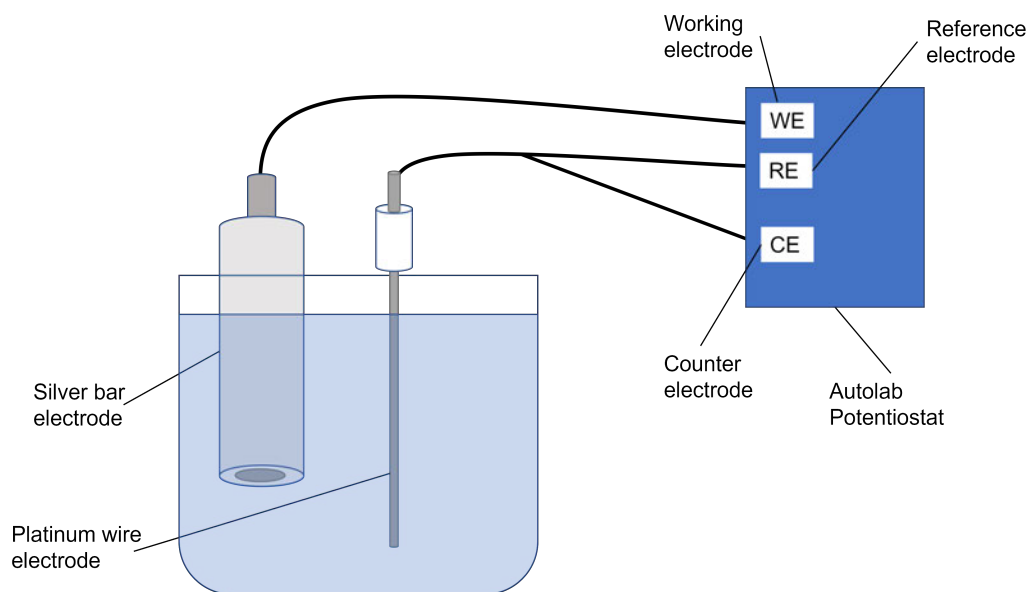
(a) Systematic diagram of Ag electrode conversion to Ag/AgCl on bar electrode
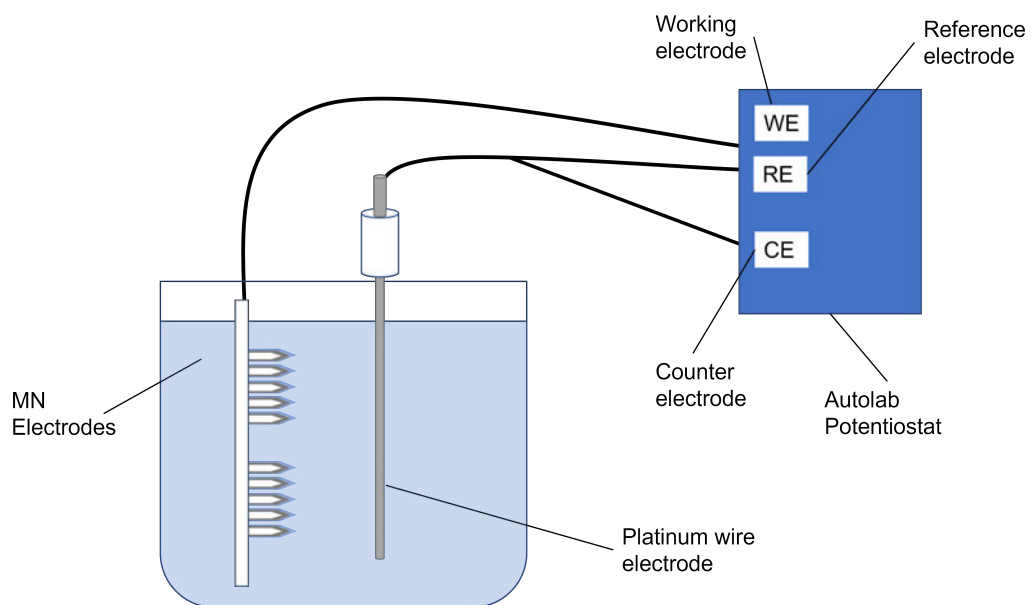
(b) Systematic diagram of Ag electrode conversion to Ag/AgCl on MN electrodes

Figure 2.12: Systematic diagram of preparation of silver electrodes, coating in AgCl in a two electrode system

2.2.9 Determination of chloride chronopotentiometry with two silver electrodes

The converted electrodes where then set up for chloride sensing as seen in Figure 2.13. A solution of 100mM KCl (potassium chloride) (Sigma Aldrich CAS 7447-40-7), phosphate buffer of pH 7.4 (potassium phosphate dibasic, CAS 7758-11-4 and potassium phosphate monobasic, CAS 7778-77-0) was used as a stock solution which was then diluted further with phosphate buffer to give the required concentration range. The Ag/AgCl converted silver bar electrodes were used as the working and reference electrodes along side a platinum wire electrode as a counter electrode, see Figure 2.13a. A current of 1mA was applied for a pulse of 5 seconds and the resulting voltage was recorded. This was repeated by rinsing the electrodes and then replacing the chloride solutions with a different concentration. In the case of the MN chloride sensing setup as seen in Figure 2.13b, an array of MNs with two converted electrodes is connected as the working and reference electrodes with a platinum wire counter electrode. The chloride solutions were drop cast onto the MNs and left for 5 minutes to reach an equilibrium. The set up was run on an open circuit potential (OCP) to stabilise before applying the 1mA current pulse for 5 seconds and recording the corresponding potential values, then the electrode was left on open circuit potential to return to its previous baseline. These results were repeated in triplicate for each concentration before changing to a higher concentration of chloride. In between each measurement the electrodes were rinsed with deionised water. The following Autolab conditions in Table 2.4 were used.

Table 2.4: Autolab conditions for coating silver electrodes in AgCl

Autolab conditions	
Mode	Galvanostatic
Current range	10mA
OCP time	60s or when $dE/dt < 1E\text{-}06$
Applied Current	1mA
Interval time	0.01 s
Duration of pulse	5 s
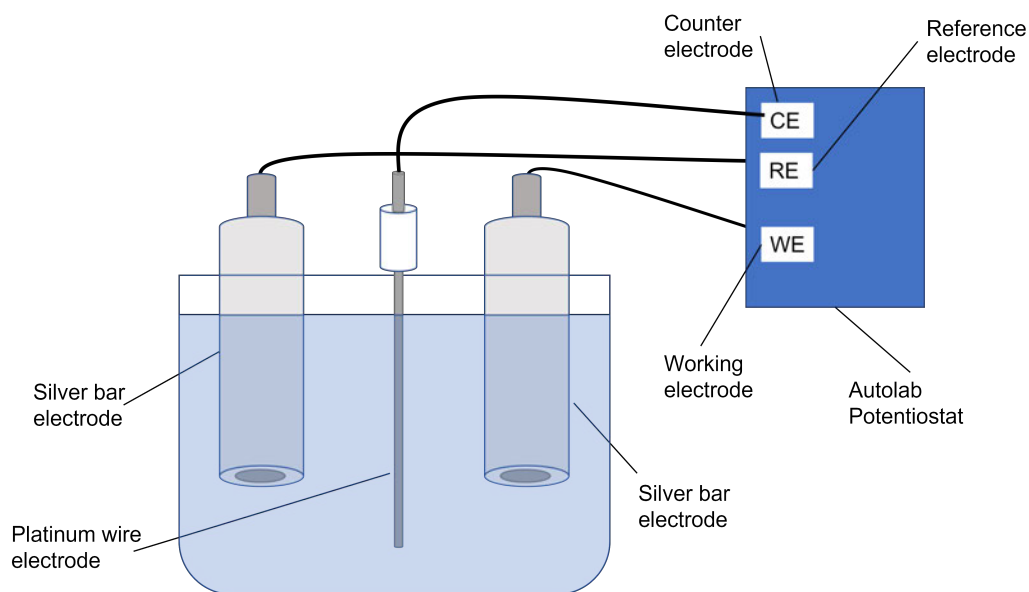
(a) Systematic diagram of Chloride sensing set up with silver bar electrodes as working and reference electrodes and a Pt counter electrode
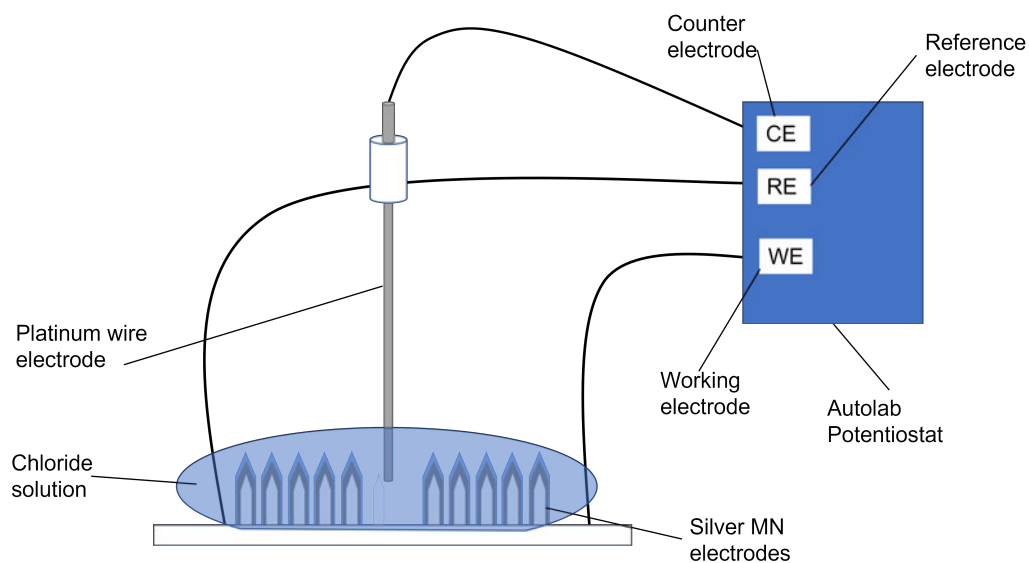
(b) Systematic diagram of Chloride sensing set up with MN array of two electrodes one each as working and reference electrodes and a Pt counter electrode

Figure 2.13: Systematic diagram of Chloride sensing set up three electrode system

2.2.10 Chemical functionalisation of platinum MN electrodes

Electro polymerisation of monomers such as phenol can be used to form films and when incorporated with an enzyme can offer one step immobilisation of the enzyme on the electrode surface. Generally, the process uses a standard 3 electrode set up to oxidise the monomer leaving radical cations that go on to polymerise and form the new polymer layer. In order to detect cholesterol the enzyme cholesterol oxidase (ChOx) was used due to its binding specificity to the cholesterol. The ChOx used was sourced from streptomyces sp and came as a lyophilized powder with $\geq$20 units/mg protein and was purchased from Sigma Aldrich (CAS 9028-76-6). The ChOx was immobilised on the platinum MN surface by electro polymerisation of phenol (Sigma Aldrich CAS 203-632-7). 3mg of the Cholesterol oxidase and 1.5mg of phenol were mixed at a ratio of 2:1 in 300µl of 100mM PBS solution (Sigma Aldrich CAS 7647-14-5, 7447-40-7). The set up for electro polymerisation uses a 3 electrode system and includes the Pt MNs as the working electrode, a platinum wire electrode (CH instruments) as the counter and an Ag/AgCl reference electrode (CH instruments). A potential of 0.9V was applied for 6 cycles to electro polymerise the phenols immobilising the ChOx. Glucose Oxidase (GOx) (Sekisui CAS 9001-37-0) was also immobilised in the same way as ChOx. 40mg of GOx and 20mg phenol were mixed in 4ml of 100mM PBS. A schematic of the electro polymerisation is shown below in Figure 2.14. The following Autolab conditions in Table 2.5 were used.

Table 2.5: Autolab conditions for coating silver electrodes in AgCl

Autolab conditions	
Mode	Potentiostatic
Current range	1mA
Bandwidth	High-speed
Applied Potential	0.9V
Interval time	1 s
Duration	900 s
Cycles	6
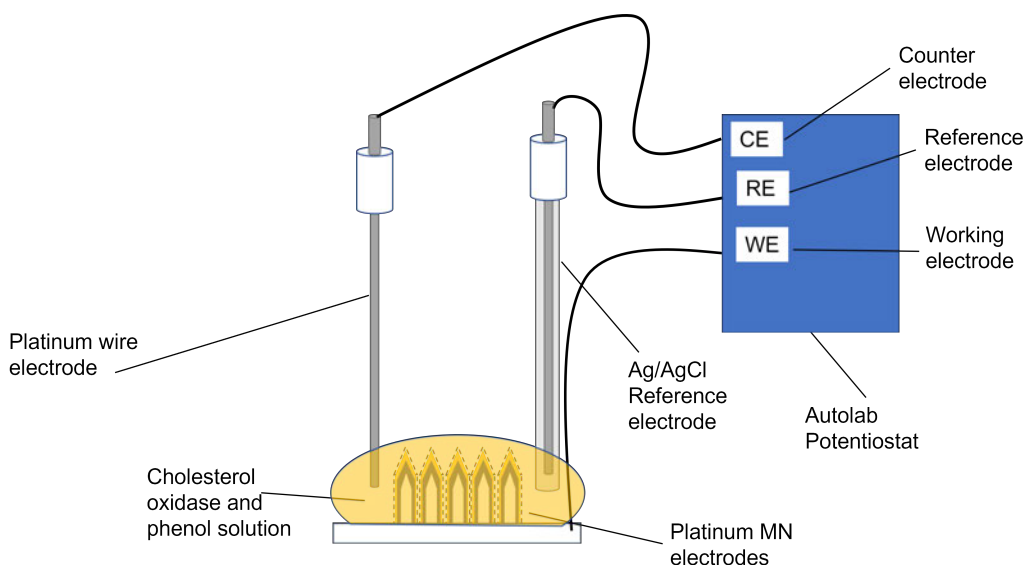
Figure 2.14: Schematic of the set up for electro polymerisation of phenols to immobilise ChOx on the MN surface

2.2.11 Determination of cholesterol using 3 electrode chronoamperometry

An Autolab running Nova 2.1.4 was used to carry out all electrochemical measurements. The Nova software was used to run and interpret the readings. This method had previously been used on MNs for a different analyte therefore no other test platform was used prior to MNs. The microneedle platforms used had been coated in the PVD with platinum, wire bonded and functionalised as described in 2.2.1, 2.2.2 and 2.2.9.

As cholesterol is practically insoluble in water and PBS, another solvent and a surfactant were used to dissolve the cholesterol in solution with PBS. Adapted from work by Yild et al and Tan et al [118, 129] a ratio of buffer:alcohol:surfactant was used. PBS as the buffer, ethanol as the alcohol and Triton X as the surfactant. This solution needed to be heated to 60°C to dissolve the cholesterol. When the solutions turn clear, have cooled and the bubbles have reduced they can be used.
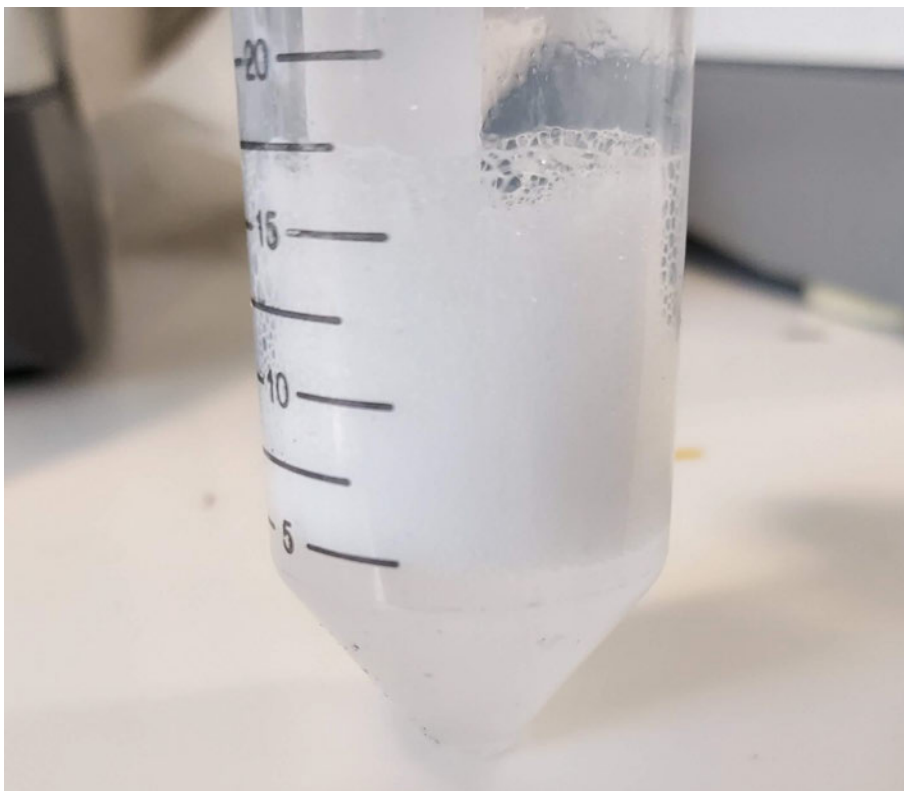
Figure 2.15: Cholesterol solution showing bubbling of the surfactant and a clear solution

The choronoamperometry set up for determination of cholesterol consists of 3 electrodes. The functionalised MN array is the working electrode, the platinum wire electrode as the counter electrode and the Ag/AgCl reference electrode as the reference electrode. This set up is shown in Figure 2.16. A baseline reading of a 0mM cholesterol solution was conducted first using the PBS/Ethanol/Triton X solution. Starting with the lowest concentration, the cholesterol solution was drop cast onto the MN array and left for 10 minutes to get to an equilibrium. A potential of 0.7V was applied to the system for 150s and the resulting final current was recorded. This was repeated by rinsing the electrodes with deionised water and then replacing with cholesterol solutions of increasing concentrations. These results were repeated in triplicate for each concentration before changing to a higher concentration of cholesterol. The following Autolab conditions in Table 2.6 were used.

Table 2.6: Autolab conditions for coating silver electrodes in AgCl

Autolab conditions	
Mode	Potentiostatic
Current range	1mA
Bandwidth	Highspeed
Applied Potential	0.7V
Interval time	1 s
Duration	60 s
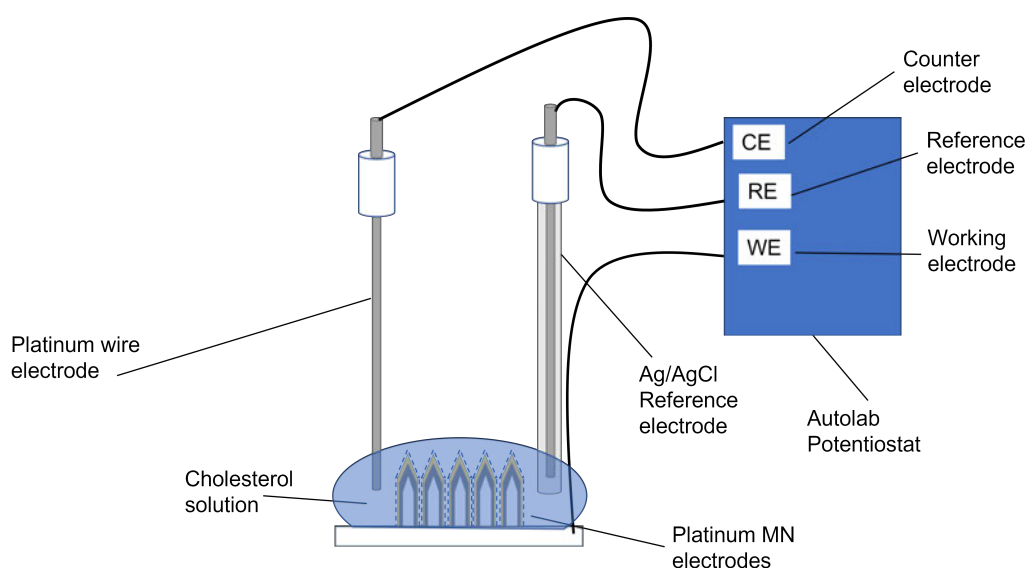
Figure 2.16: Schematic of the set up for cholesterol determination by choronoamperometry

2.2.12 Drug delivery using microneedles

2.2.12.1 Franz cell in vitro assay

Franz cells were used for drug delivery tests with MNs. A Franz cell is a two chamber glass diffusion cell where the glass chambers are separated by a membrane through which diffusion is being monitored. The membrane in this case is the porcine skin as discussed earlier. The apparatus can be seen below in Figure 2.17a. The chamber at the top is the dosing orifice and this is where the drug is administered. The lower chamber is called the receiving chamber due to this being the area that drug collects after it has diffused across the membrane. To mimic the real life application of poke and patch MN drug delivery, the dosing orifice covered in the porcine skin is left open to air.

(a) Single piece of Franz cell apparatus

(b) Franz cell set on magnetic stirrer
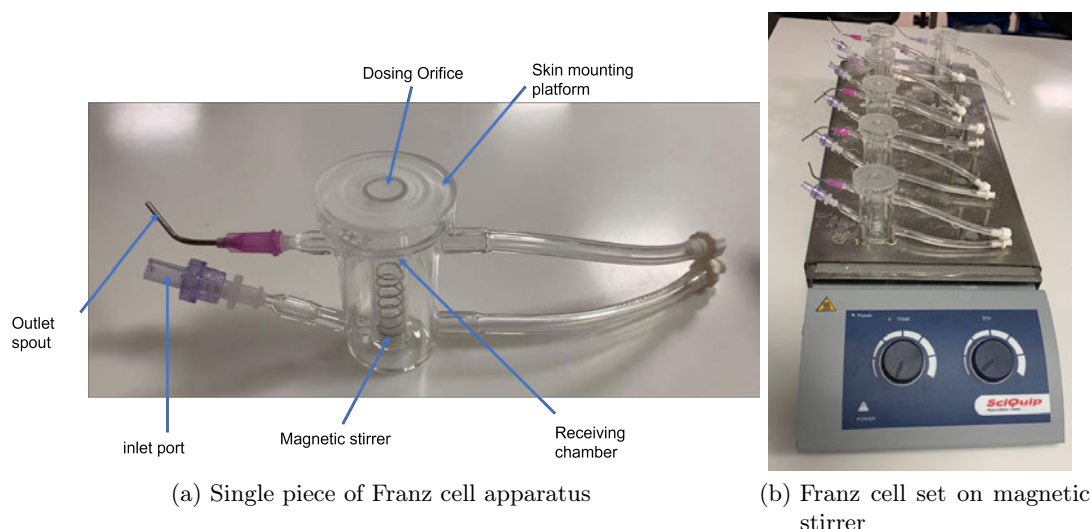
Figure 2.17: Franz Cell Experimental set up for drug delivery experiments

When in use the receiving chamber was filled with 4ml of 0.1M PBS and placed on a magnetic stirrer. The magnetic stirrer was placed in the chamber to homogenise the solution as drug diffused through to model the diffusion of drugs through the skin. The method used to apply the MNs and drug was the poke and patch method, meaning the MNs were applied and then the drug placed on top of the pores. MNs are applied using a PDMS platform 1.5cm thick and a 0.75cm clamp was used to hold the MNs in the skin for 1 minute. These pieces of porcine skin were then stretched over and clamped on top of the Franz cell skin mounting platform and the drug applied to the open circle. 50µl of the drugs was pipetted onto the open circle in contact with the skin surface and any pores made via MN or hypodermic penetration. Calcein (Sigma Aldrich CAS 154071-48-4) and Pravastatin sodium salt hydrate (Sigma Aldrich CAS 81131-70-6) are the drugs being investigated and these were made up into solutions. Calcein was made up into a concentration of 2.5µg/ml in 0.1M PBS and the pravastatin was made up to 1mg/ml and 10mg/mg concentrations in 0.1M PBS.

For sample collection 400µl of 0.1M PBS was injected into the bottom spout called the inlet which displaced the liquid in the receiving chamber that is collected from the top outlet spout. Both of these spouts have bubble traps to ensure no loss of sample. During these experiments readings were taken at 9 time points: 5, 15, 30 minutes, 1, 2, 4, 6, 8 hours and then a 24 hour reading. The PBS reading was subtracted from the calibration values to remove any background.

A calibration curve of known drug concentrations was created using a serial dilution.

The maximum concentration was diluted 10 times and every sample was taken in triplicate to evaluate validity of results. This calibration curve was then cross referenced to calculate the concentration of the drug at each time point.

As each time point had 400µl injected into the receiving chamber, the drug was diluted each time a reading was taken a dilution factor was required to account for this dilution of the drug using the volume of the Franz cell 4000µl. Seen below in Table 2.7 are the calculations for the dilution factor at each time point.

Table 2.7: Franz Cell Consecutive Dilution Factors

Time (hr)	Dilution calculation	Factor
0.083	0/4000	0
0.25	400/4000	0.1
0.5	(400*2)/4000	0.2
1	(400*3)/4000	0.3
2	(400*4)/4000	0.4
4	(400*5)/4000	0.5
6	(400*6)/4000	0.6
8	(400*7)/4000	0.7
24	(400*8)/4000	0.8

The concentration of each sample was determined using the calibration curve equation $y = mx + c$ and rearranging to find x. Then to account for the dilutions each sample was multiplied by the dilution factor corresponding to the time the sample was taken. The final concentrations were plotted into a graph depicting concentration over time. This was then converted to graph of cumulative concentration over time .

To analyse the rate of the flow of drug into the chamber of the Franz cells the flux was calculated. The flux (J) was the mass (m) divided by the area of the dosing orifice (A) and the time point (t) using the equation 2.1. The dosing orifice had a radius of 0.45cm and therefore an area of 0.6362 cm^2.

$$J = \frac{m}{At}$$ (2.1)

2.2.12.2 Fluorescent spectrometry for drug detection

Drug detection methods depended on the type of drug tested. Fluorescent spectrometry was used to measure fluorescent or fluorescent tagged drugs. This method is the measurement of the fluorescence emitted by the substance during its exposure to electromagnetic radiation at a certain wavelength. The samples were measured in a

FLUOstar® Omega spectrophotometer as it had a multi mode microplate reader with various fluorescent and UV/vis filters. The calcein used was florescent tagged therefore the florescence measured is proportional to the drug. The samples were analysed in a 96 well plate where 3 wells were each filled with 100µl so the reading were triplicate. The wavelength programmed into the plate reader was specific to the drug. This wavelength was shone at the samples and the detector within converted the corresponding light emitted into a measurement. These readings were compared to the calibration curve with the known concentrations.

2.2.12.3 High performance liquid chromatography

Non fluorescent drugs required another method such as high performance liquid chromatography (HPLC). HPLC is a technique used to separate and quantify the components of liquid samples. The samples are mixed with the liquid mobile phase and passed through a column consisting of packed porous particles (stationary phase). The differences in solubilities, nature of the column and how the drug reacts to the stationary and mobile phase changes the velocity in which it moves through the column and impacts the retention time. A Perkin Elmer Altus A-10 HPLC instrument with a PDA detector The readings are generated using UV- vis detection to determine drug concentration. The area under the peak corresponding to the drug is used as the reading. A calibration curve is created using known concentrations of the drug and their corresponding UV area readings. These calibration curves were cross referenced to find the corresponding concentrations for for the UV area values in the testing samples. For pravastatin the HPLC was used with a Phenomenex® Kinetex 5µm F5 100 Å, LC 50x4.6 mm column and a mobile phase consisting of 0.1% Trifluoroacetic acid (TFA) (Sigma Aldrich CAS 76-05-1) made up with HPLC grade water (Sigma Aldrich CAS 7732-18-5) and Acetonitrile (Sigma Aldrich CAS 75-05-8). The ratio used was 65% TFA and 35% Acetonitrile, a flow rate of 0.5ml/min and a UV-vis detection wavelength of 248 nm. Using this ratio and flow rate the retention time for the pravastatin is around 2 minutes.

2.2.12.4 Assessment of drug retention on the skin surface

To calculate drug remaining on the surface of the skin or just within the *stratum corneum* a tape stripping method was applied. Adhesive tape was cut into small strips and applied to the *stratum corneum* side of the porcine skin after the Franz cell analysis had been completed. After pressing to ensure good contact, the tape was removed and placed in 4ml of PBS. 10 more strips were applied and removed and put together

in another 4ml PBS. The first singular strip was to determine the amount of drug on the surface and the following 10 were to determine the amount remaining in the *stratum corneum*. These tape strips were covered in foil to block out any light if using a fluorescent drug and placed on a roller mixer overnight. The next day the solutions were then read using the detection method previously used for that drug.

2.2.12.5 Skin homogenisation

After the tape stripping the skin samples were homogenised in order to determine the presence of any drug remaining in the epidermis portion of the skin samples. They were homogenised using an enzyme to break down the skin and free the drug which has accumulated in the epidermis. Papain was the enzyme used and works by breaking peptide bonds that involve basic amino acids [173]. Papain was diluted to 2mg/ml in activation buffer containing, 20mM Sodium Acetate, 1mM Ethylenediaminetetraacetic acid (EDTA) and 2mM Dithiothreitol (DTT) at a pH of 6.8. The centrifuge was used to separate the dissolved skin and drug in the remaining supernatant liquid which was then tested using fluorescence spectroscopy.

3 Printed Polymer Microneedle Fabrication

The devices manufactured were based on MN patches. These needed to be fit for purpose and designed with the application of the MNs in mind. Penetration depth is an important factor in the usability of a microneedle patch for both biosensing and drug delivery applications. The MN parameters required for the MN patches to have optimised penetration and therefore surface area of MN in the skin, need to be investigated. This is especially important for microneedle biosensing as increased surface area with the ISF in the skin can improve detection and signal strength. The length of the MN needs to penetrate deep enough to contact with the ISF while the width needs to be large enough to keep the structural integrity of the MN intact. The pitch distance needs to be large enough to avoid the bed of nails effect which limits penetration of the MNs. The penetration of about 300µm into the skin would provide adequate contact to ISF in the skin.

The ML3DP process being used for these experiments is much more conducive to full size manufacture upscaling than other MN fabrication methods. The process can be semi automated and used conveyor technology to move from the screen print portion to the curing part of the process. It is also highly cost effective because as many as 20 arrays can be made at once in a machine using one stencil.To start the process of making appropriate MNs, a substrate was chosen. A polymer substrate was chosen to allow good adhesion with the MN polymer material. Polyethylene terephthalate glycol (PETG) was the polymer used as it has good flexibility and strength. 500µm thick sheets were used as this thickness combined enough flexibility with the strength to give a sturdy base that would transfer the insertion force placed on it to the MN insertion. The board thickness parameters on the DEK machine were adjusted to accommodate the addition of the substrate material on top of the board. The polymer was placed on the stencil in the squeegee zone in excess to ensure a sufficient amount was available for the process. Any leftover polymer is collected after fabrication to be used again. The squeegees used had guards on the side to minimise polymer loss. Initially the MNs

were cured using a static UV lamp, this was later switched to an LED conveyor belt lamp to more evenly distribute the UV and to lower the risk of warping due to the heat emitting from the UV lamp. The arrays were passed through the LED UV conveyor belt twice after the fabrication of each layer to ensure the layer had fully cured limiting any deformation of MNs. To be used as minimally invasive devices the MN arrays need to be sterile. This fabrication process produces sterile patches due to the UV exposure during the curing process, sterile packaging could be used to move them between machines and equipment for functionalisation purposes to keep the MNs sterile after fabrication.

3.1 Base building and basic shape

The design of the MN patches was controlled by the stencil design, including size of the holes, shape, pitch and arrangement. Pitch is the distance between the centre of each MN. To narrow down the options of the MN design, a 200µm thick stencil consisting of 2cm by 2cm patches of varying pitch and aperture diameter of circular holes was designed and ordered from MacDermid Alpha. For the base stencil the diameter of the apertures varied from 200-600µm in 100µm intervals. The minimum pitch for the smaller apertures was 700µm from the centre of one aperture to the next. The minimum pitch was increased to 800 and 900µm for the largest aperture sizes. Seen in Figure 3.1 Another stencil was also designed and created for the tipping portion of the MN fabrication process for these MNs of varying pitch and diameters. Also seen in Figure 3.1. This stencil had an aperture size 150µm due to this being the smallest possible aperture for use with the polymer used for Innoture's MN printing process using the DEK machine. The pitches of the tipping stencil matched the base stencil so the two stencils were compatible. Below are Tables 3.2 and 3.1 denoting the varying pitch diameters and apertures diameters in both stencils. The intended strategy is to build up MN arrays by first building a sturdy base shape and then testing these for penetration and improving on each iteration. Then depending on the performance of the basic shape optimise the tip portion using an iterative process and testing penetration to get the most optimal MN array for penetration using this fabrication method.
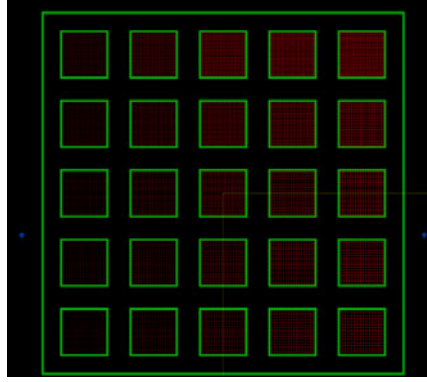
(a) Base stencil schematic of varying aperture size and pitch
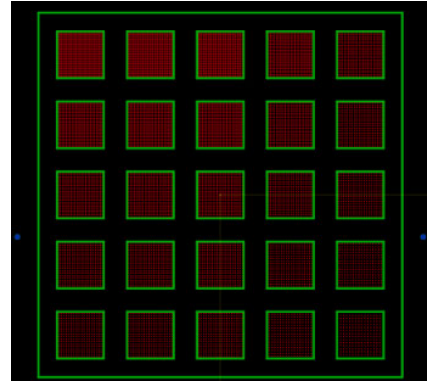
(b) Tipping stencil schematic of diameter 150μm with varying pitches matching the base stencil

Figure 3.1: Gerber file depiction of Base and tipping stencils

3.1.1 Aperture selection

Table 3.1: Grid depicting the MN arrays on the Base Stencil for MN fabrication with pitch variation (P-Pitch μm)

Aperture (μm)				
200	300	400	500	600
P=700	P=700	P=700	P=800	P=900
P=800	P=800	P=800	P=900	P=1000
P=900	P=900	P=900	P=1000	P=1100
P=1000	P=1000	P=1000	P=1100	P=1200
P=1100	P=1100	P=1100	P=1200	P=1300

Table 3.2: Corresponding grid depicting the MN arrays on the Tipping Stencil for MN fabrication with pitch variation (P-Pitch µm)

Aperture (µm)				
150	150	150	150	150
P=700	P=700	P=700	P=800	P=900
P=800	P=800	P=800	P=900	P=1000
P=900	P=900	P=900	P=1000	P=1100
P=1000	P=1000	P=1000	P=1100	P=1200
P=1100	P=1100	P=1100	P=1200	P=1300

The stencils with 400µm and 500µm apertures produced a MN with a sturdy base and had enough surface area without the width being so large that the pitches are impacted. The microneedles were made using the polymer Dymax 1180 as this was the previously optimised polymer used by Innoture Ltd for this fabrication process.

As the process involves gradually building up height, the focus was to fabricate MNs between 700 and 800µm in height by building up small even layers of polymer. Initially the difference between print gaps was kept equal with 2 passes being deposited at each 200µm interval starting at 100µm up to 500µm. Then single passes at 100µm intervals up to 1300µm as shown in Table 3.3 below. The print gaps show a taller MN as during the process the polymer gets compressed thinner than the gap. This resulted in the MNs depicted in Figure 3.2. The pressure pressure value used at the start of optimisation matched previous Innoture protocols used for similar sized arrays and aperture holes. Initially a 2kg pressure was used for the base layers but it was determined that 1 kg was sufficient through iterations. It was also adjusted to a higher pressure for the stencil with the smaller 150µm apertures to allow for adequate amount of polymer to pass through the apertures. An iterative process was used and the pressure was increased up to 2kg. This provided tips that adhered to the base shapes of the MNs and resembled sharp points.

Table 3.3: Initial fabrication procedure of the polymer ML3DP microneedles

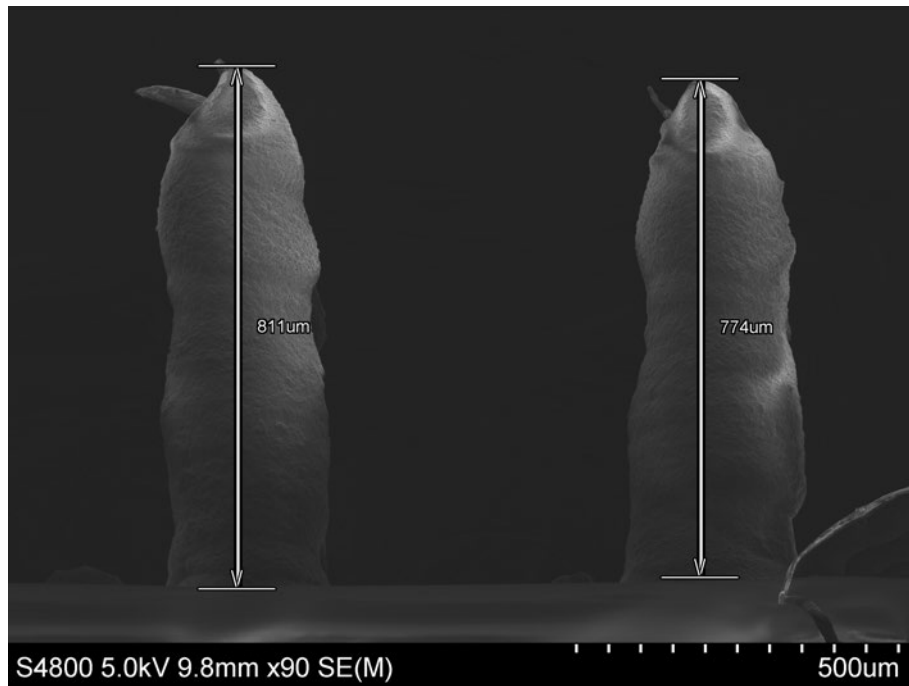| Pass No.	Print Gap (µm)	Pressure (kg)
1	0	2
2	100	1
3	100	1
4	300	1
5	300	1
6	500	1
7	600	1
8	700	1
9	800	1
10	900	1
11	1000	1
12	1100	1
13	1200	1
14	1200	1
15	1300	1

Figure 3.2: SEM image of the initial fabrication of microneedles using 400µm aperture stencil showing MNs measuring 774um and 811um in height

Long and thin MNs such as the ones depicted above would bend if handled due to

the strength of the polymer in this shape not being sufficient. The height to base width ratio is also another factor to consider. To create good base contact with the substrate several passes at print gap zero are required. For the MN bases below in Figure 3.3 this was achieved through 4 passes at a print gap of 0 allowing the aperture to fill and the base layers to be evenly deposited. For these initial 4 passes the parameters were: board thickness 2.4mm, Pressure 2kg and 0µm print gap. Then the print gap was increased to 200µm for 2 passes After it was then increased in intervals of 100µm with 2 more passes on each interval up to 600µm. This completed the base as seen in Figure 3.3. The thin layers give a cut off top to the MN base, this is not ideal as for optimal MN penetration a more tapered shaped with a sharp tip is required.

(a) SEM image of MN base using 400µm sten-cil

(b) SEM image of MN base using 500µm aperture stencil
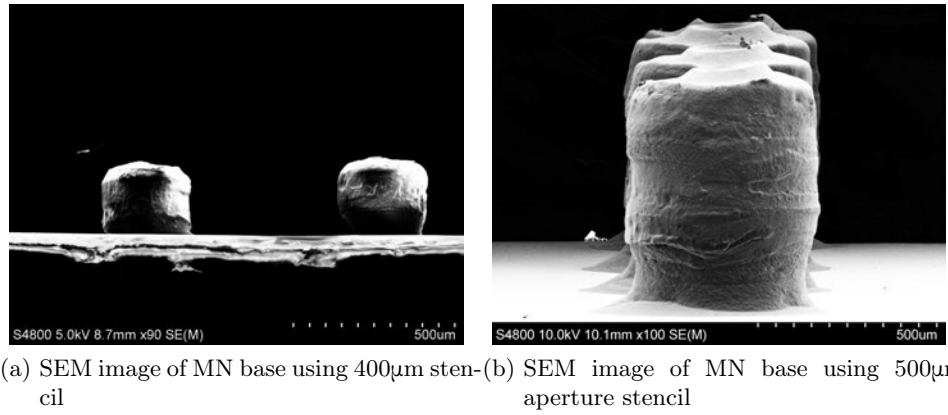
Figure 3.3: SEM image of MN Base portion of fabrication using base stencil

To obtain a more tapered shape to the MN base the print gap should be increased and number of passes reduced to make use of the necking that happens after the stencil is separated from the substrate and MNs. The separation speed is kept the same to minimise curling or bending of the tip and to keep the patches as uniform as possible. Further bases with the 400µm aperture stencil were fabricated using the procedure below in Table 3.4 and the resulting MNs are shown in Figure 3.4 :

Table 3.4: Procedure for tapered MN base using a 400μm aperture stencil

Pass No.	Print Gap (μm)	Pressure (kg)
1	0	1
2	0	1
3	0	1
4	0	1
5	400	1
6	600	1
7	800	1
8	1000	1
9	1200	1
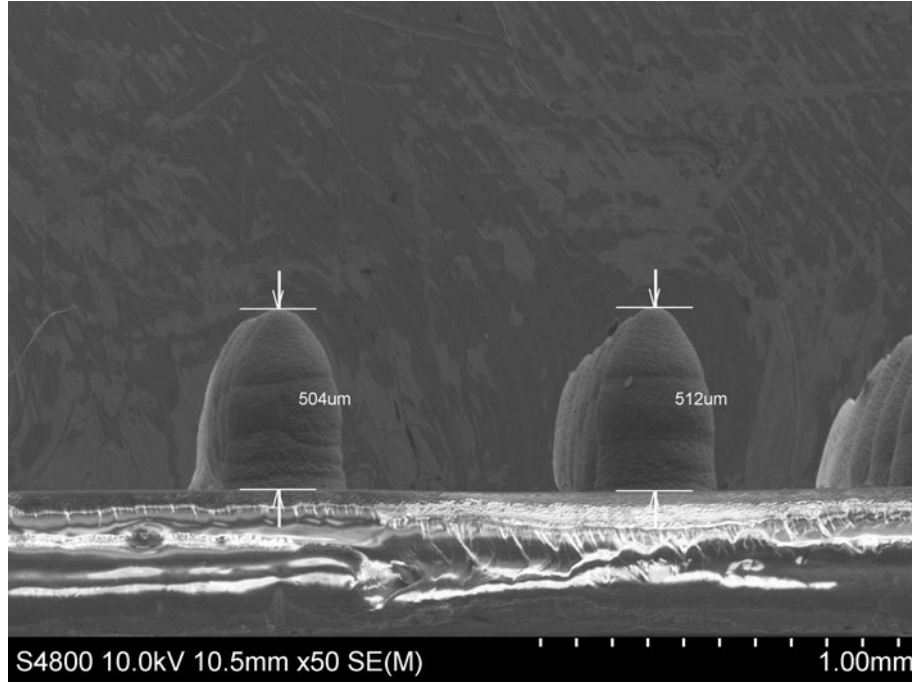
Figure 3.4: MN 400μm tapered

The 500μm aperture stencil was also used to make tapered MNs as seen below in Figure 3.5 using the settings in Table 3.5. Each time a patch was made there was a build check performed using a USB microscope.

Table 3.5: Tapered MN 500μm base

Pass No.	Print Gap (μm)	Pressure (kg)
1	0	1
2	0	1
3	0	1
4	0	1
5	500	1
6	700	1
7	900	1

These MNs yielded similar looking results with larger dimensions as can be seen in Figure 3.5 below.
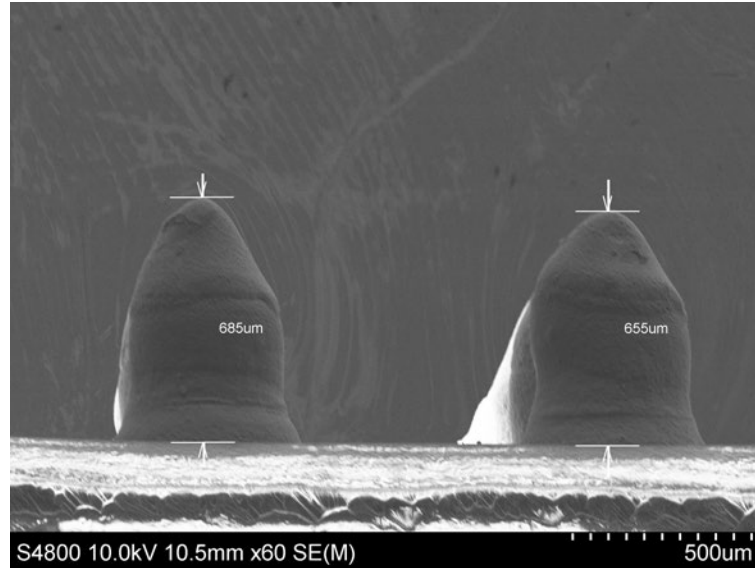
Figure 3.5: Tapered MN using a 500μm aperture stencil

The ratio of the MN base to tip was considered and this was mainly addressed by tapering the MN build so that there is a very sharp tip with a solid base. This base however should not be so wide that it reduces the distance between MNs significantly enough so that a 'bed of nails' effect occurs.

3.2 MN tip optimisation

To add the tips to the MNs a separate tipping stencil with 150μm apertures and matching pitch diameters to the base stencil was used. It was assumed that the print gap

needed for a tip on a MN needed to be the same as the last print gap used for the base in order to get sufficient contact with the MN base. To accommodate the smaller aperture size the pressure used with the tipping stencil was doubled to 2 kg. Both the 400μm and 500μm aperture MN bases were tipped with 2 passes at a print gap of 1000μm. Figure 3.6 shows that there is a large difference between the MN bases and the size of the tips and that the 500μm MNs have a much more pronounced bulge in their shape which would not be conducive to optimal penetration of the MN array. It was therefore decided that the 400μm aperture MNs had more potential for the shape to be optimised fully by varying the MN fabrication protocols than the 500μm aperture MNs following these results. The following MN fabrication protocols use the 400μm aperture stencil.
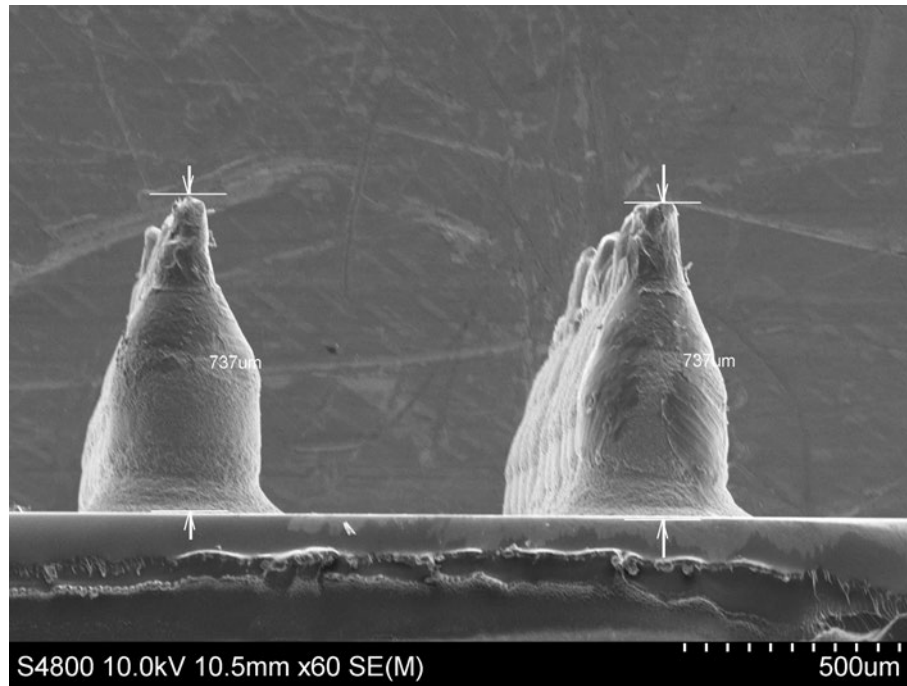
(a) 400μm base stencil tipped MNs
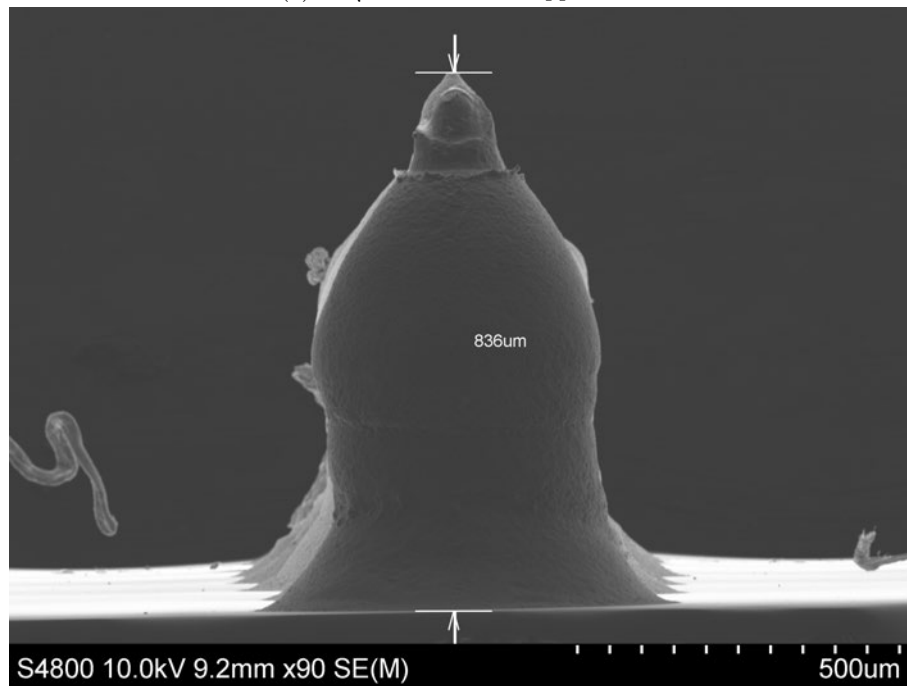
(b) 500μm base stencil tipped MNs

Figure 3.6: First protocol tipping MN using 400μm and 500μm aperture base stencils and 150μm aperture tipping stencil

The following fabrication protocol tables all start with the same foundation layers (passes 1-4) but have differing parameters for the base layers (passes 5-7) before the tip layers (passes 8-9) in order to improve the transition and shape between base and tip of the MNs. This is an iterative optimisation process to obtain optimal size and shape of MNs

	Protocol 1		
	Pass No.	Print Gap (µm)	Pressure (kg)
Base	1	0	1
	2	0	1
	3	0	1
	4	0	1
	5	500	1
	6	700	1
	7	900	1
Tip	8	1000	2
	9	1000	2

(a) protocol 1 MNs using 400µm aperture base stencil and 150µm aperture tipping stencil

	Protocol 2		
	Pass No.	Print Gap (µm)	Pressure (kg)
Base	1	0	1
	2	0	1
	3	0	1
	4	0	1
	5	600	1
	6	600	1
	7	900	1
Tip	8	1000	2
	9	1000	2

(b) Protocol 2 MNs

Table 3.6: Protocol 1-3 full MNs base and tip combined

	Protocol 3		
	Pass No.	Print Gap (µm)	Pressure (kg)
Base	1	0	1
	2	0	1
	3	0	1
	4	0	1
	5	500	1
	6	900	1
Tip	7	1000	2
	8	1000	2

(c) Protocol 3 MNs using 400µm aperture base stencil and 150µm aperture tipping stencil

As can be seen in Figure 3.7, of these protocols number 2 Table 3.7b produced the best shaped MNs due to there being no bulging, having a tapered shape and less of a 'shelf' appearance between the base portion of the MN and the tip. There was a bulging in protocol 1 and a 'shelf' appearance between the base and tip of protocol 3.
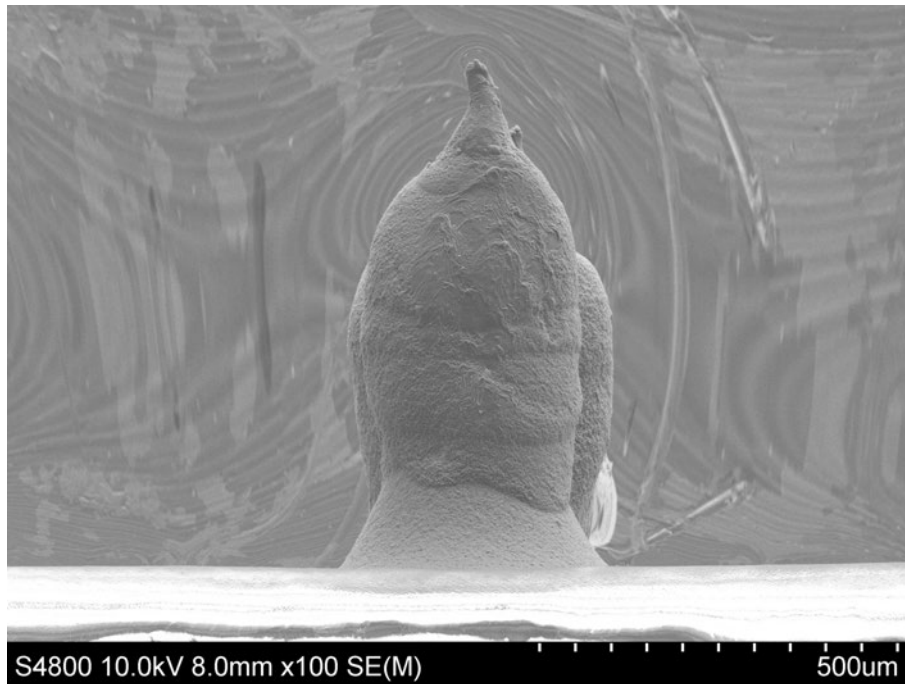
(a) SEM Protocol 1 MNs using 400µm aperture base stencil and 150µm aperture tipping stencil

Figure 3.7: SEM images of protocols 1-3 full MNs
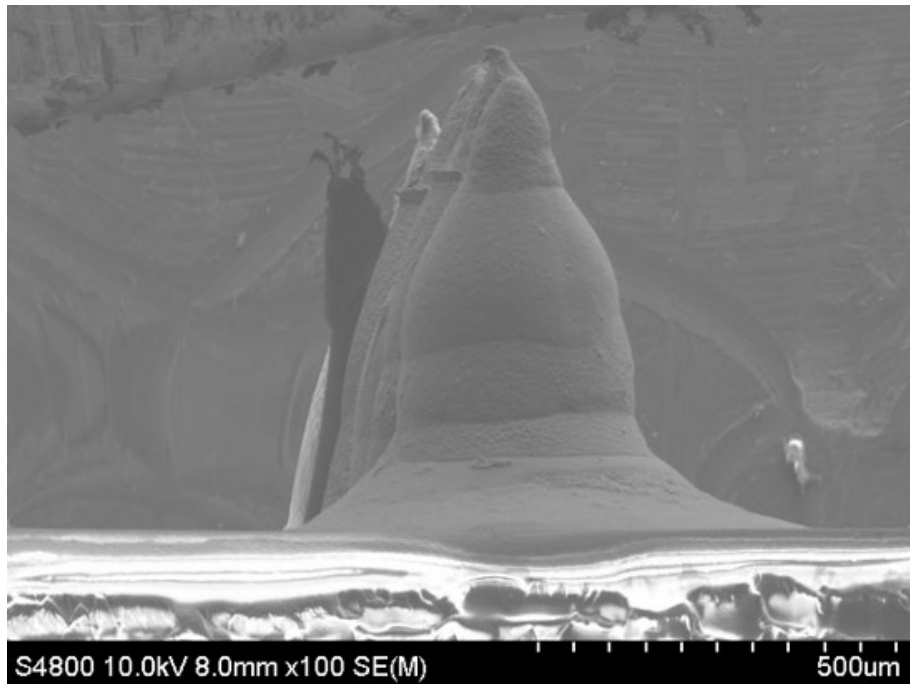
(b) SEM of Protocol 2 MNs using 400μm aperture base stencil and 150μm aperture tipping stencil

(c) SEM of Protocol 3 MNs using 400μm aperture base stencil and 150μm aperture tipping stencil

Figure 3.7: SEM images of protocols 1-3 full MNs

The following protocols in Table 3.6 were used to try to remove the 'shelf' between the tip layers and the base layers and create a more smooth transition.

	Protocol 4		
	Pass No.	Print Gap (µm)	Pressure (kg)
Base	1	0	1
	2	0	1
	3	0	1
	4	0	1
	5	600	1
	6	700	1
	7	1000	1
Tip	8	1000	2
	9	1000	2

(d) Protocol 4 MNs using 400µm aperture base stencil and 150µm aperture tipping stencil

	Protocol 5		
	Pass No.	Print Gap (µm)	Pressure (kg)
Base	1	0	1
	2	0	1
	3	0	1
	4	0	1
	5	600	1
	6	800	1
Tip	7	1000	2
	8	1000	2

(e) Protocol 5 MNs using 400µm aperture base stencil and 150µm aperture tipping stencil

	Protocol 6		
	Pass No.	Print Gap (µm)	Pressure (kg)
Base	1	0	1
	2	0	1
	3	0	1
	4	0	1
	5	600	1
	6	900	1
Tip	7	1000	2
	8	1000	2

(f) Protocol 6 MNs using 400µm aperture base stencil and 150µm aperture tipping stencil

Table 3.6: Protocols 4-6 full MNs

70

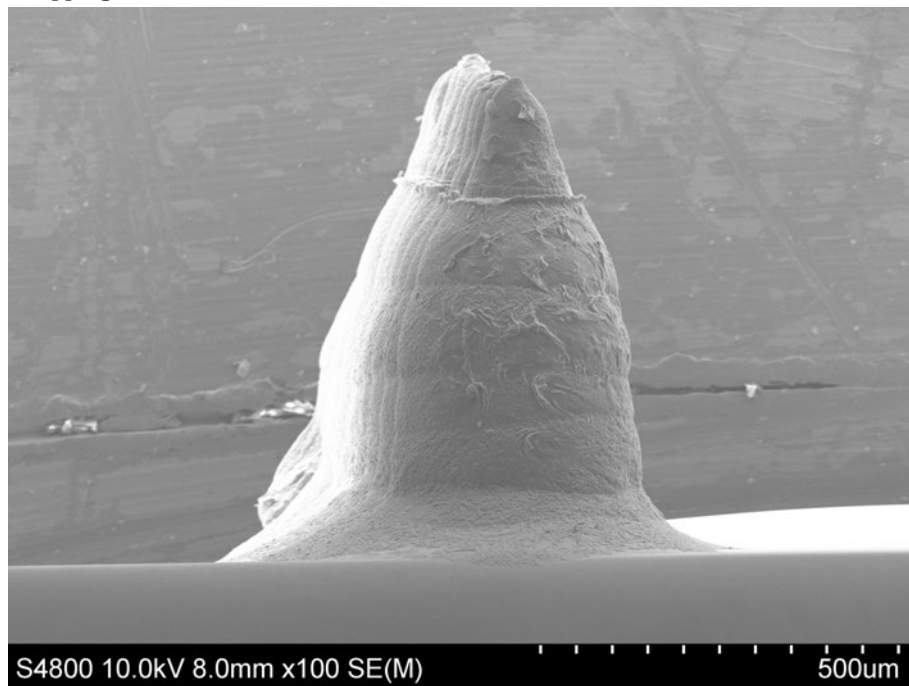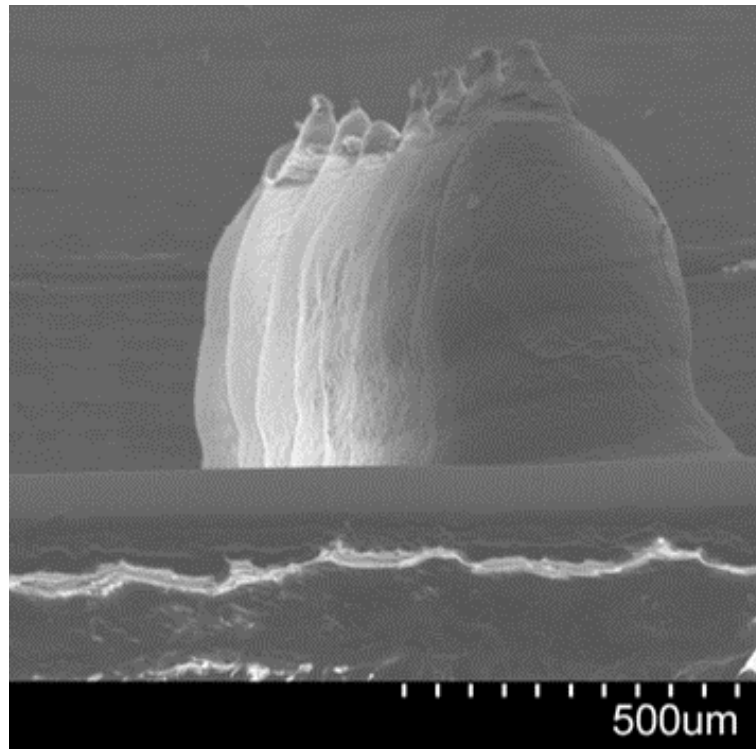(a) SEM Protocol 4 MNs using 400µm aperture base stencil and 150µm aperture tipping stencil
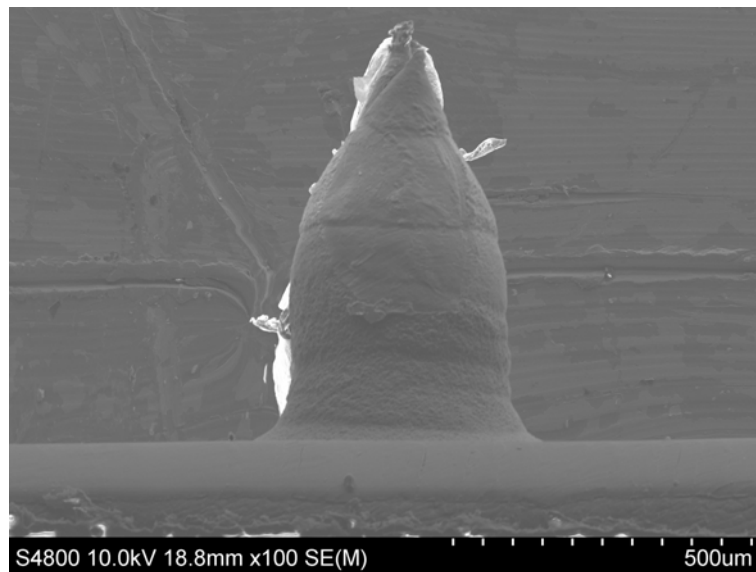
(b) SEM of Protocol 5 MNs using 400µm aperture base stencil and 150µm aperture tipping stencil

Figure 3.8: SEM images of protocols 4-6 full MNs

71
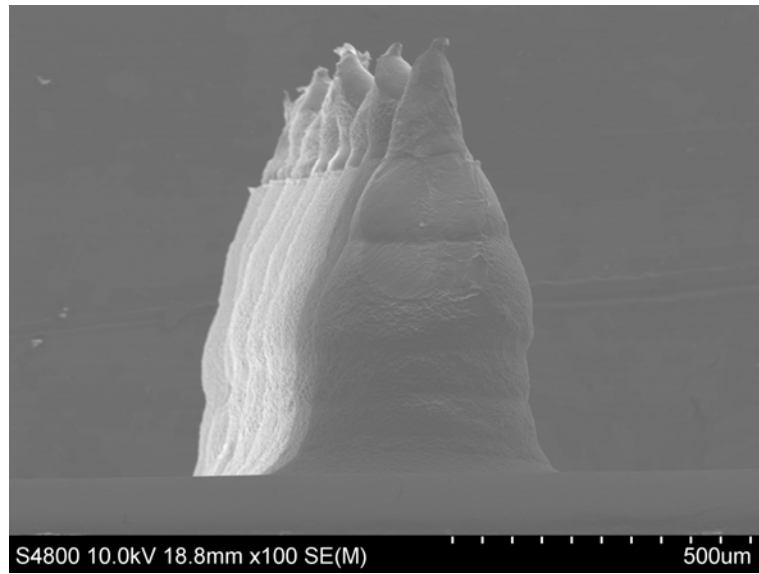
(c) SEM of Protocol 6 MNs using 400μm aperture base stencil and
    150μm aperture tipping stencil

Figure 3.8: SEM images of protocols 4-6 full MNs

Protocol number 2 was repeated due to the shape being closest to ideal. These MN arrays were fabricated several times to make sure the shape was consistent. The least consistent part of the MNs is the tip so alterations of the print heights of the tips was then investigated to obtain a nicely tapered and sharp tip.
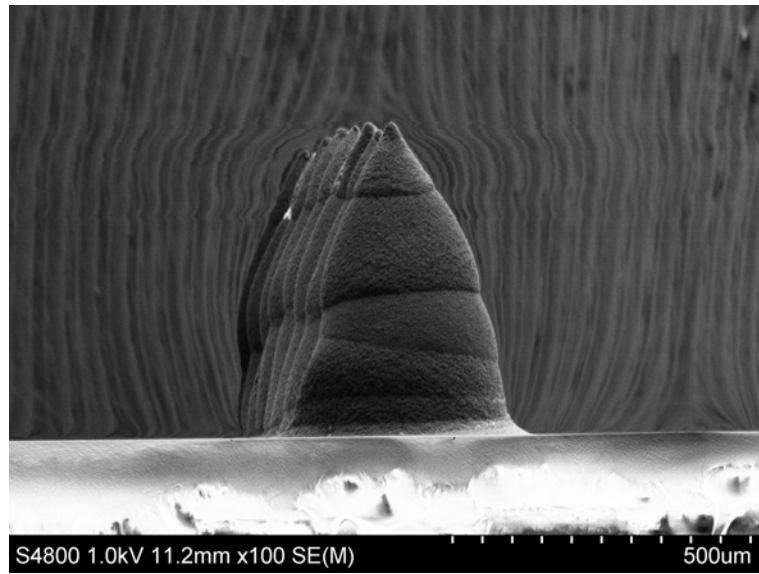
Figure 3.9: Protocol 2 repetitions using 400μm aperture base stencil and 150μm aperture tipping stencil

S4800 1.0kV 11.2mm x60 SE(M)

S4800 1.0kV 11.2mm x100 SE(M)   500um
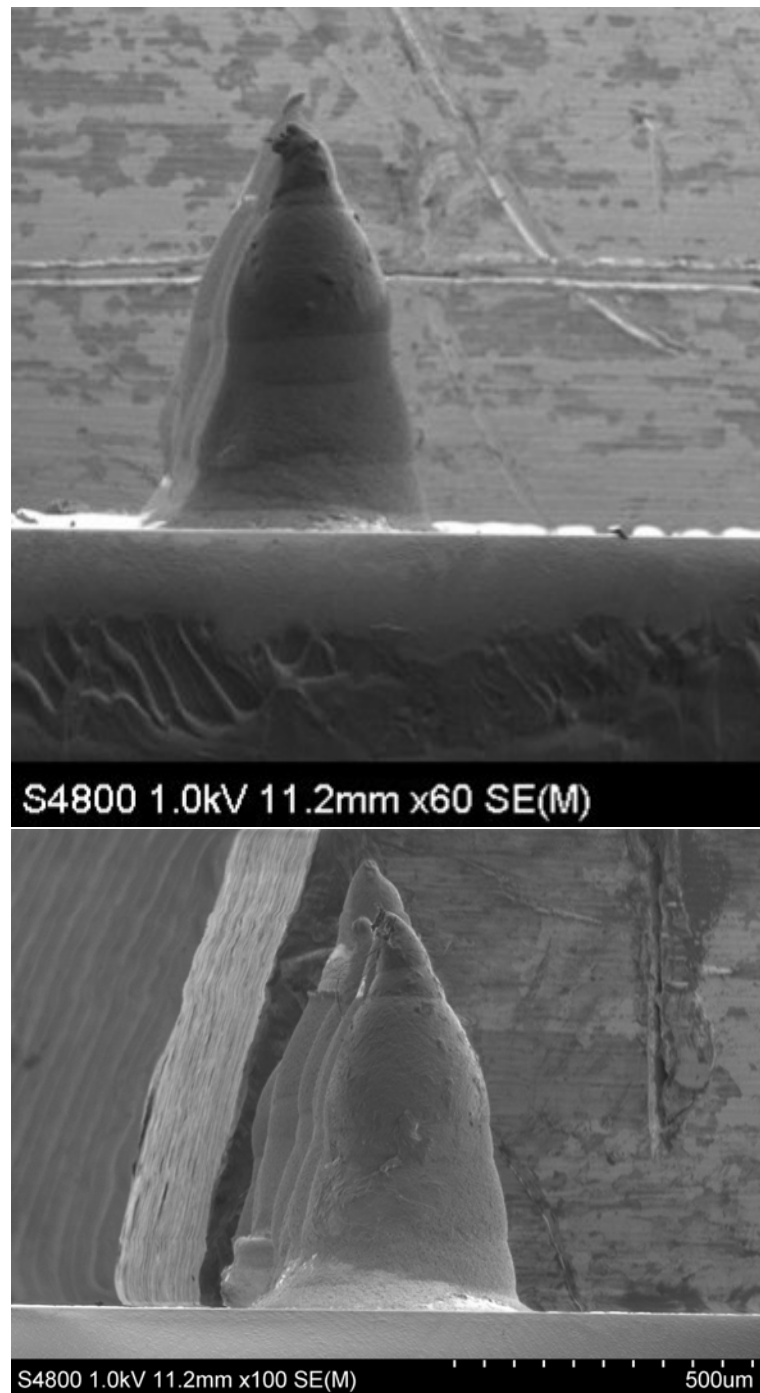
Figure 3.9: Protocol 2 repetitions using 400μm aperture base stencil and 150μm aperture tipping stencil

| | Protocol 7 | | |
	Pass No.	Print Gap (μm)	Pressure (kg)
Base	1	0	1
	2	0	1
	3	0	1
	4	0	1
	5	600	1
	6	600	1
	7	900	1
Tip	8	1000	2
	9	1100	2

(a) Protocol 7 MNs using 400μm aperture base stencil and 150μm aperture tipping stencil

| | Protocol 8 | | |
	Pass No.	Print Gap (μm)	Pressure (kg)
Base	1	0	1
	2	0	1
	3	0	1
	4	0	1
	5	600	1
	6	600	1
	7	900	1
Tip	8	1000	2
	9	1200	2

(b) Protocol 8 MNs using 400μm aperture base stencil and 150μm aperture tipping stencil

Table 3.7: Protocols 7 and 8 full MNs

Protocol 7 yielded similar results to previous protocols, however protocol 8 had a huge improvement to the percentage penetration of MNs. It appears that 49/64 MNs penetrated making the percentage 76.5%. Comparatively previous percentages were between 4.6% and 18.75% Table 3.8. Some penetration data is presented here to explain the choice of geometry, but main penetration results are presented in the following chapter.

Table 3.8: Table showing the number of N penetrations using protocols 1-8

| Protocol	1	2	3	4	5	6	7	8
Penetrated MNs out of 64	11	12	10	11	10	3	10	49
Percentage %	17.2	18.75	15.6	17.2	15.6	4.6	15.6	76.5
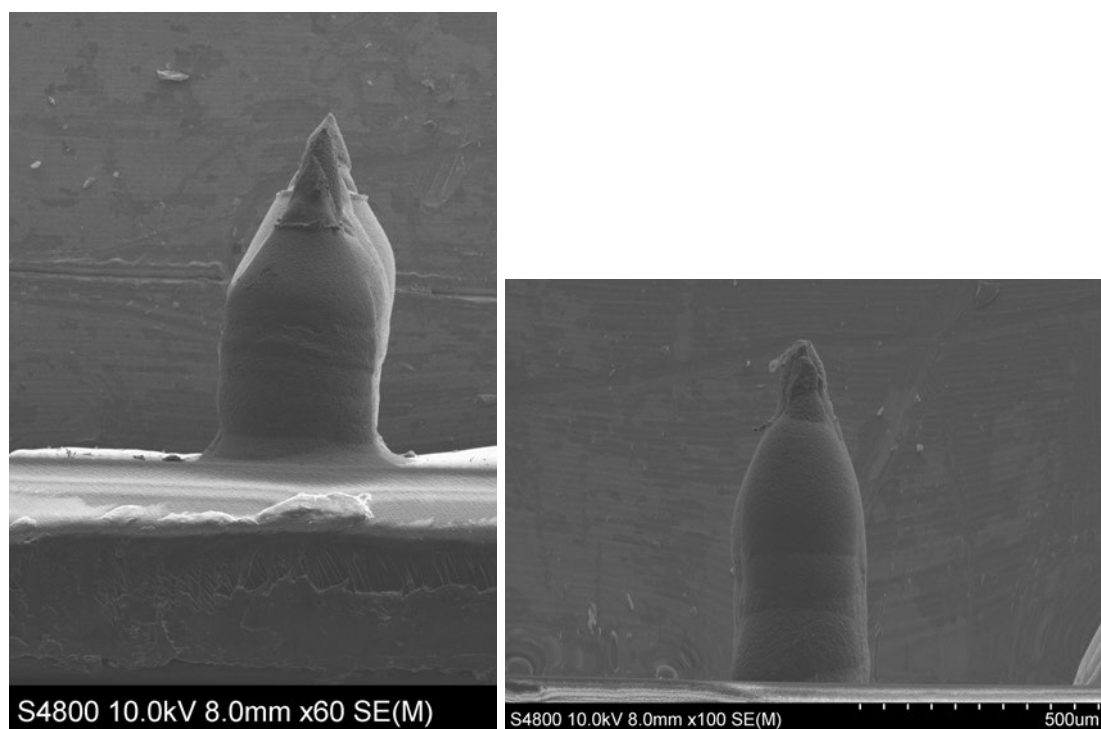
(a) Protocol 7 MN using 400μm aperture base stencil and 150μm aperture tipping stencil

(b) Protocol 8 using 400μm aperture base stencil and 150μm aperture tipping stencil

Figure 3.10: SEM images of protocols 7 and 8 full MNs using 400μm aperture base stencil and 150μm aperture tipping stencil

For successful penetration the tip diameters need to be less than 40μm. This was not as easy to control as the MN heights and base width dimensions due to relying on the necking of the polymer when the stencil is pulled away. However, the final protocol reliably produced tips under 40μm. Optimising this protocol gave an average tip of around 20μm as seen in Figures 3.11a and 3.11b. After further optimisation the tip diameter was reliably under 10μm with the average diameter of 8μm as seen in Figures 3.11c and 3.11d.
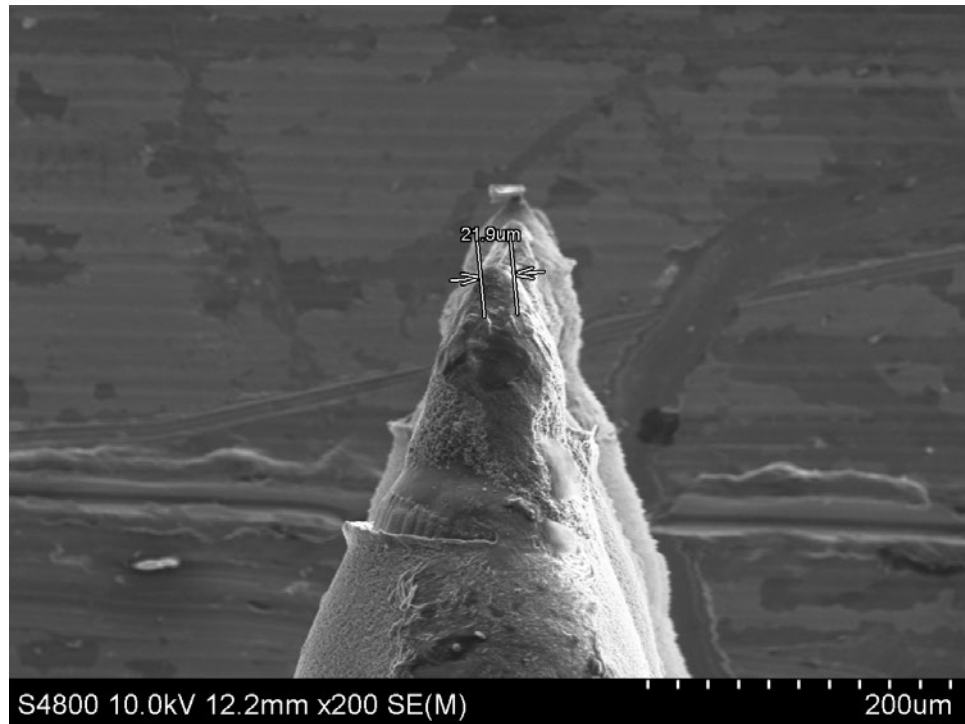
(a) Tip diameter of pre optimised protocol MNs (21.9μm)
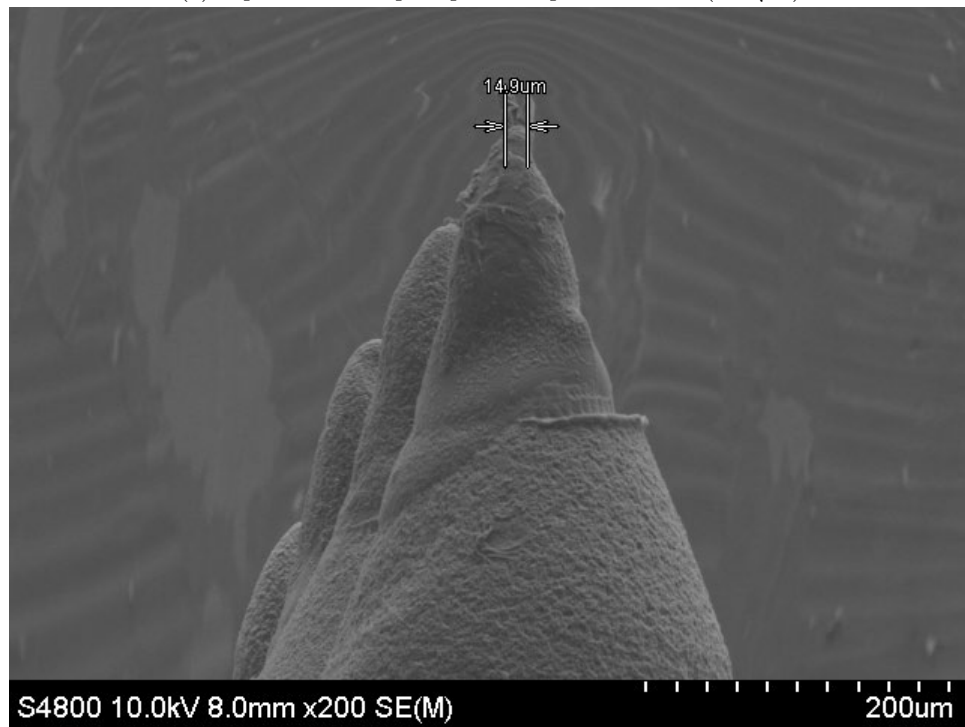
(b) Tip diameter of pre optimised protocol MNs (14.9μm)

Figure 3.11: MN tip diameters
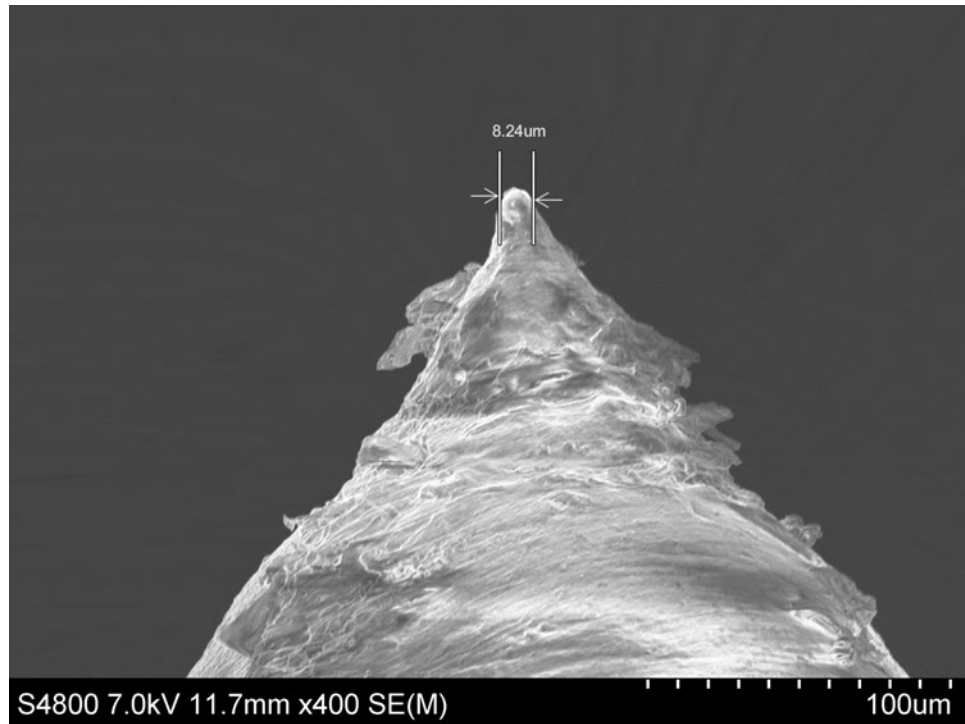
(c) Tip diameter of Final optimised MN protocol (8.24µm).

(d) Tip diameter of Final optimised MN protocol (8.21µm)

Figure 3.11: MN tip diameters on pre optimised and optimised arrays

Repetition of the penetration tests with the protocol 8 MNs showed a high percentage of MNs penetrated reliably when fabricated using this protocol (See Figure 3.12) producing reliably shaped MNs which have sufficient penetration efficiency for use in a device. MNs fabricated using this procedure and protocol were used in following functionalisation, sensing and drug delivery experiments.
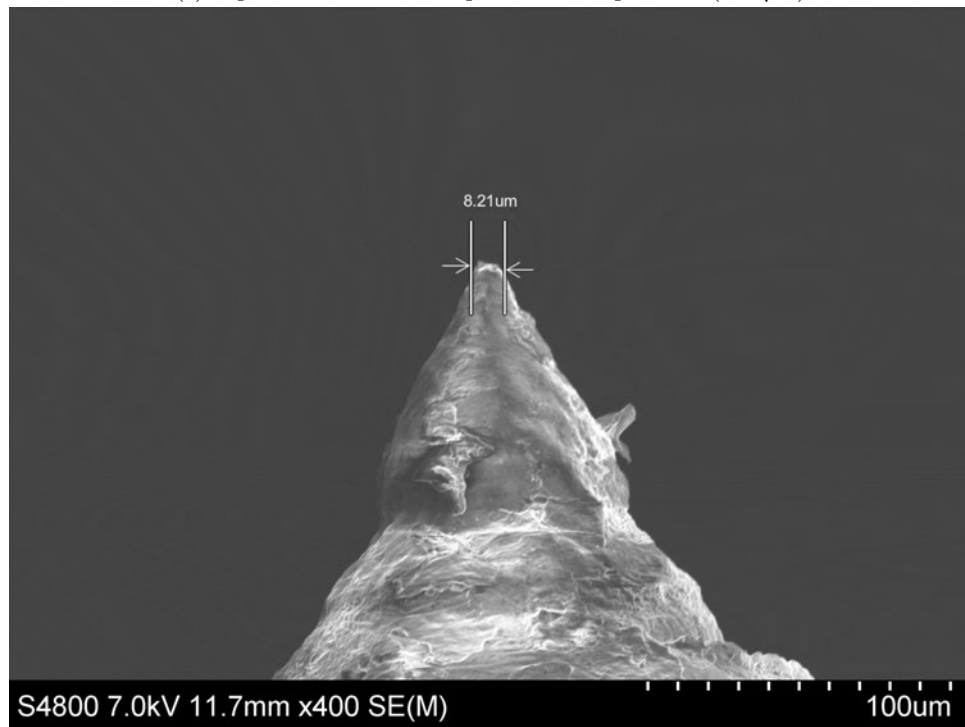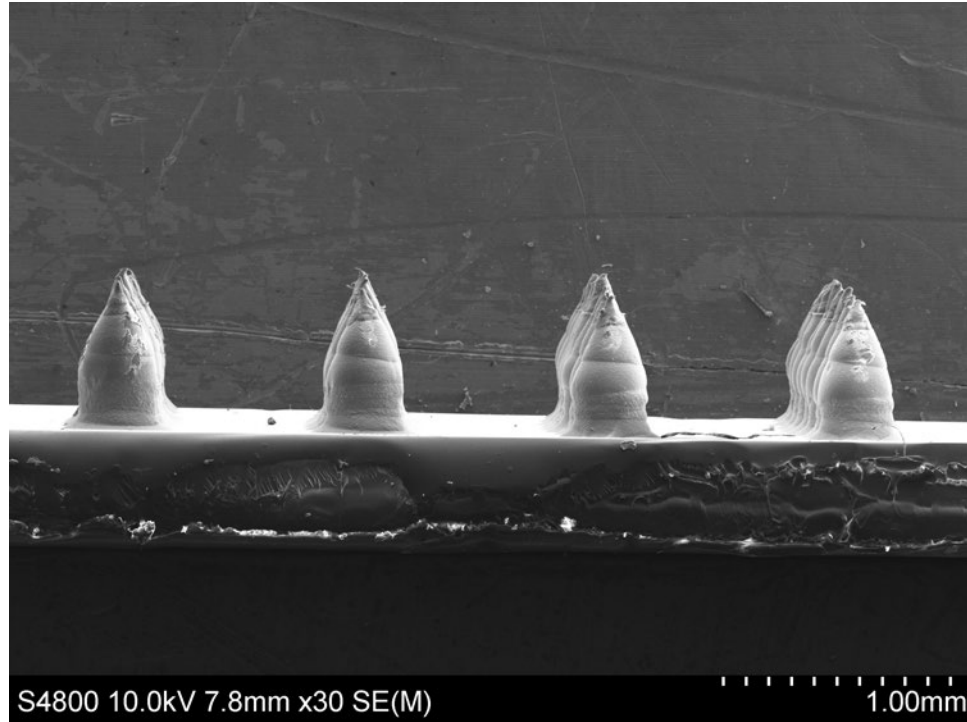

Figure 3.12: Repeat SEM of MNs using protocol 8 and using 400μm aperture base stencil and 150μm aperture tipping stencil

In summary this chapter presents the design elements of MN fabrication and their impact on penetration efficiency. The design parameters include, pitch, aperture, print gap, pressure, board thickness, separation speed and number of layers. The board thickness which corresponds to the starting layer height and separation speed which is the speed the stencil is removed from the board, were kept constant. This is due to needing a consistent starting height that ensured adhesion to the substrate (board thickness) and a separation speed that ensured consistent necking of the polymer as the stencil was removed (separation speed). Variation of pitch (distance between MNs) has been shown to impact penetration of the MN array with much less penetration occurring when the pitch is smaller due to the 'bed of nails' effect. The optimal aperture was 400μm, this yielded the most conical type shape which aided in penetration efficiency.

79

Average dimensions of the optimised MNs are 750µm height, 450µm base diameter, and 8µm tip diameter. The print gaps were varied multiple times but it was found that several passes at the 0 print gap and then evenly spaced print gaps there after, were the most efficient way to fabricate the MNs. The pressure was always higher on the initial passes to ensure good adhesion with the substrate and then lowered so it didn't impact the following print gaps due to flexing of the steel stencil. The final protocol 8 reliably produced tapered bases and tips under 10µm with the average diameter of 8µm. This extra tipping step ensured a sharp enough MN tip for penetration. This design adequately penetrated the skin after being optimised with all these parameters.

Comparatively to MNs in literature the screen printed MNs made for these experiments are much more conducive to full size manufacture upscaling. The process can be semi automated and used conveyor technology to move from the screen print portion to the curing part of the process. It is also highly cost effective because as many as 20 arrays can be made at once in a machine using one stencil. The process is also much shorter and can take less than an hour to make many arrays. There are other types of polymer MNs that have been fabricated using 3D printing or additive manufacturing technology methods and these have been made with materials such as metals and polymers. The earliest sort of 3D printing technology is stereolithography (SLA) which uses photocurable resins with a UV light and a digital micromirror device. The process consists of a liquid resin selectively cured layer by layer. This method has limitation on the materials that can be used, it can be slow and expensive. Other methods like fused deposition modelling (FDM) and 3D dispensing use thermoplastics, can lead to structures with weak mechanical properties, a rough surface and high temperature during the fabrication process. [174, 175]. The polymer MNs made here by ML3DP had the advantage of a flexible process. They can be adapted to specifications for different applications using stencils with different aperture sizes, aperture shapes, the number of passes and the type of UV curable polymer. The process had the advantage over other fabrication methods due to the ability to be made in a high mass produced environment. This results in making these MNs a lower cost option when compared to MNs made by etching or small scale printing.

Following on from this chapter and using MNs made with these geometries, the next section explores the functionalisation using metallisation and chemical functionalisation of these MNs for use as diagnostic devices.

4 Microneedle Metallisation and Functionalisation

4.1 Metallisation

4.1.1 Physical vapour deposition

Physical vapour deposition was used as the method for metallising the MN arrays. The polymer material of the substrate and MNs are not conductive therefore in order for the MN devices to work as electrochemical sensors, a layer of metal was required to make the MNs electrically conductive. This method coated the surface in a thin conformal layer of metal to create a smoother electrode surface. When utilising PVD as a means of metallisation on polymer substrates, a seed layer of metal such as titanium is required to improve adhesion and avoid metal cracking or defects which can impact the quality of a sensor surface [176]. The PVD has different conditions that can affect the deposition of metal. The most prominent of these are the amount of power used and the amount of gas let into the chamber which is under vacuum. The gas used is usually a noble gas such as argon unless metal oxides are desired and in that case oxygen is used. The balance between power supplied and gas impact the speed of metal deposition. Thicker layers of metal (e.g. few hundred nm) can take a long time to deposit if the deposition rate is low, however the lower the deposition rate, the more uniform and smaller grain the metal layer deposited is. For use as sensors the layers required are thick ($>$200nm) to ensure good conductivity therefore a slightly higher deposition rate than typically used is allowed while still limiting the power to keep within safe limits. To enable as uniform a deposit as possible on a 3D surface such as MNs, the plate inside the chamber is set to rotate. It rotates on one axis, though rotation on more than one axis would be ideal to limit a shadowing effect that leaves portions of the surface uncoated. To avoid this outcome, MN arrays with larger pitch (over 1mm) were used to reduce the shadow. In Figure 4.1 below the MNs with a 600μm pitch have shadowing of the metal deposit between the MNs. This shadowing did not occur on the MNs with the larger pitch.
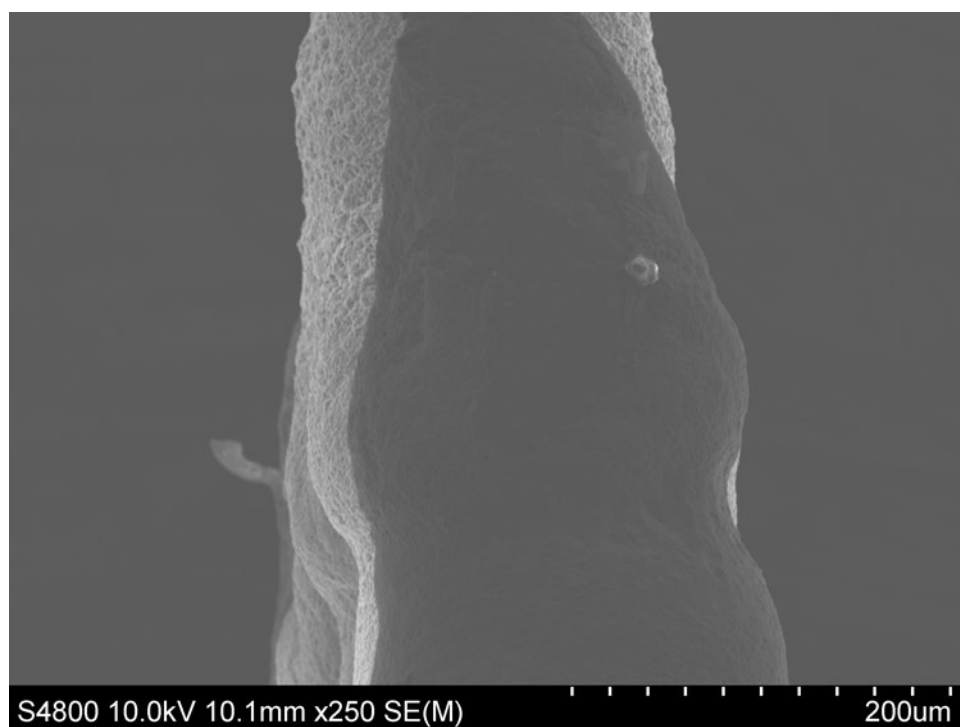
Figure 4.1: The shadow effect on platinum PVD coated MNs, 600µm pitch

The fabricated MNs needed to be functionalised to become sensor electrodes therefore the metals used were chosen based on their electrical conductivity and the way that further functionalisation could be achieved chemically using them. To detect analytes such as glucose or cholesterol a less reactive metal which has a high electrical conductivity is used to limit side reactions occurring during electrochemical readings.

Platinum was chosen as the metal layer on the MN sensor surface for the analyte detection using enzyme functionalisation. Firstly, platinum is a strong, electrochemically inert, durable metal which would lend it's strength to the structure of the polymer MNs it is coated on. It is also highly conductive and has the ability to be used as an electrochemical catalyst or as an electrode surface modifier to allow attachments of enzymes. It has the potential to enhance the electron transfer of the electrode surface which improves sensor sensitivity [177].

Silver was chosen as the electrode surface for the chloride sensors due to the specific electrochemistry used for silver detection as seen in Chapter 2. A silver metal layer can be converted into a silver/silver chloride electrode which through the application of a current can detect the voltage changes of different chloride concentrations. As this method was a direct method of detection for chloride, silver was used as a functional-

isation layer on the electrode.

An SEM was used to visually characterise these MNs after metallising the surface. The MNs to be used for sensing device development were metallised using PVD with 20nm of titanium and either 250 nm of platinum or silver depending on the desired analyte. Figure 4.2 below shows platinum coated MNs. In Figure 4.2a the complete MN array is shown and in Figure 4.2b a cross sectional diagram of the MN array. Figure 4.2c is the image of the MNs under SEM with the coating shown in Figure 4.2d. The average grain size of the silver deposition in 4.2d is 84nm which was calculated using Image J software.
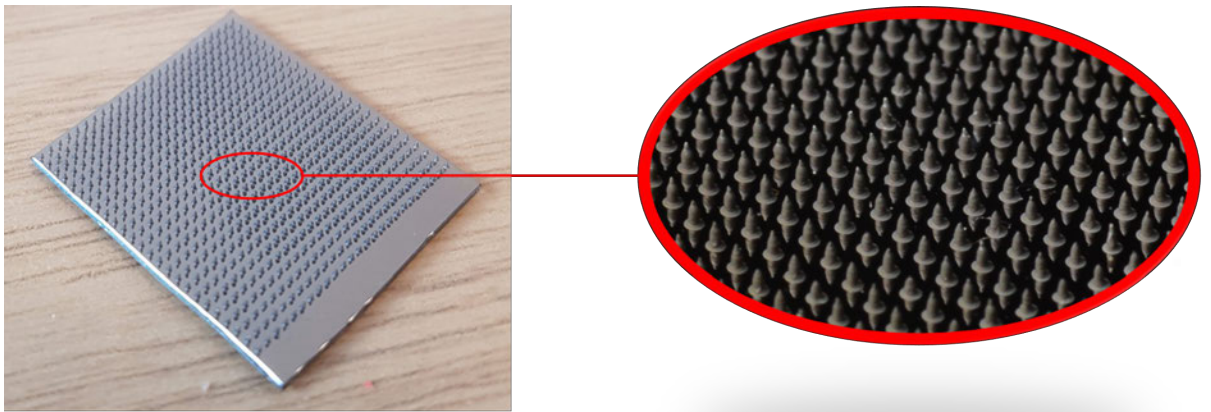
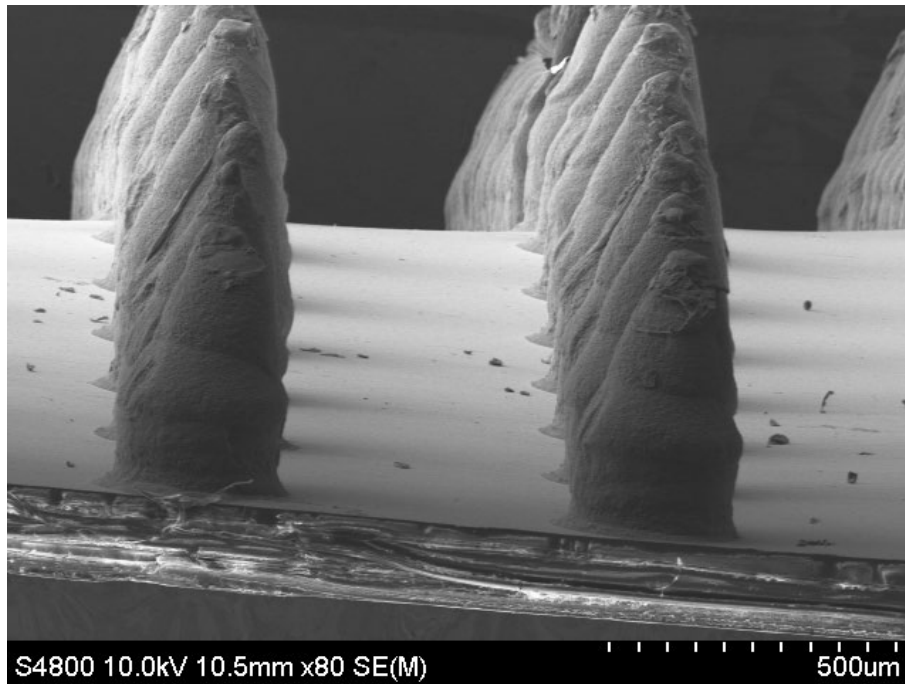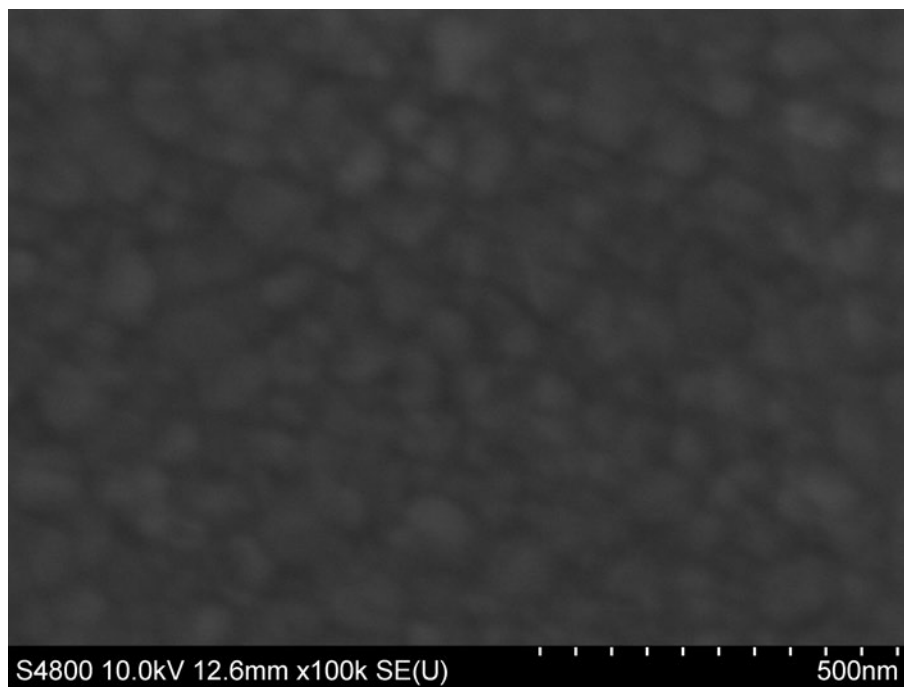(a) Titanium and Platinum Metal coated and wire bonded MNs
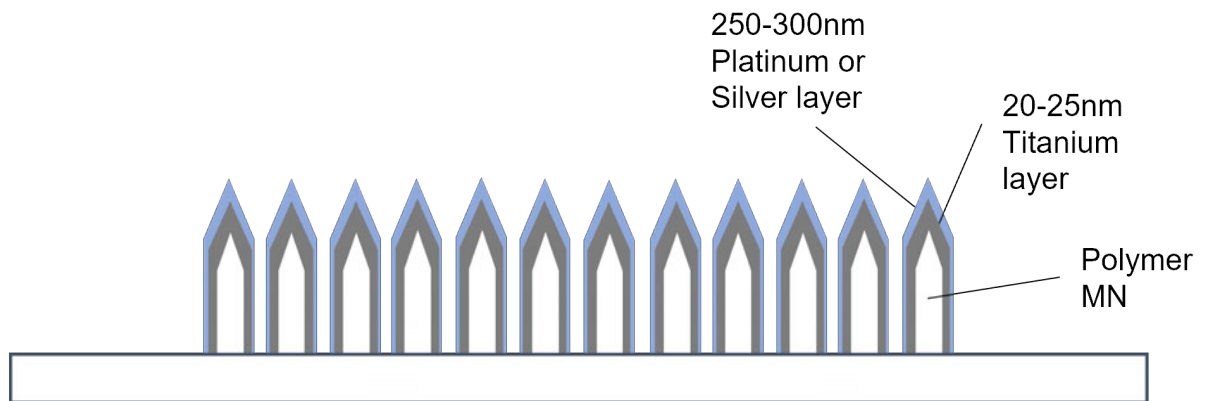
(b) Cross sectional diagram of Metallised MNs for diagnostics

Figure 4.2: Titanium and Platinum or Silver Metallised Polymer MNs and PETG substrate

(c) SEM image of Platinum coated MNs

(d) SEM image of silver metallised substrate at 100k x magnification

Figure 4.2: Titanium and Platinum or Silver Metallised polymer MNs and PETG substrate

4.1.2 Platinum MN electrochemical characterisation

To check and ensure good connection and no surface contamination, a CV scan was conducted on each platinum MN array prior to chemical functionalisation and sensing experiments. 12mg Ferrocenecarboxylic acid (FCA) (CAS 1271-42-7) purchased from Sigma Aldrich was dissolved into 10ml of PBS and used as the redox mediator for the CV measurements. The set up used a 3 electrode system with the MN array as the working electrode, a platinum wire electrode as a counter electrode (CH Instruments) and an Ag/AgCl reference electrode (CH Instruments) as the reference electrode. The scan was set between -0.4V and 0.6V with a scan rate of 0.05 V/s. The expected peaks for platinum in contact with FCA is at 0.2V for reduction and 0.3 V for oxidation in the classic CV shape for a reversible redox reaction with platinum electrodes and shows no other metals are present on the surface and all connections are good. An example is shown in Figure 4.3.
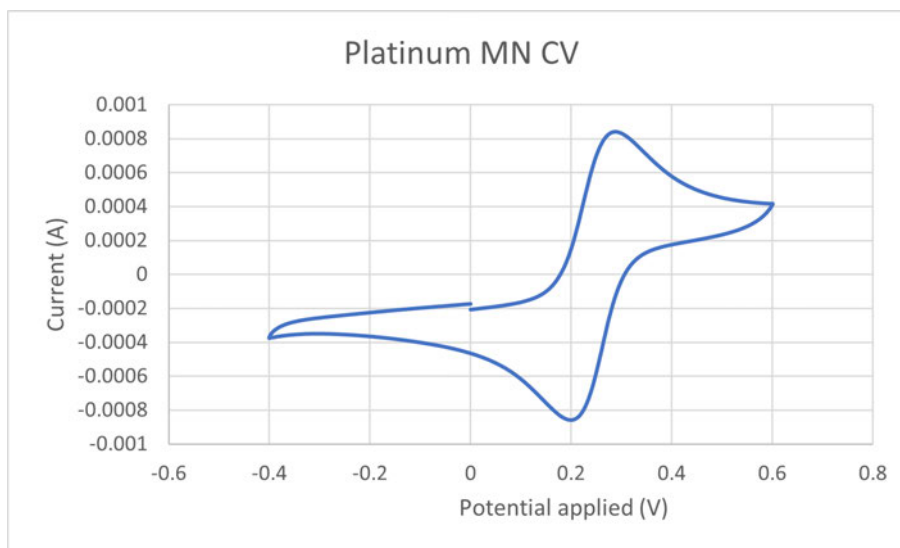
Figure 4.3: Cyclic voltammetry scan of Pt MN electrodes in contact with ferrocene carboxylic acid

4.1.3 Electro deposition

In order to improve the usability of the silver electrodes the silver layer was thickened thus making more silver available for the chloride reactions. Electro deposition was used to thicken the layer of silver on the electrodes as this is frequently used and adopted by many different industries including the electronics industries. Electro deposition

is used in industry, because this method can coat all available electrically conductive parts of a connected item, most commonly in the jewellery industry. This extra layer of silver is needed on the MNs so that there is a sufficient amount of silver on all parts of the sensor surface. The layer needs to be thicker than it is with just the PVD silver layer as the electrochemical process used in the chloride detection converts silver from the electrode surface and this can completely deplete the metal layer if there is not enough surface silver available. There are both cyanide and cyanide free methods of silver electro deposition or silver plating and there are pros and cons to both methods. The cyanide methods are generally more stable and reliable however cyanide is very toxic and can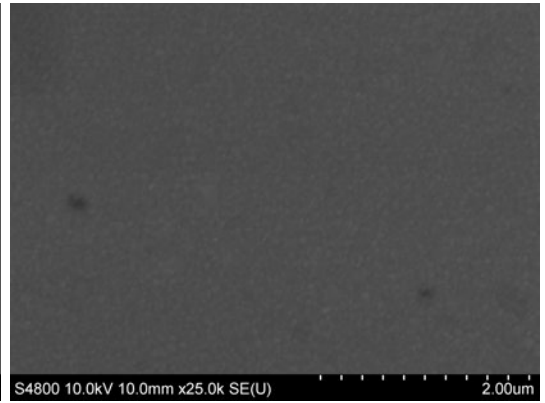 be dangerous to use. The non cyanide methods are generally less toxic however they can be less stable and sometimes more complicated [178]. Below in Figure 4.4 are the results of plating onto already PVD coated silver electrodes for 15, 30 and 45 second time intervals comparatively to a solely PVD coated electrode.
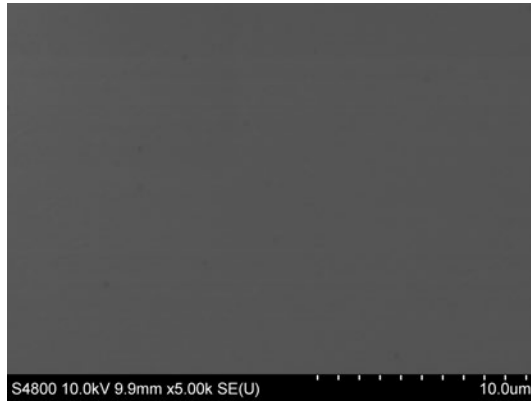
(a) PVD only silver MNs x5k

(b) PVD only silver MNs x25k
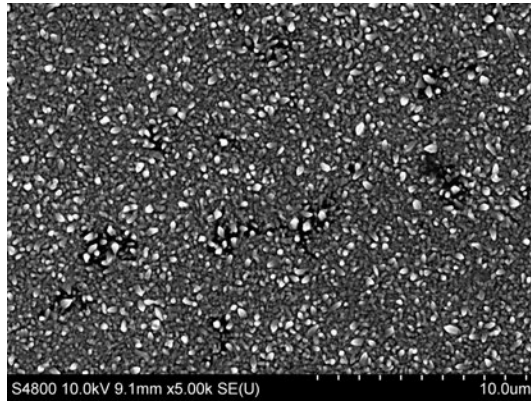
(c) Silver plated MN electrodes 15s
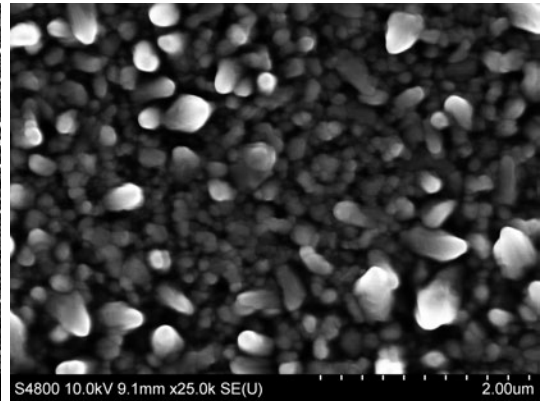
(d) Silver plated MN electrodes 15s x25k

Figure 4.4: Silver plated MN electrode arrays for 0, 15, 30 and 45s

(e) Silver plated MN electrodes 30s x5k   (f) Silver plated MN electrodes 30s x25k

(g) Silver plated MN electrodes 45s x5k   (h) Silver plated MN electrodes 45s x25k

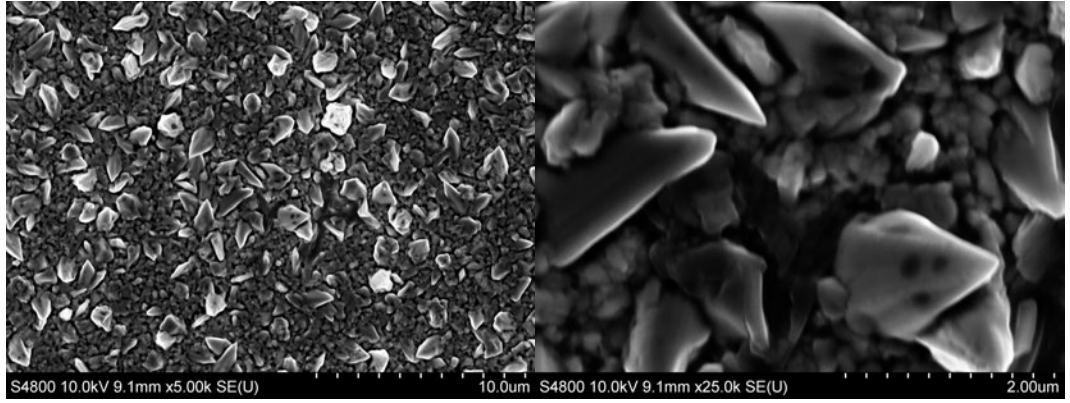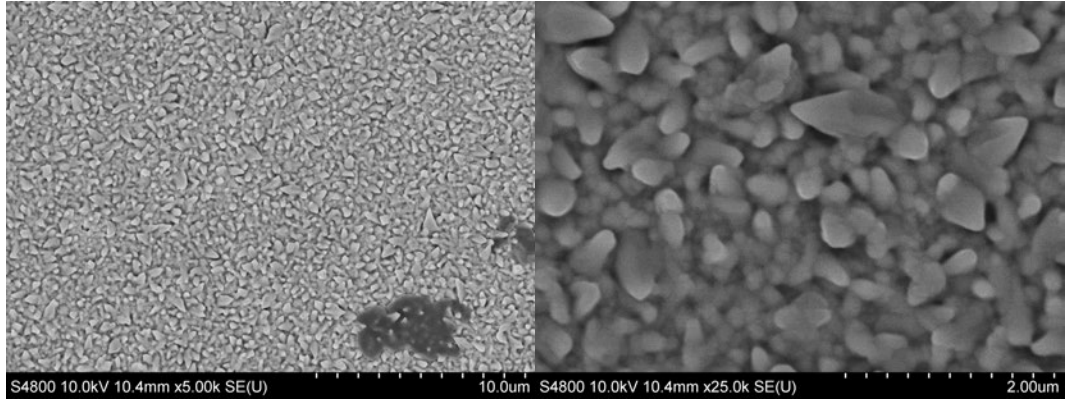Figure 4.4: Silver plated MN electrode arrays for 0, 15, 30 and 45s

Despite the texture of the MN surface, the layer covers all sides of the 3D structures as seen in Figure 4.5. The layer on the MNs plated for 45s is not as evenly distributed as the 15s and 30s and the 30s layer is the smoothest surface.

(a) SEM of 15s silver plated MNs

(b) SEM of 30s silver plated MNs

(c) SEM of 45s silver plated MNs
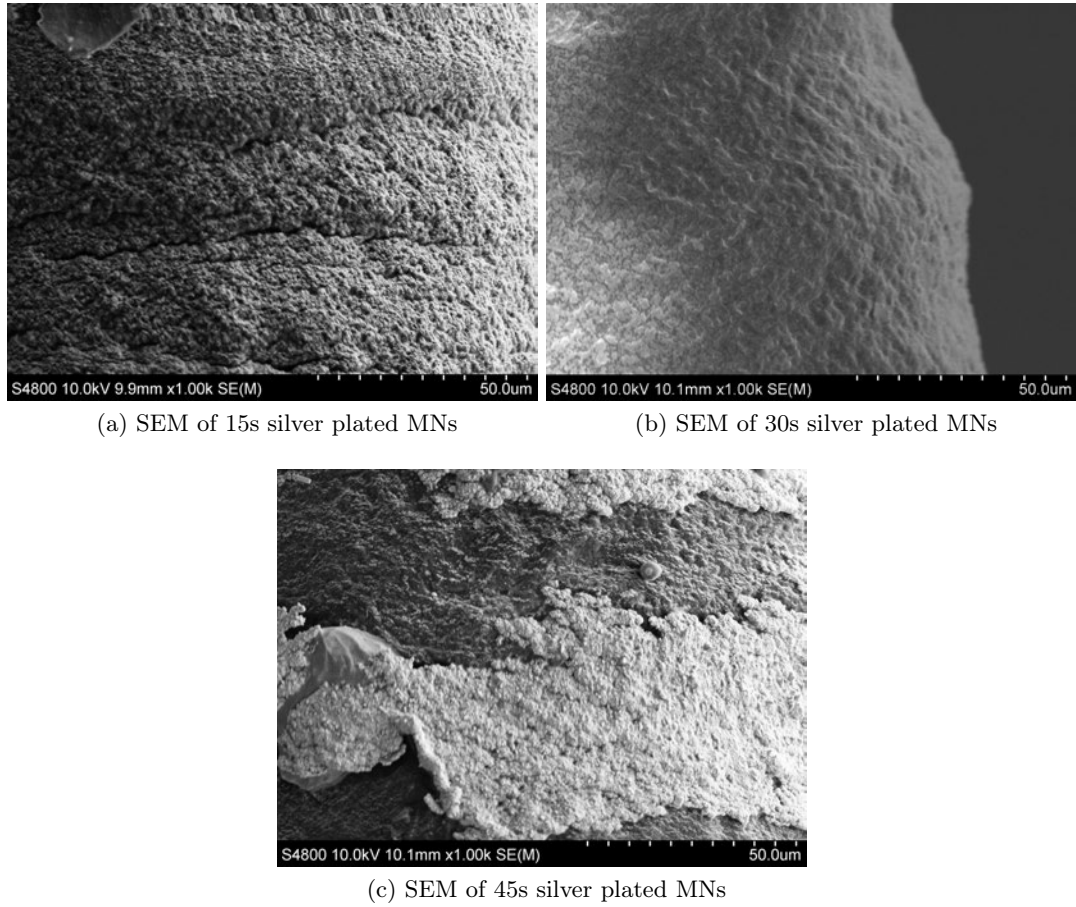
Figure 4.5: Silver plating at 15, 30 and 45s on the MN structures

As expected, the density of the layer of silver depends on the time of electro deposition. The formation of silver through this method produces a granular layer on the electrode surface. Comparatively the grains developed by the electro deposition of silver can be seen to be much larger in size than the grains produced using physical vapour deposition which makes the surface more three dimensional. This has the potential to increase surface area and then potentially improve the longevity and usability of the silver electrode due to more accessible silver. The white appearance is due to the surface being microscopically rough and hence will scatter more light. This can be avoided by adding supplement chemicals to the process of electroplating. Since the aesthetics of the electrode surface were not important for biosensing as it is with jewellery, these chemicals were not added. As the time that the voltage is applied is increased, the granules more densely cover the surface and grow in size. These differing silver layer

electrodes are used later when testing and measuring to determine the optimal silver layer before chloridisation. There are some areas of the surface where the silver appears not to have grown, this is likely due to how the silver grows in a tree like formation [179]. The trees then grow off each other and can create pockets in between each other which lead to holes. Once these holes have slightly formed there is potential for a wetting issue in which the pockets do not contact the solution from which the electro deposition takes place. Using a cyanide compound is one way to reduce the holes created by these trees. A silver cyanide silver plating solution was used when electroplating these MNs. To minimise the impact of the holes, the PVD smooth layer of silver is deposited first reduced the risk of interference from other metals in the electrochemical readings.

4.2 Chemical functionalisation

4.2.1 Phenol electro polymerisation

Electro polymerisation of monomers such as phenol can be used to form films and when incorporated with an enzyme can offer one step immobilisation of the enzyme on the electrode surface. The process uses a standard 3 electrode set up to oxidise the monomer leaving radical cations that go on to polymerise and form the new polymer layer. The process is highly controllable and can reliably control the film thickness and the loading of the enzyme. The method for detecting cholesterol required the used of an enzyme to bind to the analyte and induce the required change in voltage for measurement. Cholesterol oxidase was used due to the mechanism similarities between it and glucose oxidase which is a very widely used enzyme for glucose detection. Cholesterol oxidase has a much lower activity than glucose oxidase therefore it was pertinent to immobilise the cholesterol oxidase in the most efficient way on the surface of the MN electrodes allowing for best transport of cholesterol to the surface while blocking some other analytes with a potential to interfere with measurements.

This is achieved through the electro polymerisation of phenols on the electrode surface. Phenols can convert to polyphenol and trap and bind the cholesterol oxidase within a porous layer allowing passage of cholesterol to the cholesterol oxidase now immobilised on the surface. This immobilisation layer also prevents the enzyme being released into the body. A schematic showing the layers of a fully functionalised cholesterol MN sensor can be seen below in Figure 4.6. The amount of enzyme used was the maximum dissolvable in solution to maximise the available activity as the greater the activity, the greater the signal created by the cholesterol binding to the enzyme. Cholesterol oxidase

and phenol were used at a ratio of 2:1 in PBS solution to provide a 50mM solution for drop casting onto the MN electrode. This was the maximum dissolvable amount of enzyme. The electro polymerisation cycles were repeated 6 times with a 15 minute duration to ensure that there were no unreacted phenol left on the device and that the cholesterol oxidase was fully immobilised.
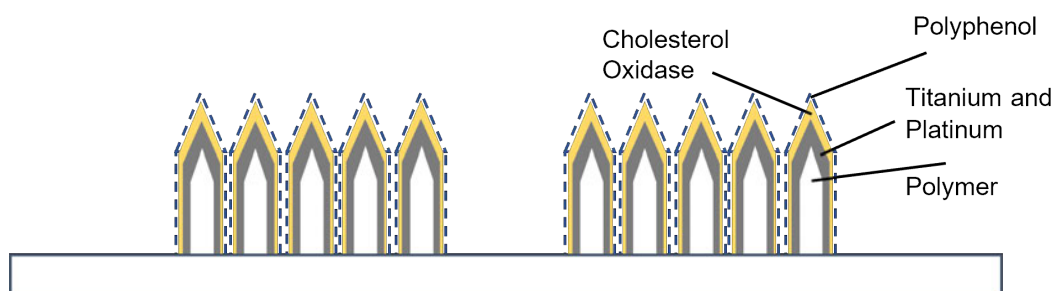
Figure 4.6: Schematic of a full functionalised MN array for cholesterol sensing

4.2.2 Electrochemical deposition

4.2.2.1 Silver chloride deposition

To act as a benchmark, results were first obtained using flat silver electrodes. The electrodes were submerged in 20ml of 100mM potassium chloride (KCl) in a beaker and a 0.5mA current was applied for 90s for the formation of silver chloride layer from the electrochemical reaction between the silver layer and the chloride ions in solution. The process of depositing chloride can be described by the systematic diagram in Figure 4.7. The silver layer is oxidised while the current is applied to the hydrated electrode which the forms AgCl from the free Cl- ions in the KCl solution.

Hydrated AgCl
layer

Pure silver

KCl solution

$Ag(s)$

$Ag^+(aq) + Cl^-(aq)$

$Cl^-(aq)$

e^-

$AgCl(s)$

$Ag^+(aq)$

$K^+(aq)$
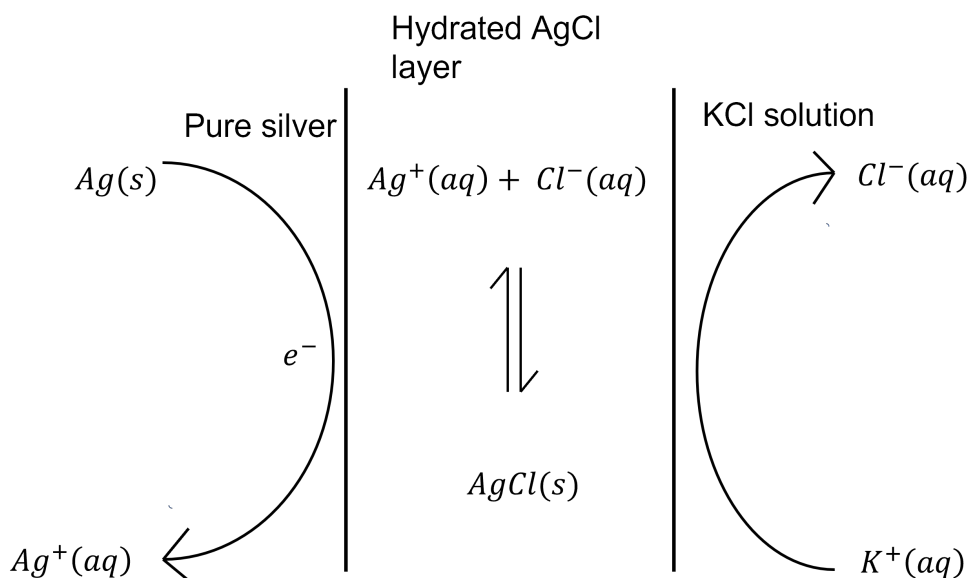
Figure 4.7: Surface reaction of coating the AgCl

Different coating times were used to coat the MNs without stripping the layer of silver from the device whilst giving enough silver chloride that the electrode had enough thickness for the chloride transfer that occurs during the readings. A lower current was used for the MNs in comparison to the planar electrodes to account for the thinner layer of silver. AgCl coating times of 30s, 45s, and 60s were performed on the PVD silver electrodes and the devices visually inspected. As is seen in Figure 4.8 the longer the coating time, the more opaque the colour of the electrodes became. The electrode coated for 30 seconds in Figure 4.8a has a cloudy dull appearance on the silver surface where chloride has been deposited. The electrode coated for 45 seconds in Figure 4.8b has a darker appearance where the chloride has been deposited, this colour change may indicate that silver oxide has also been formed. The electrode coated for 60 seconds in Figure 4.8c has a similar colour to the previous electrode but also has some areas where the layer has been depleted and damaged.
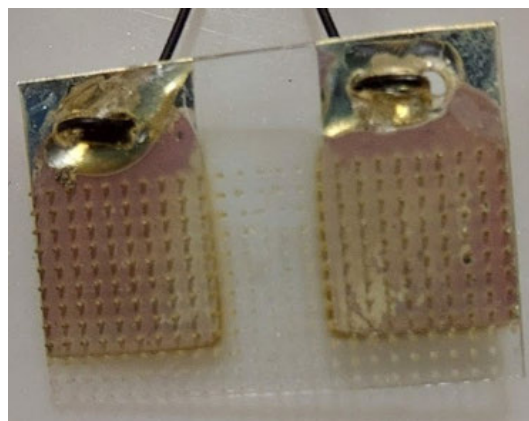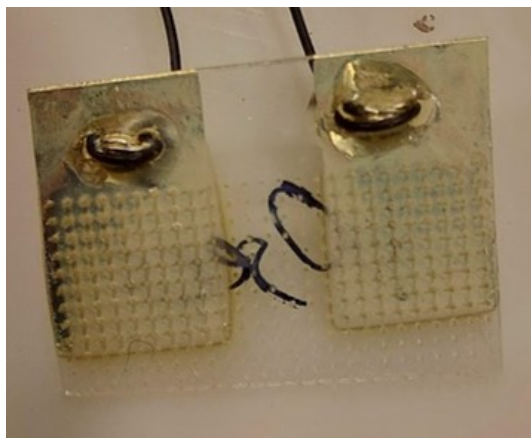
(a) Ag/AgCl electrode coated for 30s at 0.5mA   (b) Ag/AgCl electrode coated for 45s at 0.5mA
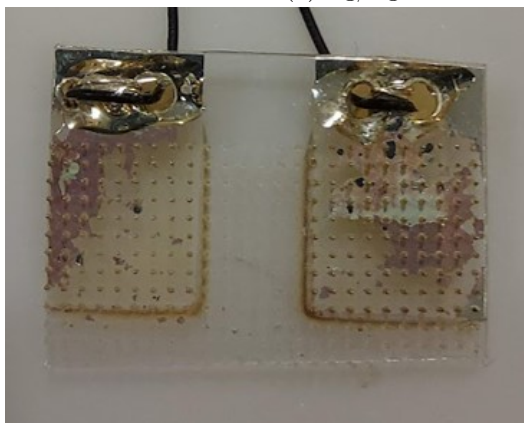
(c) Ag/AgCl electrode coated for 60s at 0.5mA (
layer degraded)

Figure 4.8: AgCl deposition on silver electrodes at different time periods

SEM images were taken after applying the current for different time periods to show how much silver chloride grain coverage there was. The results are shown in Figures 4.9, 4.10 and 4.11.
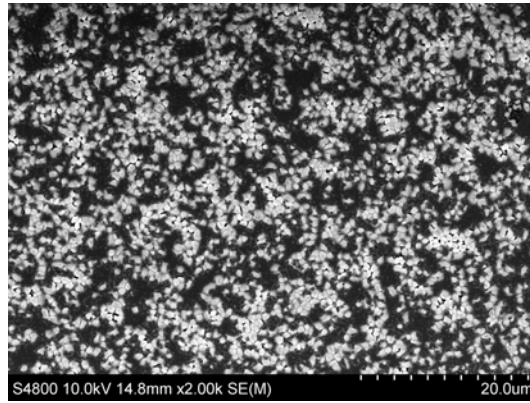
Figure 4.9: SEM image of 30s AgCl coating

After applying 0.5mA for 30s the resulting AgCl grain coverage was 36.4%.

(a) 45s 1

(b) 45s 2
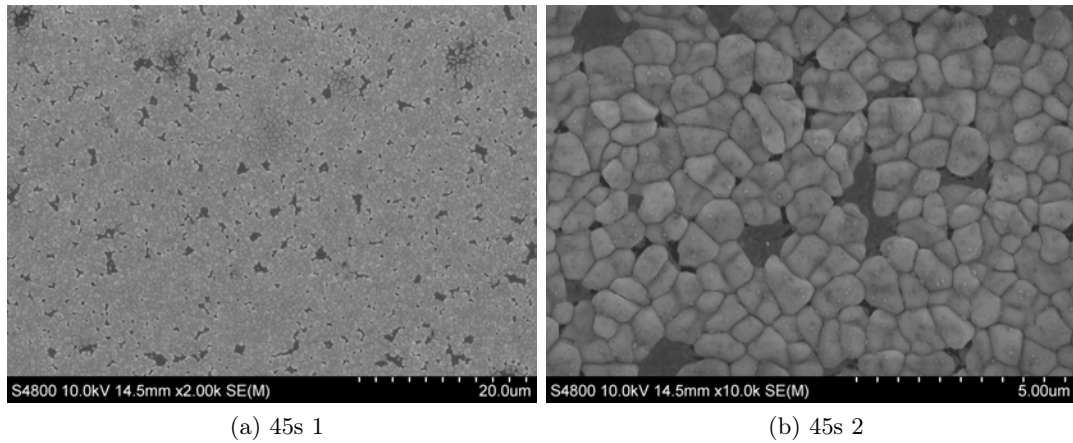
Figure 4.10: SEM image of 45s AgCl coating

After applying 0.5mA for 45s the resulting AgCl grain coverage was 88.3%.

(a) 60s 1   (b) 60s 2
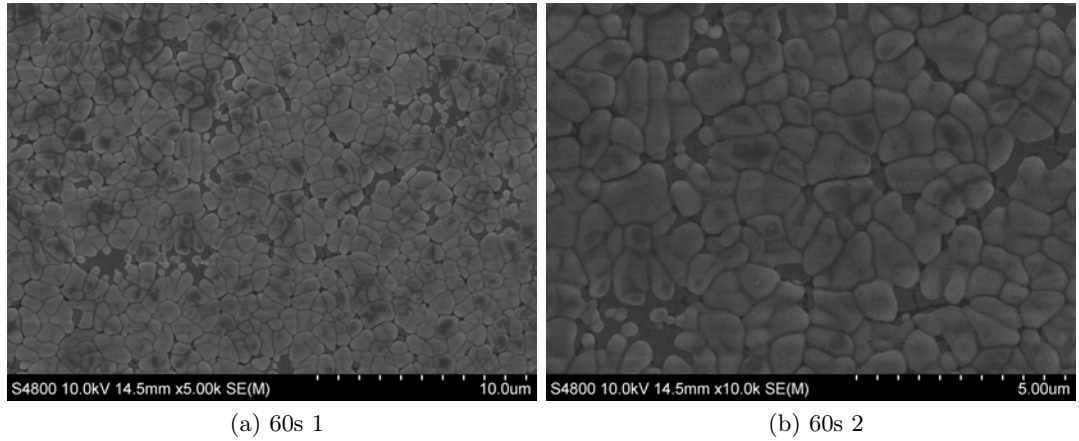
Figure 4.11: SEM image of 60s AgCl coating

After applying 0.5mA for 60s the resulting AgCl grain coverage was 91.1% in non damaged areas.

Devices that were used for the determination of chloride that had not had an electroplated silver layer on top of the PVD coating, had cracks across the coating layer as seen in Figure 4.12.
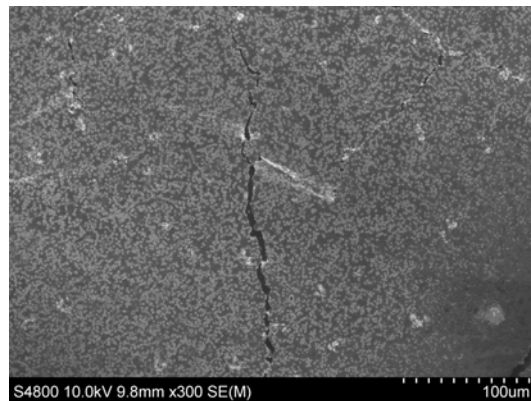
Figure 4.12: SEM of AgCl electrode cracks after use

Devices with an extra silver plated layer had no cracking and only extra AgCl on the surface after being used for the chloride determination.
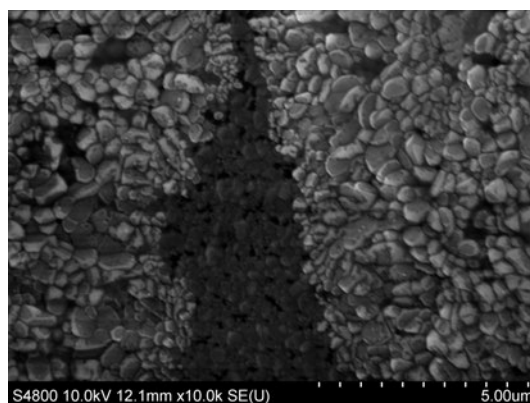
Figure 4.13: SEM of AgCl electrode after use for measurement.

These results show that the device electrodes that had thicker coatings of silver from silver plating were much more stable due to the even layer and lack of cracking. These devices were more useable and reliable than thinner only PVD coated devices and had much less risk of silver depletion when adding the chloride layer. Utilising MNs with an electro plated silver layer in chloride determination experiments reduces the chance of complete depletion of silver and therefore a resulting high voltage response that can damage the surface and prevent readings to determine the concentrations of chloride.

5 Microneedle Penetration and Mechanical Characterisation

Microneedle geometry has been previously optimised to a point using a visual technique as shown in Chapter 3. These MNs have also been metallised as shown in Chapter 4 using both platinum and silver. The following chapter investigates the penetration efficacy and mechanically characterises the MNs made with the previous geometry. The investigation here aims to optimise the MNs further using penetration and mechanical testing.

5.1 Penetration studies

5.1.1 Dye staining

Basic characterisation can be achieved using different types of dyes such as Methylene blue [180] and Trypan blue [29]. These dyes are utilised to visualise successful MN penetration into skin due to their ability to selectively stain only living (viable) cells. Viable cells are located beneath the *stratum corneum* (SC) skin barrier layer within the epidermis and so any microchannels created by breaking through the SC are able to be identified.

   Control experiments were conducted to demonstrate positive and negative staining. Figure 5.1a shows positive staining in visibly broken skin using a scalpel, which after cleaning with alcohol wipes shows deep blue staining in the broken parts of skin. Figure 5.1c illustrates that without damage the porcine skin does not show a deep blue staining. In Figure 5.1b the indentations of a MN patch are evident, this does not mean that the SC is broken and the dye staining is used to confirm skin penetration.
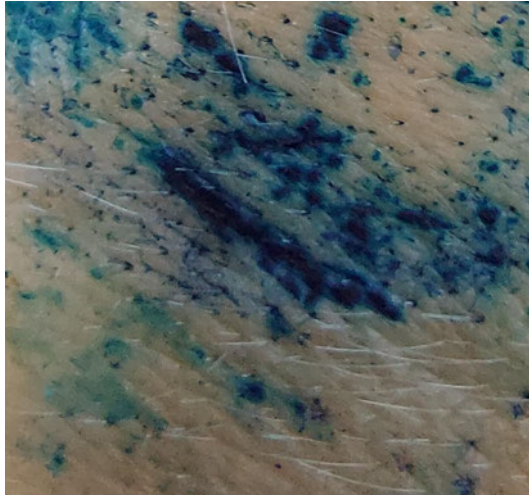
(a) Methylene blue staining of visible skin tear by scalpel

(b) Porcine skin with MN applied and no Methylene blue staining
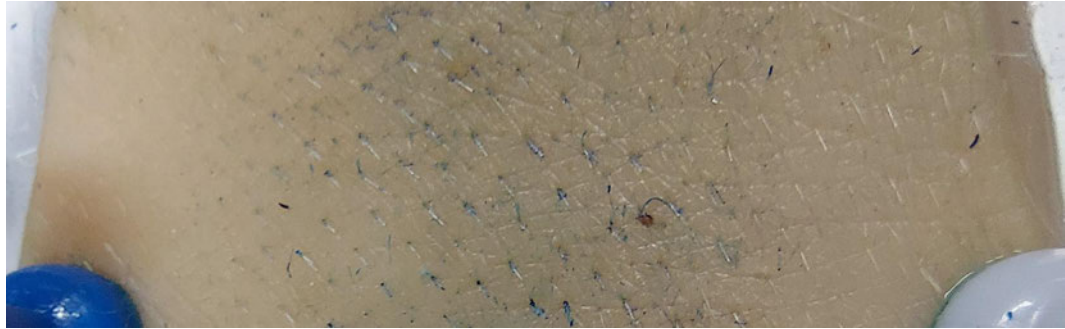
(c) Methylene staining of porcine skin with no MN or scalpel

Figure 5.1: Positive and Negative Staining controls for methylene blue staining

MNs with 1cm^2 base produced with 400μm apertures were selected based on visual geometry from Chapter 3 investigations and mythelene blue staining tests comparing both 400μm and 500μm aperture MNs applied on porcine skin using a lever and scales to apply the same pressure of 10N per cm^{2}each time. This is approximately equivalent to thumb pressure [105]. To further prove and optimised the MN geometries the penetration at the different stages of this optimisation was tested. The protocols used were the change of settings for each layer printed when fabricating these MNs. The process was iterative and the protocol adjusted depending on the penetration efficacy. The MN penetration efficiency was calculated using the number of methylene blue dots as a proportion of total number of MNs. To calculate this penetration efficiency as a percentage Equation 5.1 was used where MB is the number of methylene blue dots

produced and T is the total number of MNs.

$$\% = \frac{MB}{T}x100 \tag{5.1}$$

The microneedle arrays consisted of 8x8 (64) MNs around 700μm in height on a substrate 1cm² substrate base . To examine the effect of tipped MNs both base versions and tipped versions of the MN arrays were tested. The resulting penetration efficiency was calculated using the methylene blue results with the percentages and reference to Figures shown in Table 5.1.

Table 5.1: Penetration percentage for tipped and untipped 400 and 500μm aperture MNs

MNs	400μm base	400μm base and 150μm tip	500μm base	500μm base and 150μm tip
Penetration %	39.1	73.4	26.5	40.5
Image Figure	5.4a	5.4c	5.3a	5.3c

Repetitions saw that results for untipped 400μm aperture MNs and both tipped and untipped 500μm aperture MNs averaged at under 30% penetration efficiency. Another observation made is that the methylene blue dots made using these MNs were not as strong and clear as the ones for the tipped 400μm aperture MNs. Repetitions of 400μm aperture MNs applied on porcine skin gave penetration efficacies of up to 84%. A schematic of the tipped MN patches can be seen in Figure 5.2 and the protocols for 400μm and 500 μm aperture MN bases as seen in Table 5.2.
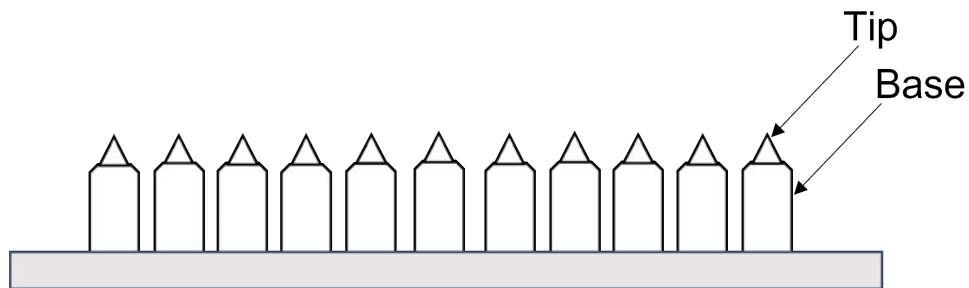
Figure 5.2: A schematic depicting the composition of the tipped MN arrays

Pass No.	Print Gap (µm)	Pressure (kg)
1	0	1
2	0	1
3	0	1
4	0	1
5	400	1
6	600	1
7	800	1
8	1000	1
9	1200	1

(a) Tapered MN 400µm base

Pass No.	Print Gap (um)	Pressure (kg)
1	0	1
2	0	1
3	0	1
4	0	1
5	500	1
6	700	1
7	900	1

(b) Tapered MN 500µm base

Table 5.2: Tapered MN 400µm and 500µm base protocols

The mythelene staining in Figures 5.3 and 5.4 below shows that the MNs made using 400µm apertures and with tips show staining with mythelene blue over most of the array compared to the MNs made using 500µm apertures and or being untipped show less staining over the applied array area.
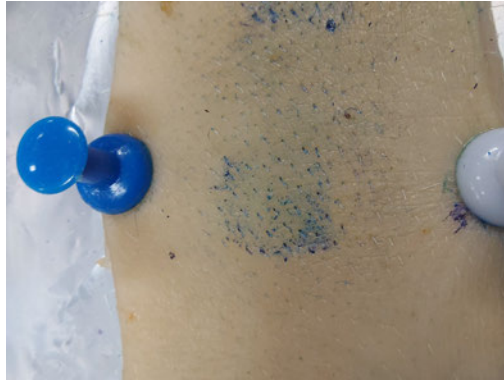
(a) 500μm aperture base MNs penetration
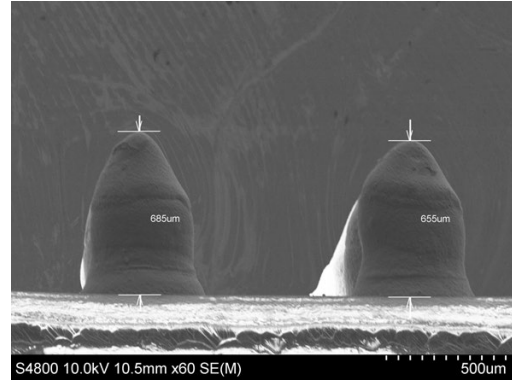
(b) SEM of Tapered MN 500μm
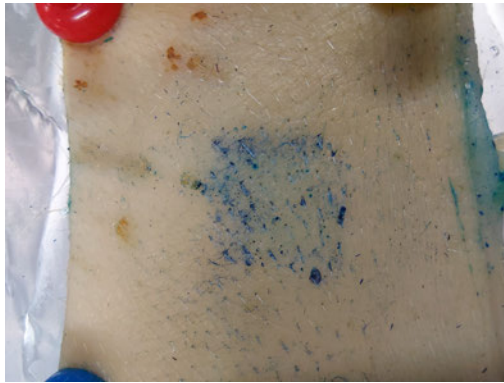
(c) 500μm aperture MN tipped
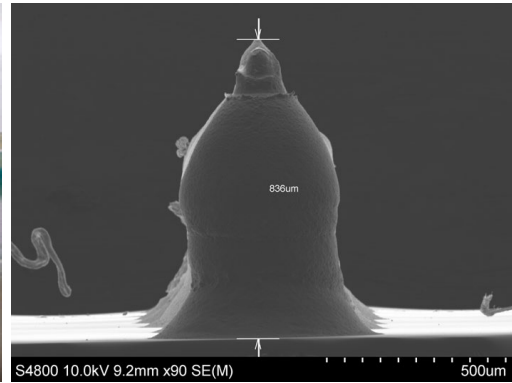
(d) SEM of 500μm tipped MNs

Figure 5.3: Tipped and untipped 500μm aperture MN comparison of penetration using methylene blue staining
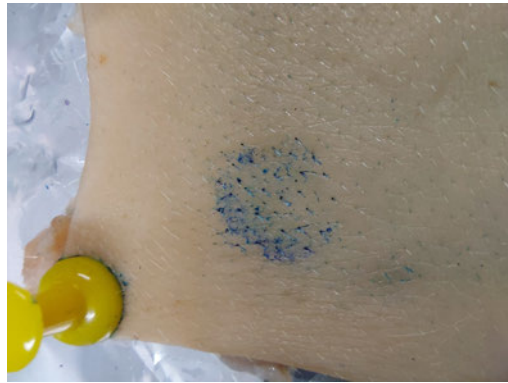
(a) 400μm aperture base MNs
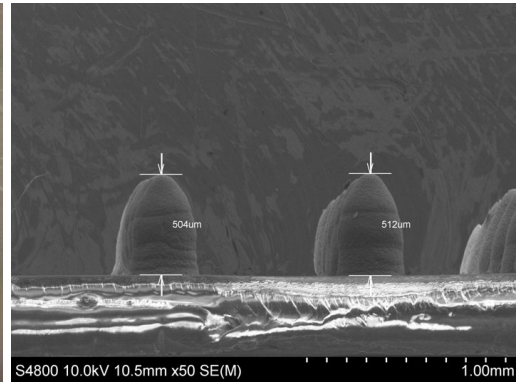
(b) MN 400μm tapered
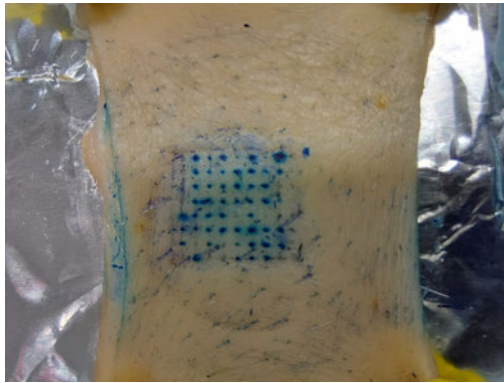
(c) Successful 400μm MN penetration Methylene blue staining
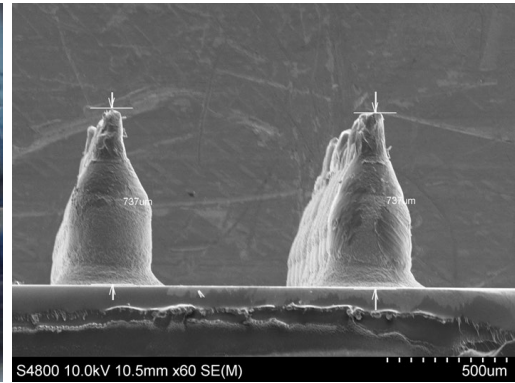
(d) 400μm tipped MNs

Figure 5.4: Tipped and untipped 400μm aperture MN comparison of penetration using methylene blue staining

When building the MNs each protocol as seen in Tables 5.3 and 5.4 was tested for the skin penetration efficiency.

	Protocol 1		
	Pass No.	Print Gap (um)	Pressure (kg)
Base	1	0	1
	2	0	1
	3	0	1
	4	0	1
	5	500	1
	6	700	1
	7	900	1
Tip	8	1000	2
	9	1000	2

(a) Protocol 1 MNs using 400µm aperture base stencil and 150µm aperture tipping stencil

	Protocol 2		
	Pass No.	Print Gap (um)	Pressure (kg)
Base	1	0	1
	2	0	1
	3	0	1
	4	0	1
	5	600	1
	6	600	1
	7	900	1
Tip	8	1000	2
	9	1000	2

(b) Protocol 2 MNs using 400µm aperture base stencil and 150µm aperture tipping stencil

	Protocol 3		
	Pass No.	Print Gap (um)	Pressure (kg)
Base	1	0	1
	2	0	1
	3	0	1
	4	0	1
	5	500	1
	6	900	1
Tip	7	1000	2
	8	1000	2

(c) Protocol 3 MNs using 400µm aperture base stencil and 150µm aperture tipping stencil

Table 5.3: Protocol 1-3 full MNs base and tip combined

		Protocol 4		
	Pass No.	Print Gap (um)	Pressure (kg)	
Base	1	0	1
	2	0	1
	3	0	1
	4	0	1
	5	600	1
	6	700	1
	7	1000	1
Tip	8	1000	2
	9	1000	2

(a) Protocol 4 MNs using 400μm aperture base stencil and 150μm aperture tipping stencil

		Protocol 5		
	Pass No.	Print Gap (um)	Pressure (kg)	
Base	1	0	1
	2	0	1
	3	0	1
	4	0	1
	5	600	1
	6	800	1
Tip	7	1000	2
	8	1000	2

(b) Protocol 5 MNs using 400μm aperture base stencil and 150μm aperture tipping stencil

		Protocol 6		
	Pass No.	Print Gap (um)	Pressure (kg)	
Base	1	0	1
	2	0	1
	3	0	1
	4	0	1
	5	600	1
	6	900	1
Tip	7	1000	2
	8	1000	2

(c) Protocol 6 MNs using 400μm aperture base stencil and 150μm aperture tipping stencil

Table 5.4: Protocols 4-6 full MNs

It was found in the majority of cases the base was too wide and so the MN bulged and

that the joins between the base stencil portion layers and the tipping stencil portion layers were not seamless enough resulting in poor penetration as seen in Figure 5.5.

(a) Protocol 1 penetration

(b) SEM Protocol 1 MNs

(c) Protocol 2 penetration

(d) SEM of Protocol 2 MNs

(e) Protocol 3 penetration

(f) SEM of Protocol 3 MNs

Figure 5.5: Penetration results of MN protocols 1-3 using methylene blue staining

(a) Protocol 4 penetration
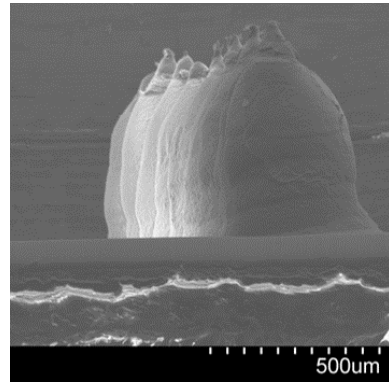
(b) SEM Protocol 4 MNs
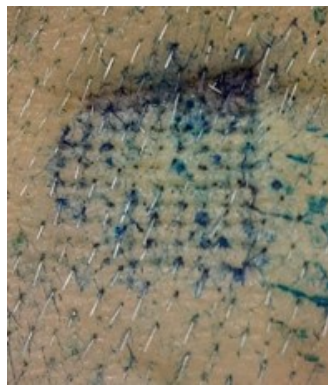
(c) Protocol 5 penetration
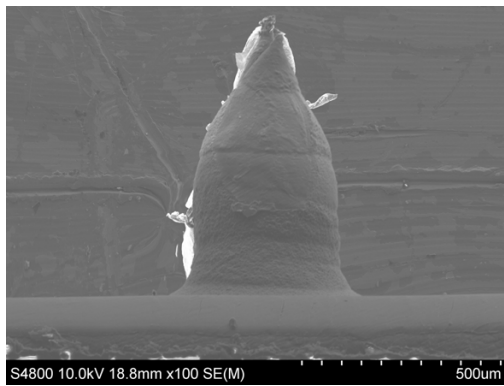
(d) SEM of Protocol 5 MNs
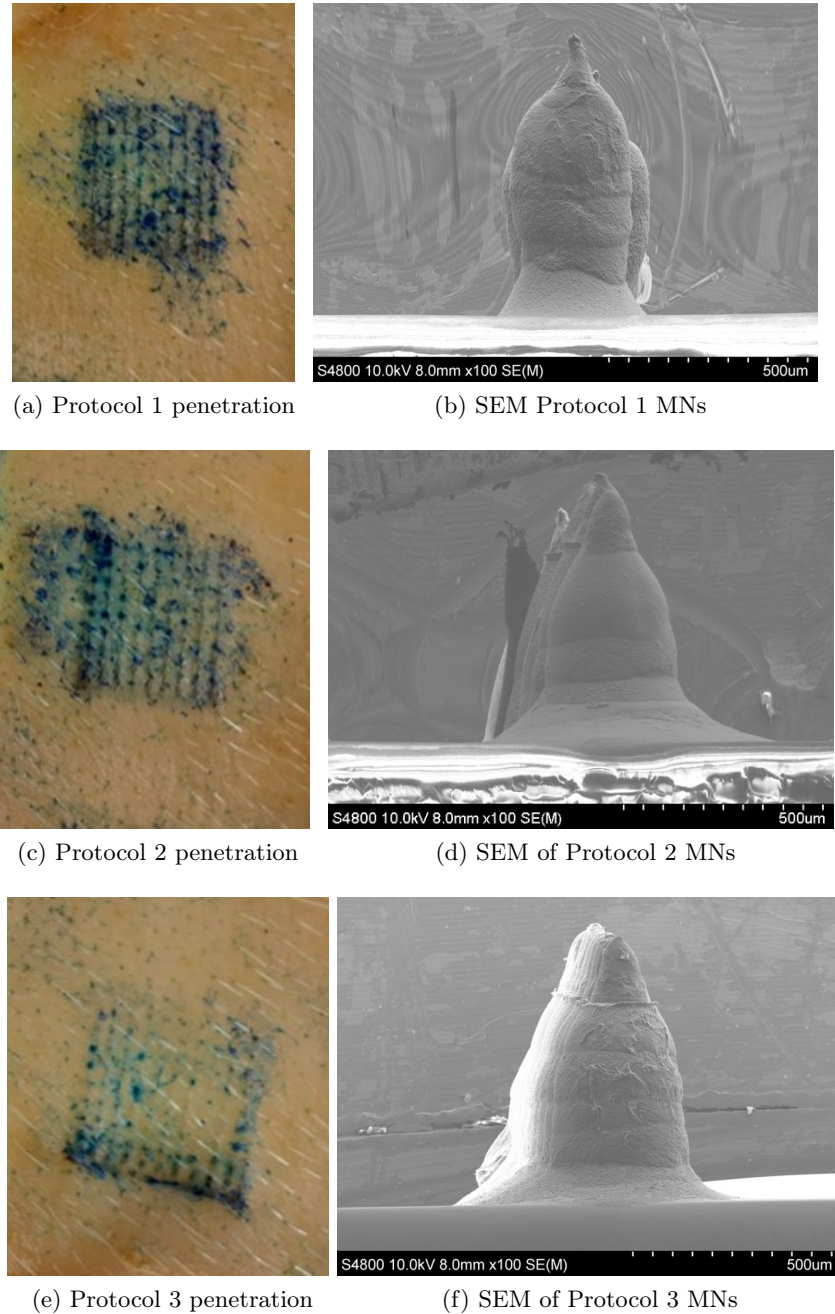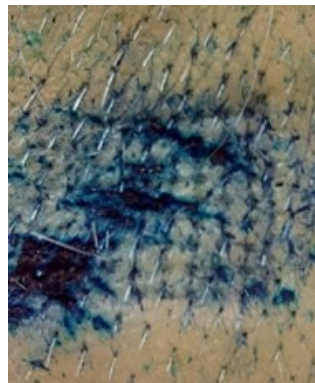

(e) Protocol 6 penetration
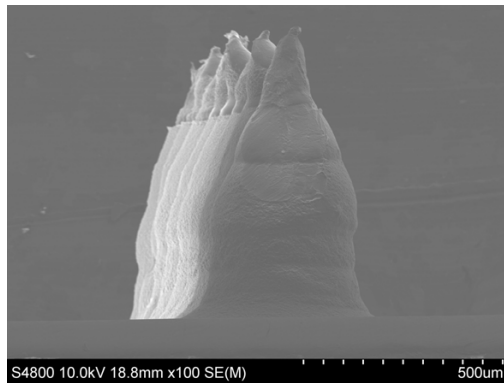
(f) SEM of Protocol 6 MNs

Figure 5.6: Penetration results of MN protocols 4-6 using mythelene blue staining

The protocols as seen in Tables 5.3 and 5.4 were then adjusted to make sharper tips and less bulging therefore better penetration. Table 5.5 shows the new protocols 7 and 8. The results of protocol 7 and 8 can be seen in Figure 5.7 where despite both

MNs having a sharp tip and being a similar height, the difference in width impacted the penetration for protocol 7. Protocol 7 resulted in MNs around 100μm wider than protocol 8. This ratio difference impacted the penetration significantly. Protocol 8 showed the best penetration as it appears 49/64 MNs have penetrated making the percentage 76.5%. As can be seen in Figure 5.7

		Protocol 7		
	Pass No.	Print Gap (um)	Pressure (kg)
Base	1	0	1
	2	0	1
	3	0	1
	4	0	1
	5	600	1
	6	600	1
	7	900	1
Tip	8	1000	2
	9	1100	2

(a) Protocol 7 MNs

		Protocol 8		
	Pass No.	Print Gap (um)	Pressure (kg)
Base	1	0	1
	2	0	1
	3	0	1
	4	0	1
	5	600	1
	6	600	1
	7	900	1
Tip	8	1000	2
	9	1200	2

(b) Protocol 8 MNs

Table 5.5: Protocols 7 and 8 full MNs using 400μm aperture base stencil and 150μm aperture tipping stencil
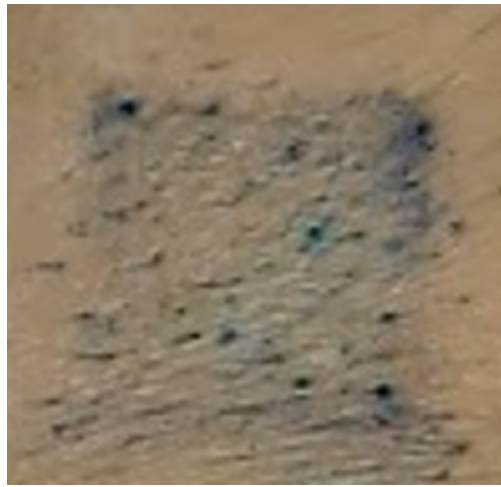
(a) Protocol 7 penetration
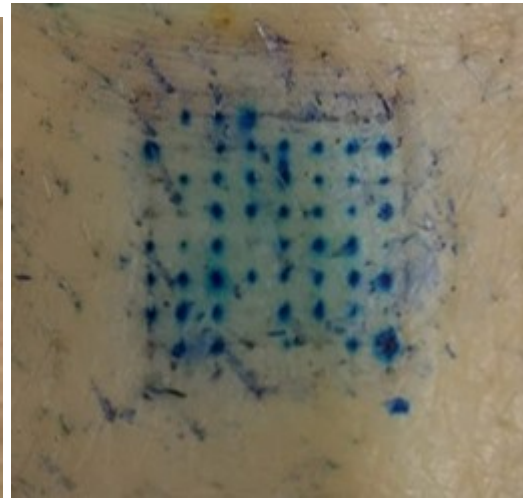
(b) Protocol 8 penetration
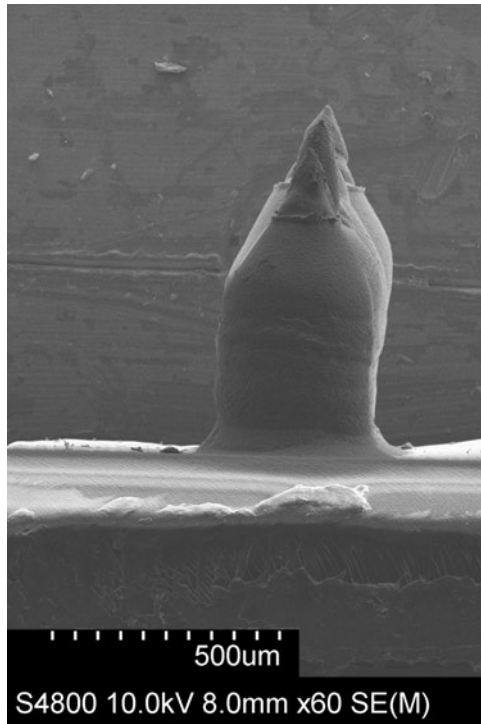
(c) SEM of MN using Protocol 7
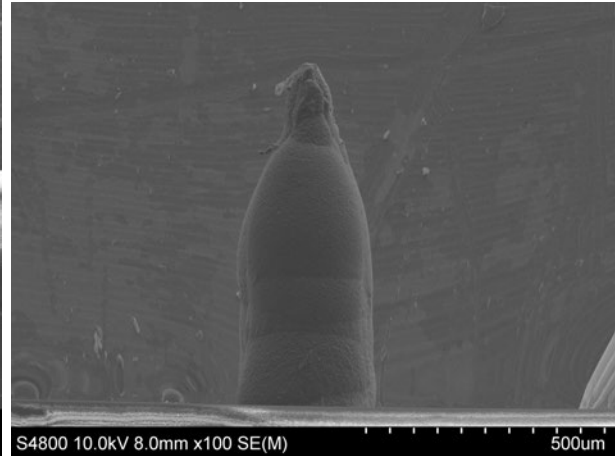
(d) SEM of MN using Protocol 8

Figure 5.7: Protocol 7 and 8 penetration results using methylene blue staining

Protocol 8 was then used with different stencils changing the pitch to demonstrate the most optimal pitch diameter for penetration. Four other pitches were investigated

including the 1100µm pitch diameter used previously with protocol 8.

Pitch was compared using these penetration tests as well. These patches had MNs of around 700µm in height and had the same area of 1cm^2 therefore the number of MNs per cm changed with the pitch. There is an optimisation between the number of MNs in an array of a certain measurement and ensuring minimisation of the 'bed of nails' effect, giving greater pressure on the MN as the force in spread over a smaller area. More MNs in the same area reduces the force on each MN so that penetrations decreased. The following images in Figure 5.8 show increase in penetration on increasing pitch. This is most likely due a lessening 'bed of nails' effect as the pitch increases.
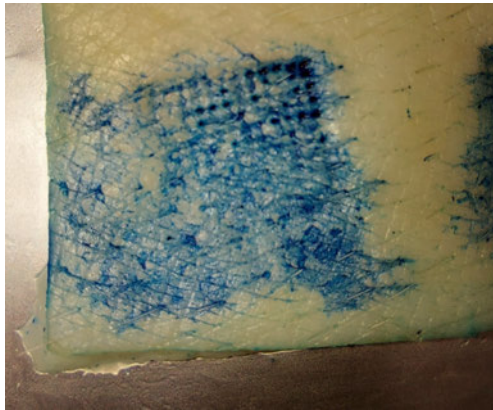
(a) 800µm pitch MN
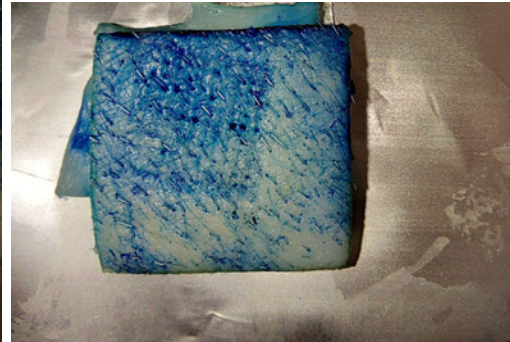
(b) 900µm pitch MN
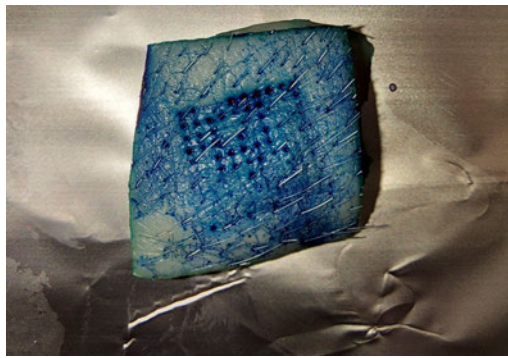
(c) 1000µm pitch MN
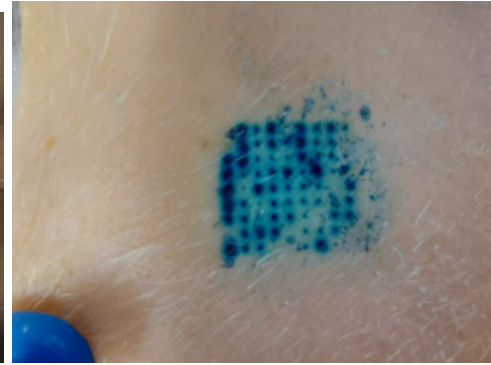
(d) 1100µm pitch MNs

Figure 5.8: MN penetration efficiency comparison by differing pitch using mythelene blue staining

Repetitions of Protocol 8 were made at the optimal pitch to assess the reproducibility of The MN arrays. As can be seen in Figure 5.9 there is high percentage efficiency of on average however the penetration varies slightly for each MN array.
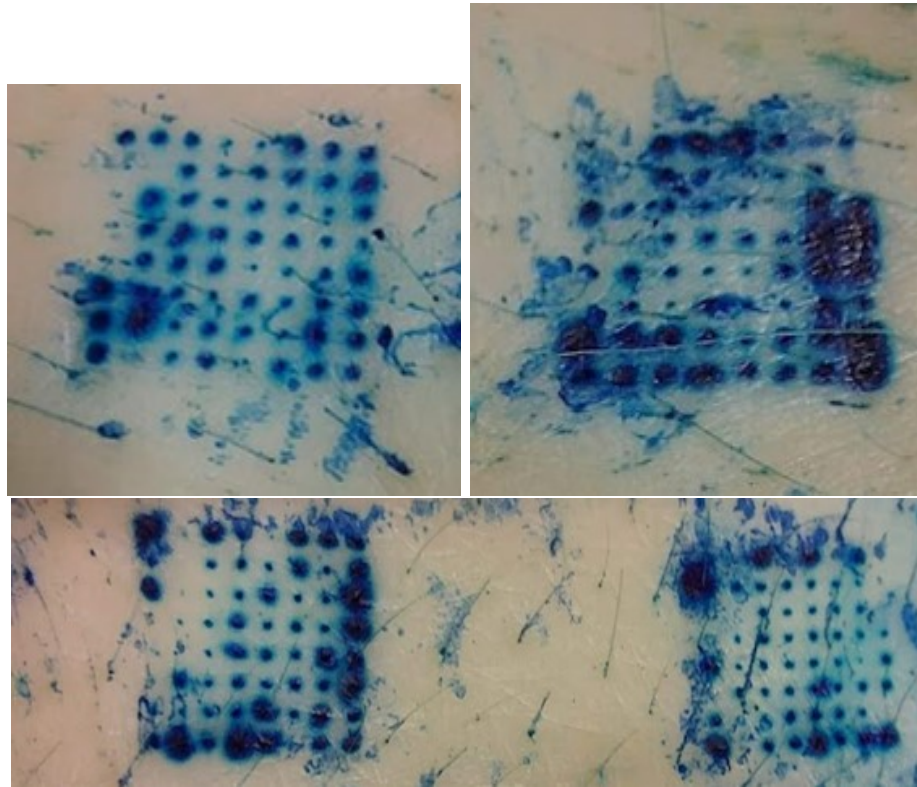
Figure 5.9: Repetitions of the methylene blue staining penetration tests of MN arrays fabricated using Protocol 8

As another comparison some 1x5 and 1x4 silicon MNs arrays were tested. These were solid silicon MNs jointly developed by Swansea University and SPTS technologies, fabricated using a novel deep silicon etching process of which the details are outlined by C. Bolton and O.Howells et al [181]. This paper outlines the process to fabricate hollow MNs however solid MNs were made using a process similar to this but eliminating steps d-f. These MNs were 700μm in height and much sharper than the polymer MNs. They had a 100% penetration efficiency and it is attributed to the smaller array size giving less bed of nails effect and that silicon etched MN have a much sharper tip than the polymer printed MNs. Seen in Figure 5.10.
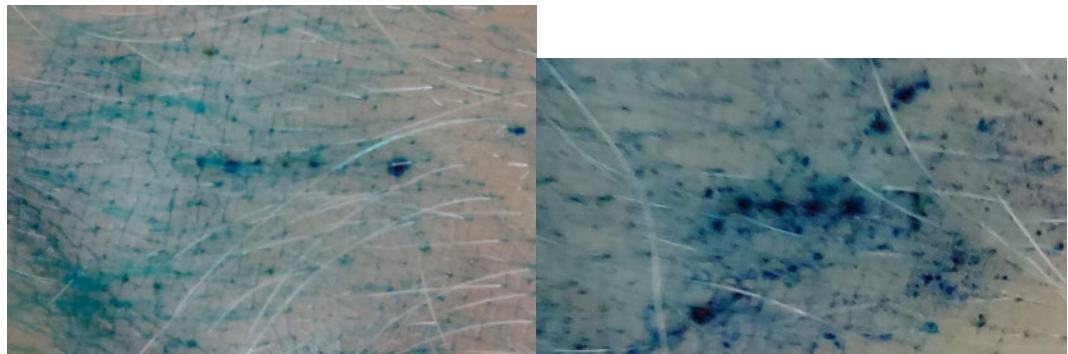
(a) Silicon 1x5 array penetration stained with methylene blue

(b) Silicon 1x4 array penetration stained with methylene blue
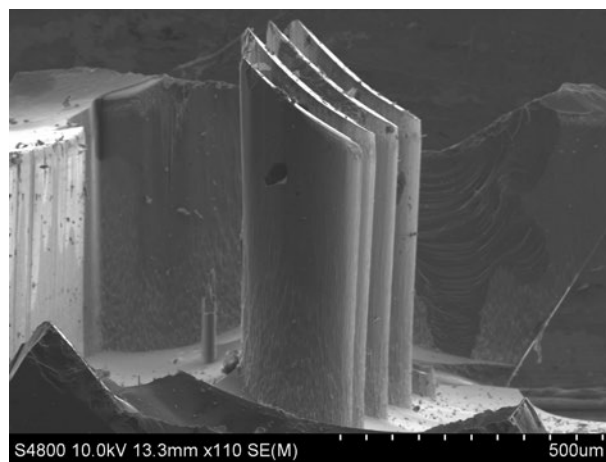
(c) SEM of silicon MNs x110

Figure 5.10: Silicon MN penetration results using methylene blue staining

In summary these results show that the optimal design for skin penetration for these polymer screen printed MNs used a 400μm aperture with a pitch of 1100μm. Protocol 8 as laid out in Table 5.5 yielded MNs with on average the highest penetration efficiency of 82.42% therefore these MNs offered penetration that would allow access to interstitial fluid for diagnostic of drug delivery purposes.

5.1.2 Histology

Histology was used to examine the cross section of the result of MN arrays applied to porcine skin for the different MN protocol designs. The protocols that didn't show up as successful penetration using methyl blue testing were also investigated using histological cross section imaging. The following images below demonstrate that while the MNs are making an indent they are not actually breaking the *stratum corneum* to access the ISF

111

on most cases. The *stratum corneum* can be seen as the dark dyed layer at the top of the skin. These images explain why when a MN array is applied it is not always the case that penetration has occurred even though an imprint is left. Comparatively an intact piece of skin has no obvious indents but there can be deviations from a straight horizontal *stratum corneum* due to hair follicles as seen in Figure 5.11.
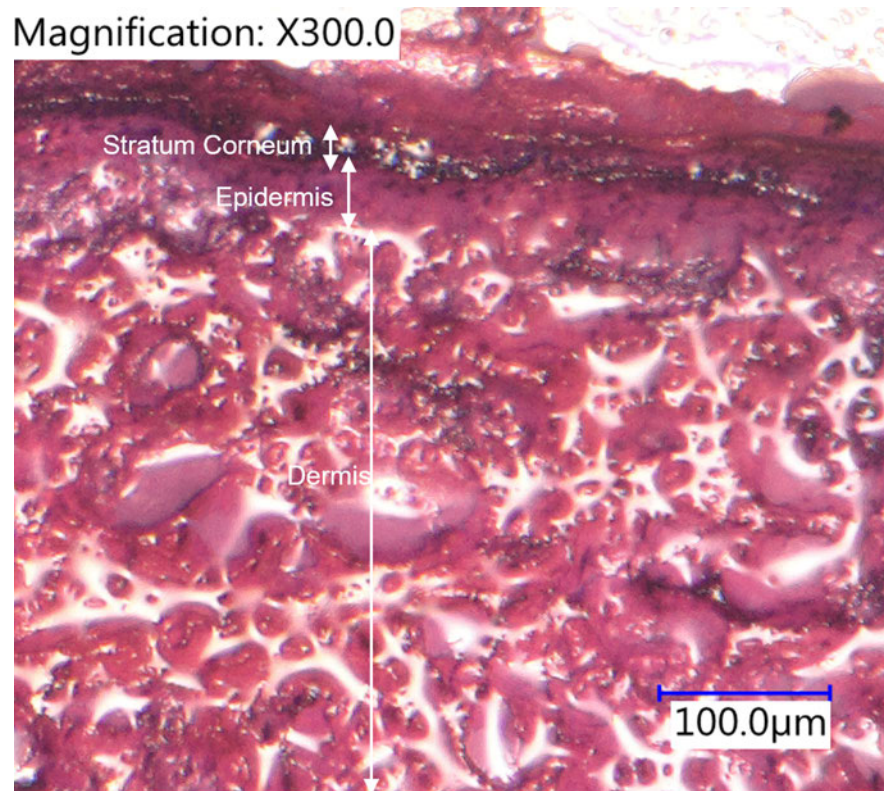
Figure 5.11: Intact Pig skin cross section labelled with skin layers
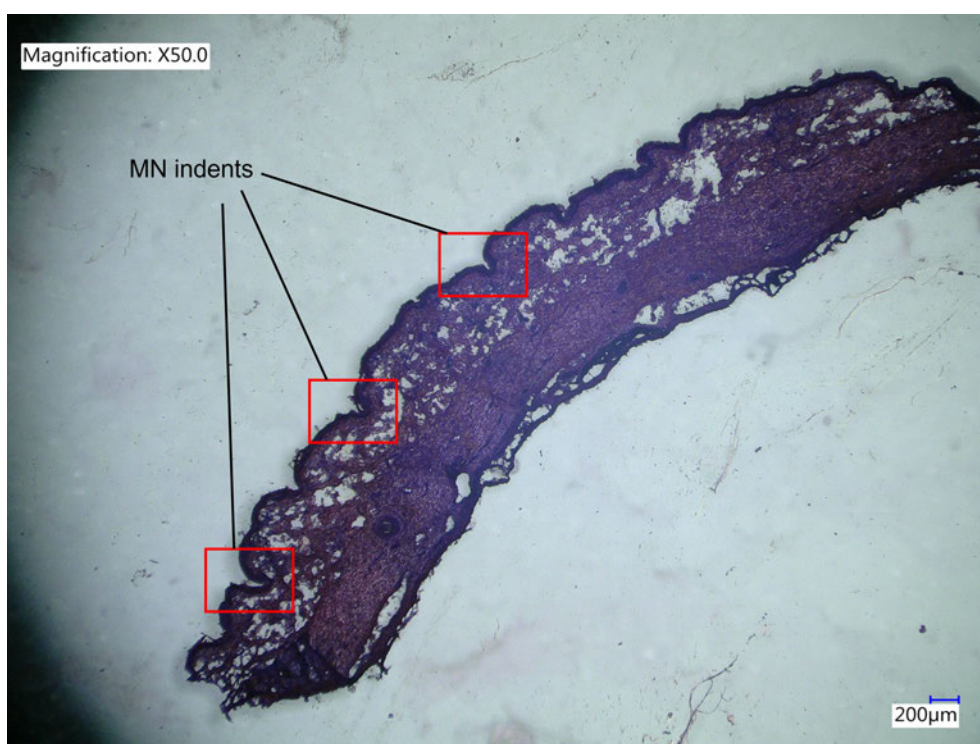
(a) Protocol 1 MN application cross section
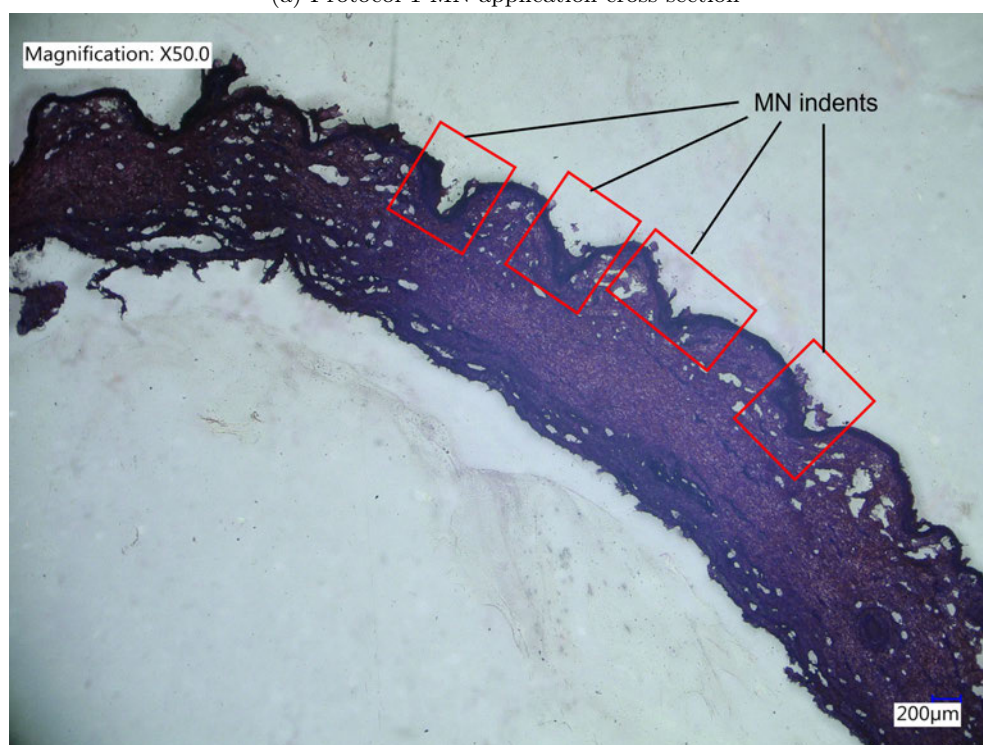
(b) Protocol 2 MN application cross section

Figure 5.12: Cross section of MNs fabricated with Protocols 1 and 2 application on Porcine skin with some indentations highlighted
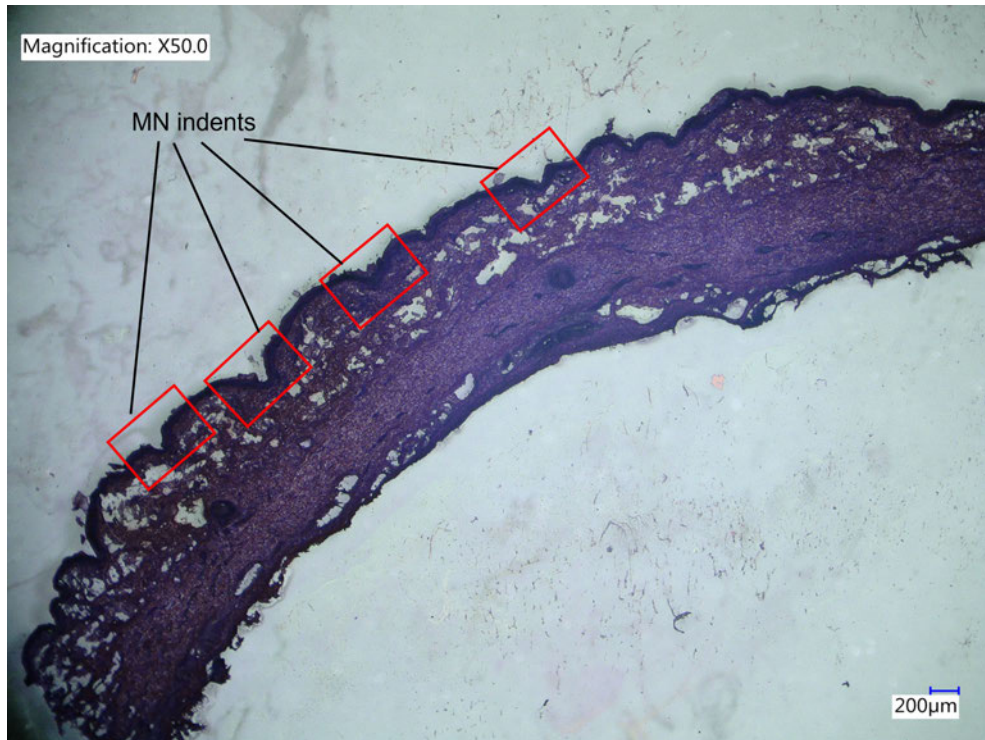
(a) Protocol 3 MN application cross section
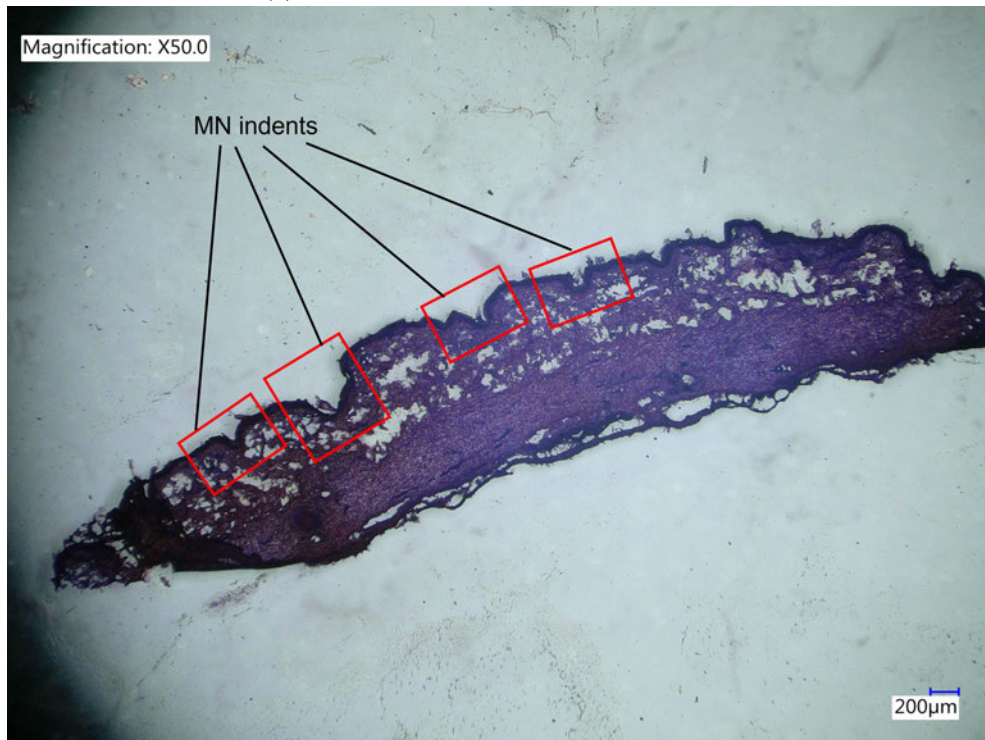
(b) Protocol 4 MN application cross section

Figure 5.13: Cross section of MNs fabricated with Protocols 3 and 4 application on Porcine skin with some indentations highlighted

These images of the results of MNs from protocols 1-4 Figures 5.12 and 5.13 illustrate that indentation can occur without breaking the *stratum corneum* layer. This is due to the skins elasticity, after a period of time these indentations would reduced as the skin returns to its normal shape.
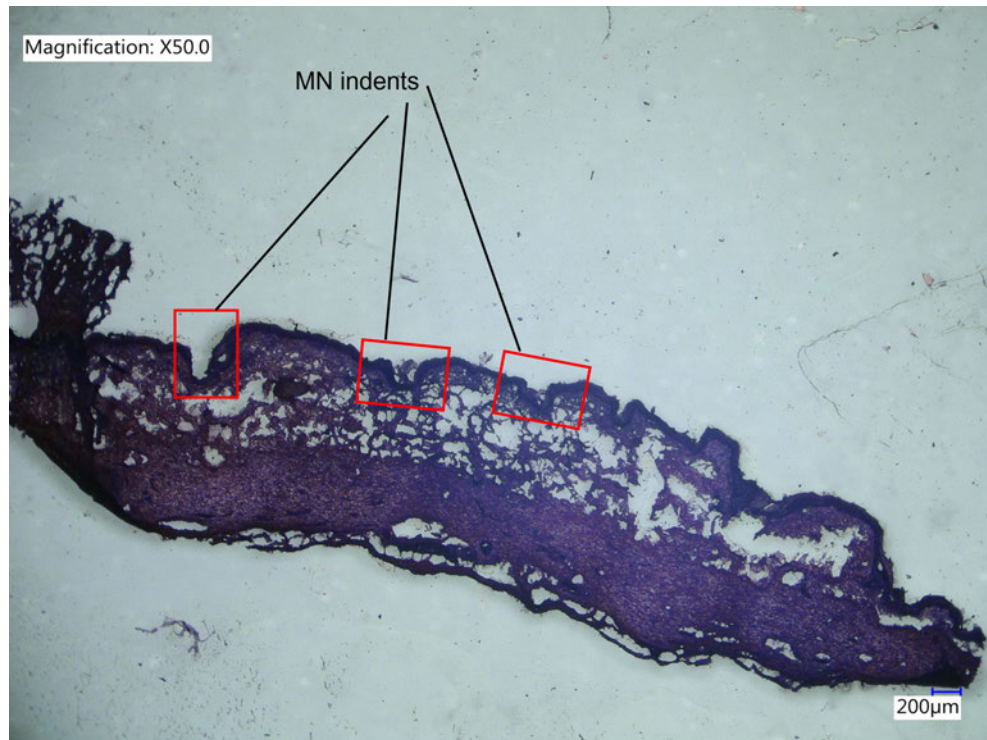
(a) Protocol 5 MN application cross section

Figure 5.14: Cross section of MNs fabricated with Protocols 5-7 application on Porcine skin with some indentations highlighted
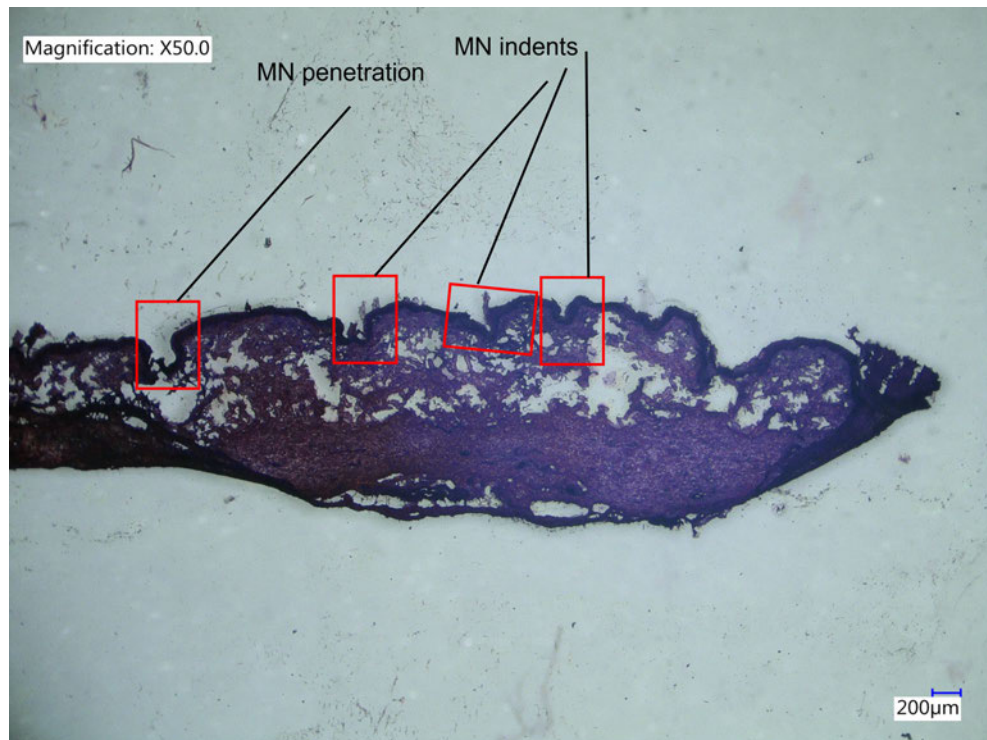
(b) Protocol 6 MN application cross section
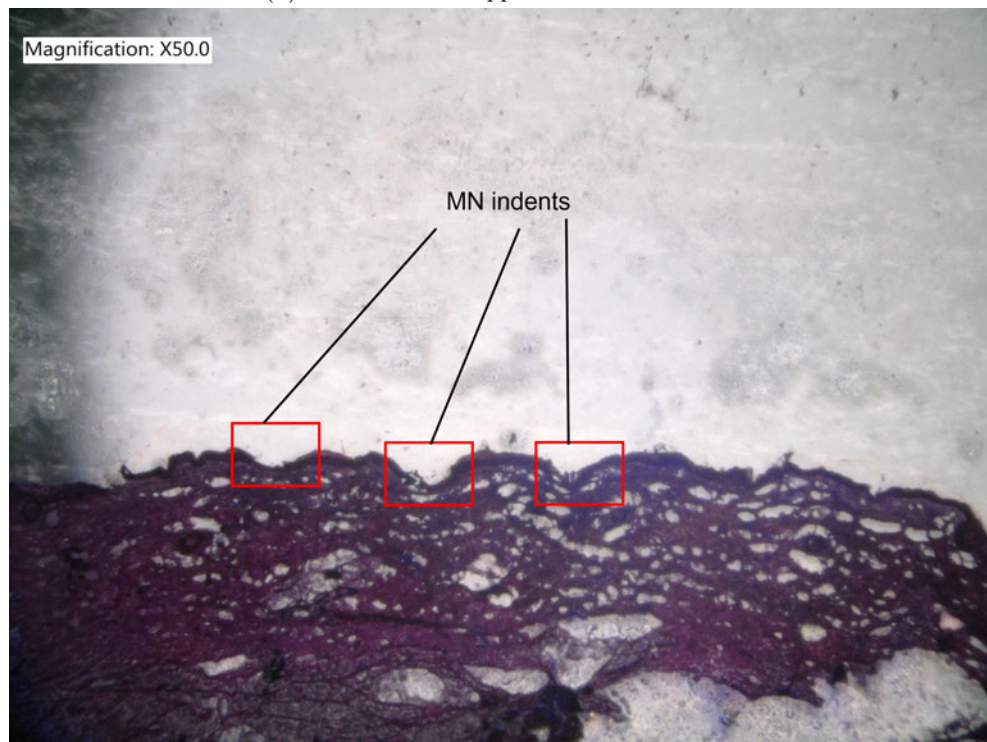
(c) Protocol 7 MN application cross section

Figure 5.14: Cross section of MNs fabricated with Protocols 5-7 application on Porcine skin with some indentations highlighted

116

The image in Figure 5.15 below shows the cross section of the final protocol 8 MN array application on porcine skin. This shows the *stratum corneum* has been broken by the MNs and a maximum penetration depths can be measured as 517μm
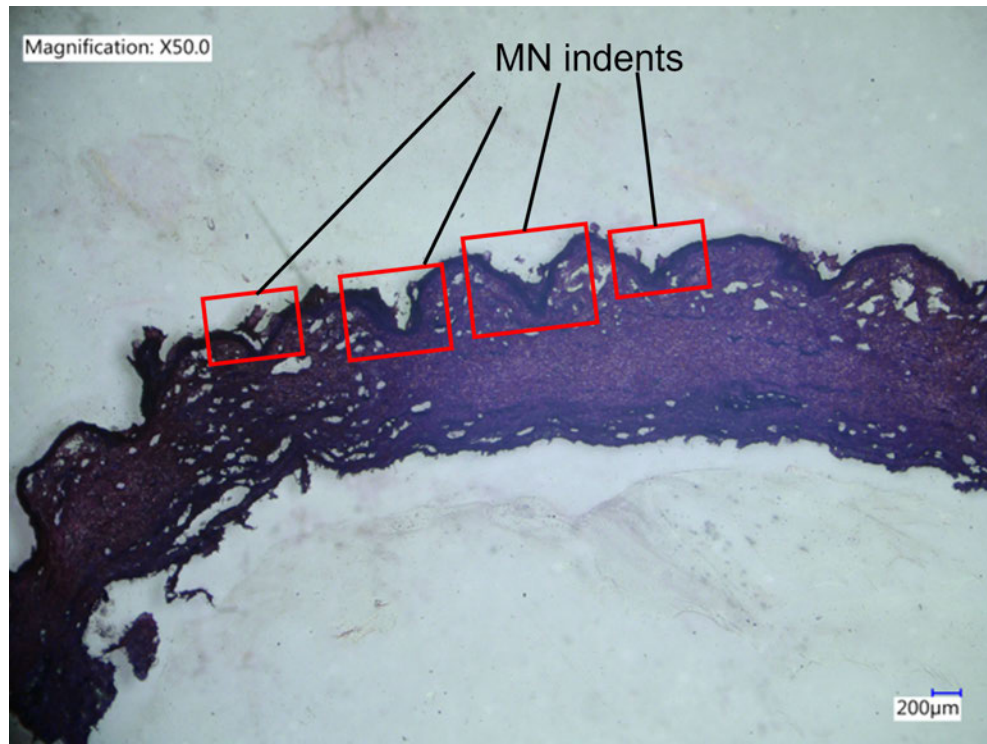
(a) 50x magnification of porcine skin after MN penetration

Figure 5.15: Histological cross sections of MNs highlighting broken portions of *stratum corneum* using final protocol 8
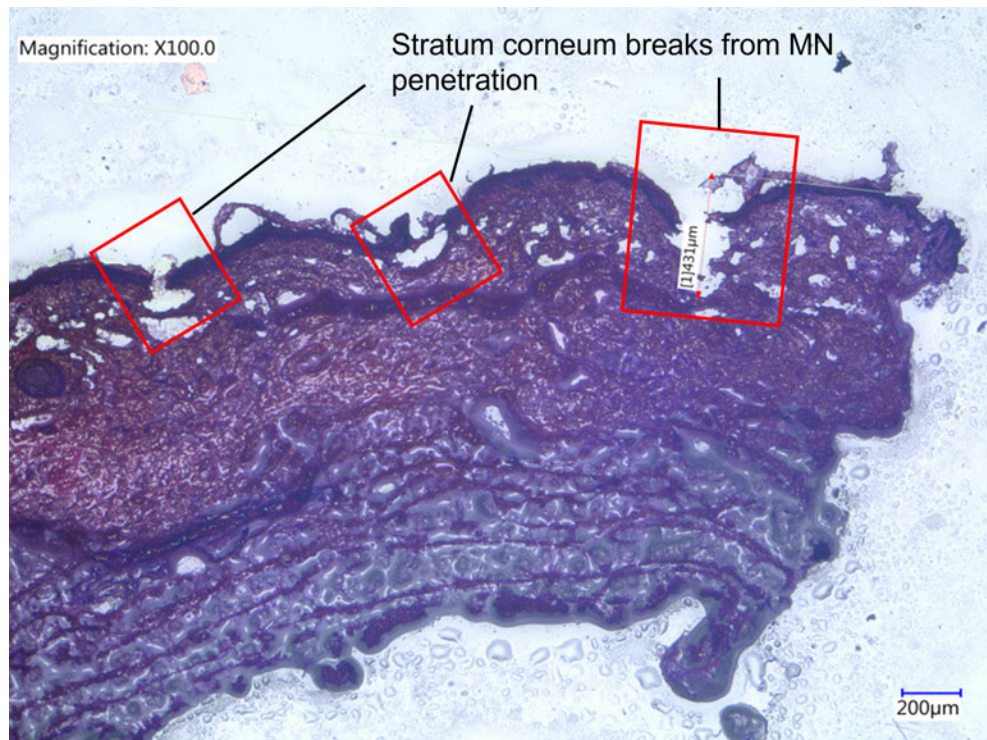
(b) 100x magnification of porcine skin after MN penetration showing a maximum penetration depth of 431μm
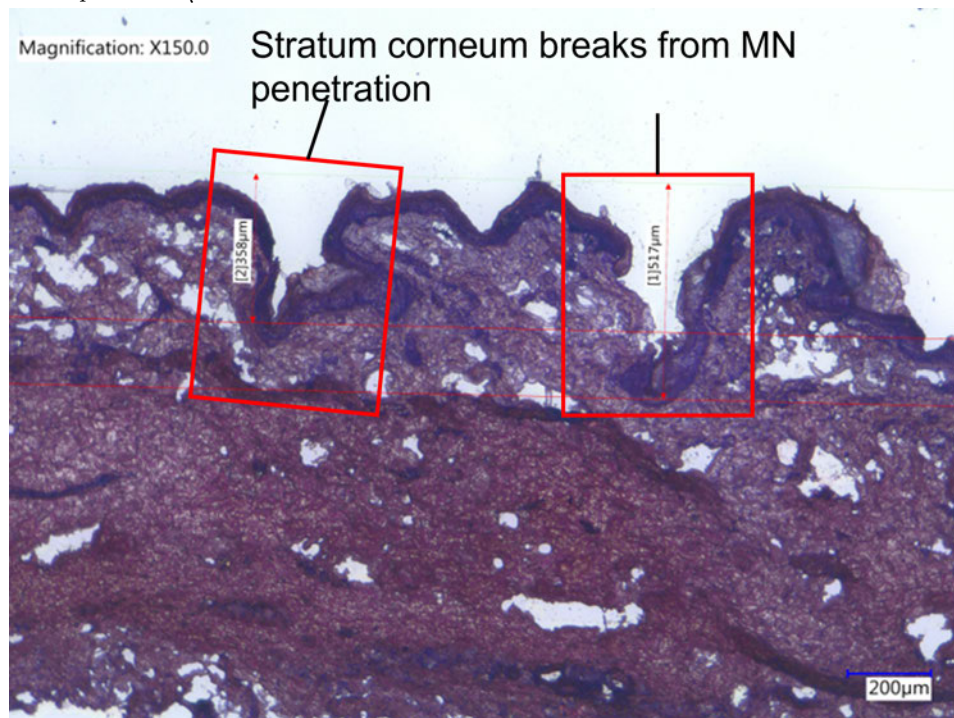
(c) 150x magnification of porcine skin after MN penetration, showing penetration depths of 358μm and 517μm

Figure 5.15: Histological cross sections of MNs highlighting broken portions of *stratum corneum* using final protocol 8

The penetration of silicon MNs were also examined as a comparison and it was found that they made very uniform and consistent and clear intents into the skin however a clear break in the *stratum corneum* could not be seen and this is most likely due to the small wall of silicon which had formed around the MN array during their fabrication process as seen in Figure 5.17. This wall will have reduced the amount of force extended through the actual MNs and therefore impacted penetration as seen in Figure 5.16. These MNs usually offer very good penetration as described in [181].
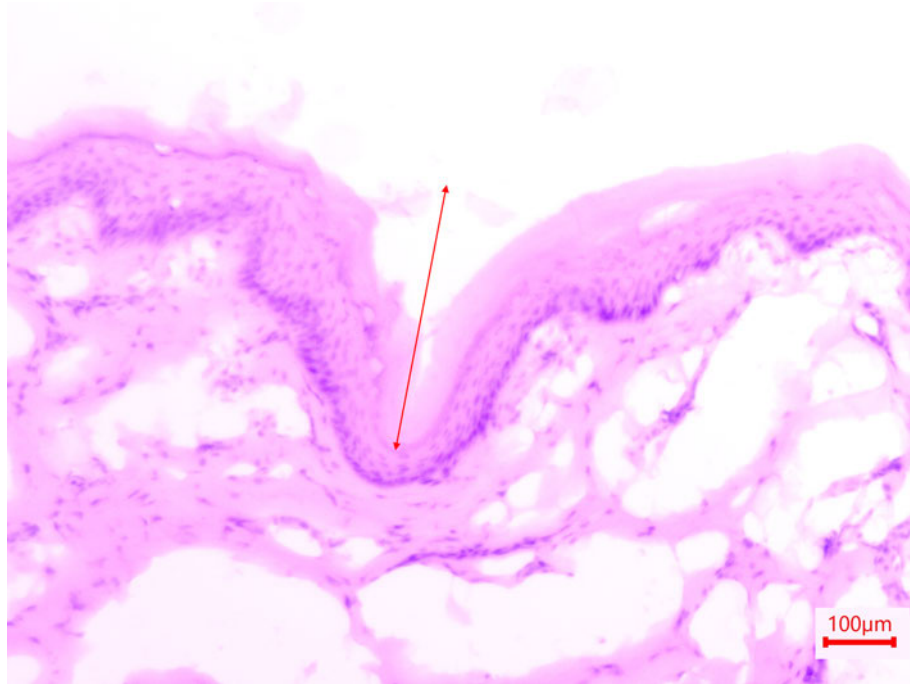
Figure 5.16: Histological cross section of pig skin after application of 1 by 5 array of Silicon MNs were applied
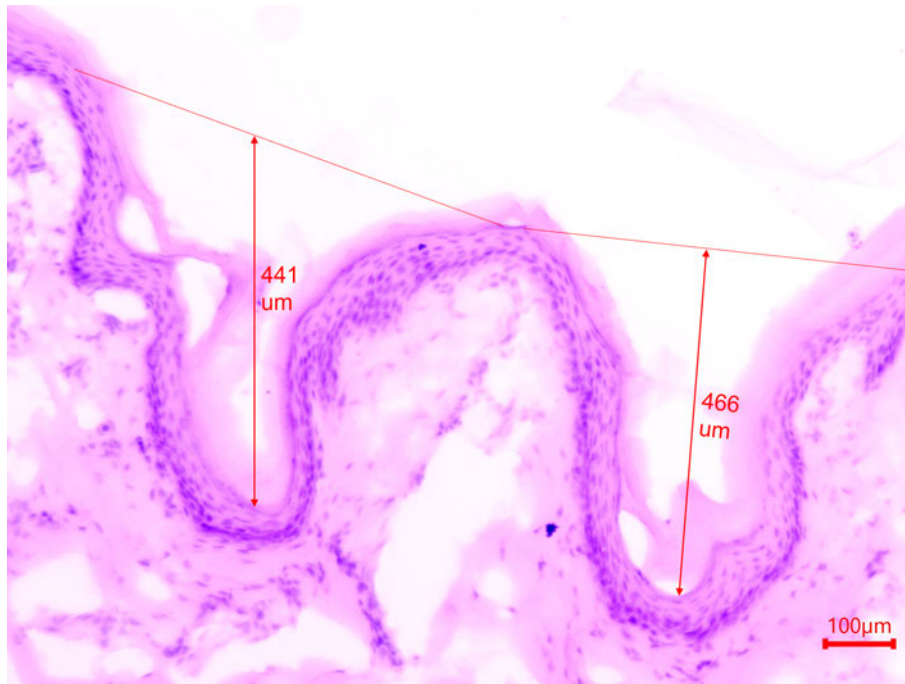
Figure 5.16: Histological cross section of pig skin after application of 1 by 5 array of Silicon MNs were applied
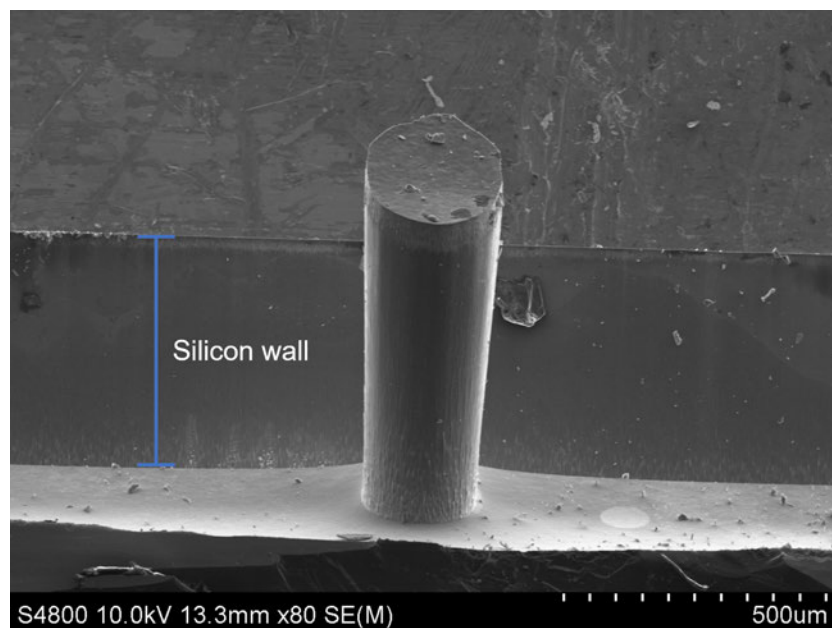
Figure 5.17: SEM of Silicon MN with silicon wall behind

In summary this shows that the optimal design for these polymer screen printed MNs used a 400μm aperture with a pitch of 1100μm. Protocol 8 as laid out in Table 5.5 yielded MNs which penetrated the skin enough to break the *stratum corneum* giving access to the ISF which can then be used for biosensing or drug delivery.

5.2 Mechanical characterisation of microneedle arrays

It is important to analyse the mechanical characteristics of MNs in order to calculate safety margins. The most tested aspect of a MN is usually the axial compression of the MN patches. This demonstrates the force it will take when compressed from above the array and can then be compared to the insertion force [22]. The ratio of insertion force to the force a MN array can withstand would be the parameter looked at when determining the safety margin, lower forces and therefore a lowered ratio would therefore be beneficial as it would help minimise pain on insertion of the MNs. MNs need to withstand the forces during insertion and not break or overly deform.

The MN arrays of 1cm^2 were mechanically tested using an electromechanical testing system in compression mode with a 1 kN load cell installed. They were then placed on the baseplate facing up while the top plate was lowered at a rate of 1 mm/min as seen in Chapter 2. Different maximum amounts of force were applied before stopping the test. MN arrays that were coated in silver using PVD (physical vapour deposition) were also tested to see what effect the coating had or how the coating was affected. These coated MNs are usually used for biosensing. The deformation of the MNs shows it to be consistent and straight without bending, they stay intact but gradually reduce in height with the tip collapsing when a certain load threshold is reached. See in Figure 5.18 and 5.19 single MNs as part of a 1cm^2 array.
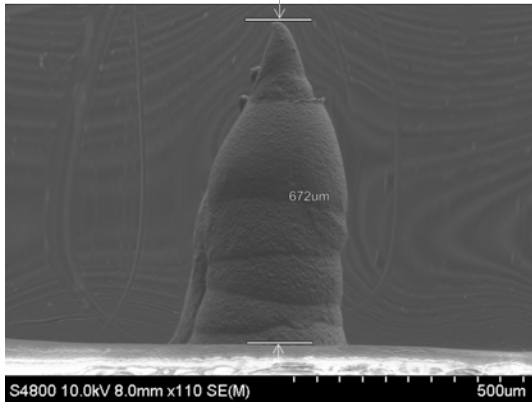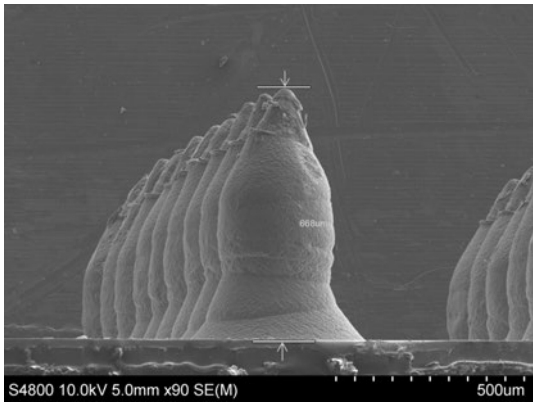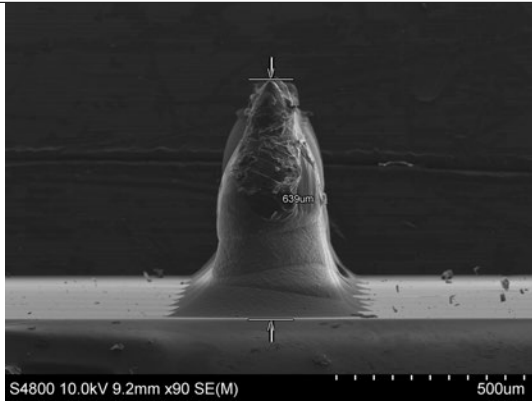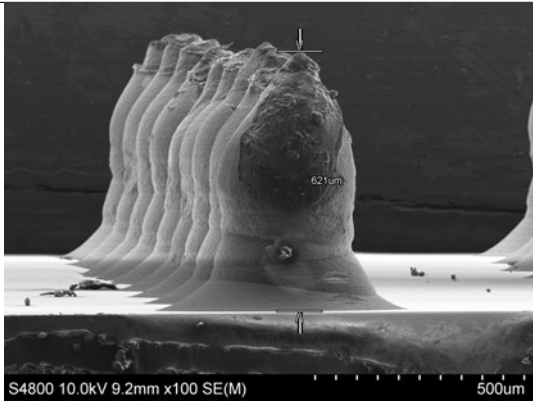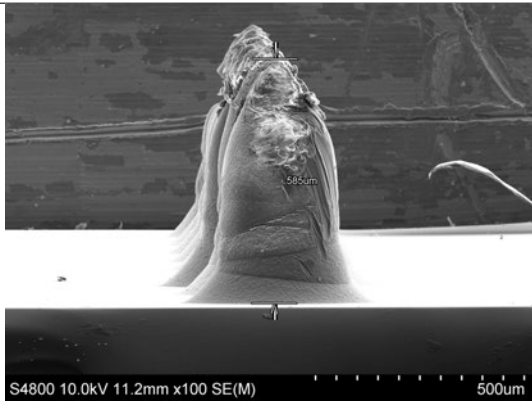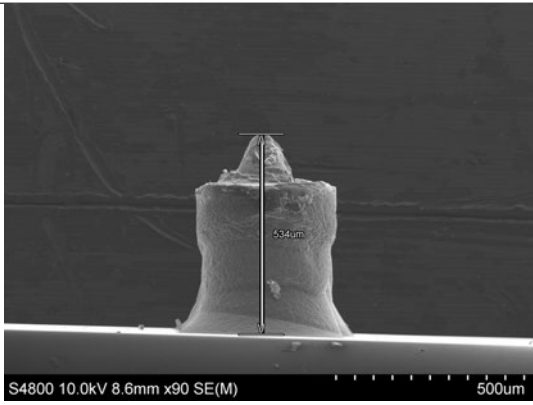
Unloaded	5N load
672μm	668μm
25N load	50N load
639μm	621μm
100N load	500N load
585μm	534μm

Figure 5.18: Effects of compression on the height of uncoated MNs under loads 0-500N
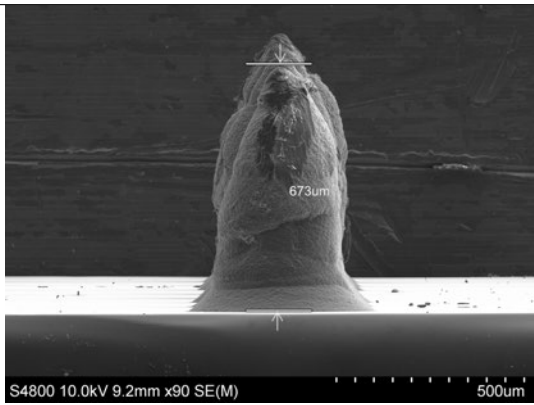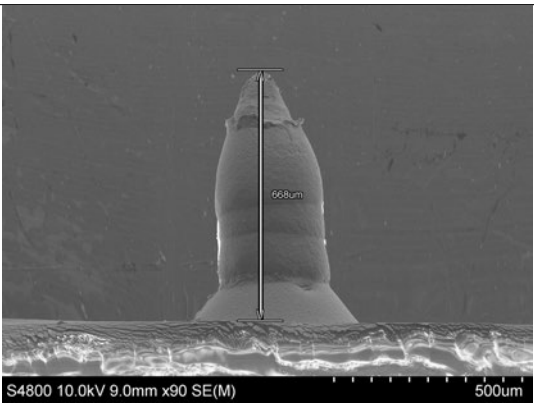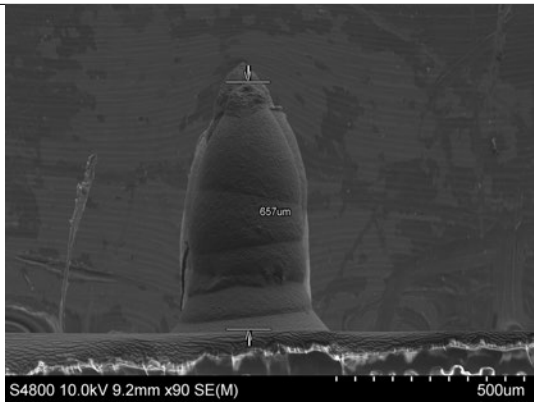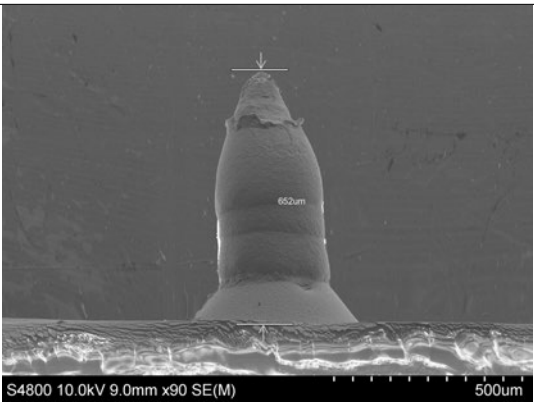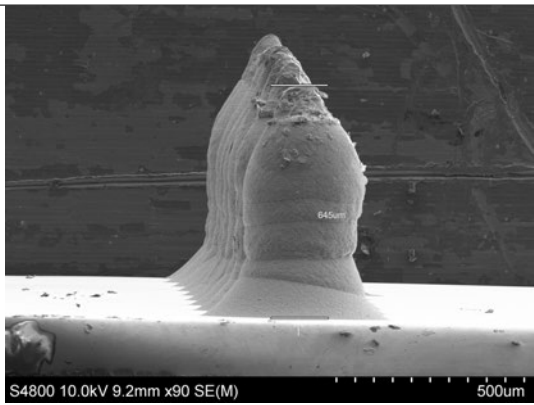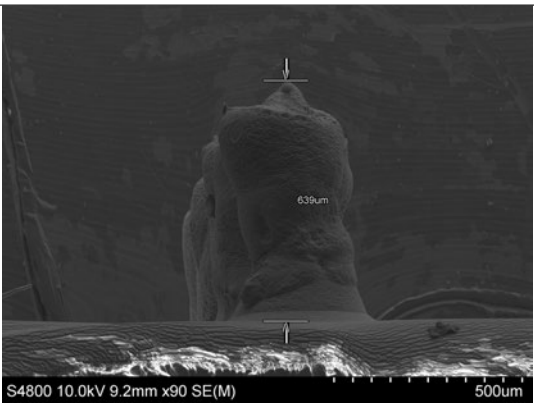
Unloaded	5N load
673µm	668µm
25N load	50N load
657µm	652µm
100N load	500N load
645µm	639µm

Figure 5.19: Effects of compression on the height of coated MNs under loads of 0-500N

The Force displacement mirrored this plastic deformation with no sudden change to indicate breakage. Comparatively the silver coated MNs deformed in a similar manner but a greater load was required to deform the MNs to the same displacement. In Figures 5.20a and 5.20b. This indicates that metal coated polymer MNs can withstand larger forces than uncoated polymer MNs before they deform.
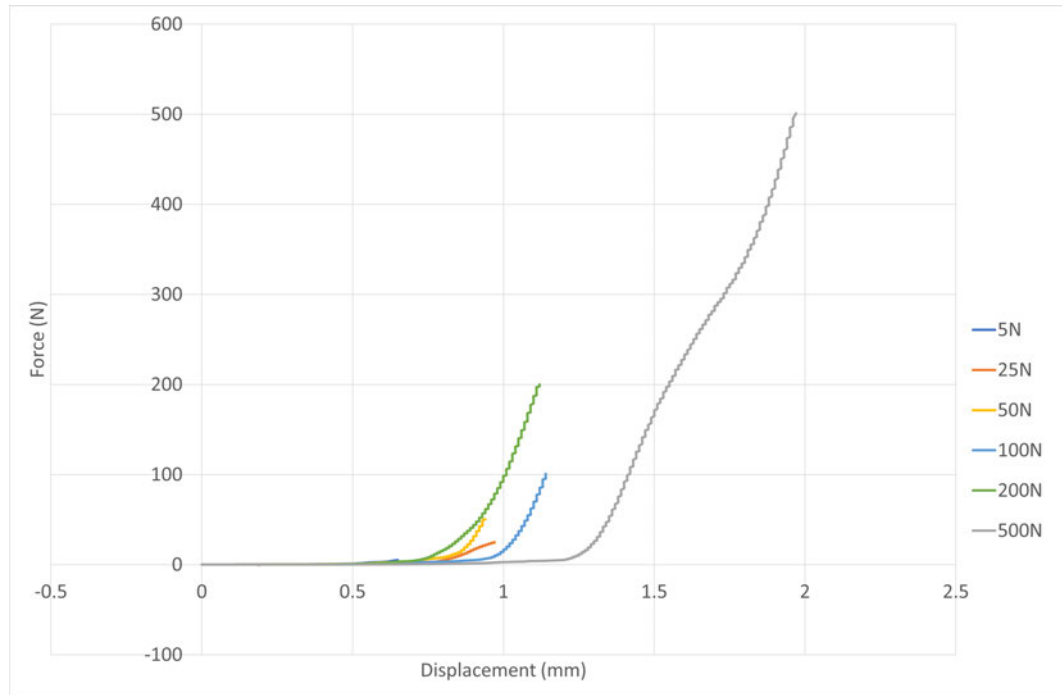
(a) Uncoated force displacement 5-500N

Figure 5.20: Coated and uncoated force displacement under different forces
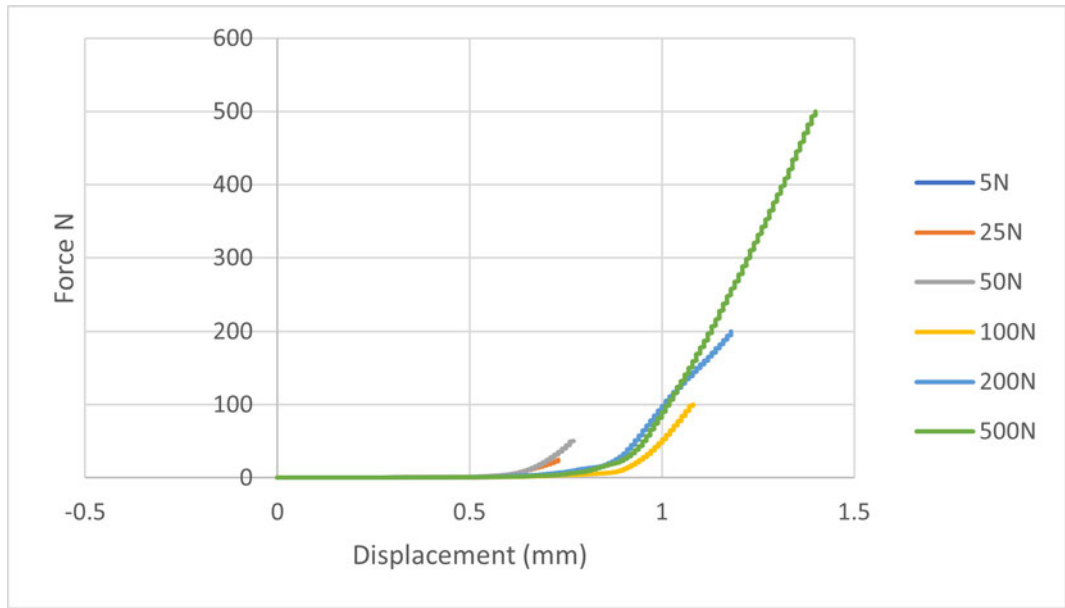
(b) Coated force displacement 5-500N

Figure 5.20: Coated and uncoated force displacement under different forces
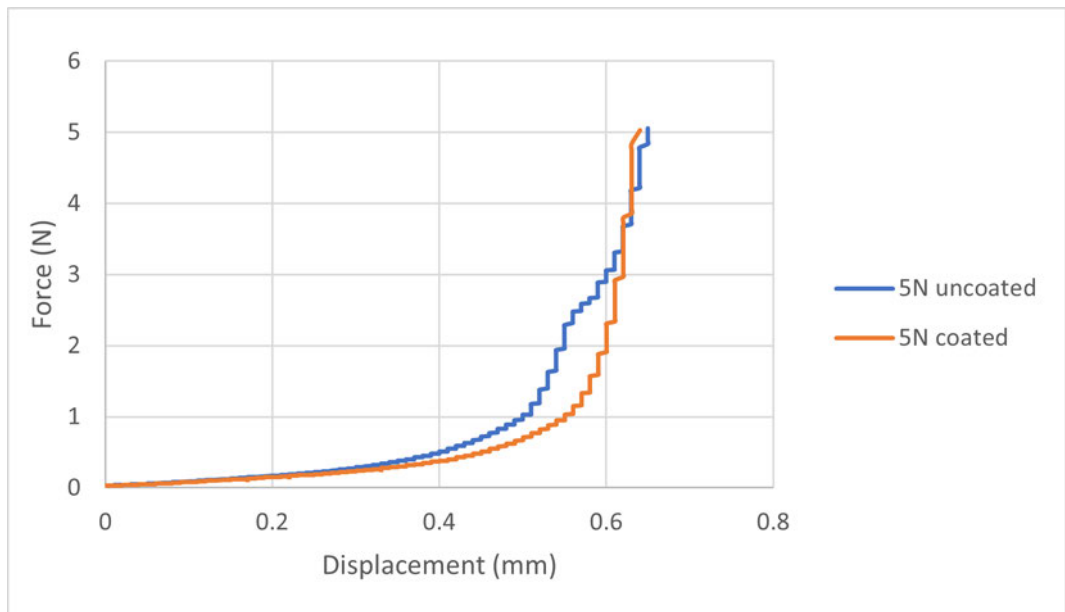
Figure 5.21: MN tip force with respect to displacement applied 5N
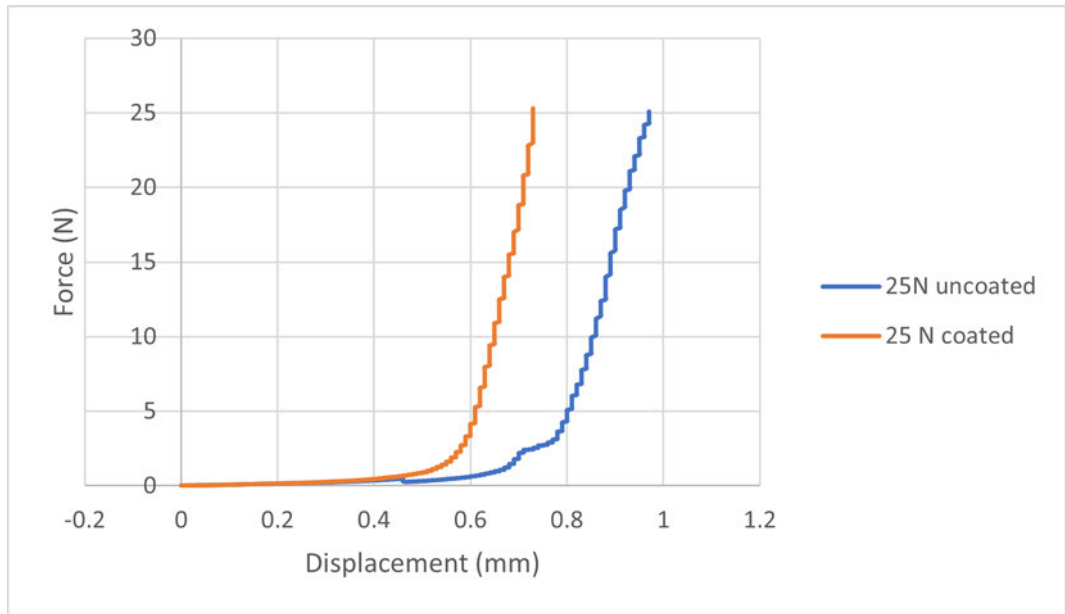
Figure 5.22: MN tip force with respect to displacement applied 25N
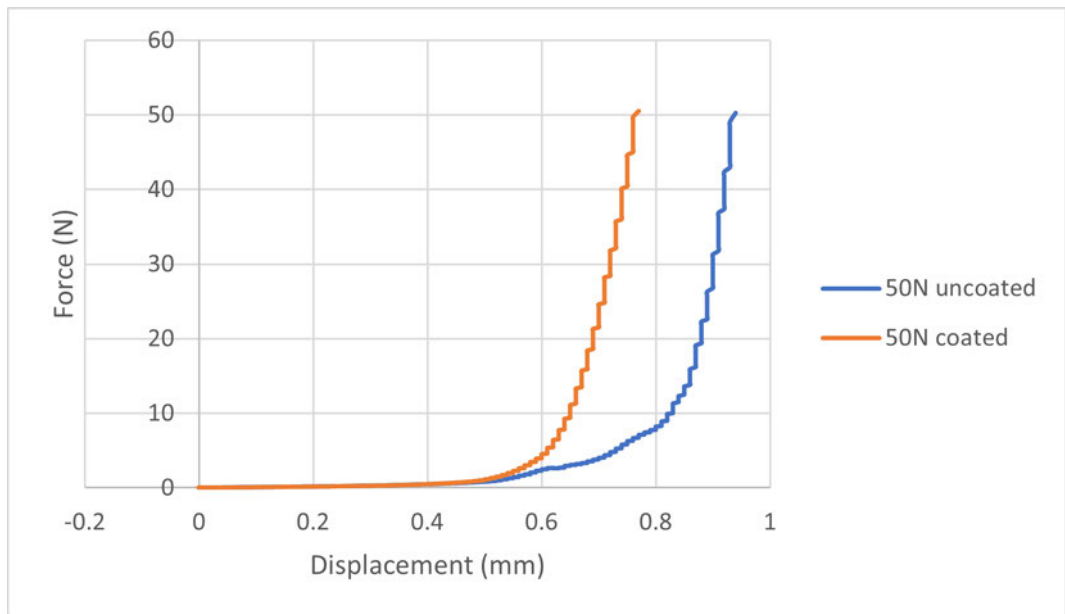
Figure 5.23: MN tip force with respect to displacement applied 50N

126
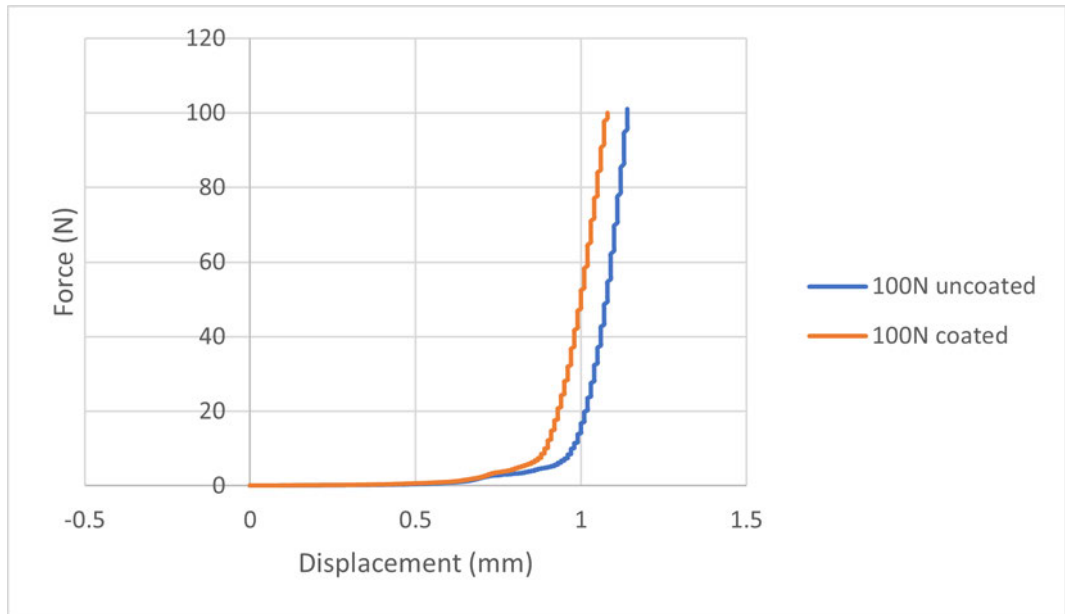
Figure 5.24: MN tip force with respect to displacement applied 100N
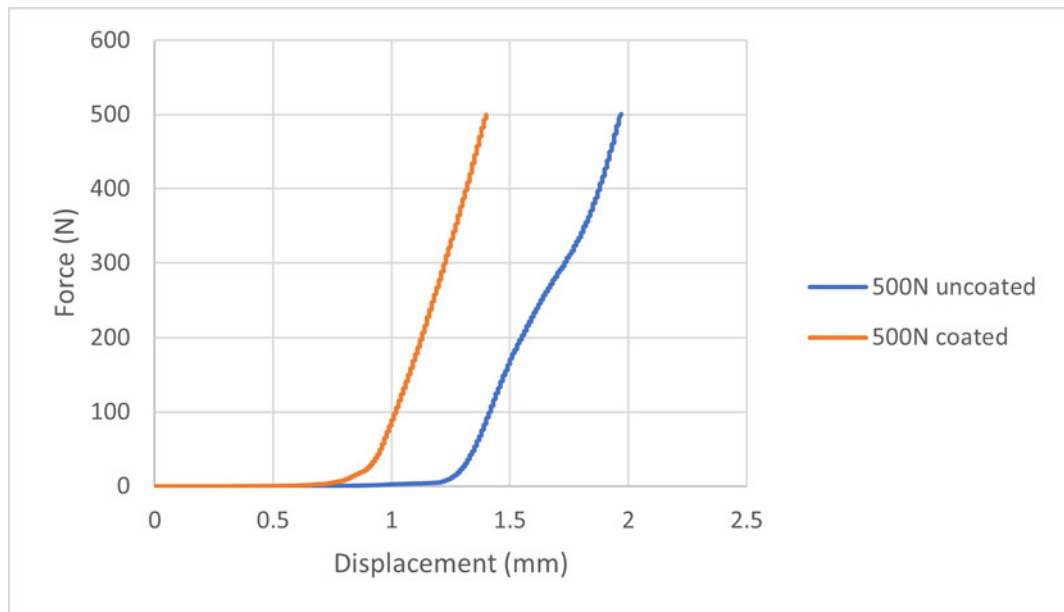
Figure 5.25: MN tip force with respect to displacement applied 500N

The insertion forces into porcine skin was analysed axially. The MN arrays were attached to the top plate and lowered towards the porcine skin at a rate of 1 mm/min up to a force of 60 N. Any sudden change in force would be indicative of insertion into the skin. Set up shown below in Figure 5.26
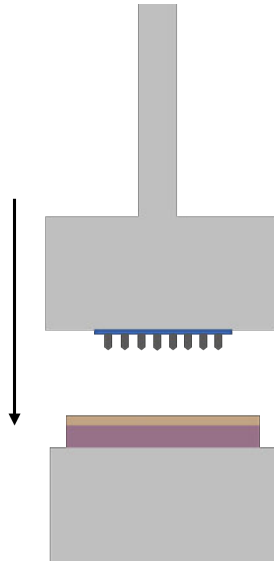
Figure 5.26: Insertion force test set up using Tinus Olsen force station and porcine skin

There is an observable force change albeit a small one at 0.1N and 0.4N for coated and uncoated MNs respectively in Figure 5.27 This could be a change as a result of contact and insertion into the skin. This would be a low insertion force and well below the required safety margins that were needed based on the axial mechanical tests of the MN arrays.
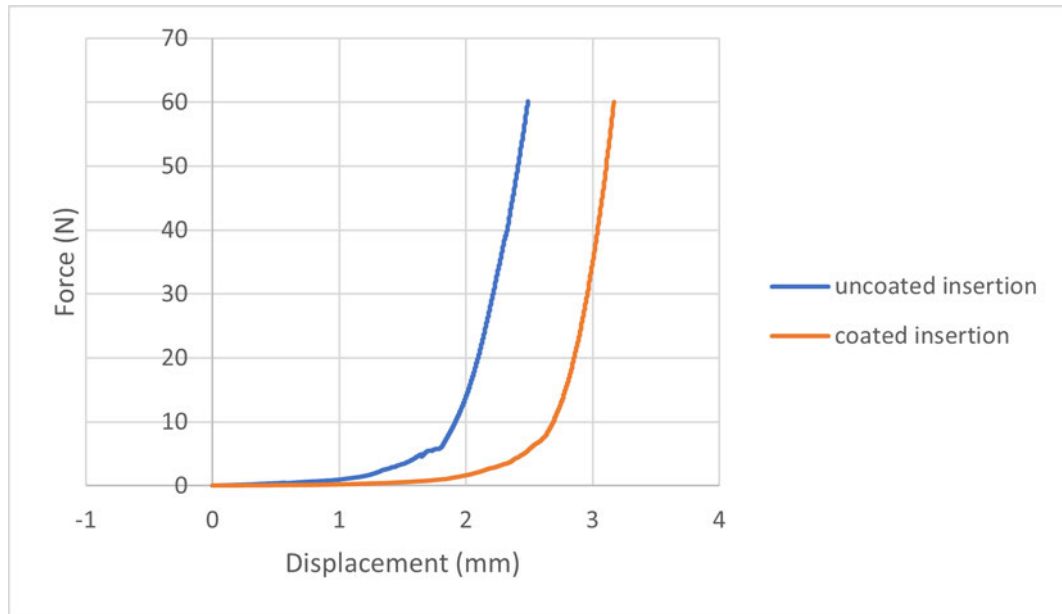
(a) Insertion force with a maximum load of 60N

Figure 5.27: Insertion force vs displacement of insertion of MNs into porcine skin
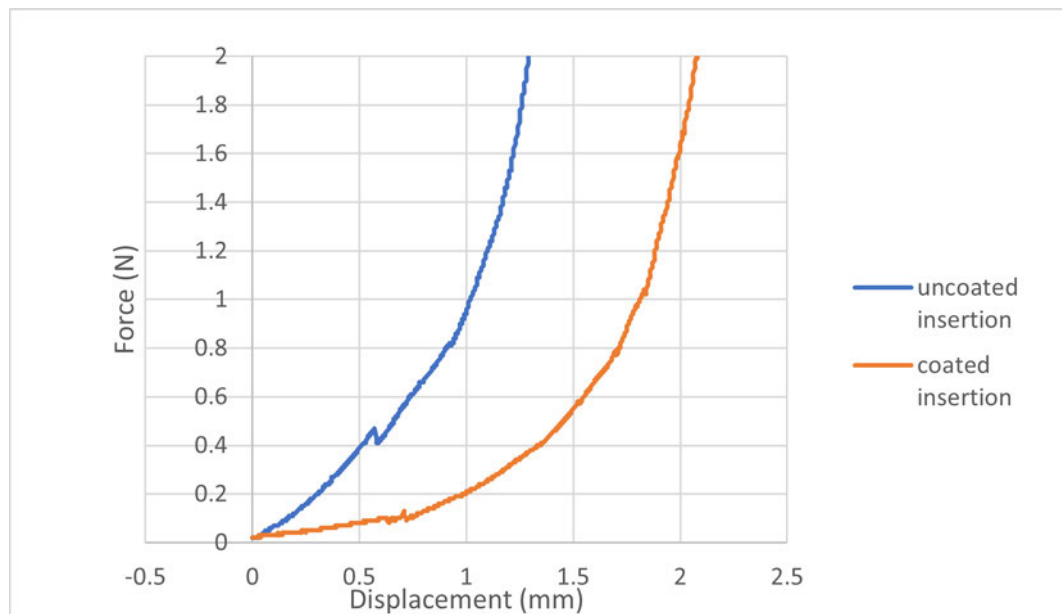
(b) Insertion force with Maximum of 2N

Figure 5.27: Insertion force vs displacement of insertion of MNs into porcine skin

In summary this chapter investigates the image and mechanical characterisation of

the MN arrays. It illustrates that the polymer MNs made using the final protocol consisting of 7 passes using a 400um aperture stencil for the base portion and 2 passes using a 150um aperture stencil for the MN tip when applied to pig skin yielded adequate penetration to break through the *stratum corneum* and thus were applicable to be used for drug delivery experiments. This is illustrated through two methods of staining, one of which is methyl blue staining of the surface of the skin samples and the other is Eosin and haematoxylin staining of cross sections of the skin. Both of these methods showed penetration of the polymer MNs. The mechanical characterisation of the MNs showed that a force higher than the penetration force required will deform the MNs and the metal coated MNs withstood an even greater force before deformation. These experiments demonstrated that both coated and uncoated MN arrays were suitable for penetration and further use in drug delivery and sensing studies.

6 Diagnostics and Microneedle Applications

6.1 Diagnostics

6.1.1 Determination of chloride

Chloride can be used as a means to diagnose cystic fibrosis, and can be measured by different methods. Chloride can be measured by potentiometry by using a Ag/AgCl electrode, as an ion selective electrode (ISE) with a reference electrode or by chronopotentiometry using similar electrodes but applying a constant current and measuring potential over time. This method has been adapted by Abbas et al [182] to use two Ag/AgCl electrodes, one acting as the working electrode and one acting as a pseudo-reference electrode.

6.1.1.1 The theory of Silver/Silver Chloride measurement methods

The Ag/AgCl ISE electrode is a second kind redox electrode therefore when it is in contact with a solution containing chloride (Cl-) ions there is an equilibrium that occurs between the Cl- ions and the AgCl at the surface of the electrode. This methods works on the basis that a silver electrode gives a half cell potential and can be determined by the Nernst equation (6.1) which can be seen below where E is the reduction potential, E^0 is the standard potential, R is the universal gas constant, T is the temperature in kelvin, n is the ion charge, F is Faraday's constant and a is the chemical activity.

$$E_{Ag/Ag^+} = E^0_{Ag/Ag^+} + \frac{RT}{nF} ln a_{Ag^+} \qquad (6.1)$$

Theoretically a silver electrode alone should respond to the silver ion activity however when there is an abundance of halide ions there will be lower silver ion activity and therefore a relatively slow reaction. An electrode coated in halide ions, in this case Cl-ions causes changes to the silver ion activity at the surface. The silver ion activity at the surface of silver electrodes coated with the Cl- ions is directly affected by the change

of the chloride activity in the bulk solution which is defined by the solubility product of the silver chloride K_{sp}.

$$K_{sp} = a_{Ag^+} a_{Cl^-} \tag{6.2}$$

The concentration of the Cl- ions in this case will determine the change in half cell potential at the working electrode [183].

6.1.1.2 The theory of chronopotentiometry using two AgCl electrodes

This method employs two silver/silver chloride electrodes in the same bulk electrolyte, one acting as a pseudo-reference electrode and one acting as a working electrode. A third counter electrode is also used to allow current to be passed through the working electrode.

This method utilises the difference between the potential difference of the bulk of the chloride solution and the potential difference at the working electrode due to chloride depletion. Before a current is passed through the working electrode, the cell is at equilibrium and both the working electrode and the pseudo-reference electrode are at the same potential. Therefore the difference between the pseudo-reference and the working electrode, ΔV is 0. When the current pulse is applied to the silver working electrode, the electrode is oxidised to produce Ag^+ which reacts with the chloride in the solution to form $AgCl$ as shown below in Equations 6.3 and 6.4.

$$Ag + e^- \rightarrow Ag^+ \tag{6.3}$$
$$Ag^+ + Cl^- \rightarrow AgCl \tag{6.4}$$

The chloride concentration at the working electrode is depleted leading to a potential difference ΔV because the half cell potentials are now different as shown in Figure 6.1[134].
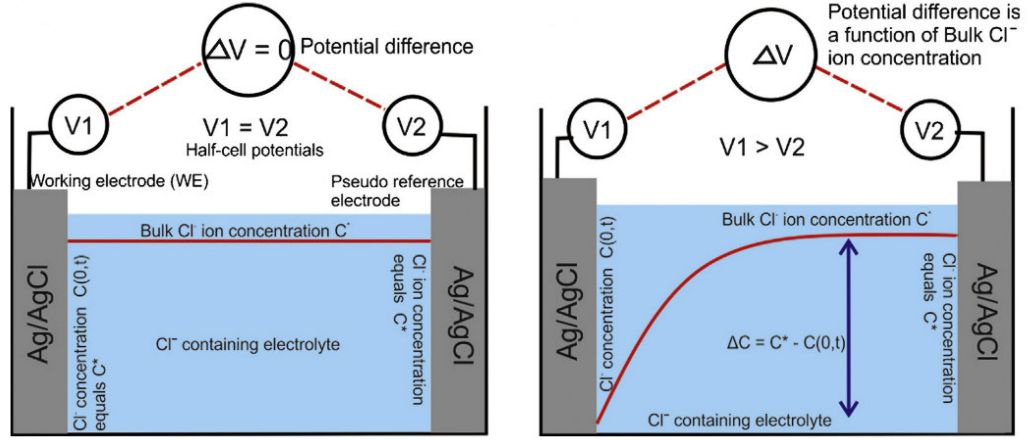
(a) Schematic showing the system at zero current giving equal half cell potentials between the electrodes resulting in no potential difference.

(b) The schematic showing the resulting profile during the anodic current pulse where the current is applied at the working electrode and the resulting depletion of chloride ions.

Figure 6.1: The schematic of the chronopotentiometry using a two Ag/AgCl electrode system

The potential difference needs to be measured within the transition time to be valid. The transition time is the time in which it takes for the Cl- ions concentration at the electrode surface to reach zero. After this time other reactions such as oxide formation can occur which interferes and therefore invalidates the results obtained. The desired current density of the applied current can be estimated using a boundary condition derived from the logarithmic term of the Nernst equation 6.1 and the potential difference at the working electrode with respect to the reference electrode as shown in Equation 6.5 [134] where C^* is the bulk Cl- ion concentration, j is the current density, D is the diffusion coefficient, t is the current pulse time, R is the universal gas constant, T is the temperature in kelvin, and F is Faraday's constant. This boundary condition is outlined in Equation 6.6.

$$\Delta V = -\frac{RT}{F}ln(1 - \sqrt{\frac{(t/D\pi)2j}{FC^*}}) \tag{6.5}$$

$$j < 0.5FC^* * \sqrt{(t/D\pi)} \tag{6.6}$$

The difference potential (ΔV) is then used to measure the concentration of Cl- ions. This is a Cl- ion sensor measurement method using a chronopotentiometry method adapted from a method devised by Abbas et al [182, 184] to measure the Cl- ions in

concrete, where a current is applied and the potential measured. Chloride determination using two Ag/AgCl electrodes utilises the mechanism of the transfer of chloride from one electrode and measuring the potential at this working electrode versus the potential of the bulk.

As the current is applied the chloride is depleted and the potential difference increases until a plateau occurs, after this point the voltage continues to rise and after reaching an inflection point the formation of silver oxide starts to occurs, this can be seen in the diagram in Figure 6.2 [134] below.
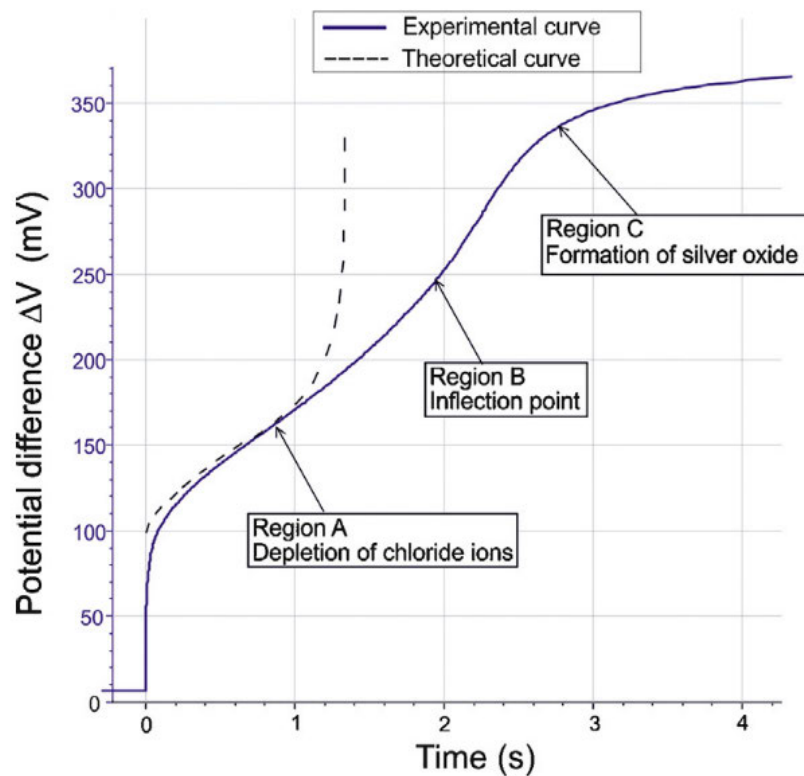
Figure 6.2: Ag/AgCl working electrode potential response against an identical Ag/AgCl reference electrode, showing both the theoretical and experimental responses

The transition time when the chloride ions are depleting increases as the concentration increases and therefore the amount of chloride ions available near the surface increases. This can be seen as a shift in the curve of the potential response over time as shown in Figure 6.3 [134].
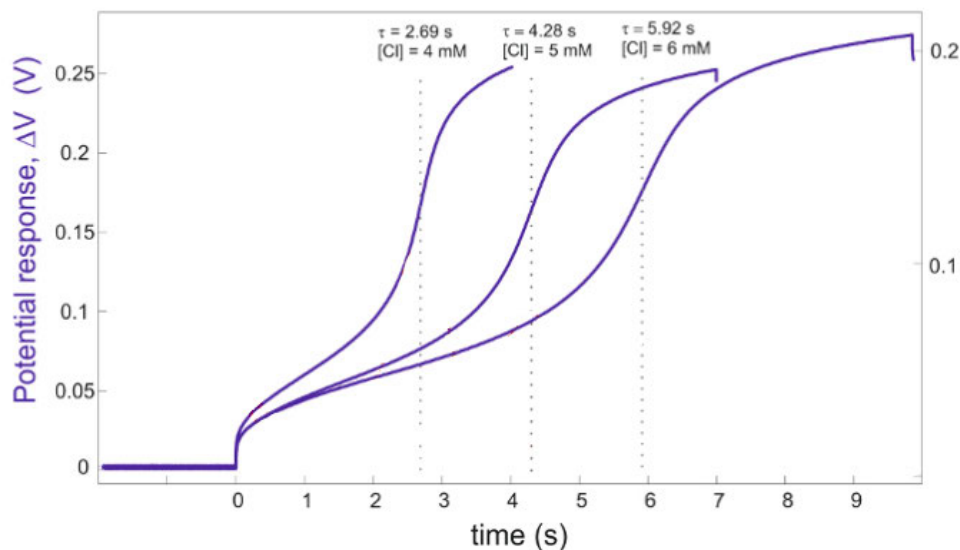
Figure 6.3: Transition times of AgCl electrode in solutions with different concentrations if Cl- ions

The Abbas method was further adapted to measure the chloride concentration by recording the ΔV at a specific time after the applied current is started. In standard chronopotentiometry the chloride concentration would be determined by plotting the transition time, when the Cl- ions are depleted at the working electrode, against the Cl- concentration. Instead Abbas measured the ΔV at a specific time after the start of the constant current and then switched the current back to zero as shown in Figure 6.4.

This is why when the same current pulse time is used to measure multiple different concentrations, the responses for higher concentrations have a lower potential difference. For the same time period the portion of the curve being analysed for higher concentrations is further away from the end of the transition time period. This difference at the same time point is illustrated in Figure 6.4 [134].
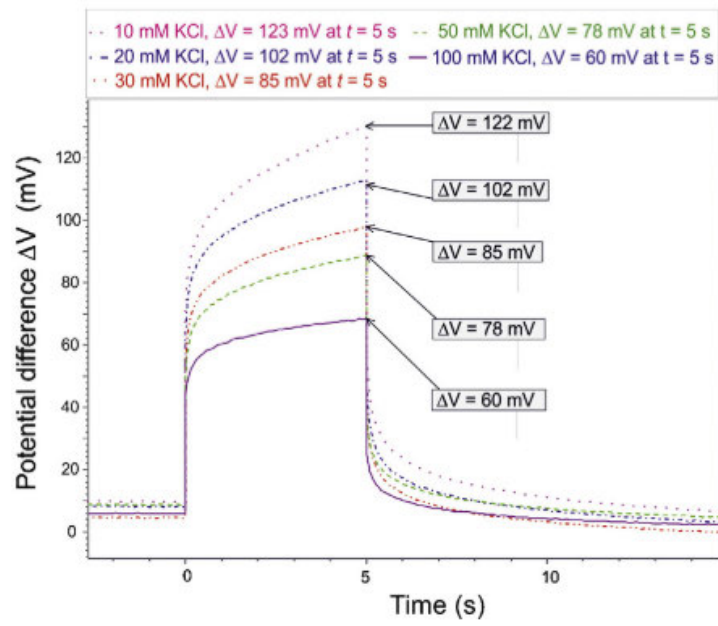
Figure 6.4: The potential difference response of the system in solutions at different concentrations of chloride

This can be plotted together in a dose response curve which should decrease exponentially towards zero as shown by the theoretical curve in Figure 6.5 [185] with a current density of 15 Am^{-2}.
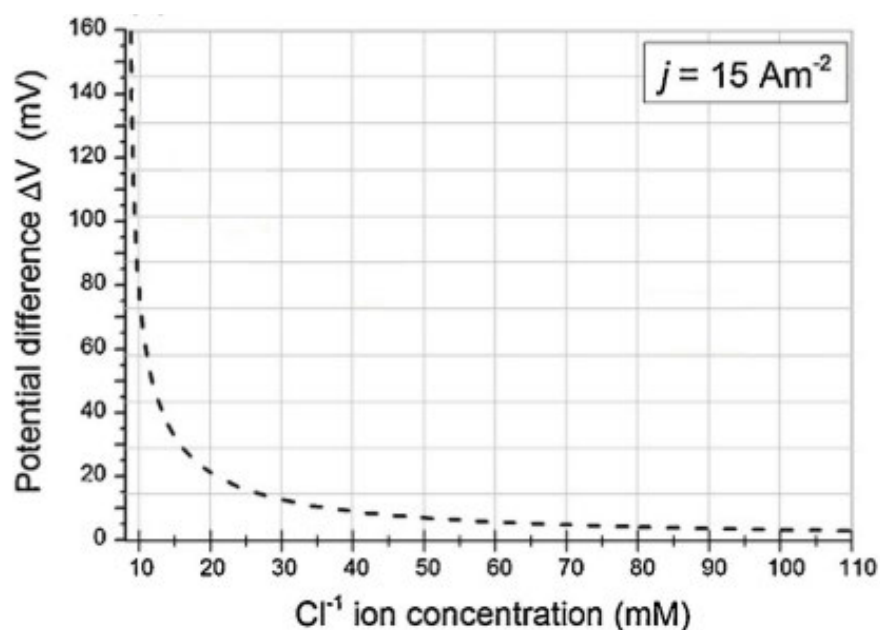
Figure 6.5: The theoretical potential difference (mV) response with respect to Chloride ion concentration (mM)

6.1.1.3 Chloride determination using silver bar electrodes

To test the adaptation of the method by Abbas et al silver bar electrodes as described in section 2.2.6 were polished and then chloride coated using a two electrode system of the silver working electrode and a platinum wire counter/reference electrode. A 1.5mA current pulse was applied for 240 seconds to yield a Ag/AgCl electrode.

Two of these Ag/AgCl electrodes were then used, one as the working and one as a reference electrode and a platinum wire electrode was used as a counter electrode. Each time a reading was run, the potential value taken for the graphs pertained to the plateau region of the Cl- ion depletion. A set of measurements was taken with 7 solutions varying in concentration from 0-100mM of KCl at a current pulse of 1.5mA for 5 seconds of each measurement using the set up as seen in Figure 2.13. The resulting dose graph based on the results in Table 6.1 can be seen below in Figure 6.7.

Table 6.1: Data for chloride dose response using silver bar electrodes. Mean values and
corresponding standard deviation error bars for 3 consecutive measurements

Dose response data for AgCl coated silver bar electrodes							
mM	2.5	5	10	20	40	80	100
Average Poten- tial	1.0542	0.9061	0.7332	0.6283	0.5529	0.5200	0.5487
Standard devi- ation	0.0738	0.0376	0.0181	0.0134	0.0042	0.0032	0.0021

An example of some of the data traces from the silver bar electrodes is shown below
in Figure 6.6.
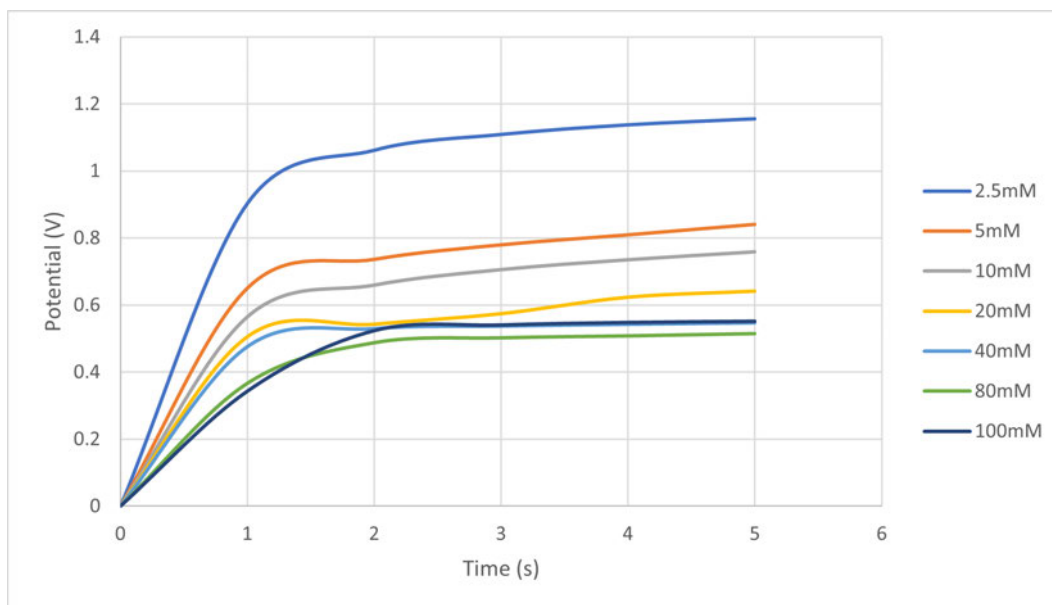
Figure 6.6: Resultant potential difference trace during current pulse for measurements
on silver bar electrodes. Reading taken every 10 ms
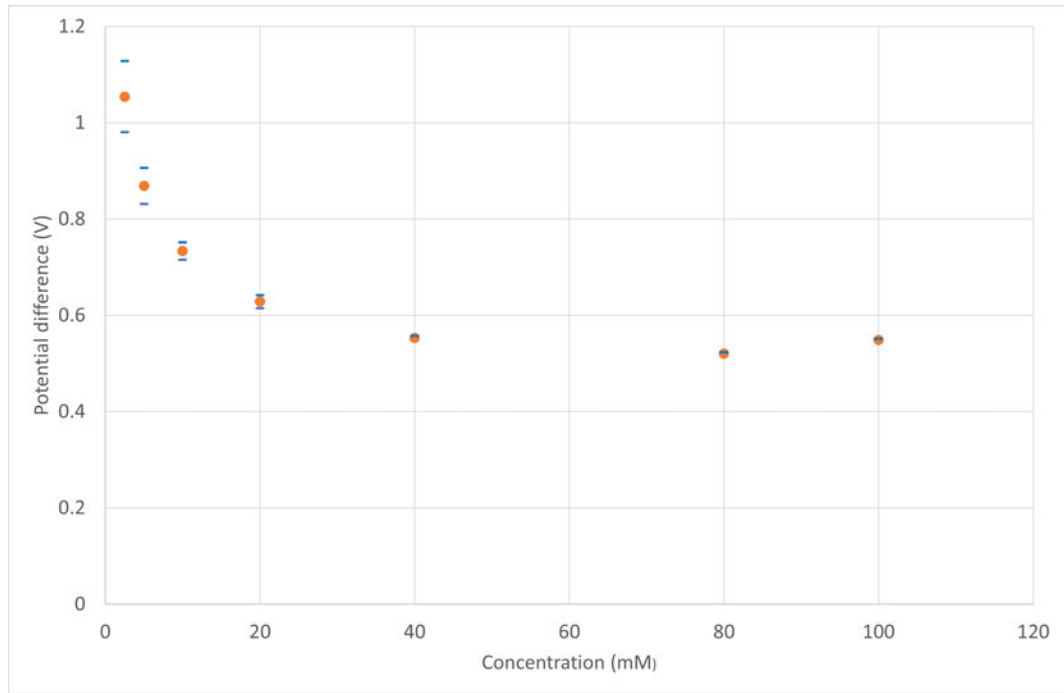
Figure 6.7: Chronopotentiometric chloride dose response using silver bar electrodes taken after 5 seconds

The results of the dose response of chloride using silver bar electrodes shows that there is a decrease in the potential difference as concentration is increased in the 5-40mM range. The rate of change is highest at low concentrations and beyond 40mM potential difference plateaus. For low concentrations of chloride the pulse has depleted the majority of the available chloride ions at the working electrode. Therefore there is a large potential difference between the electrodes. As the concentration increases, more of the available chloride ions remain in solution and so the potential difference is smaller. At high concentrations, the percentage of chloride ions removed is small compared to the chloride ions remaining in the vicinity of the working electrode and the potential difference minimal. The response relating to different concentrations relies on the current pulse applied as shown in research by Abbas et al [134].

This prompted an investigation into the optimal current for the desired concentration range. The currents pulses 0.05mA, 0.15mA, 0.5mA, 1mA and 1.5mA were investigated for concentrations 10mM, 20mM, 40mM, 60mM and 80mM due to the clinical range found in the body when diagnosing cystic fibrosis. Each dose response curve was plotted alongside each other to determine which current pulse shifted the curve enough to cover the desired concentration range as seen in Figure 6.8 based on the data in Table 6.2.

139

Table 6.2: Data table of the resulting potentials taken after a 5 second pulse of the chloride dose response at 0.05mA, 0.1mA, 0.15mA, 0.5mA, 1mA and 1.5mA current pulses.

Resulting potentials of chloride dose response	Current pulse (mA)					
Concentration (mM)	0.05	0.1	0.15	0.5	1	1.5
10	0.03029	0.04878	0.13205	038275	0.7085	0.99182
20	0.02375	0.0407	0.08746	0.34293	0.57565	0.93079
40	0.02254	0.03958	0.07864	0.33951	0.52136	0.72034
60	0.02023	0.03348	0.06119	0.32742	0.50122	0.67816
80	0.02069	0.0347	0.0563	0.32733	0.51071	0.71216
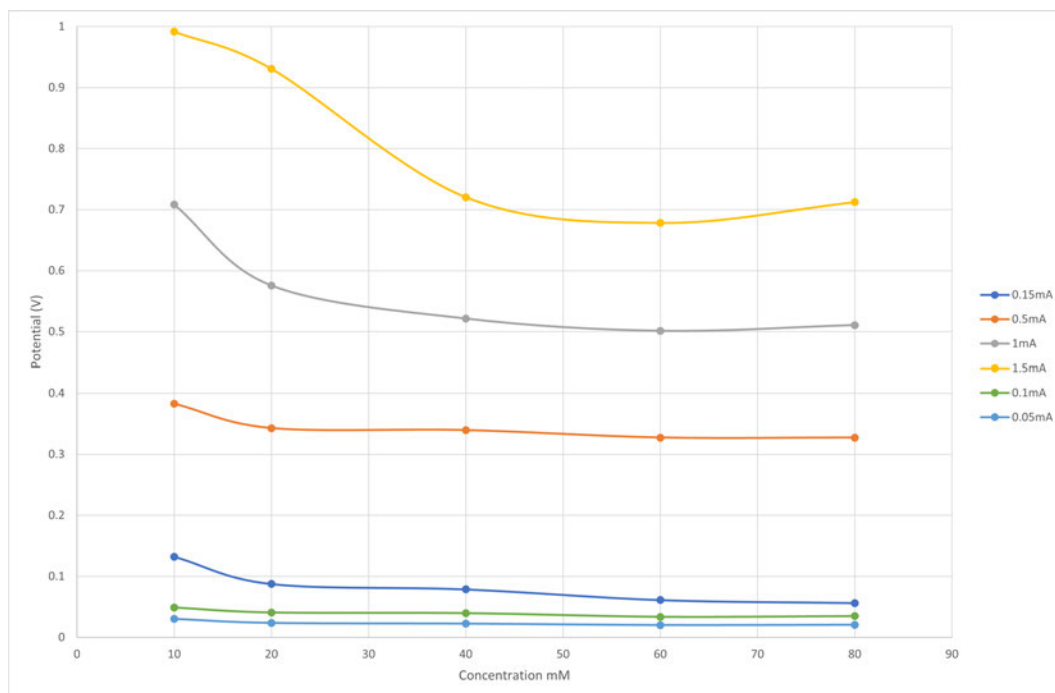
Figure 6.8: Comparison of the dose response potentials at 0.05mA, 0.1mA, 0.15mA, 0.5mA, 1mA and 1.5mA current pulses.

These results show that using a 1.5mA current is indeed the best current to use from the tested currents for the silver bar electrodes. The 1.5mA offers the largest difference in potential reading for the concentration 0-80mM range required and therefore it is

easier to distinguish between different concentrations.

These results using a 1.5mA current shows that silver electrodes can be used to determine the concentration of chloride solutions. This method can be transferred to MN electrodes to investigate whether they can be used as a sensor for chloride in the same way.

6.1.1.4 Chloride determination using MN array electrodes

The method for chloride determination was then investigated on the MN platform. The first MN devices used had a 250nm PVD coated silver layer which was then coated to give AgCl electrodes using a 100mM KCl solution and 0.5mA applied current. The response varied depending on the amount of time the AgCl coating was given. The coating of Ag to Ag/AgCl electrodes was done for 30, 45, 60 and 75s and then a dose response between 20 and 80 mM was conducted using these devices with different levels of chloride coating on $1cm^2$ arrays. These results showed a linear region and levelling off at larger concentrations. However the traces did not show the expected shape as per the theory and the previous results using solid silver electrode seen in Figure 6.7. The potential causes for this could be depletion of silver or chloride at the electrode surface during the reduction of the silver chloride process is as seen in Figure 4.7. There was not a sufficient response to measure on a 60s or 75s coating to be able to produce a dose response curve. The most likely reason for this is there was not enough silver present on the electrodes to be reduced for this length of time.

The following results are based on the devices made using a 30 and 45 second Ag/AgCl coating with a current pulse applied for 5 seconds. The potential different trace for each device coated for 30 and 45 seconds is shown in Figures 6.9 and 6.10 respectively. These show that the maximum value of the trace is increasing, this is different to previous traces as seen in Figure 6.6 for the silver bar electrodes.
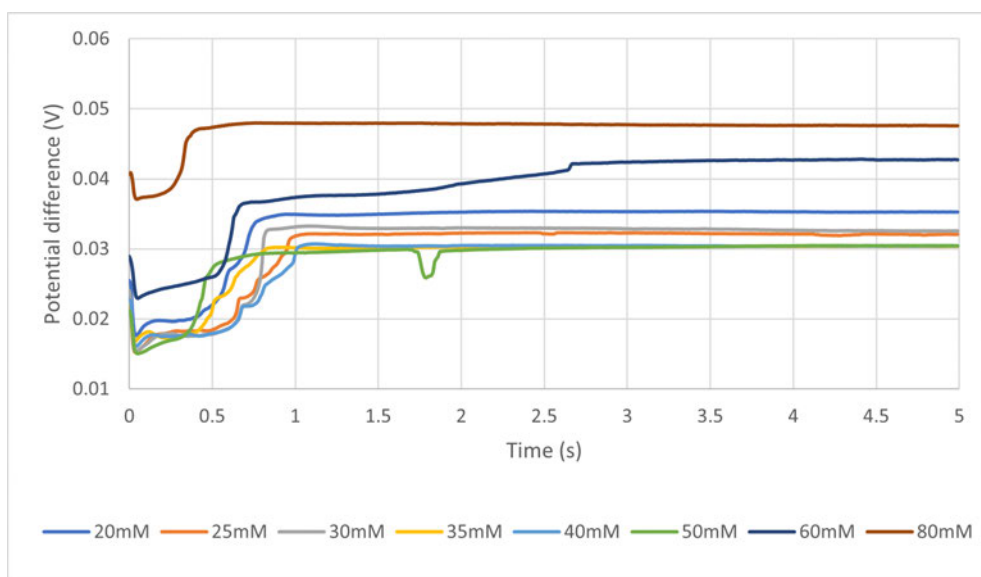
(a) 30s AgCl Device 1 chloride potential responses at various concentrations
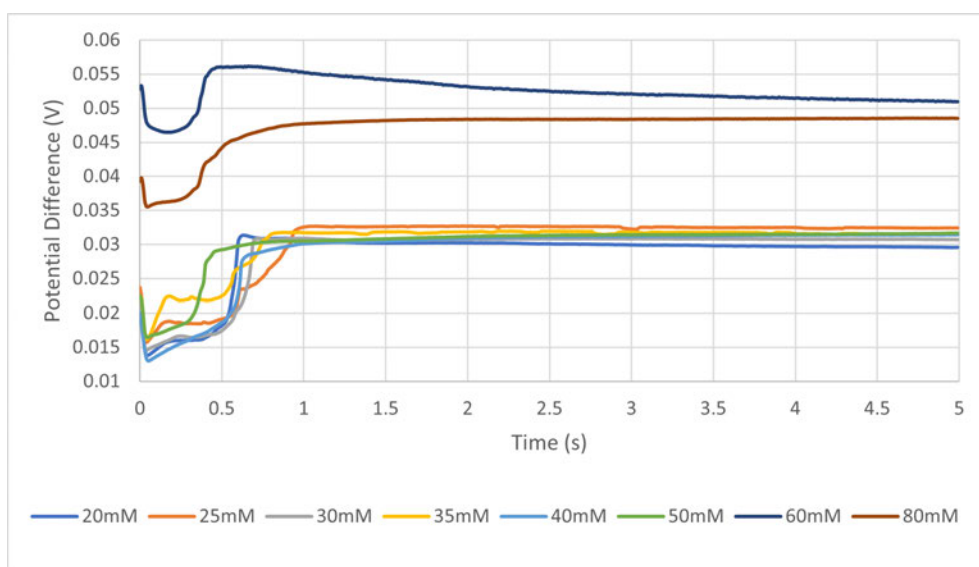
(b) 30s AgCl Device 2 chloride potential responses at various concentrations

Figure 6.9: Potential traces of chloride response using 30s AgCl coated MNs
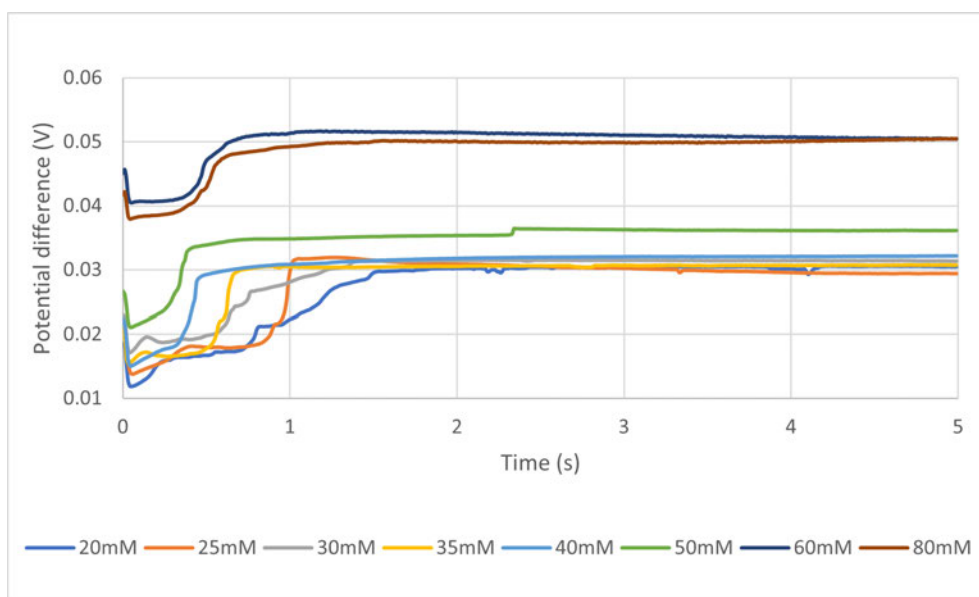
(c) 30s AgCl Device 3 chloride potential response at various concentrations

Figure 6.9: Potential traces of chloride response using 30s AgCl coated MNs
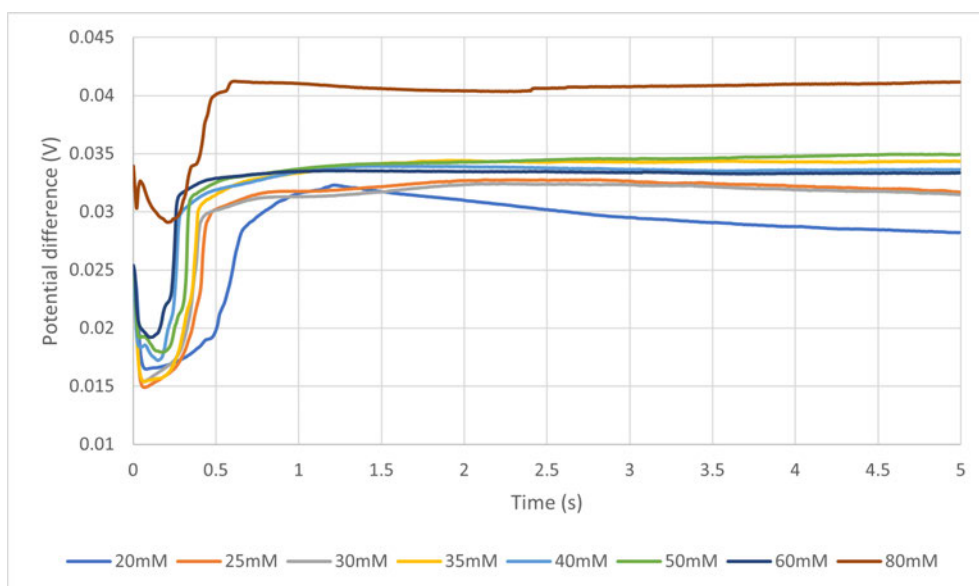
(a) 45s AgCl Device 1 chloride potential response at various concentrations

Figure 6.10: Potential traces of chloride response using 45s AgCl coated MNs
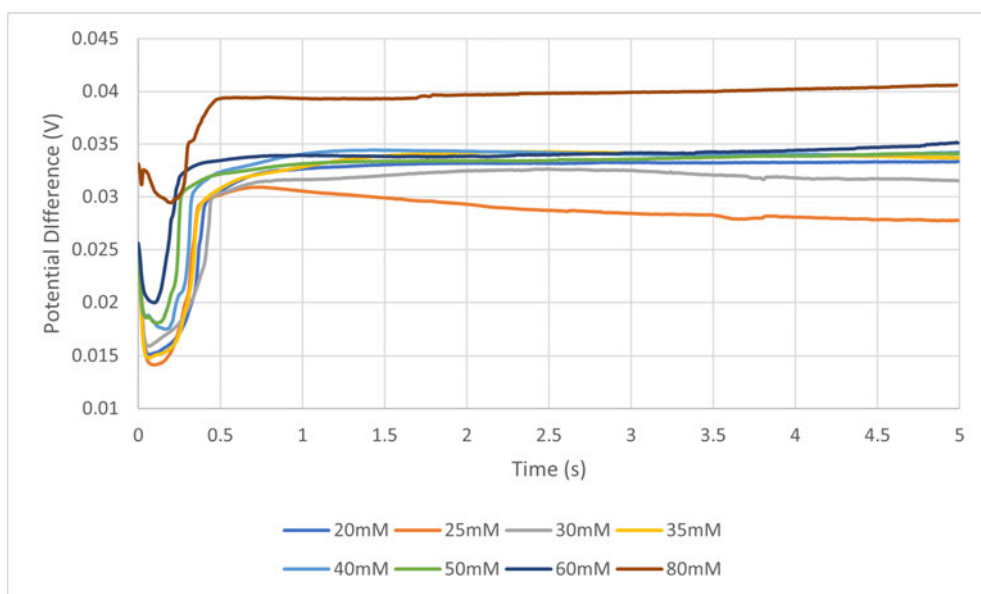
(b) 45s AgCl Device 2 chloride potential response at various concentrations
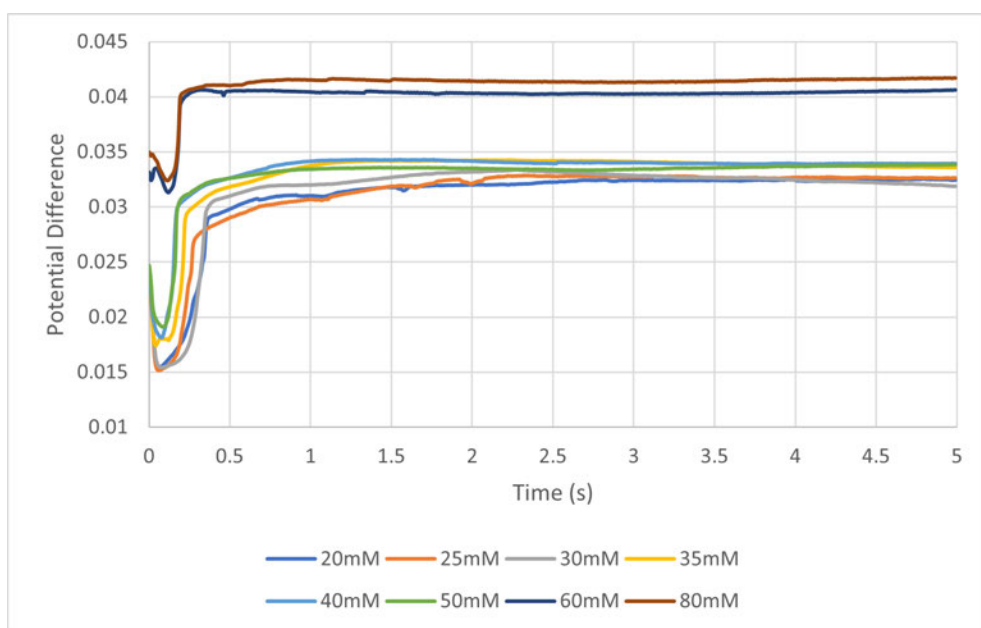
(c) 45s AgCl Device 3 chloride potential response at various concentrations

Figure 6.10: Potential traces of chloride response using 45s AgCl coated MNs

The average of the triplicate potential readings was plotted with the standard deviation error included on each point as seen in Table 6.3.

144

Table 6.3: Average and standard deviation data for dose response on devices coated in
AgCl for 30 and 45 s taken after a 5 second pulse

Dose response data for AgCl coated for 30s								
mM	20	25	30	35	40	50	60	80
Average Potential	0.0318	0.0313	0.0315	0.0309	0.0313	0.0328	0.0480	0.0489
Standard deviation	0.0025	0.0014	0.0008	0.0005	0.0007	0.0024	0.0038	0.0012
Dose response data for AgCl coated for 45s								
mM	20	25	30	35	40	50	60	80
Average Potential	0.0314	0.0307	0.0316	0.0339	0.0339	0.0343	0.0364	0.0411
Standard deviation	0.0022	0.0021	0.0002	0.0003	0.0002	0.0005	0.0031	0.0005
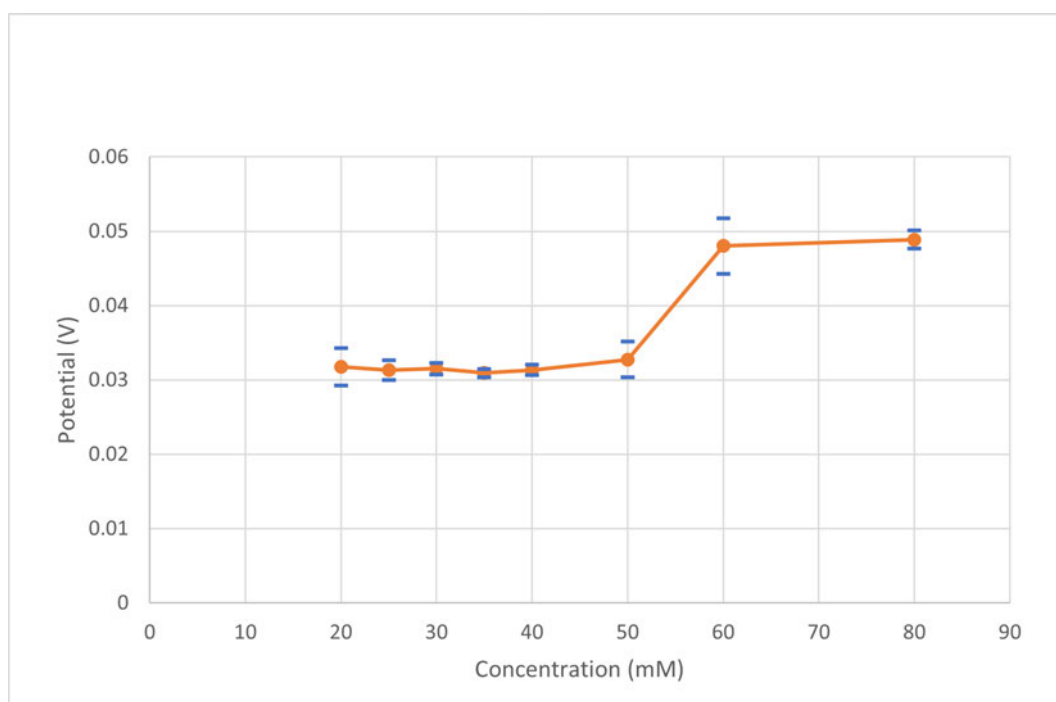
Figure 6.11: Dose response of chloride within the 20-80mM range with 30s coating
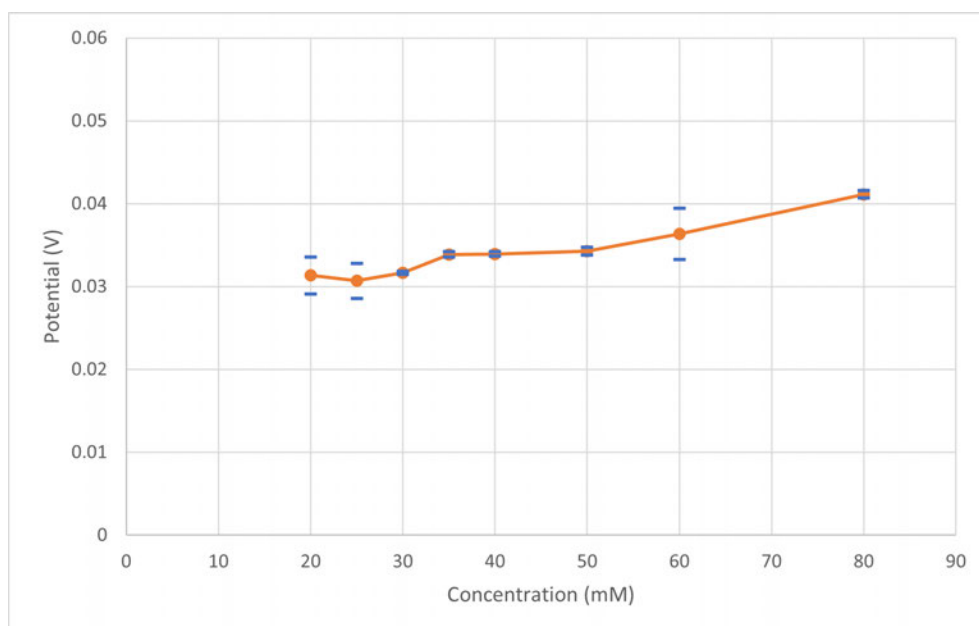
Figure 6.12: Dose response of chloride within the 20-80mM range with 45s coating

These electrodes appear to have an unexpected increase in potential which is mostly likely due to the depletion of all the available silver layer. When the silver layer is heavily depleted, it can be seen by the naked eye. The potential traces have been plotted below to further understand the underlying reactions happening in these readings for each set of dose responses. The effect is more pronounced in the electrode with the longest (45s) Ag/AgCl conversion time as this will have increased the AgCl in the Ag/AgCl ratio meaning less silver is available for conversion to AgCl during measurement. This issue did not happen with the solid silver electrodes seen in figure 6.7 which have a much more abundant supply of silver, therefore in order to alleviate the issue of silver depletion prior to use for measurement the electrodes had additional silver electroplated onto the surface to increase the thickness of the silver layer.

The silver layer of the MN arrays was increased through silver electroplating on the PVD silver surface prior to coating with chloride. The MNs were plated with silver for, 15, 30 and 45s to investigate the dose response of MN with different thicknesses of silver. The longer the plating time, the thicker the layer. The MN arrays were then

coated with chloride to be used for dose response at different concentrations of chloride solution. The potential difference traces of the 3 different silver plate thickness MN devices followed the same pattern as the theory and the results from the silver bar electrodes and these results are shown in Figure 6.13
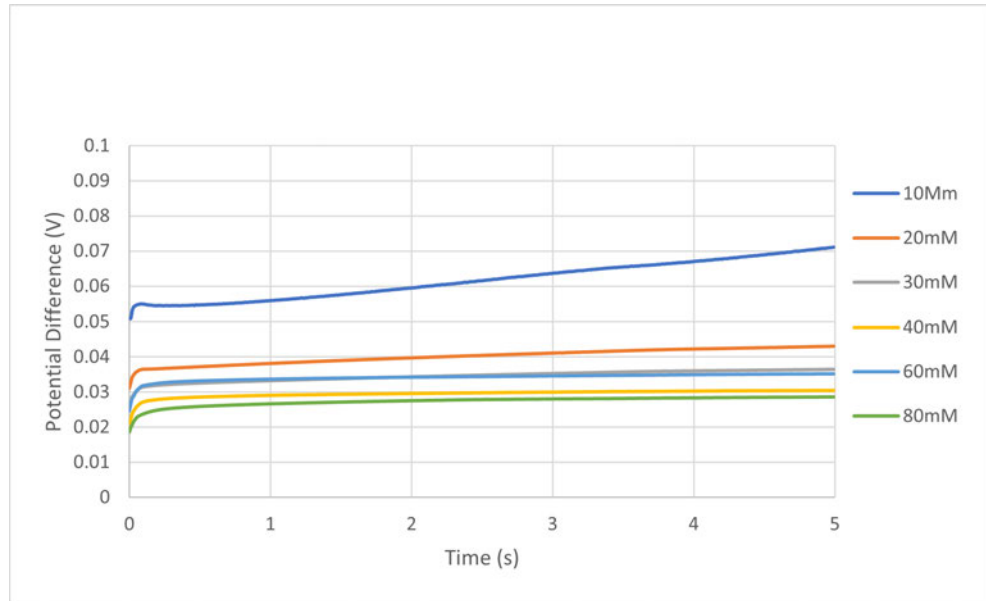
(a) Potential difference traces of 15s silver plated MNs
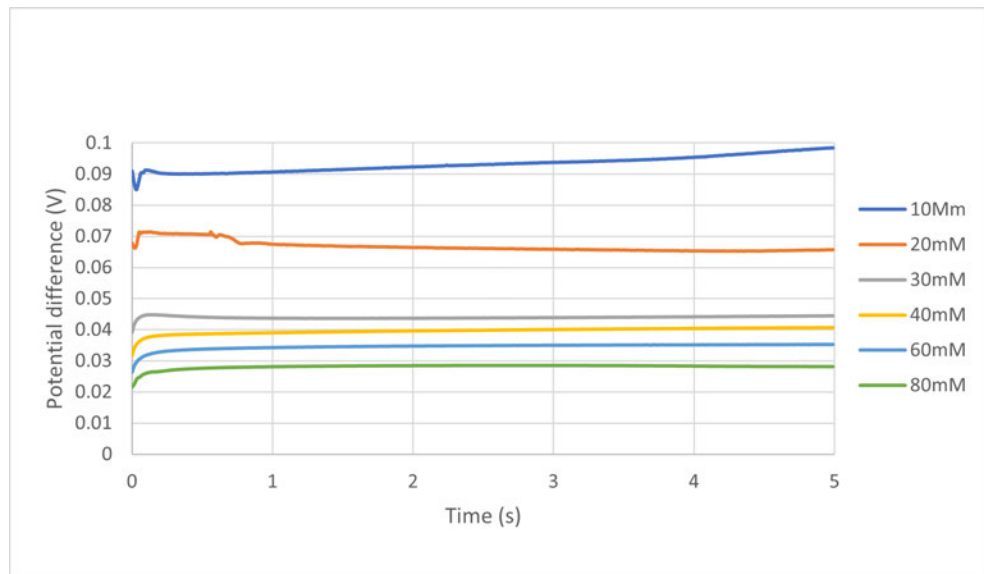
(b) Potential difference traces of 30s silver plated MNs

Figure 6.13: Potential difference traces of MNs silver plated for 15, 30 and 45s
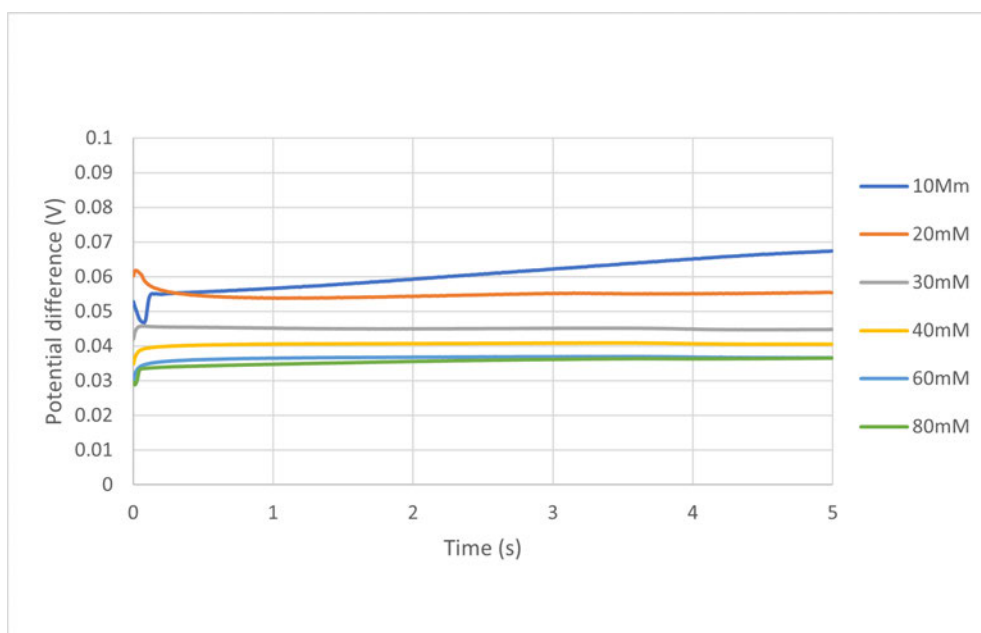
(c) Potential difference traces of 45s silver plated MNs

Figure 6.13: Potential difference traces of MNs silver plated for 15, 30 and 45s

The corresponding dose response curves for concentrations of chloride between 10mM and 80mM is plotted in Figure 6.14 using the average readings and standard deviation as shown in Table 6.4.

Table 6.4: Average and standard deviation of the resulting potential difference data from the dose response of MN arrays plated for 15, 30 and 45s taken after 5 seconds

Plating time (s)		Concentration (mM)					
		10	20	30	40	60	80
15	Average Potential	0.0718	0.0455	0.0369	0.0322	0.0332	0.0297
	Standard Deviation	0.0007	0.0024	0.0004	0.0017	0.0020	0.0011
30	Average Potential	0.0925	0.0731	0.0513	0.0457	0.0393	0.0326
	Standard Deviation	0.0059	0.0074	0.0068	0.0049	0.0040	0.0045
45	Average Potential	0.0630	0.0442	0.0326	0.0326	0.0289	0.0286
	Standard Deviation	0.0044	0.0112	0.0122	0.0081	0.0077	0.0079
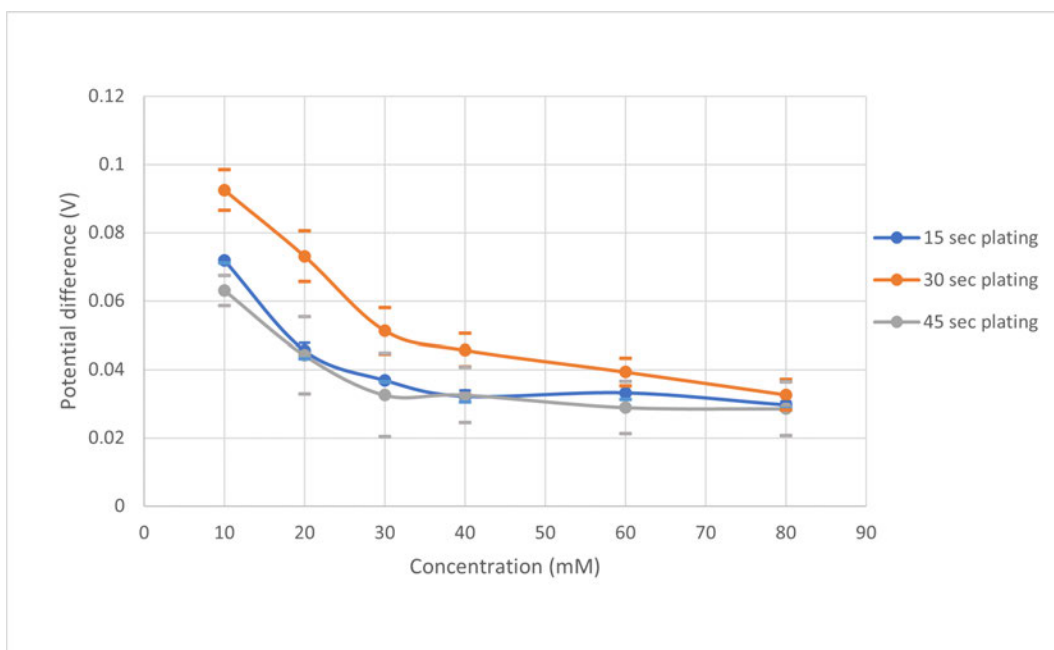
Figure 6.14: Dose response of chloride on silver plated then Ag/AgCl converted electrodes

The results show that for each silver plated MN array the potential difference decreased as the concentration of chloride increased. The curves tended towards a plateau at the higher concentrations of chloride which matched the trend in the results from the silver bar electrodes (Figure 6.7). The error bars from the response on the 45s plated MNs were larger than the error bars from the 15s and 30s MN arrays showing that the 45s plated MNs offered less reliable results. Both the 15 and 30s plated MNs had good reliability however the 30s plated MNs had a larger response and less of a plateau at higher chloride concentrations meaning that these would have the more accurate results when determining chloride concentration.

In summary, these results show that MN platforms can be adapted into working chloride sensors and have the potential to be further developed into devices suitable for use for in vivo testing of interstitial chloride.

6.1.2 Determination of cholesterol

Cholesterol is a type of lipid called a sterol, found in the human body. It is an important analyte to determine as it can be indicative of a person at higher risk of cardiovascular diseases and heart attack or stroke. It can be measured by different methods including similar methods used to determine glucose concentration.

6.1.2.1 Theory of cholesterol detection

Both cholesterol and glucose can be determined by potentiometry by using a platinum electrode functionalised with an immobilised enzyme such as cholesterol oxidase or glucose oxidase as the working electrode alongside a reference electrode or chronoamperometry using similar electrodes but applying a constant potential and measuring over time. There are 3 mechanism types to determine the concentration of cholesterol. The first generation sensors, work by detecting hydrogen peroxide, second generation sensors add a mediator to catalyse the reaction between the hydrogen peroxide and the surface and third generation sensors are direct electron transfer on the metal surface.

The first generation sensors utilise the reaction of cholesterol oxidase with oxygen to produce hydrogen peroxide. Cholesterol oxidase (ChOx) catalyses the reaction of free cholesterol to cholestenone (Cholest-4-en-3-one) Equation 6.7. The cofactor Flavin adenine dinucleotide (FAD) in ChOx is reduced which then reacts with dissolved oxygen (O_2) and produces hydrogen peroxide (H_2O_2) as seen in Figure 6.15. The H_2O_2 is then measured by the sensor by oxidising it back to dissolved oxygen and water It is then the oxidation and reduction of the hydrogen peroxide which is monitored. The equations

and mechanism are shown in Equations 6.7 and 6.8 [121, 122].

$$Cholesterol + O_2 \rightarrow Cholest - 4 - en - 3 - one + H_2O_2 \qquad (6.7)$$

$$H_2O_2 \rightarrow O_2 + 2H^+ + 2e^- \qquad (6.8)$$
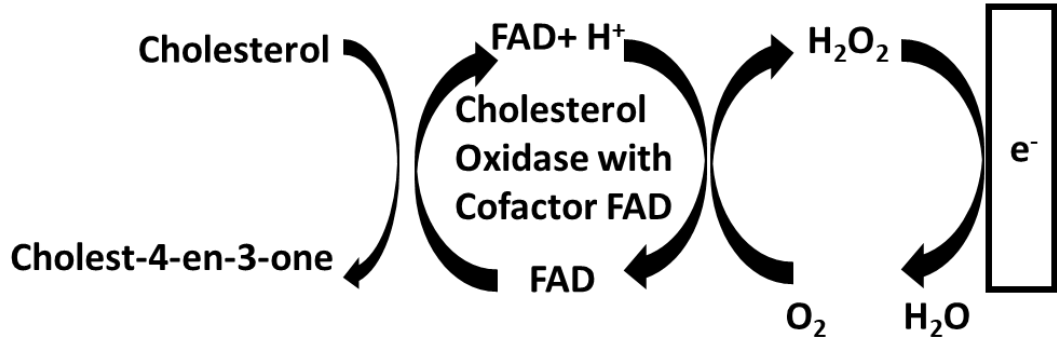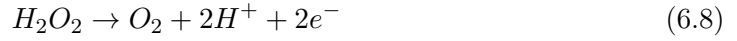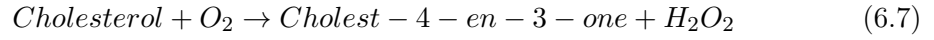
Figure 6.15: Schematic of the mechanism of a first-generation Cholesterol sensor

These first generation mechanism is the one being used for further investigation of the determination of chloride. To start, the sensors will be made to determine glucose using this method as this has previously been investigated [105] and can be used to test the suitability of this method on the printed MNs. If successful on the printed polymer MNs with determination of glucose, then cholesterol will be investigated. Due to the reaction being enzymatic, the resulting dose responses can be plotted as a Michaelis-Menten plot. The Michaelis-Menten equation derives from the equation for enzymatic reactions and is a well known and simple approach to enzyme kinetics. The equation relates substrate concentration to the velocity in a system where a substrate reversibly binds to an enzyme to form a complex that then irreversibly reacts and creates a product and regenerates the free enzyme. As depicted in Equation 6.9 where S is the substrate, E is the enzyme, ES is the complex and P is the product.

$$E + S \rightleftharpoons ES \longrightarrow E + P \qquad (6.9)$$

The Michaelis-Menten Equation 6.10 can be seen below, where S_c is the concentration of the substrate, v is the velocity, V_{max} is the max velocity achieved in the system at the maximum substrate concentrations, and K_M the Michaelis constant, which is the

substrate concentration when the reaction velocity is half of V_{max}.

$$v = \frac{V_{max}S_c}{K_M + S_c} \qquad (6.10)$$

The plot of the Michaelis-Menten equation can be depicted as a graph showing the predicted velocity as a function of the substrate concentration, depicting the parameters of V_{max} and K_M shown in Figure 6.16 [186].
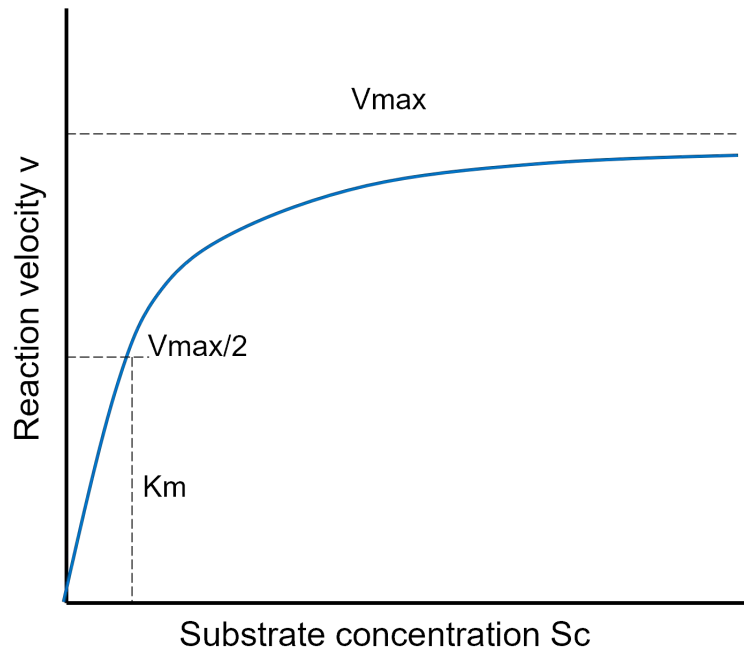
Figure 6.16: Michaelis-Menten plot depicting the reaction velocity as a function of the substrate concentration, denoting the values V_{max} and K_M

6.1.2.2 Determination of glucose on Pt MN arrays

Glucose is one of the most common analytes that MN sensing devices have been developed for and due to the enzyme glucose oxidase being similar to cholesterol oxidase the fabricated polymer MNs were functionalised and used for the determination of glucose to prove they could be used as an enzymatic sensor. Previously coated and wire bonded MNs were electro polymerised to immobilise glucose oxidase with an entrapment of polyphenols on the platinum surface of the electrode utilising the method from

Sharma et al [105].

Glucose solutions were made using 10 ml of 100mM PBS and 100mg glucose to make a 50mM stock solution which was subsequently used to make a serial dilution to obtain solutions with concentrations ranging from 0-40mM solutions as this is the expected concentration range in the ISF.

Chronoamperometry at 0.7V was performed on the MN devices to determine the glucose dose response. First PBS was drop cast onto the MN surface, 0V was applied for 5 seconds and chronoamperometry at 0.7 volts was performed for 600s, this solution was used as the 0mM solution and to remove any unreacted phenol before the glucose was added. Then concentrations of 2.5mM, 5mM, 10mM, 20mM and 40mM were consecutively drop cast, left for 5 minutes, then 0V was applied for 5 seconds and the samples run at a 0.7V potential for 60s. From the trace of the PBS solution a plateau was reached after 60s therefore it was not necessary to apply the potential for more than 60s. The current traces for each concentration of glucose are illustrated in Figure 6.17. These show an increase in the resultant current at different concentrations of glucose.
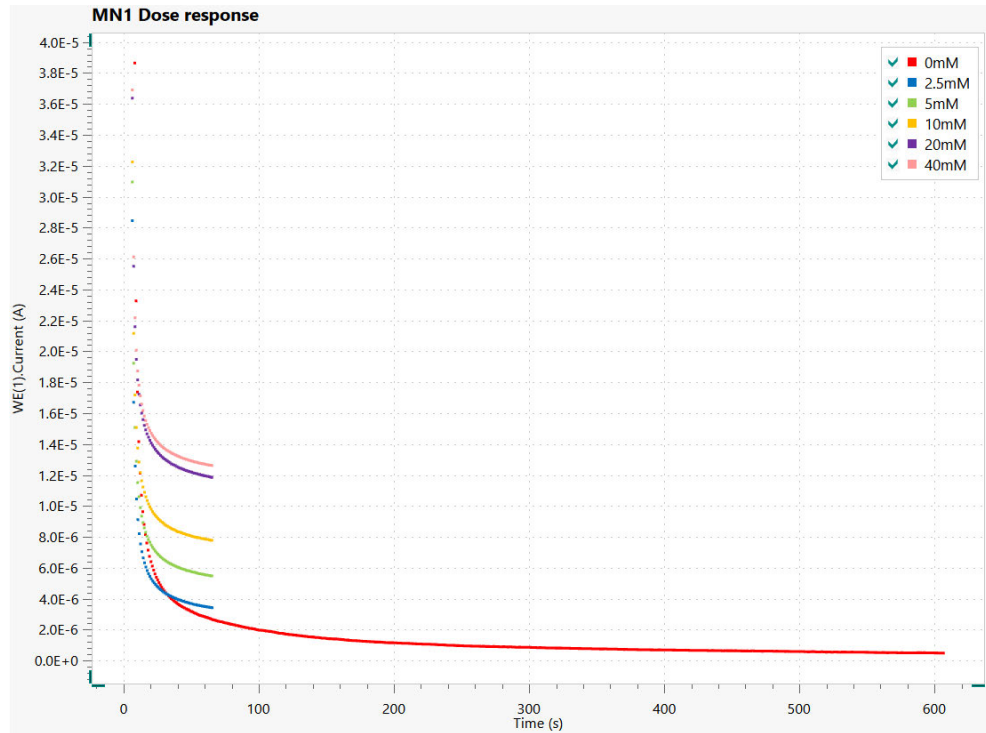
(a) Resultant current from chronoamperometry of glucose concentrations MN1

Figure 6.17: The current traces from chronoamperometry of different concentrations of glucose for 2 devices

153
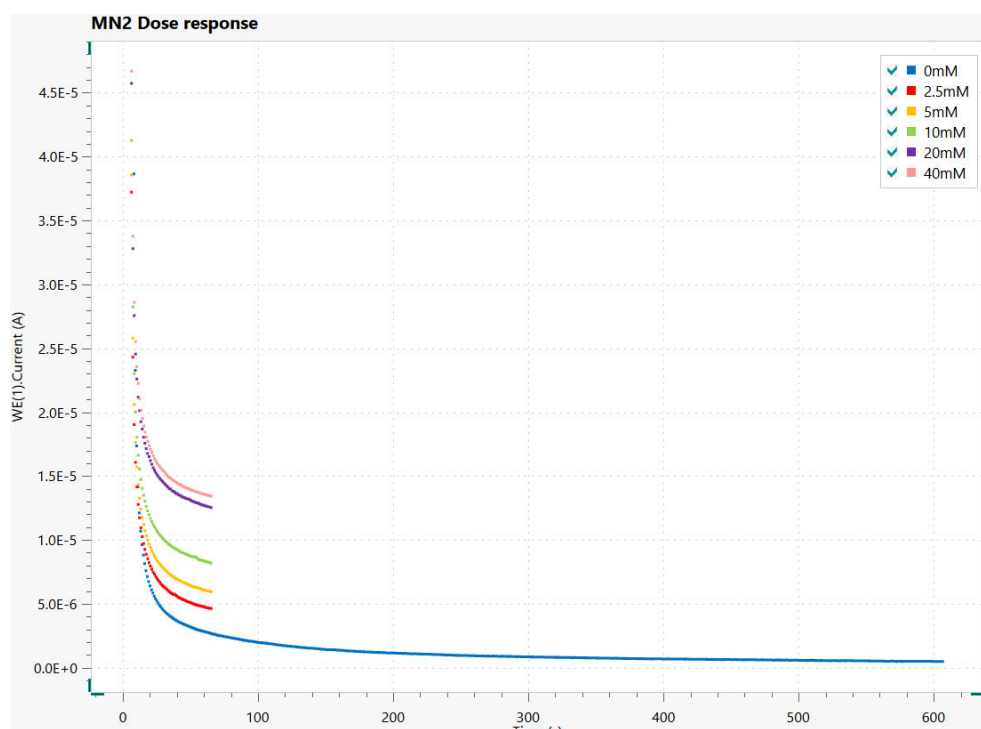
(b) Resultant current from chronoamperometry of glucose concentrations MN2

Figure 6.17: The current traces from chronoamperometry of different concentrations of glucose for 2 devices

The final current values after 60s for each concentration were recorded and used to create a Michaelis-Menten plot of the dose response. These values are shown in Table 6.5.

Table 6.5: Final current values after 60s for glucose concentrations

	Current (A)	
Concentration (mM)	MN1	MN2
0	4.88E-07	1.93E-06
2.5	3.41E-06	4.63E-06
5	5.48E-06	5.94E-06
10	7.78E-06	8.18E-06
20	1.19E-05	1.25E-05
40	1.26E-05	1.34E-05

From Table 6.5 the following dose response was plotted as shown in Figure 6.18.
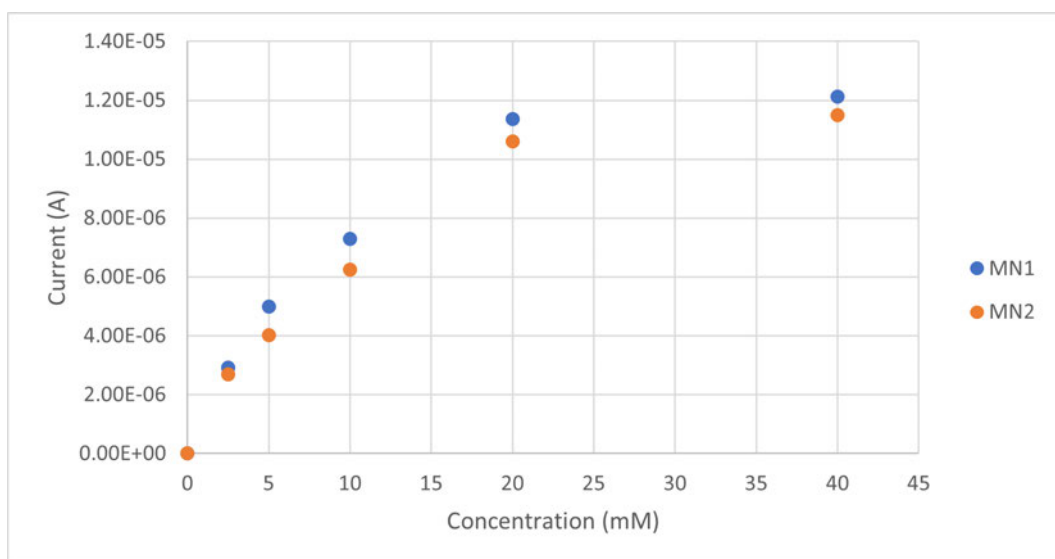
Figure 6.18: Dose response of glucose on Pt MN

This shows the two MN devices were successful in detecting this range of concentrations of glucose. The linear region was between 2.5 and 20mM glucose which was in line with the concentrations of glucose found in the body.

Therefore the devices could then be investigated using cholesterol oxidase to determine cholesterol concentration.

6.1.2.3 Determination of cholesterol on Pt MN arrays

Previously coated and wire bonded platinum MNs electrodes were electro polymerised to immobilise cholesterol oxidase with an entrapment of polyphenols on the platinum surface of the electrode and then when dried they were used for cholesterol sensing, The set up for this was a platinum coated MN Array electrode used as the working electrode, a platinum wire counter electrode and and a silver/silver chloride reference electrode. There is potential for devices using all integrated MN electrodes rather than external electrodes. This would be a requirement for testing/using in real skin.
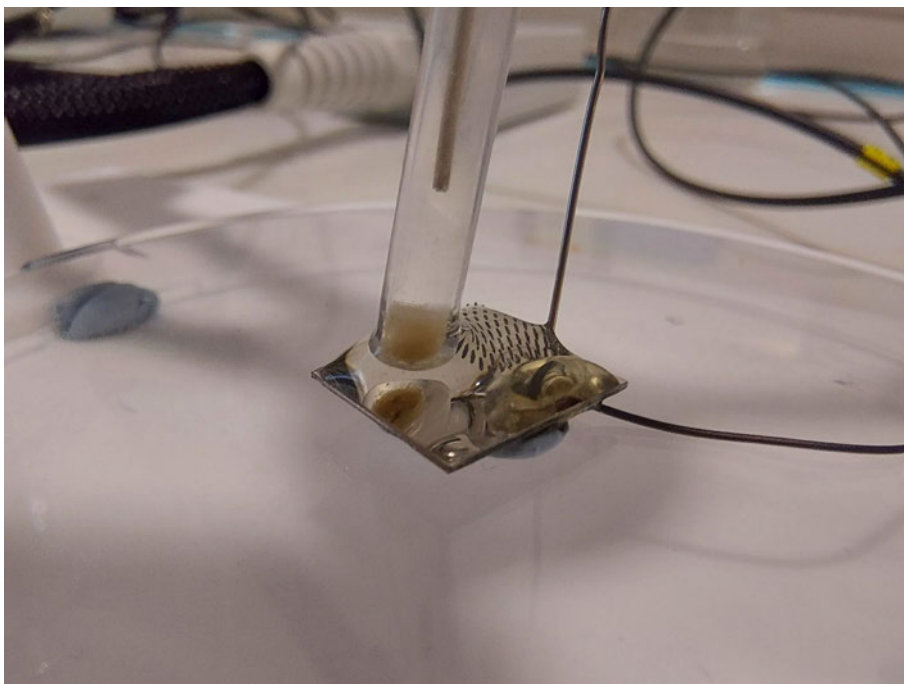
Figure 6.19: Cholesterol sensing set up

Cholesterol solutions were made with alcohol, Triton X and PBS in the ratio of 10:4:86 by weight as described by Yldrmoglu [118]. The solutions did not fully dissolve therefore a higher proportion of Triton X and ethanol was used to aid solubility. PBS was used as a base for the solutions as it increases the electro conductivity of the solutions. The cholesterol was slowly heated in ethanol and Triton X to 60°C until the solution turned clear. PBS was then added which turned the solution cloudy. It was then heated in a water bath at 60°C for 30 minutes due to a higher solubility in hot alcohol. After this the solutions were left to cool and they turned clear if the cholesterol dissolved. The cholesterol dissolved in a solution with a ratio of 20:8:72 of ethanol:tritonX:PBS giving a clear solution. A 20mM cholesterol solution using this ratio was made which was then diluted to concentrations from 1.25mM to 15mM using the solution the cholesterol had been dissolved in. This was the range was used as it covers the concentration range found in bodily fluids.

Chronoamperometry at 0.7V was performed on the MN devices to determine the cholesterol dose response. Using the same method as for the glucose sensing, PBS was drop cast onto the surface. 0V was applied for 5 seconds and chronoamperometry at 0.7 volts was performed for 600s, this was used to remove any unreacted phenol before the cholesterol was added. The diluting solution was drop cast and then run under

156

the same conditions as the PBS so that it could be used as the 0mM solution. Then concentrations 1.25mM, 2.5mM, 5 mM, 10mM, and 15 mM were consecutively drop cast. Each solution was left for 5 minutes before 0V was applied for 5 seconds and then the sample run at a 0.7V potential for 150s. Each of the concentrations of cholesterol was run for 150 seconds only as this was the time point of plateau during the dilution solution run.

The following experiments were conducted using the cholesterol concentrations to produce the following current traces seen in Figure 6.20 and the traces of the PBS only and the dilution solution are shown in 6.21.
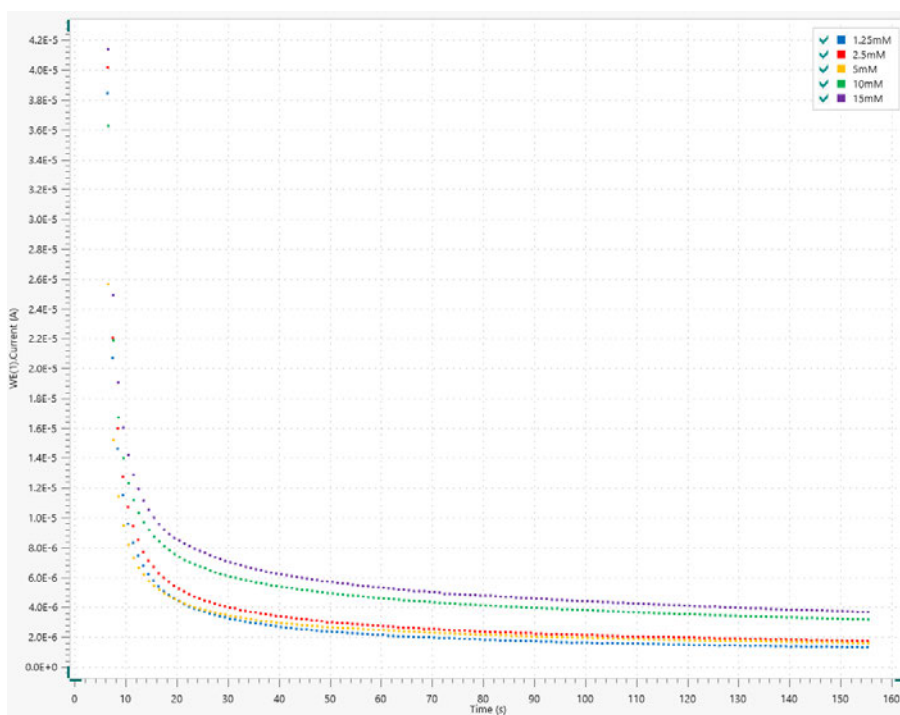
Figure 6.20: Current traces of 1.25mM, 2.5mM, 5mM, 10mM 15mM cholesterol response using the Enzyme immobilised Pt MNs using

157
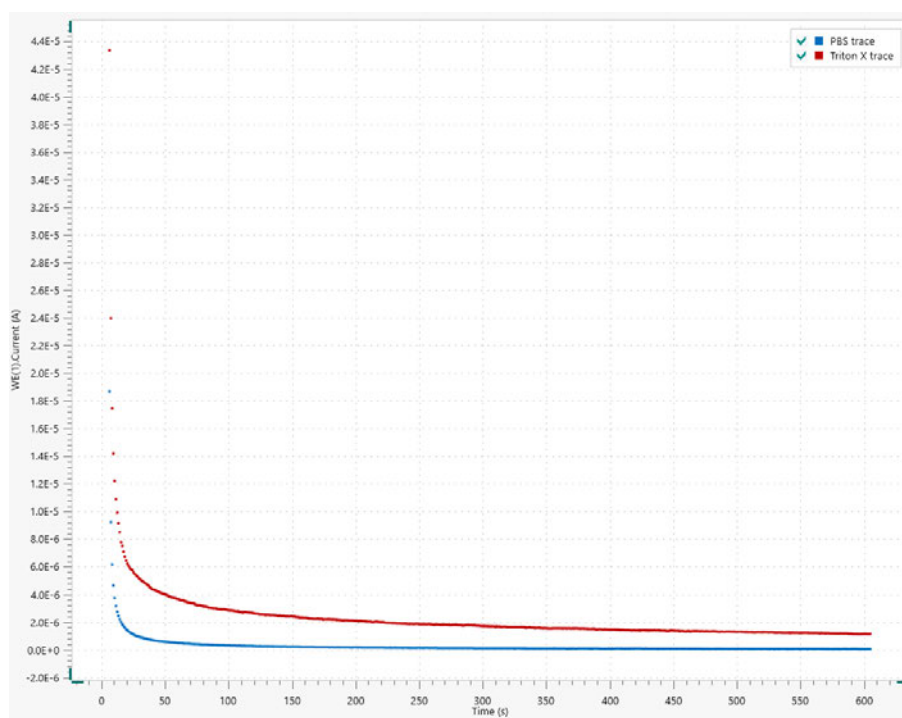
Figure 6.21: Current traces of the PBS alone and dilution solution including Triton X, ethanol and PBS response using the Enzyme immobilised Pt MNs

The graphs in Figure 6.22 have been plotted compensating for the background solution utilising the data at the end of the traces at time 155s as seen in Table 6.6. The resulting graph using the dilution solution as the background removes the background current giving a more linear plot through 0.

Table 6.6: Cholesterol sensing data including with and without the background current from the dilution solution.

Concentration (mM)	Average Current at 155s (A)	Current adjusted for background (A)
1.25	1.19E-06	8.95E-08
2.5	1.70E-06	5.98E-07
5	1.83E-06	7.25E-07
10	2.94E-06	1.83E-06
15	3.50E-06	2.39E-06
0 (Dilution solution inc Triton X)	1.14E-06	0
0 (PBS)	3.05E-08	0
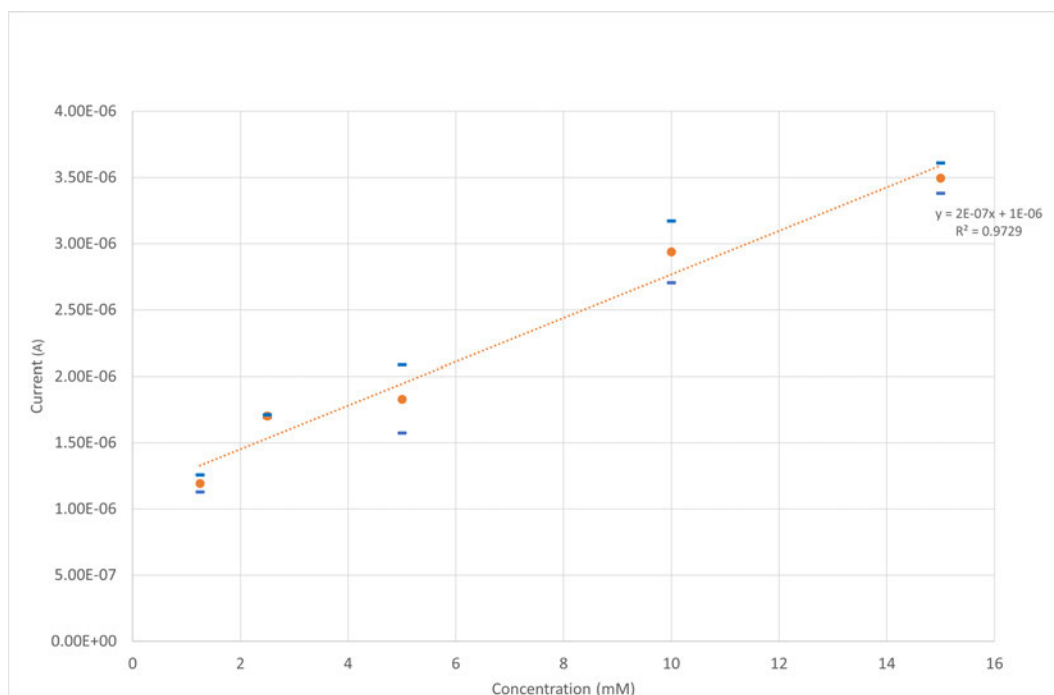
(a) Cholesterol in the Triton X, Ethanol, PBS mix dose response

Figure 6.22: Cholesterol sensing dose response

159
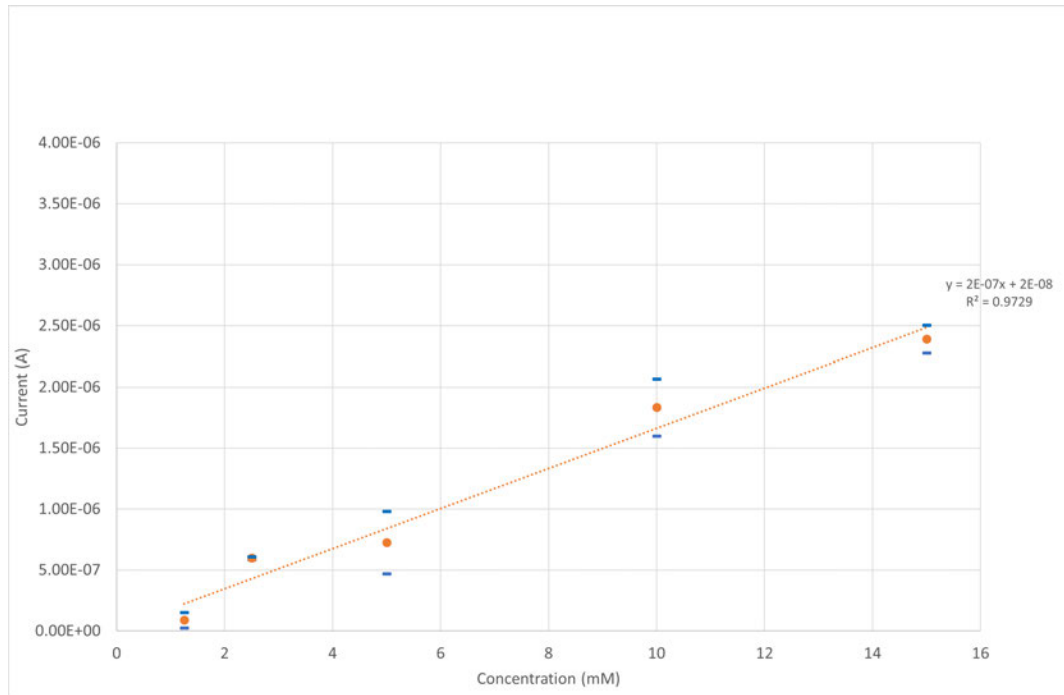
(b) Cholesterol dose response minus the values for Triton X mix solution

Figure 6.22: Cholesterol sensing dose response

This shows the MN devices were successful in detecting this range of concentrations of cholesterol. The linear region was between 1.25 and 15mM cholesterol which is in line with concentrations found in the human body.

6.2 Microneedles for Therapeutic Delivery

MNs have already been used in drug delivery for a multitude of different sorts of drugs for many different conditions, diseases and illnesses. The MNs made as described previously are being investigated for their effectiveness at drug delivery. Their ability to penetrate the skin has been proven therefore the next step to their effectiveness is to study their capability to deliver drug across the *stratum corneum* to induce a therapeutic response. The aim is to facilitate and improve the transdermal delivery of these drugs past the *stratum corneum* layer into the lower layers of the skin where in vivo the drug would then be transported by the body. In vitro studies were conducted to analyse the passive transport of the drug through the skin. To illustrate the drug delivery in context, the delivery of a positive control using a hypodermic needle and negative control of skin only alongside the results from silicon MNs made using photolithography and etching.

The silicon MNs are very sharp but expensive and can be more challenging to produce. The polymer MN arrays that are used have a much cheaper manufacture cost, due to the fact that they require less processing and cheaper equipment.

6.2.1 Calcein drug delivery

Calcein is a fluorescent small molecule drug that has been used many times to illustrate drug delivery. It can be quantified using a fluorescent microscope or plate reader therefore has an easy method for detection. It can be used as a standard drug used for testing drug delivery methods due to the lipophobicity which prevents independent natural diffusion and penetration through the *stratum corneum*. This lends it to the task of illustrating the transport through the skin due to the penetration of MNs through the *stratum corneum*. Franz cell experiments were used to model the transport of the calcein through the porcine skin after the application of MNs. Prior to this a 2.5μg/ml concentration calcein solution was made up and 50μl was pipetted onto the open area where the MNs had been applied. In order to determine the concentrations, first a calibration curve was plotted using dilutions in the range of 0-2.5 μg/ml. The calibration for this solution gave a trend line in the form y=mx+c with an intercept at 0 and an m value of 3501.8 which was used to convert from the fluorescence to concentration and shown in Figure 6.23
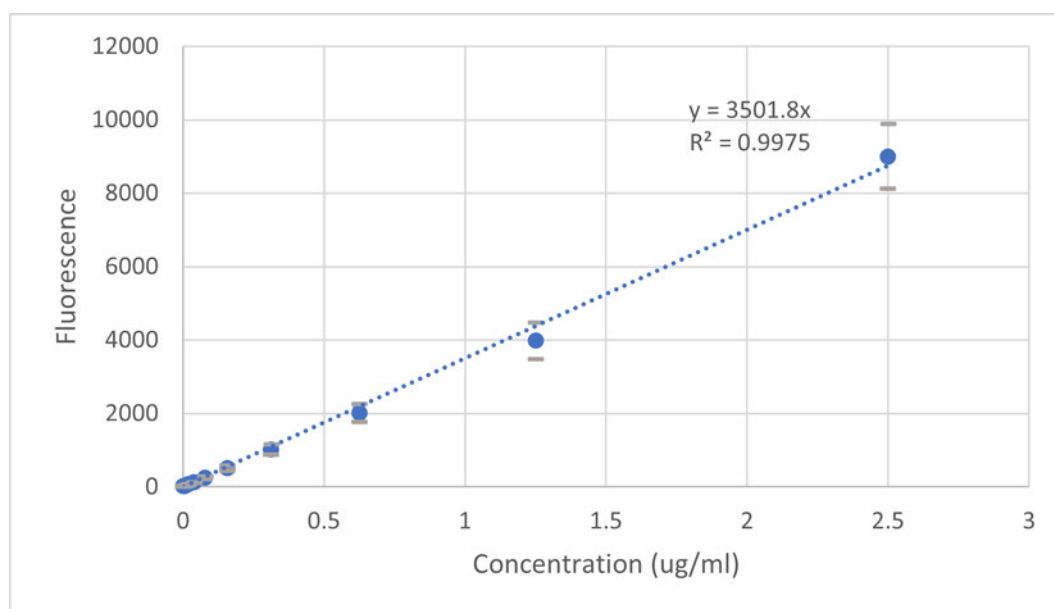
Figure 6.23: Calibration curve of calcein showing the concentration in relation to the fluorescence with the standard deviation

The samples were taken at time points over a 24 hour period including 5min, 15min, 30min, 1hr, 2hrs, 4hrs, 6hrs, 8hrs and 24hrs. These were taken by displacing the liquid in the receiving chamber with 400μl at each time point and then the samples quantified in the microplate reader. The calibration curve was utilised to find the concentrations of calcein that coincided with the fluorescent values acquired from each sample. These concentrations were then analysed to show the cumulative concentration data for each of the cells. Printed polymer MNs and silicon MNs were investigated for their efficiency in assisting calcein drug delivery across the skin barrier. They were compared to a positive control using a hypodermic needle illustrating ideal diffusion of drug and a negative control of the skin with no application of needles, as seen in Figure 6.24 .
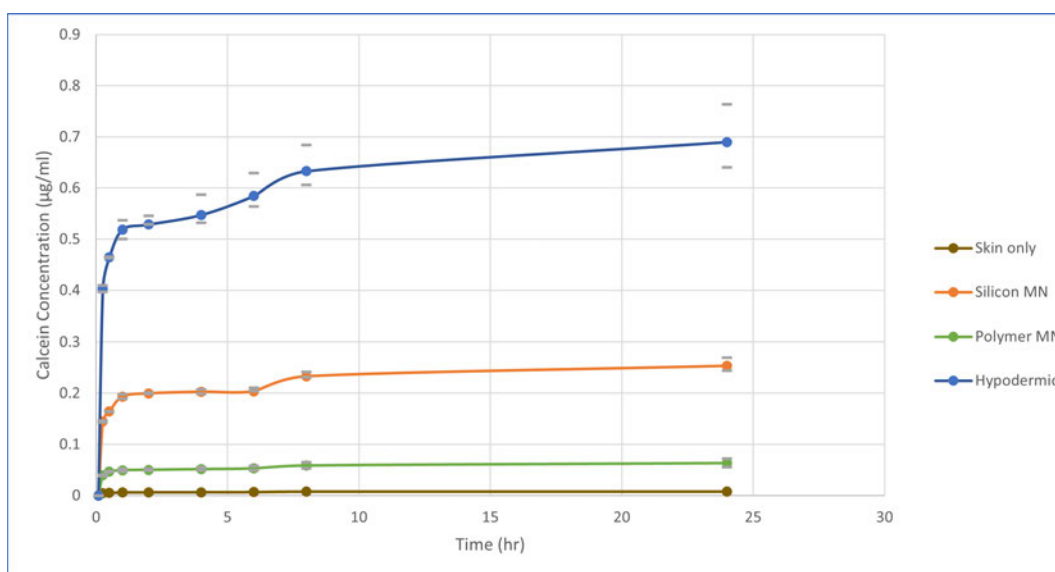
Figure 6.24: Cumulative delivery of calcein

Flux is calculated using the mass worked out from the concentration and divided by the time point and area of orifice, as seen in Table 6.7.

Table 6.7: Flux rate of Calcein over time

| Time (hr) | Flux (Js (µg/cm2/hr)) | | | |
	Polymer MNs	Silicon MNs	Hypodermic	Skin
0.083	3.194	13.499	35.925	0.404
0.25	0.069	0.839	1.792	0.015
0.5	0.125	0.664	1.667	0.014
1	0.080	0.516	1.177	0.011
2	0.042	0.277	0.619	0.006
4	0.023	0.134	0.399	0.004
6	0.014	0.088	0.187	0.003
8	0.015	0.089	0.179	0.003
24	0.004	0.024	0.045	0.001

The remaining skin was subject to the tape stripping and homogenisation procedures as previously explained in chapter 2. The solutions obtained were quantified using the fluorescent plate reader and the corresponding concentrations and masses were calculated. The first tape strip taken was the equivalent of the non absorbed drug, the next 10 tape strips taken were equivalent to the amount of drug left in the epidermis and the homogenisation was equivalent to the amount of drug remaining in the skin. The percentage permeation profile of the skin in the Franz cells treated with hypodermic needle, polymer MN and no treatment are shown in the stacked bar chart in Figure 6.25 below.
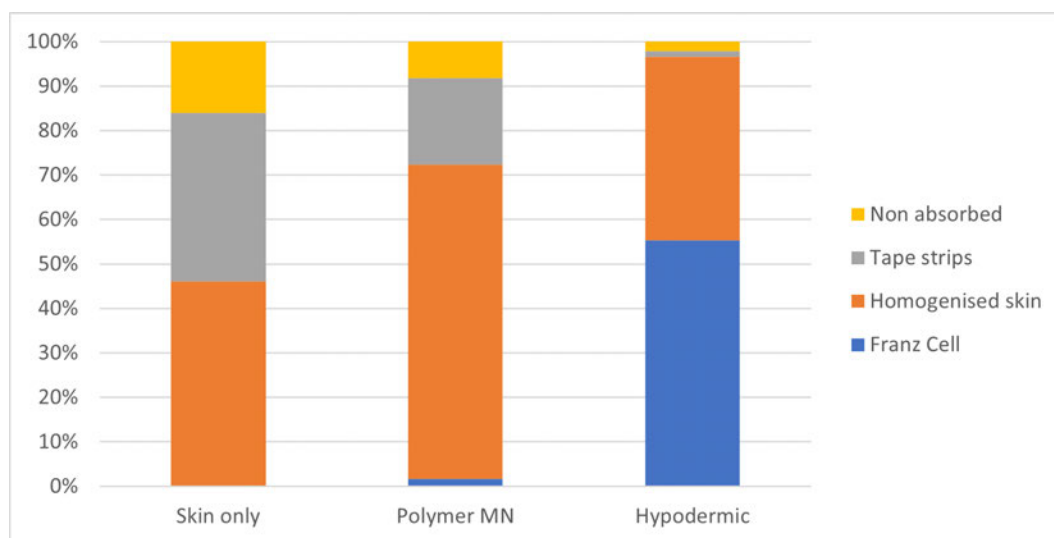
Figure 6.25: Percentage permeation of calcein in the skin using hypodermic, polymer MNs and skin only.

The results from the Franz cells show that the amount of calcein that diffuses through the Franz cell is the greatest with a hypodermic needle, the silicon MNs were about 50% less effective as hypodermic , followed by the polymer MNs which were about 50% less effective again at delivering across the skin into the Franz cell chamber over a 24hour period. While the polymer MNs were not as successful at delivering across the skin, there was a 70% delivery into the epidermis and dermis of the porcine skin Figure 6.25. This is just through passive diffusion and in a live subject there can be active diffusion from these layers of the skin aswell. The skin only result confirmed that the drug did not pass through the skin into the PBS at all without a MN or hypodermic needle applied. The flux shows that the drug permeated nearer the beginning of the experiment.

6.2.2 Pravastatin drug delivery

If cholesterol is an important analyte to monitor in patients then it would be prudent to investigate the use of MNs to deliver a drug that can be used to manage high cholesterol. Statins are the type of drug usually used to treat high levels of cholesterol including high levels of LDL cholesterol. Pravastatin is a type of statin drug which is water soluble which lends well to testing using PBS as the solvent for drug delivery investigations. Pravastatin was quantified by using HPLC, this takes longer to obtain results than a plate reader but gives accurate results by separating the pravastatin from any other components in the samples. Franz cell experiments were used to model the transport of the pravastatin through the porcine skin after the application of MNs. Solutions of 1mg/ml and 10mg/ml concentrations of pravastatin was made up in 0.1M PBS and 50µl was pipetted onto the open area where the MNs had been applied. In order to determine the concentrations, first a calibration curve as shown in Figure 6.26.
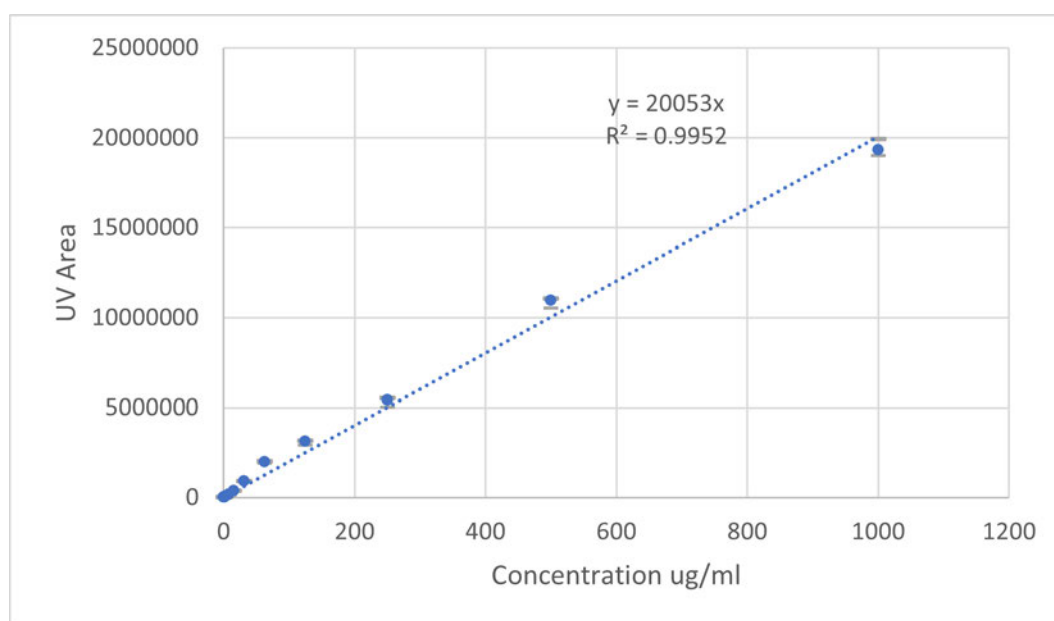
Figure 6.26: Pravastatin calibration curve

The samples were taken at time points over a 24 hour period including 5min, 15min, 30min, 1hr, 2hrs, 4hrs, 6hrs, 8hrs and 24hrs. These were taken by displacing the liquid in the receiving chamber with 400μl at each time point and then the samples were quantified using the HPLC. The calibration curve was utilised to find the concentrations of pravastatin that coincided with the UV area values acquired from each sample. These concentrations were then analysed to show the cumulative concentration data for each of the cells. Printed polymer MNs and silicon MNs were investigated for their efficiency in assisting pravastatin drug delivery across the skin barrier. They were compared to a positive control using a hypodermic needle illustrating ideal diffusion of drug and a negative control of the skin with no application of needles. Figure 6.27 shows the cumulative results of 1mg/ml drug added.
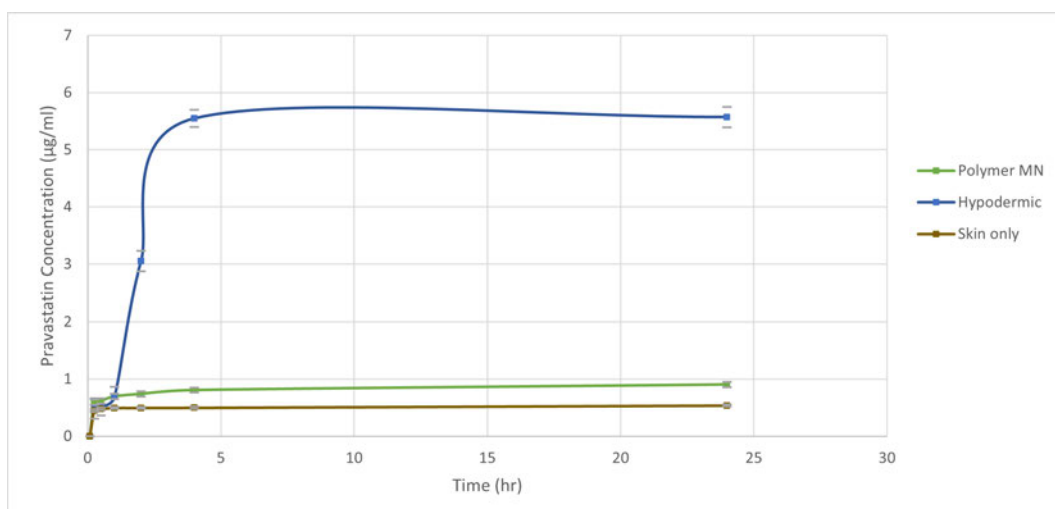
Figure 6.27: 1mg/ml pravastatin poke and patch drug delivery comparing Hypodermic and microneedles

Figure 6.28 shows the cumulative results of 10mg/ml drug added with the data used shown in Table 6.8.

Table 6.8: Cumulative concentration of Pravastatin over time

Time (hr)	Concentration (µg/ml)			
	Polymer MNs	Silicon MNs	Hypodermic	Skin
0.083	0	0	0	0
0.25	49.166	1.786	3.407	1.694
0.5	53.597	39.584	38.341	1.722
1	57.975	47.955	39.919	1.780
2	61.928	51.992	47.988	1.805
4	62.684	87.878	56.368	1.820
6	72.377	97.107	86.014	2.159
8	73.225	111.696	107.739	2.481
24	82.707	174.541	146.071	2.503
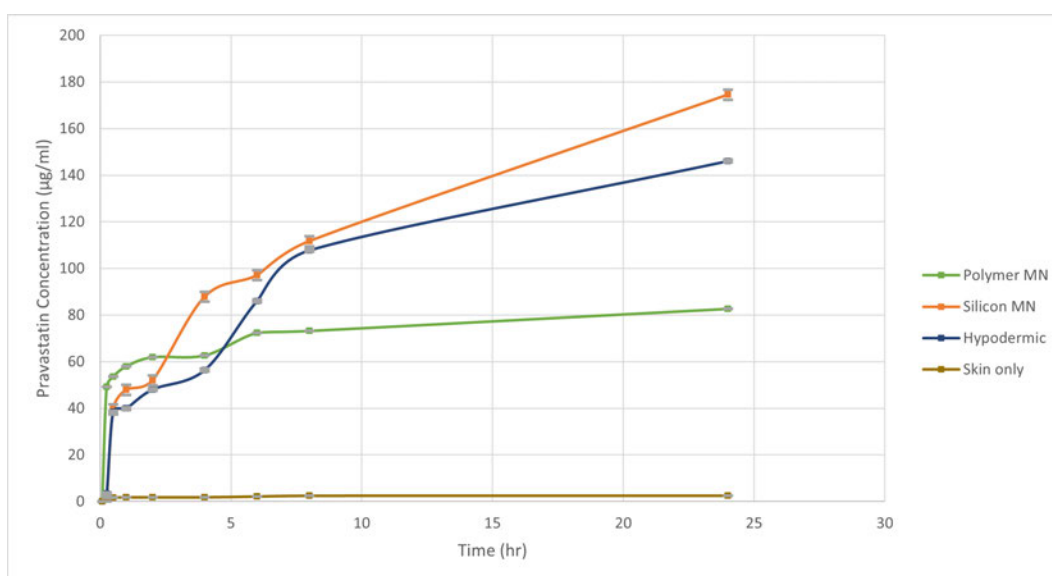
Figure 6.28: 10mg/ml pravastatin poke and patch drug delivery comparing Hypodermic and microneedles

Flux is calculated using the concentration divided by the time point and area. Table 6.9 shows the flux rates for the 1mg/ml pravastatin applied and Table 6.10 shows the flux rates for the 10mg/ml pravastatin applied.

Table 6.9: Flux rate of 1mg/ml pravastatin over time

Time (hr)	Flux (Js (µg/cm2/hr))		
	Polymer MNs	Hypodermic	Skin
0.083	46.873	38.965	37.62
0.25	0.653	0.795	1.225
0.5	0.650	0.775	0.969
1	0.804	1.449	0.381
2	0.261	8.171	0.185
4	0.026	0.162	0.096
24	0.030	0.033	0.026

Table 6.10: Flux rate of 10mg/ml pravastatin over time

Time (hr)	Flux (Js (µg/cm2/hr))			
	Polymer MNs	Silicon MNs	Hypodermic	Skin
0.083	4196.452	151.053	272.567	130.426
0.25	156.677	5.220	4.817	0.701
0.5	134.053	477.923	441.711	0
1	94.556	291.595	230.782	0.365
2	34.850	133.107	140.756	0.263
4	18.613	10.143	83.551	0.154
6	2.251	16.434	24.634	0.458
8	1.022	0.859	35.550	0.090
24	2.825	16.751	1.807	0.024

These results show that the amount of pravastatin that diffuses through the Franz cell is the greatest with a hypodermic needle, the silicon MNs were about 50% less effective as hypodermic , followed by the polymer MNs which were about 50% less effective again at delivering across the skin into the Franz cell chamber over a 24hour period Drug was found to be in the dermis and epidermis layers of the skin using the polymer MNs. The skin only result confirmed that the drug did not pass through the skin into the PBS at all without a MN or hypodermic needle applied.

In summary this chapter investigates the use for these MNs in the diagnostic and therapeutic sectors and how it would be applied to real world situations. They can be used as sensor platforms to determine glucose, chloride and cholesterol. If the external reference and counter electrodes are changed to integrated MN electrodes alongside the working MN electrode they can be used in skin. These MNs can facilitate the delivery of calcein and pravastatin across the skin barrier.

Conclusion and Future Work

This work has examined the fabrication and use of polymer MNs in both diagnostic and therapeutic applications.

The polymer MNs were prepared by ML3DP which is a highly flexible process. It can be adapted to specifications for different applications using stencils with different aperture sizes, aperture shapes, the number of passes and the type of UV curable polymer. The process also has the advantage over other fabrication methods due to the ability for high volume manufacturing which can be easily adapted . This reduces the cost of making these MNs to a much lower level when compared to MNs made by etching or small scale printing. These polymer MNs may not penetrate as well as metallic or silicon MNs and aren't inherently conductive but may be safer as the material is not at risk of breaking off and is biocompatible.

The starting point of MN fabrication produced MNs using 200μm aperture stencils making cylindrical round tipped MNs therefore the MNs optimised for desired height, stability and penetration efficiency, fabricated by ML3DP required a build which used a wider diameter aperture at the base depositions and a smaller diameter aperture at the needle tip end. The optimal aperture was 400μm, this yielded the most conical type shape which aided in penetration efficiency. This produced MNs which were sharper and had a better penetration efficacy than the starting point. The print gaps were varied multiple times but it was found that several passes at the 0 print gap and then evenly spaced print gaps there after were the most efficient way to fabricate the MNs. The pressure was always higher on the initial passes to ensure good adhesion with the substrate and then lowered so it did not impact the following print gaps due to flexing of the steel stencil. The final protocol 8 reliably produced tips under 10μm with the average diameter of 8μm with the use of a 150μm aperture tipping stencil. This extra tipping step ensured a sharp enough MN tip for penetration.

The protocol that yielded MNs with on average the highest penetration efficiency of 82.42% and therefore these MNs offered penetration that would allow access to interstitial fluid for diagnostic of drug delivery purposes utilised separate stencils for the base and tip portions of the MN fabrication. It had fewer passes (layers) with larger

print gaps allowing the tapered conical shape with a sharp tip to be formed for optimal penetration. It was proved that when these polymer MNs, made using this optimised protocol, when applied to pig skin yielded adequate penetration. The MNs broke through the *stratum corneum* and thus were applicable to be used for drug delivery experiments or diagnostic experiments. These results confirmed that the sharpness of the tip is critical in the success of penetration and height and width of the MNs are also important factors for penetration efficiency. The with the tip diameters of on average under 10μm had penetration efficiencies of between 76.56% and 82.42% where tips with diameters of 20μm and larger only had penetration efficiencies of up to 18.75%.

The mechanical characterisation of the MNs showed that a force 3 times higher than a typical penetration force of 10N will deform the MNs significantly and permanently and the metal coated MNs withstood an even greater force before deformation. These experiments demonstrated that both coated and uncoated MN arrays were mechanically suitable for penetration and use in drug delivery and sensing studies and held up to the forces put upon them during penetration .

The image characterisation of MN devices, used as diagnostic electrodes showed that thicker coatings of silver, due to an extra silver plated layer were much more stable because of the even layer and lack of cracking. Therefore they were more useable and reliable than thinner only PVD silver coated devices. The MNs with a thicker silver layer also had a lower risk of the silver being depleted during the conversion to silver chloride. Utilising MNs with an electro plated silver layer in chloride determination experiments also reduces the chance of complete depletion of the silver layer during the current pulse when using the chloride chronopotentiometry measurement method..

The electrochemical experimental results showed that using silver bar electrodes with a 1.5mA applied current successfully showed the response of the concentration of chloride solutions in the required range between 2.5 and 40mM using MN platforms. MN platforms using a similar method to the silver bar electrodes were adapted into working chloride sensors and successfully showed the response of the concentration of chloride solutions in a similar range to the bar electrodes.

The MN devices were functionalised by immobilising glucose oxidase on the platinum surface and were then successful in detecting a range of concentrations of glucose. The linear detection region was between 2.5 and 20mM glucose which was in line with the concentrations of glucose found in the human body.

The method used for determining glucose with MN devices was investigated using cholesterol oxidase to determine cholesterol concentration. The MN devices were functionalised by immobilising cholesterol oxidase on the platinum surface and were then

also successful in detecting the desired range of concentrations of cholesterol. The linear region was between 1.25 and 15mM cholesterol which is in line with concentrations found in the human body.

These ML3DP polymer MNs were shown to be capable of delivering substances across the skin barrier, such as up to 0.06ug/ml small molecule drug model calcein and up to 80ug/ml large molecule drugs such as pravastatin through a 'poke and patch' method.

Future work to improve the use of MNs as electrodes to determine chloride would be to increase the silver coating further to avoid depletion during conversion of silver to silver chloride. This could lead to investigations in determining higher concentrations of chloride using larger applied currents to increase the range.

To improve accuracy of cholesterol determination, an optimisation of the cholesterol solutions to minimise the use of triton X and ethanol in the effort to reduce the background current and lower the detection limit. These solutions could also be altered to emulate the true contents of the interstitial fluid that would be the fluid tested when using these MNs in practice. These sensors utilised external reference and counter electrodes therefore to be considered for use in human or animal testing, integrated MN reference and counter electrodes should be investigated as the potential or current response could be different for the smaller volumes that would be present in these situations. Further drug delivery tests using 3D human skin cultures could be investigated. Microneedles could also be altered so that they perform both sensing and delivery functions in coupled analytes such as cholesterol and pravastatin. These would be useful in long term monitoring of different diseases and long term conditions that patients experience.

Bibliography

[1] The Manual's Editorial Staff. Common Medical Tests; 2010. Available from: https://www.msdmanuals.com/home/resources/common-medical-tests/common-medical-tests.

[2] Kora P, Ooi CP, Faust O, Raghavendra U, Gudigar A, Chan WY, et al. Transfer learning techniques for medical image analysis: A review. Biocybernetics and Biomedical Engineering. 2022;42(1):79-107. Available from: https://doi.org/10.1016/j.bbe.2021.11.004.

[3] Ghosh A, Nishtala K. Biofluid lipidome: a source for potential diagnostic biomarkers. Clinical and Translational Medicine. 2017;6(1).

[4] Kong K, Kendall C, Stone N, Notingher I. Raman spectroscopy for medical diagnostics â From in-vitro biofluid assays to in-vivo cancer detection. Advanced Drug Delivery Reviews. 2015 jul;89:121-34.

[5] Vashist SK. Point-of-care diagnostics: Recent advances and trends. Biosensors. 2017;7(4):10-3.

[6] Aggarwal A, Pathak S, Goyal R. Clinical and economic outcomes of continuous glucose monitoring system (CGMS) in patients with diabetes mellitus: A systematic literature review. Diabetes Research and Clinical Practice. 2022 apr;186:109825.

[7] Ng KW, Lau WM. Skin deep: The basics of human skin structure and drug penetration. In: Percutaneous Penetration Enhancers Chemical Methods in Penetration Enhancement: Drug Manipulation Strategies and Vehicle Effects; 2015. .

[8] Montagna W. The Structure and Function of Skin. 3rd ed. New York, London: Academic Press; 1974. Available from: https://books.google.co.uk/books?id=50Zgf-ZBP5gCprintsec=frontcoverv=onepageqf=false.

[9] Halder J, Gupta S, Kumari R, Gupta GD, Rai VK. Microneedle Array: Applications, Recent Advances, and Clinical Pertinence in Transdermal Drug Delivery. Journal of Pharmaceutical Innovation. 2021;16(3):558-65.

[10] Waghule T, Singhvi G, Dubey SK, Pandey MM, Gupta G, Singh M, et al.. Microneedles: A smart approach and increasing potential for transdermal drug delivery system. Elsevier Masson SAS; 2019.

[11] Zhao L, Wen Z, Jiang F, Zheng Z, Lu S. Silk/polyols/GOD microneedle based electrochemical biosensor for continuous glucose monitoring. RSC Advances. 2020.

[12] Donnelly RF, Raj Singh TR, Woolfson AD. Microneedle-based drug delivery systems: Microfabrication, drug delivery, and safety. Europe PMC Funders; 2010. Available from: /pmc/articles/PMC2906704/?report=abstract https://www.ncbi.nlm.nih.gov/pmc/articles/PMC2906704/.

[13] McAllister DV, Henry S, Allen MG, Prausnitz MR. Microfabricated microneedles: A novel appraoch to transdermal drug delivery. Proceedings of the Controlled Release Society. 1998;87(25):30-1.

[14] Davis SP, Landis BJ, Adams ZH, Allen MG, Prausnitz MR. Insertion of microneedles into skin : measurement and prediction of insertion force and needle fracture force. Journal of Biomechanics. 2004;37(8):1155-63.

[15] Haq MI, Smith E, John DN, Kalavala M, Edwards C, Anstey A, et al. Clinical administration of microneedles: Skin puncture, pain and sensation. Biomedical Microdevices. 2009;11(1):35-47.

[16] Tran BQ, Miller PR, Taylor RM, Boyd G, Mach PM, Rosenzweig CN, et al. Proteomic Characterization of Dermal Interstitial Fluid Extracted Using a Novel Microneedle-Assisted Technique. Journal of proteome research. 2018;17:479-85.

[17] Heck AJR. Suction blister fluid as potential body fluid for biomarker proteins. Proteomics. 2007;7:3638-50.

[18] Miller PR, Taylor RM, Tran BQ, Boyd G, Glaros T, Chavez VH, et al. Extraction and biomolecular analysis of dermal interstitial fluid collected with hollow microneedles. Communications Biology. 2018;1(1). Available from: http://dx.doi.org/10.1038/s42003-018-0170-z.

[19] Strassner JP, Rashighi M, Ahmed Refat M, Richmond JM, Harris JE. Suction blistering the lesional skin of vitiligo patients reveals useful biomarkers of disease activity. Journal of the American Academy of Dermatology. 2017 may;76(5):847-55.e5.

[20] Samant PP. MICRONEEDLE BASED DEVICE TO SAMPLE INTERSTITIAL FLUID THROUGH SKIN A Dissertation Presented to The Academic Faculty; 2018.

[21] Kim Yc, Park Jh, Prausnitz MR. Microneedles for drug and vaccine delivery â. Advanced Drug Delivery Reviews. 2012;64(14):1547-68. Available from: http://dx.doi.org/10.1016/j.addr.2012.04.005.

[22] Larrañeta E, Lutton REM, Woolfson AD, Donnelly RF. Microneedle arrays as transdermal and intradermal drug delivery systems: Materials science, manufacture and commercial development. Elsevier Ltd; 2016.

[23] Bodhale DW, Nisar A, Afzulpurkar N. Design, Fabrication and Analysis of Silicon Microneedles for Transdermal Drug Delivery Applications. Springer, Berlin, Heidelberg; 2010. p. 84-9. Available from: https://link.springer.com/chapter/10.1007/978-3-642-12020-6$_2$1.

[24] Chiappini C. Porous silicon microneedles and nanoneedles. In: Handbook of Porous Silicon: Second Edition. vol. 1-2. Springer International Publishing; 2018. p. 185-201. Available from: https://link.springer.com/referenceworkentry/10.1007/978-3-319-71381-6$_1$34.

[25] Bhattacharya S, Kam DH, Song L, Mazumder J. Characterization of individual microneedles formed on alloy surfaces by femtosecond laser ablation. Metallurgical and Materials Transactions A: Physical Metallurgy and Materials Science. 2012;43(8):2574-80.

[26] Yan XX, Liu JQ, Jiang SD, Yang B, Yang CS. Fabrication and testing of porous Ti microneedles for drug delivery. Micro and Nano Letters. 2013.

[27] Niinomi M, Nakai M. Titanium-Based Biomaterials for Preventing Stress Shielding between Implant Devices and Bone. International Journal of Biomaterials. 2011;2011.

[28] Vinayakumar KB, Kulkarni PG, Nayak MM, Dinesh NS, Hegde GM, Ramachandra SG, et al. A hollow stainless steel microneedle array to deliver

insulin to a diabetic rat. Journal of Micromechanics and Microengineering. 2016;26(6).

[29] Verbaan FJ, Bal SM, van den Berg DJ, Groenink WHH, Verpoorten H, Lüttge R, et al. Assembled microneedle arrays enhance the transport of compounds varying over a large range of molecular weight across human dermatomed skin. Journal of Controlled Release. 2007 feb;117(2):238-45.

[30] Hartmann XHM, Van Der Linde P, Homburg EFGA, Van Breemen LCA, De Jong AM, Luttge R. Insertion process of ceramic nanoporous microneedles by means of a novel mechanical applicator design. Pharmaceutics. 2015;7(4):503-22.

[31] Lippincott Williams Wilkins. Ceramic Microneedles Resist Breakage, Ease Injections and Draws. Journal of Clinical Engineering. 2008 apr;33(2):65-6. Available from: https://journals.lww.com/jcejournal/Fulltext/2008/04000/Ceramic$_{M}$icroneedles$_{R}$esist$_{B}$reakag

[32] Ita K. Ceramic microneedles and hollow microneedles for transdermal drug delivery: Two decades of research. Editions de Sante; 2018.

[33] Singh P, Carrier A, Chen Y, Lin S, Wang J, Cui S, et al.. Polymeric microneedles for controlled transdermal drug delivery. Elsevier B.V.; 2019.

[34] Wang M, Hu L, Xu C. Recent advances in the design of polymeric microneedles for transdermal drug delivery and biosensing. Royal Society of Chemistry; 2017. Available from: http://xlink.rsc.org/?DOI=C7LC00016B.

[35] Ye Y, Yu J, Wen D, Kahkoska AR, Gu Z. Polymeric microneedles for transdermal protein delivery. Elsevier B.V.; 2018. Available from: /pmc/articles/PMC6020694/?report=abstract https://www.ncbi.nlm.nih.gov/pmc/articles/PMC6020694/.

[36] Jang SJ, Doshi T, Nerayo J, Caprio A, Alaie S, Auge J, et al. Microneedle patterning of 3D nonplanar surfaces on implantable medical devices using soft lithography. Micromachines. 2019;10(10).

[37] Special Chem. Polycarbonate (PC) Plastic: Properties, Uses, Structure - Guide;. Available from: https://omnexus.specialchem.com/selection-guide/polycarbonate-pc-plastic.

[38] Thakur RRS, Tekko IA, Al-Shammari F, Ali AA, McCarthy H, Donnelly RF. Rapidly dissolving polymeric microneedles for minimally invasive intraocular drug delivery. Drug Delivery and Translational Research. 2016 dec;6(6):800-15. Available from: /pmc/articles/PMC5097091/?report=abstract https://www.ncbi.nlm.nih.gov/pmc/articles/PMC5097091/.

[39] Hong X, Wu Z, Chen L, Wu F, Wei L, Yuan W. Hydrogel Microneedle Arrays for Transdermal Drug Delivery Citation. Nano-Micro Letters. 2014;6(3):191-9. Available from: www.nmletters.orghttp://dx.doi.

[40] Kolli CS, Banga AK. Characterization of solid maltose microneedles and their use for transdermal delivery. Pharmaceutical Research. 2008 jan;25(1):104-13. Available from: https://pubmed.ncbi.nlm.nih.gov/17597381/.

[41] Ventrelli L, Marsilio Strambini L, Barillaro G, Ventrelli L, Strambini LM, Barillaro G. Microneedles for Transdermal Biosensing: Current Picture and Future Direction. Advanced Healthcare Materials. 2015. Available from: www.advhealthmat.de.

[42] Gittard SD, Ovsianikov A, Chichkov BN, Doraiswamy A, Narayan RJ. Two-photon polymerization of microneedles for transdermal drug delivery. Expert Opinion on Drug Delivery. 2010 apr;7(4):513-33. Available from: http://www.tandfonline.com/doi/full/10.1517/17425241003628171.

[43] Ribet F, Stemme G, Roxhed N. Real-time intradermal continuous glucose monitoring using a minimally invasive microneedle-based system. Biomedical Microdevices. 2018.

[44] Mandal A, Boopathy AV, Lam LKW, Moynihan KD, Welch ME, Bennett NR, et al. Cell and fluid sampling microneedle patches for monitoring skin-resident immunity. Science Translational Medicine. 2018 nov;10(468):2227. Available from: https://stm.sciencemag.org/content/10/467/eaar2227 https://stm.sciencemag.org/content/10/467/eaar2227.abstract.

[45] Zimmermann S, Fienbork D, Stoeber B, Flounders AW, Liepmann D. A microneedle-based glucose monitor: Fabricated on a wafer-level using in-device enzyme immobilization. In: TRANSDUCERS 2003 - 12th International Conference on Solid-State Sensors, Actuators and Microsystems, Digest of Technical Papers; 2003. .

[46] Long TS, Sokol RJ. Molding polycarbonate: Moisture degradation effect on physical and chemical properties. Polymer Engineering and Science. 1974 dec;14(12):817-22. Available from: http://doi.wiley.com/10.1002/pen.760141202.

[47] Borcak K, Sirbubalo M, Tucak A. Coated 3D Printed PLA Microneedles as Transdermal Drug Delivery Systems. In: CMBEBIH 2019. January; 2020. p. 735-42.

[48] Farah S, Anderson DG, Langer R. Physical and mechanical properties of PLA, and their functions in widespread applications â A comprehensive review. Elsevier B.V.; 2016.

[49] Choi SO, Park JH, Choi Y, Kim Y, Gill HS, Yoon YK, et al. An electrically active microneedle array for electroporation of skin for gene delivery. In: Digest of Technical Papers - International Conference on Solid State Sensors and Actuators and Microsystems, TRANSDUCERS '05. vol. 2; 2005. p. 1513-6.

[50] Designer Data. Poly(methyl methacrylate);. Available from: https://designerdata.nl/materials/plastics/thermo-plastics/poly(methyl-methacrylate).

[51] Delpino Gonzales O, Nicassio A, Eliasson V. Evaluation of the effect of water content on the stress optical coefficient in PMMA. Polymer Testing. 2016 apr;50:119-24.

[52] Evens T, Malek O, Castagne S, Seveno D, Van Bael A. A novel method for producing solid polymer microneedles using laser ablated moulds in an injection moulding process. Manufacturing Letters. 2020 apr;24:29-32.

[53] British Plastics Federation. Polypropylene (PP);. Available from: https://www.bpf.co.uk/plastipedia/polymers/pp.aspx.

[54] Asahi Kasei. Polypropylene Processing Guidelines;. Available from: www.akplastics.com.

[55] Dymax Corporation. MD ® MEDICAL DEVICE ADHESIVES 1180-M-Gel Product Data Sheet Ultra Light-Weld ® 1180-M-Gel Multipurpose Adhesive for Plastics and Metal APPLICATIONS FEATURES RECOMMENDED SUBSTRATES BIOCOMPATIBILITY; 2008. Available from: www.dymax.com/kr.

[56] Sun W, Araci Z, Inayathullah M, Manickam S, Zhang X, Bruce MA, et al. Polyvinylpyrrolidone microneedles enable delivery of intact proteins for diagnostic and therapeutic applications. Acta Biomaterialia. 2013;9(8):7767-74. Available from: /pmc/articles/PMC3800147/?report=abstract https://www.ncbi.nlm.nih.gov/pmc/articles/PMC3800147/.

[57] Park YH, Ha SK, Choi I, Kim KS, Park J, Choi N, et al. Fabrication of Degradable Carboxymethyl Cellulose (CMC) Microneedle with Laser Writing and Replica Molding Process for Enhancement of Transdermal Drug Delivery. Biotechnology and Bioprocess Engineering. 2016;21:110-8.

[58] Sahputra IH, Alexiadis A, Adams MJ. Effects of Moisture on the Mechanical Properties of Microcrystalline Cellulose and the Mobility of the Water Molecules as Studied by the Hybrid Molecular Mechanics-Molecular Dynamics Simulation Method. Journal of Polymer Science Part B: Polymer Physics. 2019 apr;57(8):454-64. Available from: http://doi.wiley.com/10.1002/polb.24801.

[59] Zhu H, Zhu S, Jia Z, Parvinian S, Li Y, Vaaland O, et al. Anomalous scaling law of strength and toughness of cellulose nanopaper. Proceedings of the National Academy of Sciences of the United States of America. 2015 jul;112(29):8971-6. Available from: www.pnas.org/cgi/doi/10.1073/pnas.1502870112.

[60] Demir YK, Akan Z, Kerimoglu O. Sodium Alginate Microneedle Arrays Mediate the Transdermal Delivery of Bovine Serum Albumin. PLoS ONE. 2013 may;8(5). Available from: /pmc/articles/PMC3651096/?report=abstract https://www.ncbi.nlm.nih.gov/pmc/articles/PMC3651096/.

[61] Fadhilah Bt Ibrahim S, Aisyah N, Azam NM, Anuar K, Amin M. Sodium alginate film: the effect of crosslinker on physical and mechanical properties. IOP Conference Series: Materials Science and Engineering. 2019;509.

[62] Rangel-Marrón M, Montalvo-Paquini C PE, López-Malo A. Optimization of the moisture content, thickness, water solubility and water vapor permeability of sodium alginate edible films; 2013. Available from: https://www.semanticscholar.org/paper/Optimization-of-the-moisture-content-

[63] Nguyen HX, Banga AK. Fabrication and Characterization of Maltose Microneedles for Transdermal Drug Delivery. Therapeutic Delivery. 2017;8(5):249-64.

[64] Liu S, Yeo DC, Wiraja C, Tey HL, Mrksich M, Xu C. Peptide delivery with poly(ethylene glycol) diacrylate microneedles through swelling effect. Bioengineering Translational Medicine. 2017 sep;2(3):258-67. Available from: http://doi.wiley.com/10.1002/btm2.10070.

[65] Soule SA, Cashman KV. The mechanical properties of solidified polyethylene glycol 600, an analog for lava crust. Journal of Volcanology and Geothermal Research. 2004 jan;129(1-3):139-53.

[66] Migdadi EM, Courtenay AJ, Tekko IA, McCrudden MTC, Kearney MC, McAlister E, et al. Hydrogel-forming microneedles enhance transdermal delivery of metformin hydrochloride. Journal of Controlled Release. 2018 sep;285:142-51.

[67] Donnelly RF, McCrudden MTC, Alkilani AZ, Larrañeta E, McAlister E, Courtenay AJ, et al. Hydrogel-forming microneedles prepared from "super swelling" polymers combined with lyophilised wafers for transdermal drug delivery. PLoS ONE. 2014 oct;9(10). Available from: /pmc/articles/PMC4216095/?report=abstract https://www.ncbi.nlm.nih.gov/pmc/articles/PMC4216095/.

[68] Swapp S. Scanning Electron Microscopy (SEM);. Available from: https://serc.carleton.edu/research$_e$ducation/geochemsheets/techniques/SEM.html.

[69] Demir YK, Akan Z, Kerimoglu O. Characterization of Polymeric Microneedle Arrays for Transdermal Drug Delivery. PLoS ONE. 2013 oct;8(10):77289. Available from: /pmc/articles/PMC3806750/?report=abstract https://www.ncbi.nlm.nih.gov/pmc/articles/PMC3806750/.

[70] Coulman S, Allender C, Birchall J. Microneedles and other physical methods for overcoming the stratum corneum barrier for cutaneous gene therapy. Begell House Inc.; 2006.

[71] Lutton REM, Woolfson AD, Donnelly RF. Microneedle arrays as transdermal and intradermal drug delivery systems : Materials science , manufacture and commercial development. Materials Science and Engineering R: Reports. 2016;104:1-32.

[72] Kalluri H, Kolli CS, Banga AK. Characterization of microchannels created by metal microneedles: Formation and closure. AAPS Journal. 2011 sep;13(3):473-81. Available from: /pmc/articles/PMC3160154/?report=abstract https://www.ncbi.nlm.nih.gov/pmc/articles/PMC3160154/.

[73] Roxhed N, Gasser TC, Griss P, Holzapfel GA, Stemme G. Penetration-enhanced ultrasharp microneedles and prediction on skin interaction for efficient transdermal drug delivery. Journal of Microelectromechanical Systems. 2007 dec;16(6):1429-40.

[74] Larrañeta E, Moore J, Vicente-Pérez EM, González-Vázquez P, Lutton R, Woolfson AD, et al. A proposed model membrane and test method for microneedle insertion studies. International Journal of Pharmaceutics. 2014.

[75] Enfield J, O'Connell ML, Lawlor K, Jonathan E, O'Mahony C, Leahy M. In-vivo dynamic characterization of microneedle skin penetration using optical coherence tomography. Journal of Biomedical Optics. 2010;15(4):046001. Available from: http://biomedicaloptics.spiedigitallibrary.org/article.aspx?doi=10.1117/1.3463002.

[76] Yuan W, Chen D, Sarabia-Estrada R, Guerrero-Cázares H, Li D, Quiñones-Hinojosa A, et al. Theranostic OCT microneedle for fast ultrahigh-resolution deep-brain imaging and efficient laser ablation in vivo. Science Advances. 2020 apr;6(15):eaaz9664. Available from: https://advances.sciencemag.org/content/6/15/eaaz9664 https://advances.sciencemag.org/content/6/15/eaaz9664.abstract.

[77] Zahn JD, Talbot NH, Liepmann D, Pisano AP. Microfabricated Polysilicon Microneedles for Minimally Invasive Biomedical Devices; 2000. 4.

[78] Park JH, Allen MG, Prausnitz MR. Biodegradable polymer microneedles: Fabrication, mechanics and transdermal drug delivery. Journal of Controlled Release. 2005;104(1):51-66.

[79] Khanna P, Strom JA, Malone JI, Bhansali S. Microneedle-based automated therapy for diabetes mellitus. Journal of Diabetes Science and Technology. 2008;2(6):1122-9.

[80] Forvi E, IAENG M, Soncini M, Bedoni M, Rizzo F, Casella M, et al. A Method To Determine The Margin Of Safety For Microneedles Arrays. London; 2010.

[81] Ashraf MW, Afzulpurkar N, Nisar A, Tayyaba S. Fabrication and analysis of hollow microneedles and polymeric piezoelectric valveless micropump for transdermal drug-delivery system. IET Communications. 2012.

[82] Ripolin A, Quinn J, Larrañeta E, Vicente-Perez EM, Barry J, Donnelly RF. Successful application of large microneedle patches by human volunteers. International Journal of Pharmaceutics. 2017 apr;521(1-2):92-101.

[83] Zainal Abidin HE, Ooi PC, Tiong TY, Marsi N, Ismardi A, Mohd Noor M, et al. Stress and Deformation of Optimally Shaped Silicon Microneedles for Transdermal Drug Delivery. Journal of Pharmaceutical Sciences. 2020:1-8. Available from: https://doi.org/10.1016/j.xphs.2020.04.019.

[84] Manea F. Electrochemical Techniques for Characterization and Detection Application of Nanostructured Carbon Composite. In: Modern Electrochemical Methods in Nano, Surface and Corrosion Science. InTech; 2014. p. 32-54. Available from: http://dx.doi.org/10.5772/58633.

[85] Esfandyarpour R, Esfandyarpour H, Javanmard M, Harris JS, Davis RW. Microneedle biosensor: A method for direct label-free real time protein detection. Sensors and Actuators, B: Chemical. 2013;177:848-55. Available from: http://dx.doi.org/10.1016/j.snb.2012.11.064.

[86] Caffarel-Salvador E, Brady AJ, Eltayib E, Meng T, Alonso-Vicente A, Gonzalez-Vazquez P, et al. Hydrogel-forming microneedle arrays allow detection of drugs and glucose in vivo: Potential for use in diagnosis and therapeutic drug monitoring. PLoS ONE. 2015;10(12):1-21.

[87] Miller PR, Narayan RJ, Polsky R. Microneedle-based sensors for medical diagnosis. Journal of Materials Chemistry B. 2016;4(8):1379-83.

[88] Takeuchi K, Kim B. Functionalized microneedles for continuous glucose monitoring. Nano Convergence. 2018;5(1). Available from: https://doi.org/10.1186/s40580-018-0161-2.

[89] Mohan AMV, Windmiller JR, Mishra RK, Wang J. Continuous minimally-invasive alcohol monitoring using microneedle sensor arrays. Biosensors and Bioelectronics. 2017;91(January):574-9. Available from: http://dx.doi.org/10.1016/j.bios.2017.01.016.

[90] Mishra RK, Vinu Mohan AM, Soto F, Chrostowski R, Wang J. A microneedle biosensor for minimally-invasive transdermal detection of nerve agents. Analyst. 2017;142(6):918-24.

[91] Gowers SAN, Freeman DME, Rawson TM, Rogers ML, Wilson RC, Holmes AH, et al. Development of a Minimally Invasive Microneedle-Based Sensor for Continuous Monitoring of β-Lactam Antibiotic Concentrations in Vivo. ACS Sensors. 2019 apr;4(4):1072-80.

[92] Senel M, Dervisevic M, Voelcker NH. Gold microneedles fabricated by casting of gold ink used for urea sensing. Materials Letters. 2019.

[93] Ranamukhaarachchi SA, Padeste C, Dübner M, Häfeli UO, Stoeber B, Cadarso VJ. Integrated hollow microneedle-optofluidic biosensor for therapeutic drug monitoring in sub-nanoliter volumes. Scientific Reports. 2016;6(June):1-10. Available from: http://dx.doi.org/10.1038/srep29075.

[94] Skaria E, Patel BA, Flint MS, Ng KW. Poly(lactic acid)/Carbon Nanotube Composite Microneedle Arrays for Dermal Biosensing. Analytical Chemistry. 2019;91(7):4436-43.

[95] Dardano P, Caliò A, Di Palma V, Bevilacqua MF, Di Matteo A, De Stefano L. Glucose sensing electrode system based on polymeric microneedles. In: SAS 2016 - Sensors Applications Symposium, Proceedings; 2016. .

[96] Barrett C, Dawson K, O'Mahony C, O'Riordan A. Development of Low Cost Rapid Fabrication of Sharp Polymer Microneedles for In Vivo Glucose Biosensing Applications. ECS Journal of Solid State Science and Technology. 2015.

[97] Hwa KY, Subramani B, Chang PW, Chien M, Huang JT. Transdermal microneedle array-based sensor for real time continuous glucose monitoring. International Journal of Electrochemical Science. 2015.

[98] Katz E, Bückmann AF, Willner I. Self-powered enzyme-based biosensors [8]; 2001.

[99] Jina A, Tierney MJ, Tamada JA, McGill S, Desai S, Chua B, et al. Design, development, and evaluation of a novel microneedle array-based continuous glucose monitor. Journal of Diabetes Science and Technology. 2014.

[100] Valencia E, Marin A, Hardy G. Impact of oral L-glutamine on glutathione, glutamine, and glutamate blood levels in volunteers. In: Nutrition; 2002. .

[101] Radiometer. Lactate as an aid in sepsis diagnosis and management - Radiometer;. Available from: https://www.radiometer.co.uk/en-gb/diagnostics/sepsisdetection/lactate.

[102] EKF Diagnostics. Lactate testing for athletes | EKF;. Available from: https://www.ekfdiagnostics.com/lactate-testing-for-athletes.html.

[103] Rathee K, Dhull V, Dhull R, Singh S. Biosensors based on electrochemical lactate detection: A comprehensive review. Biochemistry and Biophysics Reports. 2016;5(November 2015):35-54. Available from: http://dx.doi.org/10.1016/j.bbrep.2015.11.010.

[104] Pundir CS, Narwal V, Pundir CS. A Bird's Eye View of Lactate Biosensors Journal of Intensive and Critical Care. Journal of Intensive and Critical Care. 2017;3(3). Available from: http://www.imedpub.com/http://criticalcare.imedpub.com/.

[105] Sharma S, Saeed A, Johnson C, Gadegaard N, Cass AE. Rapid, low cost prototyping of transdermal devices for personal healthcare monitoring. Sensing and Bio-Sensing Research. 2017 apr;13:104-8.

[106] Bollella P, Sharma S, Cass AEG, Antiochia R. Microneedle-based biosensor for minimally-invasive lactate detection. Biosensors and Bioelectronics. 2019 jan;123:152-9.

[107] Caliò A, Dardano P, Di Palma V, Bevilacqua MF, Di Matteo A, Iuele H, et al. Polymeric microneedles based enzymatic electrodes for electrochemical biosensing of glucose and lactic acid. Sensors and Actuators, B: Chemical. 2016.

[108] North Carolina State University. Wearable, low-cost sensor to measure skin hydration – ScienceDaily; 2017. Available from: https://www.sciencedaily.com/releases/2017/01/170130111030.htm.

[109] Vulpe C. Hydration Measurement Methods for Athletes; 2017. Available from: https://www.brianmac.co.uk/articles/article249.htm.

[110] Cystic Fibrosis Trust. What is cystic fibrosis?;. Available from: https://www.cysticfibrosis.org.uk/what-is-cystic-fibrosis?gclid=CjwKCAjwztL2BRATEiwAvnALcjQYsef-MF98EDhl8FzMjyLzeCC9MCLn8nhne9aWaxrE4bi-bgAuchoCCcYQAvD$_B$wE.

[111] Emaminejad S, Gao W, Wu E, Davies ZA, Nyein HYY, Challa S, et al. Autonomous sweat extraction and analysis applied to cystic fibrosis and glucose monitoring using a fully integrated wearable platform. Proceedings of the National Academy of Sciences of the United States of America. 2017 may;114(18):4625-30.

[112] Jin J, Ouyang X, Li J, Jiang J, Wang H, Wang Y, et al. Nucleic acid-modulated silver nanoparticles: A new electrochemical platform for sensing chloride ion. Analyst. 2011;136(18):3629-34.

[113] Dong H, Zhang L, Liu W, Tian Y. Label-Free Electrochemical Biosensor for Monitoring of Chloride Ion in an Animal Model of Alzhemier's Disease. ACS Chemical Neuroscience. 2017 feb;8(2):339-46.

[114] Kwak B, Park S, Lee HS, Kim J, Yoo B. Improved Chloride Ion Sensing Perform-ance of Flexible Ag-NPs/AgCl Electrode Sensor Using Cu-BTC as an Effective Adsorption Layer. Frontiers in Chemistry. 2019 sep;7:637. Available from: https://www.frontiersin.org/article/10.3389/fchem.2019.00637/full.

[115] Bujes-Garrido J, Arcos-Martínez MJ. Development of a wearable electrochemical sensor for voltammetric determination of chloride ions. Sensors and Actuators, B: Chemical. 2017 mar;240:224-8.

[116] Heart UK. Understand your cholesterol results;. Available from: https://www.heartuk.org.uk/cholesterol/understanding-your-cholesterol-test-results-.

[117] Ahmadraji T, Killard AJ. Measurement of total cholesterol us-ing an enzyme sensor based on a printed hydrogen peroxide elec-trocatalyst. Analytical Methods. 2016 apr;8(13):2743-9. Available from: https://pubs.rsc.org/en/content/articlehtml/2016/ay/c6ay00468g https://pubs.rsc.org/en/content/articlelanding/2016/ay/c6ay00468g.

[118] YÄ±ld±r±moluF, ArslanF, eteS, Y aarA.PreparationofaPolypyrrole − Polyvinylsulphonate(6435 − 45.Availablefrom : http : //www.mdpi.com/1424 − 8220/9/8/6435.

[119] Freire RS, Pessoa CA, Mello LD, Kubota LT. Direct electron trans-fer: An approach for electrochemical biosensors with higher selectiv-ity and sensitivity. Sociedade Brasileira de Quimica; 2003. Avail-able from: http://www.scielo.br/scielo.php?script=sci$_a$rttextpid = $S0103 − 50532003000200008lng = ennrm = isotlng = enhttp :$ $//www.scielo.br/scielo.php?script = sci_abstractpid = S0103 −$ $50532003000200008lng = ennrm = isotlng = en.$

[120] Noma A, Nakayama K. Polarographic Method for Rapid Microdetermination of Cholesterol with Cholesterol Esterase and Cholesterol Oxidase; 1976. 3.

[121] Devi S, Kanwar SS. Cholesterol Oxidase: Source,Properties and Applications. Insights in Enzyme Research. 2018;01(01).

[122] Lin X, Ni Y, Kokot S. Electrochemical cholesterol sensor based on cholesterol oxidase and MoS2-AuNPs modified glassy carbon electrode. Sensors and Actuators, B: Chemical. 2016 oct;233:100-6.

[123] Alagappan M, Immanuel S, Sivasubramanian R, Kandaswamy A. Development of cholesterol biosensor using Au nanoparticles decorated f-MWCNT covered with polypyrrole network. Arabian Journal of Chemistry. 2020 jan;13(1):2001-10.

[124] Li J, Peng T, Peng Y. A Cholesterol Biosensor Based on Entrapment of Cholesterol Oxidase in a Silicic Sol-Gel Matrix at a Prussian Blue Modified Electrode. Electroanalysis. 2003 jul;15(12):1031-7. Available from: http://doi.wiley.com/10.1002/elan.200390124.

[125] Wisitsoraat A, Karuwan C, Wong-ek K, Phokharatkul D, Sritongkham P, Tuantranont A. High sensitivity electrochemical cholesterol sensor utilizing a vertically aligned carbon nanotube electrode with electropolymerized enzyme immobilization. Sensors. 2009 nov;9(11):8658-68. Available from: /pmc/articles/PMC3260606/?report=abstract https://www.ncbi.nlm.nih.gov/pmc/articles/PMC3260606/.

[126] Nien PC, Chen PY, Ho KC. Fabricating an amperometric cholesterol biosensor by a covalent linkage between Poly(3-thiopheneacetic acid) and cholesterol oxidase. Sensors. 2009;9(3):1794-806.

[127] Paul S. Biomedical Engineering and its Applications in Healthcare. Springer Singapore; 2019. Available from: https://books.google.co.uk/books?id=Ake9DwAAQBAJpg=PA147lpg=PA147dq=second+gener$6_0 sig = ACfU3U2nekD0UjY8pJQn8JqLqT6b-gkw5Qhl = ensa = Xved = 2ahUKEwj0hs7JoL7qAhXSasAKHSkkBS0Q6AEwAXoECA0QAQv = onepage.$

[128] Karyakin AA, Karyakina EE, Gorton L. Amperometric biosensor for glutamate using Prussian Blue-based 'artificial peroxidase' as a transducer for hydrogen peroxide. Analytical Chemistry. 2000 apr;72(7):1720-3. Available from: https://pubs.acs.org/sharingguidelines.

[129] Tan X, Li M, Cai P, Luo L, Zou X. An amperometric cholesterol biosensor based on multiwalled carbon nanotubes and organically modified sol-gel/chitosan hybrid composite film. Analytical Biochemistry. 2005 feb;337(1):111-20.

[130] Vidal JC, Espuelas J, Garcia-Ruiz E, Castillo JR. Amperometric cholesterol biosensors based on the electropolymerization of pyrrole and the electrocatalytic effect of Prussian-Blue layers helped with self-assembled monolayers. Talanta. 2004 oct;64(3):655-64.

[131] Zhang H, Liu R, Zheng J. Seed-mediated synthesis of polyaniline/Au nanocomposite and its application for a cholesterol biosensor. Synthetic Metals. 2013;167(1):5-9. Available from: http://dx.doi.org/10.1016/j.synthmet.2013.01.020.

[132] Rahman MM, Asiri AM. One-step electrochemical detection of cholesterol in the presence of suitable K3Fe(CN)6/phosphate buffer mediator by an electrochemical approach. Talanta. 2015 aug;140:96-101.

[133] Lata K, Dhull V, Hooda V. Fabrication and Optimization of ChE/ChO/HRP-AuNPs/c-MWCNTs Based Silver Electrode for Determining Total Cholesterol in Serum. Biochemistry Research International. 2016. Available from: http://dx.doi.org/10.1155/2016/1545206.

[134] Abbas Y, Olthuis W, Van Den Berg A. A chronopotentiometric approach for measuring chloride ion concentration. Sensors and Actuators, B: Chemical. 2013 nov;188:433-9.

[135] Gao J, Huang W, Chen Z, Yi C, Jiang L. Simultaneous detection of glucose, uric acid and cholesterol using flexible microneedle electrode array-based biosensor and multi-channel portable electrochemical analyzer. Sensors and Actuators, B: Chemical. 2019 may;287:102-10.

[136] Chen W, Li H, Shi D, Liu Z, Yuan W. Microneedles As a Delivery System for Gene Therapy. Frontiers in Pharmacology. 2016 may;7(137). Available from: http://journal.frontiersin.org/Article/10.3389/fphar.2016.00137/abstract.

[137] Xie L, Zeng H, Sun J, Qian W. Engineering Microneedles for Therapy and Diagnosis :. Micromachines. 2020:1-28.

[138] Kirkby M, Hutton ARJ, Donnelly RF. Microneedle Mediated Transdermal Delivery of Protein, Peptide and Antibody Based Therapeutics: Current Status and Future Considerations. NLM (Medline); 2020.

[139] Li S, Li W, Prausnitz M. Individually coated microneedles for co-delivery of multiple compounds with different properties. Drug Delivery and Translational Research. 2018 oct;8(5):1043-52.

[140] Liu L, Kai H, Nagamine K, Ogawa Y, Nishizawa M. Porous polymer microneedles with interconnecting microchannels for rapid fluid transport. RSC Advances. 2016;6(54):48630-5. Available from: http://dx.doi.org/10.1039/C6RA07882F.

[141] Ji J, Tay FEH, Miao J, Iliescu C. Microfabricated microneedle with porous tip for drug delivery. Journal of Micromechanics and Microengineering. 2006;16:958-64.

[142] Nagamine K, Kubota J, Kai H, Ono Y, Nishizawa M. An array of porous microneedles for transdermal monitoring of intercellular swelling. Biomedical Microdevices. 2017 sep;19(3):1-6.

[143] Martanto W, Davis SP, Holiday NR, Wang J, Gill HS, Prausnitz MR. Transdermal Delivery of Insulin Using Microneedles in Vivo. Pharmaceutical research. 2004;21(6):947-52.

[144] Pettis RJ, Harvey AJ. Microneedle delivery: Clinical studies and emerging medical applications; 2012. Available from: http://www.future-science.com/doi/10.4155/tde.12.13.

[145] Daddona PE, Matriano JA, Mandema J, Maa YF. Parathyroid hormone (1-34)-coated microneedle patch system: Clinical pharmacokinetics and pharmacodynamics for treatment of osteoporosis. Pharmaceutical Research. 2011 jan;28(1):159-65. Available from: https://link.springer.com/article/10.1007/s11095-010-0192-9.

[146] Gupta J, Denson DD, Felner EI, Prausnitz MR. Rapid local anesthesia in humans using minimally invasive microneedles. Clinical Journal of Pain. 2012.

[147] Li X, Zhao R, Qin Z, Zhang J, Zhai S, Qiu Y, et al. Microneedle pretreatment improves efficacy of cutaneous topical anesthesia. American Journal of Emergency Medicine. 2010.

[148] Rouphael NG, Paine M, Mosley R, Henry S, McAllister DV, Kalluri H, et al. The safety, immunogenicity, and acceptability of inactivated influenza vaccine delivered by microneedle patch (TIV-MNP 2015): a randomised, partly blinded, placebo-controlled, phase 1 trial. The Lancet. 2017 aug;390(10095):649-58. Available from: https://linkinghub.elsevier.com/retrieve/pii/S0140673617305755.

[149] Bio-Nano Technology Co L. Applications-Suzhou Natong Bio-Nano Technology Co., Ltd.;. Available from: http://www.nanomed-skincare.com/about/?23.html.

[150] BD. - News Events - BD Soluviaâ¢ Microinjection System Used For First Approved Intradermal Influenza Vaccine in the European Union;. Available from: https://www.bd.com/contentmanager/b$_a$rticle.asp?Item$_I$D = 23817ContentType$_I$D = 1BusinessCode = 20001d = s = dTitle = dc = dcTitle = .

[151] Bragazzi NL, Orsi A, Ansaldi F, Gasparini R, Icardi G. Fluzone® intra-dermal (Intanza®/Istivac® Intra-dermal): An updated overview. Taylor and Francis Inc.; 2016. Available from: /pmc/articles/PMC5085005/?report=abstract https://www.ncbi.nlm.nih.gov/pmc/articles/PMC5085005/.

[152] RAPHAS. Cosmetic Area | RAPHAS;. Available from: http://www.raphas.com/en/business/cosmetic.

[153] Nanopass Technologies. Homepage - NanoPass Technologies Ltd;. Available from: https://www.nanopass.com/.

[154] Ellison TJ, Talbott GC, Henderson DR. VaxiPatchâ¢, a novel vaccination system comprised of subunit antigens, adjuvants and microneedle skin delivery: An application to influenza B/Colorado/06/2017. Vaccine. 2020 jul;38:6839-48. Available from: https://linkinghub.elsevier.com/retrieve/pii/S0264410X20309580.

[155] R R Singh T, J Dunne N, Cunningham E, F Donnelly R. Review of Patents on Microneedle Applicators. Recent Patents on Drug Delivery Formulation. 2011.

[156] Leone M, van Oorschot BH, Nejadnik MR, Bocchino A, Rosato M, Kersten G, et al. Universal applicator for digitally-controlled pressing force and impact velocity insertion of microneedles into skin. Pharmaceutics. 2018;10(4).

[157] McAllister DV. MICRONEEDLE PATCH APPLICATOR SYSTEM. United States Patent. 2016;2(12).

[158] Yang J, Liu X, Fu Y, Song Y. Recent advances of microneedles for biomedical applications: drug delivery and beyond. Chinese Academy of Medical Sciences; 2019.

[159] Doddaballapur S. Microneedling with dermaroller. Journal of Cutaneous and Aesthetic Surgery. 2009;2(2):110. Available from: /pmc/articles/PMC2918341/?report=abstract https://www.ncbi.nlm.nih.gov/pmc/articles/PMC2918341/.

[160] Majid I. Microneedling therapy in atrophic facial scars: An objective assessment. Journal of Cutaneous and Aesthetic Surgery. 2009;2(1):26. Available from: /pmc/articles/PMC2840919/?report=abstract https://www.ncbi.nlm.nih.gov/pmc/articles/PMC2840919/.

[161] clinic S. Swiss Clinic Skin Roller | Free Shipping | Lookfantastic;. Available from: https://www.lookfantastic.com/swiss-clinic-skin-roller/12090926.html?affil=thggpsadswitchcurrency=GBPshippingcountry=GBthg$_p$pc$_c$ampaign 71700000047040816adtype $=$ $plaproduct_id$ $=$ $12090926gclid$ $=$ $CjwKCAjwltH3BRB6EiwAhj0IUBkvESY0TkYjV4nIfliRnZYaK2VT9hl_p-$ VKA.

[162] Dermaroller. Premium Skin Roller - ZGTS Dermaroller 192, 540 Micro Needle Titanium Gold Coated Scar Reduction Dermaroller Therapy;. Available from: http://www.zgts.in/.

[163] Dermaroller. Original Dermaroller: schöne Haut mit Microneedling zuhause | Dermaroller GmbH | Home Skin Care Shop;. Available from: https://www.original-dermaroller.de/de/home-skin-care.

[164] Dermaroller. Derma Roller - 2.5mm | SkinRadiance;. Available from: https://skinradiance.org/collections/derma-rollers/products/skin-radiance-2-5mm-body-derma-roller-professional-best-derma-roller-for-stretch-marks-use-on-wrinkles-stretch-marks-acne-hair-loss-scar-removal-pitted-skin-and-hyper-pigmentation-use-with-skin-r.

[165] Sabri AH, Cater Z, Ogilvie J, Scurr DJ, Marlow M, Segal J. Characterisation of mechanical insertion of commercial microneedles. Journal of Drug Delivery Science and Technology. 2020 aug;58:101766.

[166] Bellus Medical. Frequently Asked Questions | SkinPen by Bellus Medical;. Available from: https://skinpen.com/faq-skinpen/.

[167] Bellus Medical. SkinPen Efficacy on Acne Scars on the Face and/or

Back - Full Text View - ClinicalTrials.gov; 2016. Available from: https://clinicaltrials.gov/ct2/show/NCT02646917.

[168] Bellus Medical, Biolabs E. SkinPen® + Skinfuse® Microneedling Study BACK-GROUND. Addison, Texas; 2017.

[169] Zitstika. Home | ZitStickaâ¢ â ZitSticka UK;. Available from: https://zitsticka.co.uk/.

[170] CosMED. CosMED Pharmaceutical Co. Ltd.,;. Available from: https://cosmed-pharm.co.jp/lang-en/.

[171] Faraji G, Kim HS, Kashi HT. Introduction. In: Severe Plastic Deformation. Elsevier; 2018. p. 1-17.

[172] Nanakoudis A. What is SEM? Scanning Electron Microscopy Explained; 2019. Available from: https://www.thermofisher.com/blog/materials/what-is-sem-scanning-electron-microscopy-explained/.

[173] Amri E, Mamboya F. Papain, a plant enzyme of biological importance: A review. American Journal of Biochemistry and Biotechnology. 2012;8(2):99-104.

[174] Dabbagh SR, Sarabi MR, Rahbarghazi R, Sokullu E, Yetisen AK, Tasoglu S. 3D-printed microneedles in biomedical applications. iScience. 2021;24(1):102012. Available from: https://doi.org/10.1016/j.isci.2020.102012.

[175] Detamornrat U, McAlister E, Hutton ARJ, Larrañeta E, Donnelly RF. The Role of 3D Printing Technology in Microengineering of Microneedles. Small. 2022;18(18).

[176] Ozkucur N, Wetzel C, Hollstein F, Richter E, Funk RHW, Monsees TK. Physical vapor deposition of zirconium or titanium thin films on flexible polyurethane highly support adhesion and physiology of human endothelial cells. Journal of Biomedical Materials Research - Part A. 2009;89(1):57-67.

[177] Yu H, Yu J, Li L, Zhang Y, Xin S, Ni X, et al. Recent Progress of the Practical Applications of the Platinum Nanoparticle-Based Electrochemistry Biosensors. Frontiers in Chemistry. 2021;9(May):1-20.

[178] Pizzetti F, Salvietti E, Giurlani W, Emanuele R, Fontanesi C, Innocenti M. Cyanide-free silver electrodeposition with polyethyleneimine and 5,5-dimethylhydantoin as organic additives for an environmentally friendly formulation. Journal of Electroanalytical Chemistry. 2022 apr;911:116196.

[179] Nishino J. Structure Control of Silver Tree by Pulse Electro-deposition Method via AgNO3 Aqueous Solution. ECS Meeting Abstracts. 2008:2-3.

[180] Wu L, Shrestha P, Iapichino M, Cai Y, Kim B, Stoeber B. Characterization method for calculating diffusion coefficient of drug from polylactic acid (PLA) microneedles into the skin. Journal of Drug Delivery Science and Technology. 2021 feb;61:102192.

[181] Bolton CJW, Howells O, Blayney GJ, Eng PF, Birchall JC, Gualeni B, et al. Hollow silicon microneedle fabrication using advanced plasma etch technologies for applications in transdermal drug delivery. Lab on a Chip. 2020 jul;20(15):2788-95. Available from: https://pubs.rsc.org/en/content/articlehtml/2020/lc/d0lc00567c https://pubs.rsc.org/en/content/articlelanding/2020/lc/d0lc00567c.

[182] Abbas Y, de Graaf DB, Olthuis W, van den Berg A. Dynamic electrochemical measurement of chloride ions. Journal of Visualized Experiments. 2016;2016(108):2-9.

[183] Robbins J. Ions in solution 2: An introduction to electrochemistry. 2nd ed. A PW, editor. Oxford: Oxford University Press; 1979.

[184] Abbas Y, Olthuis W, Van Den Berg A. A chronopotentiometric approach for measuring chloride ion concentration. Sensors and Actuators, B: Chemical. 2013;188:433-9. Available from: http://dx.doi.org/10.1016/j.snb.2013.07.046.

[185] Abbas Y, Pargar F, Koleva DA, van Breugel K, Olthuis W, van den Berg A. Non-destructive measurement of chloride ions concentration in concrete â A comparative analysis of limitations and prospects. Construction and Building Materials. 2018;174:376-87. Available from: https://doi.org/10.1016/j.conbuildmat.2018.04.135.

[186] Nath A. Michaelis-Menten Kinetics and Briggs-Haldane Kinetics; 2007. Available from: https://depts.washington.edu/wmatkins/kinetics/michaelis-menten.html.